

# ULF oscillations in the terrestrial magnetosphere

Peter Francis Tullet  
[BSc Physics, MSc Astrophysics]

A thesis submitted to Lancaster University for the degree of Doctor of Philosophy

16<sup>th</sup> October 2009



Space Plasma Environment and Radio Science Group  
Department of Communication Systems  
InfoLab 21  
Lancaster University  
Lancaster  
LA1 4WA

With grateful thanks  
to ExH

Fascination lies in the magic of the extraordinary  
Ralph Anstoetz

I declare that the work contained in this thesis is my own, except where stated otherwise.  
No part of this thesis has been submitted for a higher degree anywhere other than to  
Lancaster University

# ULF oscillations in the terrestrial magnetosphere

## Abstract

The terrestrial magnetosphere is pervaded by ULF oscillations of the space-plasma electric and magnetic fields. A ULF null direction-finding technique was devised for ground magnetometer data which showed an underlying high-latitude direction of arrival biased towards the morning sector. To understand this, the classical Helmholtz equation, which explains the propagation of electromagnetic and acoustic waves, was numerically solved for simulated plane-parallel ULF waves incident on MHD magnetospheric data. The resulting simulation shows waveguiding around the terrestrial Alfvén gradient through the region threaded by high-latitude magnetic field-lines, as well as the existence of ULF lobes in the magnetotail and diffraction of ULF waves in the tail plasma sheet.

Polar satellite ULF data was classified into six magnetospheric groups during the Autumn seasons of 2002 and 2003 at times when the Polar satellite field line trace was between Finland and Greenland. Thirty-nine observations are presented where the magnetospheric signals coincided with a terrestrial event. Three of the magnetospheric groups are concerned with Poynting flux impulses [PFIs] and their detection in Polar satellite data was shown to be coincident with enhanced absorption in IRIS riometer data. These PFIs were shown to mark the time when the trajectories of charged particles are redirected towards the Earth. The intensity of these PFIs was shown to be sufficient to provide electrons with auroral energy. Multiple pulsed PFIs were also observed which could transfer substantial energy to trapped electrons, be related to oscillatory magnetic reconnection and explain auroral optical modulation. Observations were made of magnetospheric events related to the onset and expansion phase of substorms and of a related phenomena which had the useful property of temporal and spatial localisation that enabled it to be mapped and the sequence of ionospheric precipitation deduced. Eleven observations were also made of the electromagnetic quadrature signature of field line resonance.

<b>Contents</b>	<b>Page</b>
Figure list	9
Table list	11
Acronym list	12
Acknowledgements	13
Acknowledgements for geophysical data	14

## **Part I Space plasma physics**

<b>1.0</b>	<b>Introductory background</b>	<b>16</b>
1.1	Electric and magnetic fields	17
1.2	The terrestrial magnetic field	18
1.2.1	The geomagnetic field of internal origin	18
1.2.2	The geomagnetic field of external origin	19
1.3	Geomagnetic shells	19
1.4	Space plasma	21
1.5	Plasma shocks	22
1.6	Plasma instability	22
1.7	Solar wind	24
1.7.1	Interaction between the solar wind and the terrestrial magnetosphere	25
1.8	Magnetic reconnection	28
1.9	Dayside magnetic reconnection	29
1.10	Plasma convection cycle	31
1.11	Geomagnetic substorms	32
1.11.1	Substorm growth phase	32
1.11.2	Substorm expansion phase [intensification]	33
1.11.3	Substorm recovery phase	36
1.12	The ionosphere	37
1.12.1	Ionospheric Hall currents	37
1.12.2	Field-aligned currents	38
1.13	The tail plasma sheet	39
1.14	Aurora	41
1.14.1	Ionospheric auroral electric fields	43

<b>2.0</b>	<b>ULF waves</b>	45
2.1	Introduction	45
2.1.1	Classification of pulsations	46
2.1.2	Pc5 and Pi2 waves	47
2.2	Sources of ULF waves	48
2.2.1	External excitation of ULF waves	49
2.2.2	Internal excitation of ULF waves	51
2.3	ULF wave phenomena	51
2.3.1	Polarisation of ULF waves	51
2.3.2	Interaction of ULF waves with the ionosphere	52
2.3.3	Interaction of ULF waves with relativistic electrons	53
2.4	ULF resonance	53
2.4.1	Field line resonance	55
2.4.2	Cross phase technique	56
2.4.3	Magnetospheric waveguide and cavity modes	58
2.5	Poynting flux	59
2.5.1	Derivation of the Poynting flux theorem	59
2.5.2	Interpretation of $\mathbf{E} \times \mathbf{H}$	61
2.5.3	Poynting flux vector for ULF oscillations	62
2.5.4	Detection of electromagnetic waves	63
2.5.5	Poynting flux signature of electromagnetic standing waves	64
2.5.6	Ionospheric Poynting flux	65
<b>3.0</b>	<b>Instrumentation and data processing</b>	66
3.1	Ground based instruments	66
3.1.1	Fluxgate magnetometers	66
3.1.2	IMAGE chain	68
3.1.3	SAMNET	69
3.1.4	Greenland magnetometers	70
3.1.5	Canadian CARISMA magnetometers	70
3.1.6	IRIS riometer	71
3.2	Polar satellite instruments	72

## Part II Studies

<b>4.0</b>	<b>A null phase-difference technique for ULF wave direction-finding</b>	<b>76</b>
4.1	Introduction	76
4.2	Ionospheric and ground magnetometer phase-difference	76
4.3	Frequency domain observations of phase-difference	77
4.4	Analysis in the Geocentric Solar Ecliptic [GSE] frame of reference	78
4.5	Ionospheric phase speed estimation	81
4.6	Discussion and conclusions	82
<b>5.0</b>	<b>Solving the Helmholtz equation for the magnetosphere</b>	<b>83</b>
5.1	Introduction	83
5.2	Helmholtz equation	84
5.3	Helmholtz equation solution for highly idealised data	85
5.4	Helmholtz equation solution for magnetospheric model data	86
5.5	Discussion and conclusions	89
<b>6.0</b>	<b>Poynting flux classification of ULF oscillations</b>	<b>91</b>
6.1	Introduction	91
6.2	Magnetospheric classification groups	91
6.3	The thirty-nine magnetospheric events	94
6.3.1	Temporal coincidence	99
6.3.2	Geographic separation of temporal coincidence	101
6.3.3	Coincidence and association	101
6.4	Poynting flux vectors	102
6.5	Examples of events in the magnetospheric groups	106
6.5.1	Magnetospheric Group I event 1600-1700UT on 2002-12-17	106
6.5.2	Magnetospheric Group II event 1800-1900UT on 2002-12-27	107
6.5.3	Magnetospheric Group III event 1630-1730UT on 2003-11-22	109
6.5.4	Magnetospheric Group IV event 1800-1900UT on 2003-11-09	111
6.5.5	Magnetospheric Group V event 2100-2200UT on 2003-10-19	113
6.5.6	Magnetospheric Group VI event 2200-2300UT on 2003-10-03	116
6.6	Discussion and conclusions	118

<b>7.0</b>	<b>Poynting flux impulses [PFIs] in the dusk-sector auroral zone</b>	122
7.1	Introduction	122
7.2	PFIs associated with geomagnetic substorms	122
7.2.1	Events with substorm signatures	124
7.2.2	Substorm at 1710UT on 2002-11-22	125
7.3	PFIs and opposing ground magnetometer deflection [OGMD] events	127
7.3.1	Observations of opposing ground magnetometer deflections	128
7.3.2	Ionospheric mapping of the null deflection	130
7.3.3	OGMD event at 1900UT on 2003-11-12	132
7.3.4	OGMD event at 1638UT on 2003-11-22	133
7.4	Discussion and conclusions	135
<b>8.0</b>	<b>Polar satellite observations of Group V quadrature events</b>	138
8.1	Introduction	138
8.2	Observations of Group V quadrature oscillations	140
8.3	Magnetogram oscillations preceding magnetospheric resonance	142
8.4	Group V quadrature oscillations associated with substorms	144
8.5	Quadrature oscillations associated with magnetogram notches	145
8.5.1	Notch event at 1911UT on 2003-10-26	146
8.6	Discussion and conclusions	149
<b>9.0</b>	<b>Concluding remarks</b>	151
9.1	Narrative summary	151
9.2	Future work	157
9.2.1	Auroral arc optical modulation in relation to PFIs	157
9.2.2	PFI source location	160
9.2.3	Magnetospheric cavity oscillations	160
<b>Appendix 1</b>	<b>Magnetohydrodynamics [MHD]</b>	162
A1.1	General background	162
A1.2	Electron Plasma Frequency	162
A1.3	Debye length	163
A1.4	Maxwell's equations	163
A1.4.1	Gauss's law	163

A1.4.2	No magnetic monopoles	164
A1.4.3	Faraday's law	165
A1.4.4	Ampère - Maxwell law	165
A1.5	The governing equations of magnetohydrodynamics	166
A1.5.1	Conservation of electric charge	166
A1.5.2	Conservation of mass	166
A1.5.3	Conservation of momentum	166
A1.5.4	Adiabatic equation of state	167
A1.5.5	Ohm's Law for a plasma	167
A1.5.6	Induction equation	167
A1.5.7	Diffusion of electric and magnetic fields through a plasma	168
A1.6	Magnetohydrodynamic waves	168
A1.6.1	Magnetic pressure and tension on a flux tube	168
A1.6.2	Alfvén shear and compressional waves	170
A1.6.3	Derivation of magnetohydrodynamic wave dispersion	171
A1.6.4	Waves propagating parallel to the field lines	175
A1.6.5	Waves propagating obliquely to the field lines	176
A1.6.6	Friedrich diagram	177
A1.6.7	E:B ratio for Alfvén waves	178
A1.6.8	Summary	179
A1.7	The existence of electromagnetic-hydrodynamic waves	180
<b>Appendix 2</b>	<b>Coordinate system transformations</b>	<b>185</b>
A2.1	Universal time [UT] and Julian day [JD]	186
A 2.2	Geographic coordinates [GEO]	187
A2.3	Geomagnetic coordinates [MAG]	187
A 2.4	Geocentric ecliptic inertial [GEI] coordinates	187
A2.5	Geocentric solar ecliptic [GSE] coordinates	188
A2.6	Geocentric solar magnetospheric [GSM]	188
A2.7	Solar magnetic [SM] coordinates	189
A2.8	Spacecraft-centred field-aligned coordinates	189
<b>Appendix 3</b>	<b>Multiphysics</b>	<b>191</b>
A3.1	MATLAB to .txt file conversion	191

A3.2	Using Multiphysics with magnetospheric data	193
<b>Appendix 4</b>	<b>IAGA data format</b>	194
<b>Appendix 5</b>	<b>Location of ground magnetometers</b>	196
<b>Appendix 6</b>	<b>Processing of Polar satellite data</b>	198
<b>Appendix 7</b>	<b>Figures for Poynting flux studies</b>	200
<b>Bibliography</b>		238

**CD** Helmholtz equation simulation movie

**Figure list**

Figure 1.1	Artists impression of the terrestrial magnetosphere	16
Figure 1.2	Geomagnetic shells	20
Figure 1.3	Multiple auroral arcs	20
Figure 1.4	Auroral arc filamentation	23
Figure 1.5	Solar wind flux rope structure	24
Figure 1.6	Laboratory plasma shock	25
Figure 1.7	Plasma $\log_{10}(\beta)$ map	26
Figure 1.8	Magnetospheric current systems	27
Figure 1.9	Ionospheric current circuits	28
Figure 1.10	Petscheck magnetic reconnection geometry	29
Figure 1.11	Reconnected flux rope	30
Figure 1.12	Plasma flow cycle	31
Figure 1.13	Substorm current wedge	33
Figure 1.14	Magnetic reconnection in the magnetotail	34
Figure 1.15	Near-Earth Neutral Line model of magnetic reconnection	36
Figure 1.16	Field lines from the Earth to the tail plasma sheet	40
Figure 1.17	Auroral oval	41
Figure 1.18	EISCAT radar at Sodankylä	44
Figure 2.1	Magnetospheric ULF waves	49
Figure 2.2	Poynting flux theorem <i>Gedanken</i> experiment	61
Figure 3.1	Magnetometer huts at Tähtele, Finland	67
Figure 3.2	Location of the IMAGE ground magnetometer network	68

Figure 3.3	Location of the SAMNET ground magnetometers	69
Figure 3.4	Location of the Greenland ground magnetometers	70
Figure 3.5	Location of the Canadian CARISMA magnetometers	71
Figure 3.6	IRIS riometer	71
Figure 3.7	Polar spacecraft instruments	73
Figure 3.8	Berkeley and Goddard magnetic field data	74
Figure 4.1	Time-delay measurements from 2002-01-01 to 2002-03-01	79
Figure 5.1	Helmholtz equation solution for a laboratory ripple tank	84
Figure 5.2	Helmholtz equation solution for an Alfvén gradient	86
Figure 5.3	The last frame from the Helmholtz equation simulation movie	88
Figure 5.4	ULF wave pressure profile along the Earth-Sun axis	90
Figure 6.1	Groups III to VI in the magnetospheric classification scheme	92
Figure 6.2	Number of events in each magnetospheric group	99
Figure 6.3	Clock diagram depicting MLT of the thirty-nine events	99
Figure 6.4	Timing of IRIS riometer absorption events relative to PFIs	100
Figure 6.5	Map of Polar satellite field-line traces	100
Figure 6.6	Propagation relative to the magnetic field	103
Figure 6.7	Explanation of $+S_z$ and $-S_z$ signals in Polar satellite data	104
Figure 6.8	E:B ratio versus Poynting flux intensity	105
Figure 6.9	Group I 1600-1700UT on 2002-12-17	107
Figure 6.10	Group II 1800-1900UT on 2002-12-27	108
Figure 6.11	Poynting vector quiver plot 1630-1730UT on 2003-11-22	109
Figure 6.12	Group III 1630-1730UT on 2003-11-22	110
Figure 6.13	Poynting vector quiver plot 1800-1900UT on 2003-11-09	111
Figure 6.14	Group IV 1800-1900UT on 2003-11-09	112
Figure 6.15	Poynting vector quiver plot 2100-2200UT on 2003-10-19	114
Figure 6.16	Group V 2100-2200UT on 2003-10-19	115
Figure 6.17	Poynting vector quiver plot 2200-2300UT on 2002-10-03	116
Figure 6.18	Group VI 2200-2300UT on 2002-10-03	117
Figure 7.1	Substorm onset times relative to Poynting flux impulses	124
Figure 7.2	Poynting vector quiver plot 1700-1800UT on 2002-11-22	125
Figure 7.3	Aurora at 1722UT on 2002-11-22	126
Figure 7.4	Polar satellite UVI observations	126
Figure 7.5	HEL-FAR OGMD event at 1622UT on 2003-11-22	128

Figure 7.6	OGMD times relative to Poynting flux impulses	130
Figure 7.7	OGMD event at 1638UT on 2003-11-22	131
Figure 7.8	Map of the OGMD event at 1900UT on 2003-11-12	132
Figure 7.9	Map of the OGMD event at 1638UT on 2003-11-22	134
Figure 7.10	MIRACLE equivalent ionospheric current plot	135
Figure 8.1	Quadrature oscillation phasor diagram	142
Figure 8.2	Quadrature oscillation at 1458UT on 2003-12-15	143
Figure 8.3	Quadrature oscillations and substorm expansion	144
Figure 8.4	ACE satellite plots of solar wind parameters	146
Figure 8.5	Magnetogram notch at 1911UT on 2003-10-26	147
Figure 8.6	Notch frequency versus latitude at 1911UT on 2003-10-26	148
Figure 9.1	Quiet auroral arc	157
Figure 9.2	Keogram and differential keogram 1800-1830UT 2002-10-16	158
Figure 9.3	IRIS riometer keogram 1800-1900UT on 2002-10-16	160
Figure 9.4	Poynting flux bands in the dayside magnetosphere	161
Figure A1.1	Magnetic forces on an element of a magnetic flux tube	170
Figure A1.2	Magnetic field displacements and wavevectors	171
Figure A1.3	Magnetic field and plasma pressure displacements	177
Figure A1.4	Friedrich polar plot of phase velocity	177

#### Table list

Table 1.1	Wave speeds in the solar wind	25
Table 2.1	IAGA classification of ULF pulsations with additional notes	46
Table 4.1	GSE coordinates of the underlying ULF source direction	81
Table 6.1	The thirty-nine magnetospheric and terrestrial events	95- 98
Table 6.2	Observations of geomagnetic shell Poynting flux vectors	105
Table 7.1	Events with ground substorm signatures	123
Table 7.2	Observations of OGMD events	129
Table 8.1	Observations of Group V quadrature oscillations	141
Table 9.1	Auroral optical modulation frequencies	157
Table A1.1	Summary of dispersion relationships	179
Table A1.2	Extract from Alfvén's Nobel Prize lecture	184
Table A5.1	Location of ground magnetometers	198

## Acronym list

AC	Alternating Current
ACE	Advanced Composition Explorer satellite
AGU	American Geophysical Union
AKR	Auroral Kilometric Radiation
ASC	All-Sky Camera
AU	Astronomical Unit
BBF	Bursty Bulk Flow
BGS	British Geological Survey
CARISMA	Canadian Array for Realtime Investigations of Magnetic Activity
CME	Coronal Mass Ejection
CRB	Convection Reversal Boundary
DC	Direct Current
DFT	Discrete Fourier Transform
DMI	Danish Meteorological Institute
EFI	Electric Field Instrument [on Polar satellite]
EISCAT	European Incoherent Scatter Radar
EMF	Electro-Motive Force
FAC	Field-Aligned Current
FGM	Fluxgate Magnetometer
FTE	Flux Transfer Event
GSE	Geocentric Solar Ecliptic coordinate system
GSM	Geocentric Solar Magnetospheric coordinate system
IAGA	International Association of Geomagnetism and Aeronomy
IGRF	International Geomagnetic Reference Field
IMAGE	International Monitor for Auroral Geomagnetic Effects
IMF	Interplanetary Magnetic Field
IRIS	Imaging Riometer for Ionospheric Studies
JD	Julian Date
KHI	Kelvin-Helmholtz Instability
LANL	Los Alamos National Laboratory
MATLAB	MATrix LABoratory [MathWorks Inc.]
MFI	Magnetic Field Instrument [on Polar satellite]
MIRACLE	Magnetometers Ionospheric Radars All-Sky Cameras Large Experiment

MHD	Magnetohydrodynamic
MLT	Magnetic Local Time
NENL	Near-Earth Neutral Line
OGMD	Opposing Ground Magnetometer Deflection [author]
PCB	Polar Cap Boundary
PFI	Poynting Flux Impulse [author]
PSBL	Plasma Sheet Boundary Layer
RAL	Rutherford Appleton Laboratory
$R_E$	Earth Radii [approximately 6400km]
SAMNET	Sub-Auroral Magnetometer Network
SGO	Sodankylä Geophysical Observatory
SSC	Sudden Storm Commencement
SuperDARN	Super Dual Auroral Radar Network
THEMIS	Time History of Events and Macroscale Interactions during Substorms
TLR	Tail Line Resonance [author]
ULF	Ultra Low Frequency
QMW	Queen Mary and Westfield College
UT	Universal Time

## Acknowledgements

Many great people were encountered in the course of these studies and I have tried here to thank everyone who helped along the way.

Professor Chris Owen first inspired the interest in this subject through his space plasma lectures and project work on the MSc Astrophysics course at QMW.

Everyone in the Space Plasma Environment and Radio Science Group at Lancaster University made a tremendous contribution including my supervisors Professor Farideh Honary and

Dr Jim Wild but also Professor Mike Kosch, Dr Mick Denton, Dr Andrew Kavanagh,

Dr Andrew Senior, Dr Patrick Daum, Dr Steve Marple, Dr Mathew Beharrell,

Dr Mila Mihaylova and Dr Nicola Longden.

Most helpful discussions and correspondence were had with: Claire Povah [Lancaster University], Peter Loftus, Dr Terry Johnson, Professor Forrest Mozer [University of Berkeley], Professor David Burgess [QMW], Dr Joseph E. Borovsky [LANL], Dr Ruth Bamford [RAL], Dr James McLaughlin [University of St Andrews], Professor Mike Hapgood [RAL], Anna Dzougoutov and Nils Malm [COMSOL Stockholm].

Dr Chris Turbitt [BGS] kindly arranged a visit to the Lerwick Geomagnetic Observatory to discuss the magnetometer observations with Les Thomson and Billy Hamilton.

Some work was carried out at the Sodankylä Geophysical Observatory in Finland and thanks for this wonderful experience are due to: Dr Jyerki Manninen, Dr Esa Turunen, Tero Raita, Aarne Ranta, Johannes Kultima, Virranniemi Maire, Dr Craig Rodger [University of Otago] and the beautiful singing of the Sodankylä choir.

### **10.3 Acknowledgements for geophysical data**

The author wishes to formally thank the Director of the Sodankylä Geophysical Observatory, Professor Tauno Turunen, the members of the Aeronomy Group under Dr Esa Turunen and to Tero Raita for technical assistance in analysing archived data. This work was kindly funded by a Lapbiat grant.

The Miracle network is operated as an international collaboration under the leadership of the Finnish Meteorological Institute.

The IMAGE magnetometer data are collected as a joint European collaboration. IFSI-INAF (Italy) and the University of Oulu maintain the ITACA ASCs and the ASC in Sodankylä.

The SAMNET ground magnetometers were funded by PPARC and operated by the Space Plasma Environment and Radio Science Group at Lancaster University.

The Imaging Riometer for Ionospheric Studies [IRIS] is operated by the Department of Communication Systems at Lancaster University [UK] in collaboration with the Sodankylä Geophysical Observatory, and funded by the Science and Technology Facilities Council [STFC].

The author would like to thank Dr I. R. Mann and the CARISMA team for data. CARISMA is operated by the University of Alberta and funded by the Canadian Space Agency.

Dr Hans Gleisner at the DMI in Copenhagen kindly provided the Greenland ground magnetometer data.

The author would also like to thank the ACE satellite SWEPAM team and the ACE Science Centre for access to online verified data.

# Part I

## Space plasma physics

Voersint eer Ghij begint

Old Dutch proverb

## 1.0 Introductory background

This thesis is about Ultra Low Frequency [ULF] oscillations in the electric and magnetic fields that are observed in the terrestrial magnetosphere. It begins here with some aspects relating electric and magnetic fields followed by some notes on the terrestrial magnetic field and the useful concept of geomagnetic shells. Studies of whistling atmospherics [Storey 1953] had shown that the terrestrial magnetosphere is pervaded by the fourth state of matter known as plasma and some features of this are described here because ULF oscillations sometimes take the form of physical displacements of the plasma and its associated magnetic fields, as in the case of the Alfvén waves described in Appendix 1.

Notes are then given on the solar wind because of its role in transferring energy from the Sun to the magnetosphere. ULF oscillations are excited by the solar wind either directly, as a result of interactions upstream or near the boundary of the magnetosphere, or indirectly as a result of the transfer of solar wind kinetic energy to magnetic potential energy in the magnetotail followed by impulsive release in the processes of magnetic reconnection.

This mechanism and associated oscillations are related to the much studied subject of geomagnetic substorms and an introduction to this phenomena is described here because it was shown that ULF waves are involved in the transfer and switching of energy to the ionosphere. Some notes are included here on two important spatial regions that have a bearing on these studies: the ionosphere, because the ground magnetometer signature of events depends on currents flowing in this region and the tail plasma sheet, as this was found to be the source of the Poynting flux Impulses [PFIs] observed in Polar satellite data. Finally, as these magnetospheric process manifest themselves in the precipitation of charged particles into the ionosphere a little background is given on the magnificent natural phenomena of the aurora.

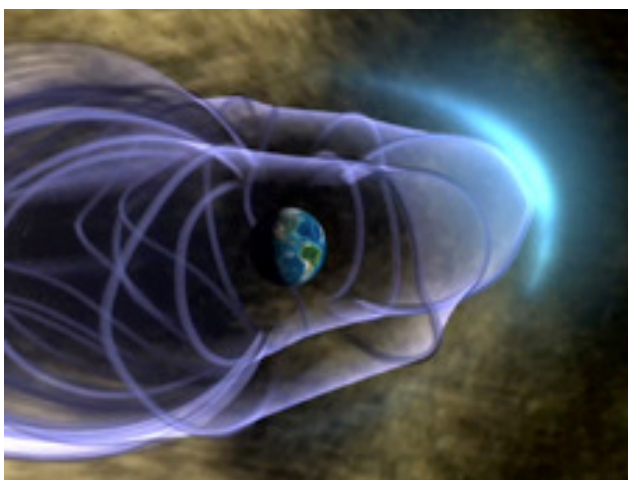


**Figure 1.1**

### **Artistic impression of the terrestrial magnetosphere**

The shape of the magnetospheric cavity is determined by the solar wind parameters. This drawing particularly emphasises the polar cusp structure which gives rise to ULF waveguides around the Earth. [NASA]

The terrestrial magnetosphere is a cavity formed in the solar wind because the *frozen in* plasma in the magnetic field of the solar wind is excluded by the Earth's magnetic field [Allan and Poulter 1992]. This concept of plasma *frozen* into a magnetic field is described in Appendix 1. The idea of the magnetospheric cavity was developed by Chapman and other workers in the 1930s [Chapman and Bartels 1940].

The artistic impression in Figure 1.1 shows a view of the terrestrial magnetosphere that suggests it may not be so mathematically elegant as often drawn . It shows the heating of plasma where the supersonic and super Alfvénic solar wind encounters the Earth's magnetic field [Figures 1.8 and 1.9] and the waveguides in the magnetospheric cavity around the Earth through which fast mode Alfvén waves propagate as shown by the Helmholtz equation study in Chapter 6. Just visible on the far left is part of the tail plasma sheet which was found to be the source of impulsive signals that were detected by their Poynting flux signature and described in Chapters 7 and 8. ULF waves have scale sizes with dimensions comparable to that of the magnetosphere.

### 1.1 Electric and magnetic fields

An electric field is a spatial region within which forces are experienced by electrically charged particles as a result of the presence of electrically charged particles in that region. These [Coulomb] forces arise from the exchange of *virtual photons* between the charged particles. Since these *virtual photons* have zero mass they travel at the speed of light and transmit the electric force over infinite distances. The classical radial inverse-square electric field strength  $E_r$  component at a distance  $r$  from a point charge  $q$  is given by:

$$E_r = \frac{1}{4\pi\epsilon_0} \frac{q}{r^2} \quad [\text{Ohanian 1994}] \quad (1.1)$$

A magnetic field arises when electrical charges are moving relative to the rest frame of an observer and it communicates the force between one moving charge and another. In special relativity the laws of electromagnetism can be written in a four dimensional invariant form which different observers divide differently into electric and magnetic components

[Smith 1960]. It is thus the relativistic correction to Equation (1.1) that accounts for the phenomena of magnetism. The observed electric and magnetic fields  $\mathbf{E}_{\text{obs}}$  and  $\mathbf{B}_{\text{obs}}$  depend upon the relative velocity  $\mathbf{v}$  of the observer's frame of reference. If  $v \ll c$  the frame transformations are given by:

$$\mathbf{E}_{\text{obs}} \simeq \mathbf{E} + \mathbf{v} \times \mathbf{B} \quad \text{and} \quad \mathbf{B}_{\text{obs}} \simeq \mathbf{B} \quad (1.2)$$

Electric and magnetic fields have associated energy densities [Ohanian 1994]:

$$u_E = \frac{\epsilon_0}{2} E^2 \quad \text{and} \quad u_B = \frac{1}{2\mu_0} B^2 \quad (1.3) \text{ and } (1.4)$$

This potential energy may be partially transferred into other forms, such as the kinetic energy of charged particles and MHD wave energy, when magnetic reconnection takes place.

## 1.2 The terrestrial magnetic field

A magnetic field can be expressed as the gradient of a magnetic potential, although this quantity is not itself directly measurable. The magnetic potential at any point with spherical polar coordinates  $[r, \theta, \phi]$  is given by [Lowrie 1997]:

$$W = R_E \sum_{n=1}^{\infty} \left( A_n r^n + \frac{B_n}{r^{n+1}} \right) \sum_{l=0}^n Y_n^l(\theta, \phi) \quad (1.5)$$

where:  $R_E$  is the radius of the Earth

The spherical harmonic function  $Y_n^l(\theta, \phi)$  describes the variation of the potential over the surface of a sphere of radius  $r$ . The coefficients  $A_n$ , which are very much smaller than the  $B_n$  coefficients, describe the contribution to the potential that arises from sources outside the Earth: *the geomagnetic field of external origin*. The coefficients  $B_n$  describe the contribution to the potential that arises from sources within the Earth: *the geomagnetic field of internal origin*. For each value of  $n$  there are different dependences on  $r$  [ $r$ ,  $r^2$ ...  $r^{-1}$ ,  $r^{-2}$  ...]

### 1.2.1 The geomagnetic field of internal origin

A global model of the *geomagnetic field of internal origin* is provided by the International Geomagnetic Reference Field [IGRF] which is usually based on coefficients up to  $n=10$ . In this study IGRF data was used to verify the sign of the Polar satellite magnetometer data.

The *geomagnetic field of internal origin* with  $n=1$  is called the dipole field and three terms which are denoted  $g_1^0$   $g_1^1$   $h_1^1$  define the value of the three orthogonal dipole components.

For 1995 the coefficients:  $g_1^0 = -29,682\text{nT}$ ,  $g_1^1 = -1,789\text{nT}$  and  $h_1^1 = 5.318\text{nT}$  combined to define a resultant dipole field component which was tilted at  $10.7^\circ$  to the axis of rotation. This tilted dipole field accounts for about 95% of the total *geomagnetic field of internal origin* at the surface of the Earth. Its origin is thought to reside in a dynamo mechanism in

the outer liquid iron core of the Earth. The change in the values of these coefficients with time is known as a *secular variation* and historically the location of the auroral oval has also been affected by these secular changes.

### **1.2.2 The geomagnetic field of external origin**

The magnetic field measured at the surface of the Earth is influenced by events on the Sun as well as by electrical storms and man-made activity. Ground magnetometers respond to the magnetic field caused by electrical currents flowing in the ionosphere, the sea and the ground and these currents depend upon electric fields in the ionosphere, electrical conductivity in the ionosphere and upon the supply of charged particles to the ionosphere. Although the concept of magnetic potential may be more fundamental it is often useful to visualise the lines of magnetic field that follow the potential gradient. Magnetic field strength is not constant along these field lines but weakens with increasing distance from the Earth. Because of the interaction with the solar wind the terrestrial magnetic field is far from dipolar in the tail region of the magnetosphere. However when magnetic reconnection takes place in the tail the contribution to the total field from the geomagnetic field of external origin decreases in a process referred to as dipolarisation – a reversion to a more dipole like field.

### **1.3 Geomagnetic shells**

Surfaces of constant magnetic potential in a dipolar magnetic field are called *geomagnetic shells* and an image generated in MATLAB showing a quarter of two closely-spaced shells is shown in Figure 1.2. Although the geomagnetic field is far from being dipolar, because of the higher coefficients and because the field is compressed by the solar wind on the dayside and greatly elongated on the nightside, the concept was found useful, even though the actual geomagnetic shells referred to are greatly distorted. The basis vectors for the field-aligned coordinate system used in these studies and described in Section A2.8 consists of a unit vector normal to the local geomagnetic shell pointing outward from the magnetosphere  $\hat{\mathbf{x}}$ , a unit vector tangential to the local geomagnetic shell  $\hat{\mathbf{y}}$  and a unit vector along the magnetic field line  $\hat{\mathbf{z}}$ . The description *shell propagation* refers in this thesis to propagation in the local field-aligned y-z plane. Geomagnetic shells may be specified by their L number, which is conceptually the distance, measured in Earth-radii from the centre of the Earth, that a dipolar shell intersects the plane of the geomagnetic equator.

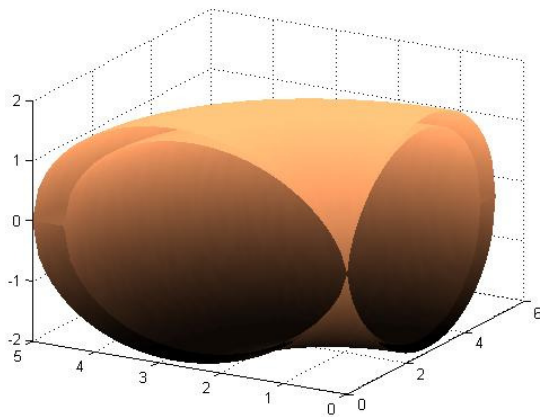


**Figure 1.2**

**Geomagnetic shells**

A MATLAB generated representation of a quarter of two closely spaced toroidal geomagnetic shells with  $L=4.5$  and  $L=5$ .

Substituting  $r = 1$  into the polar equation of a dipolar field line:  $r = L \cos^2\theta$  [Chapman 1951] shows that the invariant geomagnetic latitude  $\Lambda$  that a particular  $L$  shell intersects the surface of the Earth is given by:

$$\Lambda = \cos^{-1}\left(L^{-0.5}\right) \quad (1.6)$$

For example:  $\Lambda = 50^\circ \rightarrow L=2.4$     $\Lambda=60^\circ \rightarrow L=4$     $\Lambda=70^\circ \rightarrow L=8.5$

On the night-side geomagnetic dipolar shell distortion means that the invariant geomagnetic latitude  $\Lambda$  is less than the value given by Equation 1.6.

Since charged particles are subject to gradient and curvature drift [Kivelson and Russell 1995] they may remain on the same shell even though they drift across field lines. Geomagnetic shells can also define the boundaries between different plasma regions with field-aligned current sheets present on the shell boundaries. Ionospheric precipitation structures and quiet auroral arcs [Figure 1.3] may be revealing these boundaries between plasma regimes. A model has been suggested [Lyatsky et al. 1999] that describes the formation of multiple auroral arcs from interference between multiple field-line resonances on adjacent  $L$  shells.



**Figure 1.3 Multiple auroral arcs**

This photograph, showing four quiet auroral arcs aligned approximately east-west, was taken by the author from the frozen Kittila River, Finland on 2008-03-28 and suggests that geomagnetic shells may have a physical basis in delineating the boundary between regions of different plasma parameters

## 1.4 Space plasma

The first use of the word plasma in Physics has been attributed to Irving Langmuir who used it in 1928 to describe a neutral ionised gas [Braithwaite 2008]. Plasma can be created by a source of energy, such as the nuclear reactions in a star, electric currents, ultra-violet light and other frequencies of electromagnetic radiation and also by collisions between particles. Hydrogen is the most abundant element in the Universe and only 13.6eV is required to ionise the electron from its ground state. The nuclear reactions within the core of stars generate sufficient energy to ionise all the hydrogen in the entire star and the Universe comprises galaxies of stars – so it is sometimes said that plasma comprises 99% or more of the observable Universe.

Plasma may be described as a quasi-neutral ensemble of comingling species of positively and negatively charged ions and electrons, although it may also contain some neutral particles as in the ionosphere. The requirement for quasi-neutrality means that the scale of the system should be large compared to the Debye length [Section A1.3], which is a measure of charge screening, and this requires that the number of particles of each species in their Debye spheres should be large compared to unity [Sturrock 1994]. Quasi-neutrality can be violated by thermal fluctuations over distances less than the Debye length.

Because of the long-range nature of electromagnetic forces the plasma collision cross-section is many orders of magnitude greater than the particle dimensions. Plasmas are said to be collisionless if the mean free path of a charged particle is greater than the scale size of the system. This happens when the plasma density is low and when the plasma temperature is high enough for the particles to be moving sufficiently fast for the recombination rate to be low. The solar wind is a good example of a collisionless plasma as the mean free path is  $\sim 1A.U.$  A significant difference between a collisionless plasma and a gas is that in a collisionless plasma the ions and electrons can have different velocity distributions and widely different temperatures. This gives rise to regions with different plasma parameters with boundaries between them. These different plasma parameters can include different *frozen in* magnetic fields [Section A1.5.7]. Another important difference between a plasma and a gas is that collisions in a gas act to give the particles a Maxwell-Boltzmann distribution of velocities. This is not the case in a space plasma where the distribution of ion and electron energies can have multiple peaks. The presence of charged particles and the lack of collisions give space plasmas a very high electrical conductivity.

Where there is a magnetic field this high conductivity is along the field lines since a particle with charge  $q$  moving at velocity  $\mathbf{v}$  experiences the Lorentz force:

$$\mathbf{F}_{\text{Lorentz}} = q(\mathbf{v} \times \mathbf{B}) \quad (1.7)$$

that causes it to spiral helically around magnetic field lines.

The long range nature of electromagnetic forces also means that plasma can exhibit collective behaviour such as oscillations and instabilities. Electrons move rapidly in response to an electric field and the effect is to cancel the applied electric field. At lower frequencies where the slowly changing electric field gives the electrons time to respond the applied electric field may be completely cancelled out in the frame of reference of the plasma - this gives rise to the magnetohydrodynamic [MHD] low-frequency approximation to a plasma. ULF Alfvén waves [Section A1.6] are a notable example of a MHD phenomenon.

In the Polar satellite electric field data used in these studies the assumption of a zero field-aligned component of electric field had been applied in order to generate three axis data from the two spin-plane electric field sensors. However effects that are not taken into account in MHD can result in non-zero field-aligned electric fields which can accelerate ions and electrons along the field lines.

### **1.5 Plasma shocks**

Shocks arise when the particle speed is greater than the wave speed [Kivelson and Russell 1995 – D. Burgess, Baumjohann and Treumann 2006]. Upstream of a plasma shock the plasma is super-sonic and downstream it is sub-sonic. A fast mode shock arises where the plasma speed upstream of the shock is super-Alfvénic and super-sonic and downstream it is sub-Alfvénic and sub-sonic, as occurs in the solar wind at the terrestrial bowshock. Shocks also exist within the solar wind where a fast stream of particles from the Sun encounters a slower moving stream. Whereas MHD waves propagate adiabatically, so that the plasma parameters stay constant, a plasma shockfront is a non-adiabatic process in which the change of speed is accompanied by a change in the plasma parameters, including plasma density and plasma temperature.

### **1.6 Plasma instability**

Plasma is able to form self-organising structures of various forms as a result of a current flowing through it. A well-known plasma phenomenon is the z-pinch whereby an axial current along the z axis gives rise to azimuthal flux tubes that compress the plasma around the z axis. Particles following spiral paths in the same sense around field lines give rise to

short range repulsive forces as a result of the magnetic field created by their circular component of motion around the field line and long range repulsive forces as a result of the magnetic field created by their axial component of motion along the field line: these forces can cause a plasma current sheet to filament. Whilst examining all-sky camera images in Finland the frame shown in Figure 1.4 was encountered. There is some striation visible in the auroral arc that may have been caused by current filamentation. The interest in this process from the point of view of these studies is whether current flowing through plasma could cause it to oscillate and sustain field-line resonance.

Laboratory experiments at LANL with high plasma currents have suggested that cylindrical current sheets self-organise themselves into 58 current filaments which can reduce to smaller numbers 42, 35, 28, 14, 7, 4. It has been suggested that these highly filamented structures may even have been observed in the aurora in pre-historic times and that a record of this is preserved in ancient rock art [Peratt 2003].

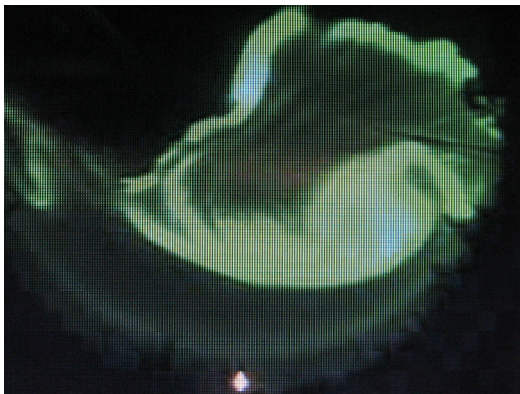


**Figure 1.4 Auroral arc filamentation**

Sodankylä all-sky camera frame taken at 1829UT on 2002-10-16 of a filamented auroral structure overhead.

Pine trees and the moon are visible around the lower horizon.

[Sodankylä Geophysical Observatory]

The classical Kelvin-Helmholtz Instability [KHI] that is responsible for waves on the sea also has a plasma equivalent arising from the shearing motion along a boundary between two plasma streams. It occurs in the ionosphere, where it gives rise to scintillation of radio signals, and on the magnetosphere boundary, where it is often cited as a possible source of ULF waves. If the pressure balance between the magnetosphere and the solar wind is perturbed so that the magnetosphere slightly bulges outwards the solar wind speed in the magnetosheath is forced to increase and the Bernoulli Effect reduces the solar wind pressure on the magnetosphere. This positive feedback disturbs the equilibrium further so that ripples develop on the magnetopause [Prölss 2004].

## 1.7 Solar wind

The solar wind comprises quasi-neutral plasma with a particle density of  $1 \times 10^7 \text{m}^{-3}$  to  $5 \times 10^7 \text{m}^{-3}$  [Kivelson and Russell 1995 – R.L Mc Pherron] ejected from the Sun and travelling at a typical speed of  $450 \text{kms}^{-1}$  [ $300 \text{kms}^{-1}$  -  $1000 \text{kms}^{-1}$ ] outwards through the interplanetary medium. This means that it takes about four days to travel from the Sun to the Earth. The ionised material comprises mainly  $\text{H}^+$  with some  $\text{He}^{++}$  and a typical particle energy of  $100 \text{eV}$  -  $1 \text{keV}$ . Embedded in the solar wind is a magnetic field with a strength of 3 -  $30 \text{nT}$ .

The Sun rotates about its axis every 25.4 days and material from a particular active region on the solar surface is ejected into the interplanetary space in different directions at different times. Linking of plasma parcels by magnetic field lines gives rise to the Parker spiral pattern of solar wind magnetic field directions. At the Earth the solar wind magnetic field makes an angle of  $\sim 45^\circ$  to the Sun-Earth line [depending upon the solar wind speed] which means that there is an asymmetry between the dawn and the dusk side of the magnetosphere, which may have implications for the reported asymmetric magnetospheric source of ULF waves on the dawnside [Baker et al. 2003].

At low solar latitudes the magnetic field of the Sun is approximately dipolar but the higher latitude field lines are carried away by the solar wind and these lines of opposite polarity are separated by a current sheet. The undulating shape of this current sheet [sometimes described as a ballerina's skirt] means that the Earth encounters inwards and outwards directed magnetic flux during the 27 day solar rotation period as seen from the Earth.

Images from the A and B STERIO satellites have shown the filamentary structures of coronal mass ejections [CME] [Mostl et al. 2009] and evidence for flux ropes<sup>(1)</sup> and it has been suggested that the entire interplanetary region may be filled with flux rope structure derived from the Sun and subjected to the Parker spiral effect [Figure 1.5]. Whether this really is the case remains to be seen. The solar wind may carry coherent ULF waves from events on the Sun. As shown in the approximate data in Table 1.1 a typical solar wind speed of  $450 \text{kms}^{-1}$  would give rise to Mach numbers that are both supersonic and super-Alfvénic. These waves are thought to be Alfvén shear-mode waves because the slow or fast MHD modes [Appendix 1] would be damped before they reached 1 AU [Walker 2005].

---

<sup>(1)</sup> Magnetic field lines twisted around an axis like ropes made of smaller strands are referred to as flux ropes [Kivelson and Russell 1995]. Flux ropes can be regarded as flux tubes that have been twisted as a result of the vortical motion of the surface(s) on which they terminate [Sturrock 1994]. The resulting magnetic field configuration varies from toroidal along the central axis through helical to poloidal on the surface of the flux rope [Prölss 2003], although more complex structures may be encountered.

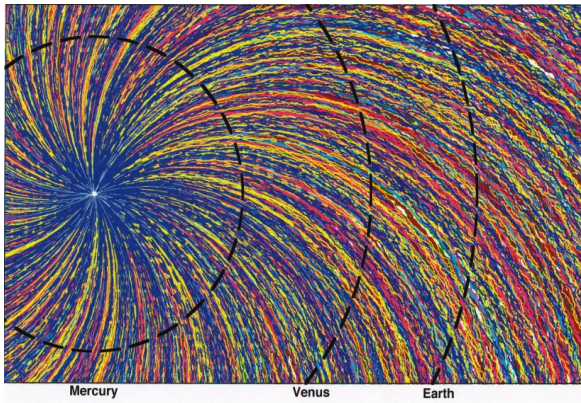


**Figure 1.5**

**Solar wind flux rope structure.**

Sections of flux rope detached from the Sun may be embedded in the solar wind as shown in this artistic impression [Joseph E. Borovsky - private communication].

Alfvén speed $v_A$	$v_A = \frac{B}{\sqrt{\mu_0 \rho_m}}$	$34.5 \text{ km s}^{-1}$
Sound speed $c_s$	$c_s = \sqrt{\frac{\gamma(kT_e + kT_p)}{m_e + m_p}}$	$40.6 \text{ km s}^{-1}$
Hybrid speed $v$	$v = \sqrt{v_A^2 + c_s^2}$	$53.3 \text{ km s}^{-1}$

**Table 1.1**

**Wave speeds in the solar wind**

Number density =  $10^7 \text{ m}^{-3}$

Electron temperature  $T_e =$  ion

temperature  $T_p = 10^5 \text{ K}$

Magnetic field strength  $B = 5 \text{ nT}$

[Walker 2005]

**1.7.1 Interaction between the solar wind and the terr**

An approximately parabolic shock front known as the magnetosphere bow shock is generated as the super-sonic and super-Alfvénic solar wind approaches the Earth. Typically it is located at about  $14R_E$  from the Earth and the standoff distance of the bow shock from the nose of the magnetopause is about  $4R_E$ . Laboratory experiments at the Rutherford Appleton Laboratory aimed at protecting future space explorers using magnetic fields around their spaceships and colonies yielded the image of a plasma beam encountering a dipolar magnetic field shown in Figure 1.6 [Bamford 2008]. There are similarities here to the way in which the solar wind interacts with the terrestrial magnetosphere since the terrestrial magnetic field acts to deflect the solar wind particles around the Earth.



**Figure 1.6 Laboratory plasma shock.**

A mini-magnetosphere was created by a dipolar magnetic field in laboratory studies of spacecraft shielding. The purple shock front was formed where a supersonic plasma beam encountered the magnetised plasma [Bamford 2008].

Since a plasma shock is a non-adiabatic process some of the kinetic energy in the supersonic solar wind is transferred to heat in the shock front. This generates warm plasma in the magnetosheath region between the bow shock and the plasmapause.

The ratio of the thermal pressure  $p$  to the magnetic pressure:  $B^2 / 2\mu_0$  in a plasma is ascribed the Greek letter  $\beta$  so that:

$$\beta = 2\mu_0 p / B^2 \quad (1.8)$$

A plasma is referred to as *cold* if:  $\beta \ll 1$  which really means that a plasma is *cold* if its thermal pressure is small compared to its magnetic pressure, even though its thermal temperature might be quite high.

Plasmas for which  $\beta \geq 1$  or equivalently  $\log_{10}(\beta) \geq 0$  are referred to as *warm* plasmas and depending upon the scale size of the system may be collisionless [Kivelson and Russell 1996]. The  $\log_{10}(\beta)$  map of a cross-section through the magnetosphere shown in Figure 1.7 was generated as a by-product of the Helmholtz equation propagation study described in Chapter 5. It shows the warm plasma [magenta] in the magnetosheath and the cold plasma [blue] in the magnetosphere. The nose of the magnetosphere was located at about  $11R_E$  and the bowshock at about  $16R_E$ . The partial entry of warm plasma into the polar cusp region can faintly be discerned at GSM coordinates  $[8R_E \ 6R_E]$  and at  $[2R_E \ 10R_E]$  as well as the warm plasma in the tail current sheet. The significance of this map to these studies is that the propagation speed for fast mode MHD waves depends upon both the Alfvén speed and the speed of sound, the latter depending on the value of the plasma  $\beta$  parameter.

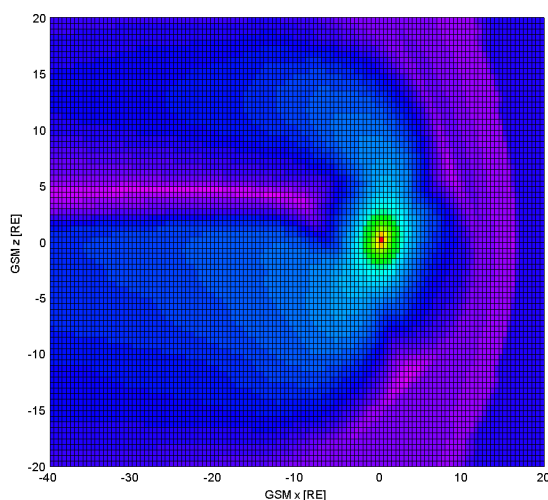


**Figure 1.7**

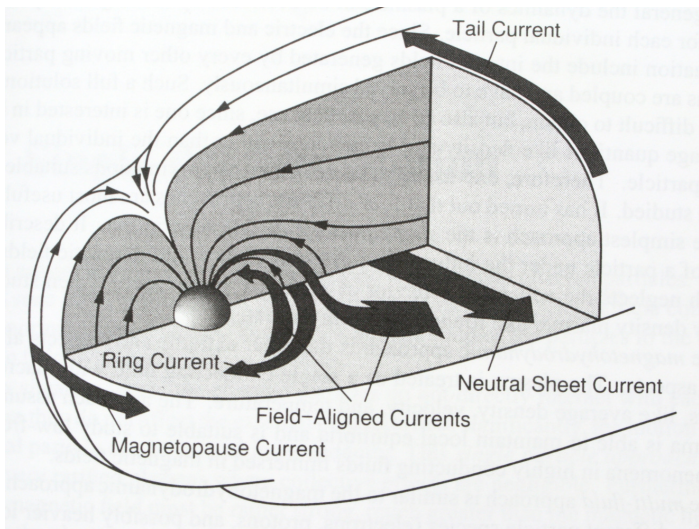
**Plasma  $\log_{10}(\beta)$  map**

$\log_{10}(\beta)$  on the  $y_{GSM}=0$  plane for MHD model data for 1200UT on 2002-09-16. Warm plasma is defined by  $\beta > 1$  or  $\log_{10}(\beta) > 0$  and is colour coded magenta. This image shows the presence of warm plasma in the magnetosheath and the tail current sheet.

In equilibrium the distance of the nose of the magnetosphere from the Earth is determined by an energetic balance between the solar wind kinetic energy and the energy in the terrestrial magnetic field strength at that distance:

$$\rho_m v^2 = B^2 / 2\mu_0 \quad (1.9)$$

where:  $v$  is the solar wind speed,  $\rho_m$  is the solar wind mass density and  $B$  is the terrestrial magnetic field strength. It is also given by the balance between the  $\mathbf{j} \times \mathbf{B}$  pressure due to the magnetopause current density shown in Figure 1.8 and the solar wind dynamic ram pressure:

$$p_{sw} \propto \rho_m v^2 \quad (1.10)$$


**Figure 1.8**  
**Magnetospheric current systems**

Current sheets occur on the boundaries between different plasma regimes.  
[from Baumjohann and Treumann 1997]

From this it follows that an increase in the solar wind dynamic ram pressure gives rise to an enhancement in the eastwards flowing magnetopause current.

The solar wind dynamic ram pressure controls the size of the magnetospheric cavity that supports oscillations: sudden increases in the solar wind ram pressure may compress the magnetosphere and initiate pulsations [Southwood and Kivelson 1990], [Korotova and Sibeck 1994]. The resulting variation in the magnetopause position has been studied with over 1000 crossings of the ISEE satellite [Song 1994].

Variations in the solar wind over the solar cycle are complex but a statistical study of IMP-8 spacecraft data between 1974 and 1988 [Luhmann, Petrinec and Russell 1994] showed that only  $|B_z|$  varied in phase with the sunspot number. This was attributed to the greater number of CMEs that occur near sunspot maximum. At solar minimum the neutral sheet is fairly flat and nearly parallel to the ecliptic plane resulting in lower solar wind speeds at the Earth. At solar maximum the coronal holes, which are the source of high speed solar wind, are smaller and weaker. So it is in the period between solar minimum and solar maximum

when the changing inclination of the magnetic neutral sheet is expected to bring the higher latitude and higher speed solar wind to the ecliptic plane, with consequences for the generation of ULF waves by velocity-shear. The solar wind speed has been found to increase with heliomagnetic latitude [Newkirk and Fisk 1985].

The plasma number density follows a different pattern and is greatest near the magnetic neutral sheet so the solar wind dynamic ram pressure is strongest just after solar maximum due to the velocity enhancement and also around the time of solar minimum due to the density enhancement. Polar satellite data from the years 2002 and 2003, just after a period of solar maximum, were used in these studies. Another aspect to the solar wind interaction with the terrestrial magnetic field is the EMF which is generated across the polar regions by the solar wind plasma flow across open field lines [Prölss2003]. A schematic hybrid diagram illustrating the currents associated with this is shown in Figure 1.9.

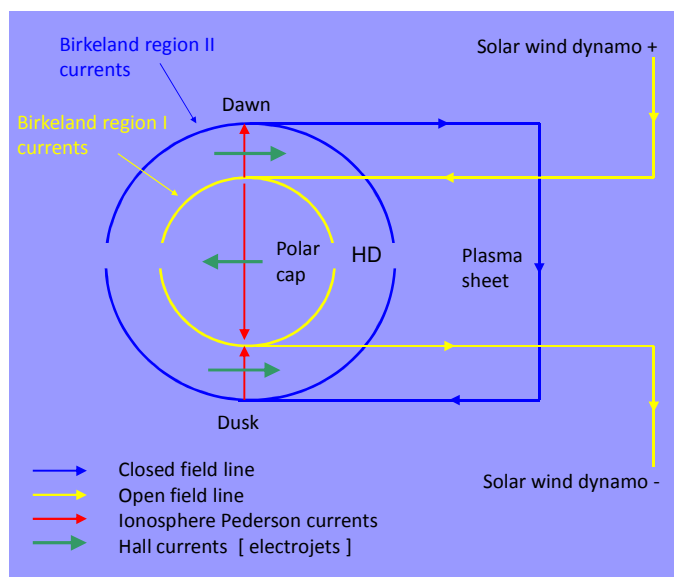


**Figure 1.9**

**Ionospheric current circuits**

This schematic hybrid diagram by the author illustrates the eastward and westward electrojets before and after the time of local midnight. The Harang Discontinuity is marked HD. Plasma convection is anti-parallel to the ionospheric Hall currents.

**1.8 Magnetic reconnection**

An important phenomena in the terrestrial magnetosphere is the process of magnetic reconnection between magnetised plasma regimes with opposing fields [Birn and Priest 2006]. This process is summarised as follows:

At the boundary between two plasma regimes, where the magnetic field is neutral, charged particles are no longer constrained to spiral around field lines and a diamagnetic current flows in such a direction that the associated magnetic field maintains the opposing field directions on either side. The condition for lines of magnetic flux to be frozen into a plasma are defined by the terms in the MHD induction equation [Equation A1.27] from which

comes the magnetic Reynold's number  $R_m$  [Equation A1.28] which describes the ratio of plasma convection with the field lines to plasma diffusion across the field lines. In a current sheet  $R_m$  has a small value because collisions reduce the electrical conductivity and also because the scale size of the system is small. This means that the condition for frozen in flux breaks down and the magnetic field is able to diffuse into the current sheet. The early Sweet-Parker model of magnetic reconnection was based on this diffusion of magnetic flux through the plasma but the problem was that the resulting magnetic reconnection rate was very small. A subsequent development [Petschek 1964] still required diffusion across the neutral sheet to take place but around it were four fast mode MHD shock fronts giving rise to an X-line geometry in two dimensions [Figure 1.10].

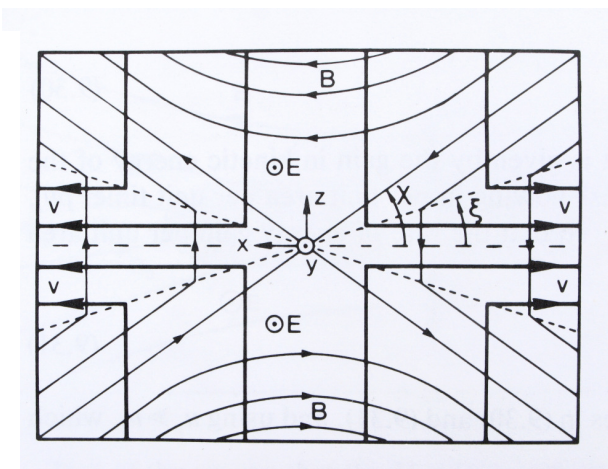


**Figure 1.10**

**Petschek magnetic reconnection geometry**

$$\odot \mathbf{E} = -\mathbf{v} \times \mathbf{B}$$

where  $\mathbf{v}$  is the plasma inflow velocity

[from Kivelson and Russell 1995]

Above and below the X-lines are the lines of un-reconnected magnetic field and to the left and right are the regions of reconnected flux. Although the X-line is still required the magnetic field is reconnected across the four radiating shock fronts which means that much more flux is reconnected than in the earlier schemes. The out-flowing plasma is heated by its passage across the shock fronts and emerges as plasma jets in both the downstream and upstream directions. The reconnected field lines are in a state of tension and this magnetic potential energy is transferred in kinetic energy of the plasma around the field lines as they move away from the reconnection X-line in opposite directions. The factors that determine the precise moment of magnetic reconnection are unknown although disturbances caused by ULF waves may have a role.

### 1.9 Dayside magnetic reconnection

One place in the magnetosphere where magnetic reconnection occurs is on the dayside magnetopause when the IMF is southwards: a magnetopause current [Chapman-Ferraro current] flows from dawn to dusk and has the effect of modifying the magnetic field profile

across the boundary. A typical value of this magnetopause current density is  $1\mu\text{A}/\text{m}^2$  [Baumjohann and Treumann 1997].

Magnetic reconnection across this current sheet often, but not always, occurs on the dayside magnetosphere when the IMF turns southward. The newly opened magnetic field lines are swept over the polar region and draped over the tail so that the terrestrial magnetic field becomes even more distended. EISCAT radar studies [Cowley, S.W.H., and M. Lockwood 1992] have shown that dayside magnetic reconnection excites the dayside plasma flow within about 5 minutes of the IMF turning southward and intense auroral displays are then typically observed 30-45 minutes later. Equally prompt decays in the plasma flow occur when the IMF turns northwards. Typically about 10-20% of the southwards IMF flux reconnects which means that the IMF magnetic circuit is then through the Earth and out at high latitudes in the southern hemisphere. Dayside magnetic reconnection occurs in pulses and gives rise to flux transfer events [FTEs] [Russell and Elphic 1979]. Figure 1.11 shows that a reconnected flux tube travelling in the L direction [defined by the coordinate system shown] through the magnetosheath would give rise to a +/-dipolar signature in the magnetic field component normal to the magnetosphere as it crossed a satellite in the magnetopause. The characterisation of FTEs [Paschmann et al. 1982] provides an idea of the time interval between multiple magnetic reconnection pulses. Across the five days when multiple FTEs were observed there was the average interval of 15 minutes between them.

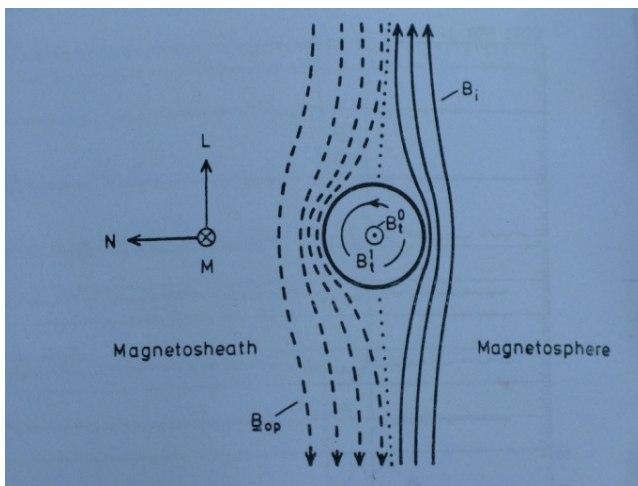


**Figure 1.11**

**Reconnected flux rope**

If this structure, travelling in the L direction is intercepted by a satellite magnetometer, it gives rise to a dipolar signature in the magnetic field component normal to the magnetosphere. [from Paschmann et al. 1982]

In the northern hemisphere polar cusp region the magnetic field lines have a southwards component which would suggest that some magnetic reconnection would occur here when the IMF turns northwards, the converse being the case in the southern hemisphere.

### 1.10 Plasma convection cycle

Magnetic reconnection on the dayside and then in the tail form part of a cycle of plasma convection in the magnetosphere that is driven by a slight reduction in the momentum of the solar wind. Magnetic reconnection on the dayside magnetosphere results in erosion of the magnetospheric plasma and field lines at a faster rate than they can be replenished by convection from the tail. During this time the nose of the magnetosphere moves nearer to the Earth. Although the magnetosheath is a region of warm plasma heated by the bow shock the scale size  $L$  is large so the conditions for frozen in flux are approximately met. The solar wind momentum drags the newly opened terrestrial field lines with their frozen-in plasma over the polar region and drapes them over the tail of the magnetosphere where they apply inwards pressure on the north and south lobes.

The action of the solar wind is therefore to transfer plasma on magnetic field lines from the dayside of the Earth to the night-side and to increase the magnetic potential energy stored in the magnetotail. Magnetic reconnection deep in the tail completes the cycle by returning plasma towards the Earth on reconnected field lines. This plasma is subject to gradient and curvature drift with the result that the plasma and the field lines eventually return to the dayside magnetosphere. The overall flow cycle time is of the order of 12 hours [Cowley 1995]. A diagram illustrating the process from the original paper [Dungey 1961] is shown in Figure 1.12.

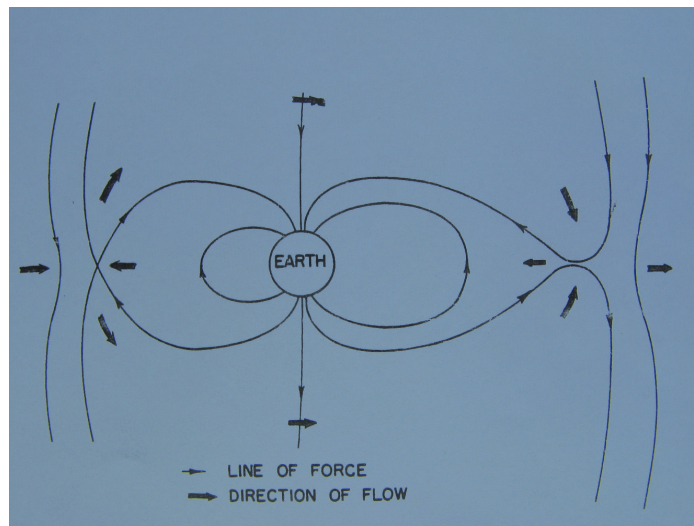


**Figure 1.12 Plasma flow cycle**

This historic diagram illustrates magnetic reconnection on open field lines that forms part of the plasma flow cycle in the magnetosphere. The actual location of open field line reconnection is deeper in the magnetotail than suggested here [Dungey 1961].

## **1.11 Geomagnetic substorms**

Geomagnetic substorms arise when magnetic potential energy stored in the magnetotail is released. They have a duration from under 1 hour to around 3 hours and may be initiated by a sequence of events in which the IMF turns southward for an hour or more before turning northward [Kivelson and Russell 1995 – R.L Mc Pherron]. The three main substorm phases, are described below.

### **1.11.1 Substorm growth phase**

Magnetic reconnection between the terrestrial field and the IMF occurs on the dayside whilst the IMF remains southward with the result that the rate of magnetic reconnection becomes greater on the dayside than the night-side. Closed field lines become open and are dragged by the solar wind over the polar cap to the tail lobes, resulting in a stretching of field lines tailwards and a thinning of the tail plasma sheet as a result of the increased magnetic pressure. The polar cap region, where magnetic field lines are open to the IMF, expands as more and more closed field lines are eroded. Global optical imaging shows that this expanding region is devoid of optical luminosity [Brittnacher et al. 1999].

The boundary of the polar cap [PCB] expands equatorward together with the field-aligned current systems and embedded auroral arcs so that an observer on the ground in the dusk sector may see quiet auroral arcs moving overhead from north to south. The Convection Reversal Boundary [CRB] acts as a proxy for the PCB and its equatorward motion during the substorm growth phase can be detected in HF coherent radar returns [Lester 2000].

Another feature associated with the growth phase of substorms is the appearance of convection vortices on the dayside [Greenwald et al. 1996]. These quasi-static features have sizes ranging from a hundred to around a thousand km and are thought to be associated with field –aligned currents which are particularly strong just before the substorm expansion phase. The enhanced solar wind dynamo associated with the open field lines increases the EMF across the magnetotail which increases the eastward and westward electrojets [Figure 1.9] and gives rise to an enhanced conductivity channel in the ionosphere. A useful result that is obtained by integrating the Biot-Savart Law is that the magnetic field remains constant at distances from a current sheet which are small compared to the physical extent of that current sheet. Thus an increase in the magnetic field detected by a satellite in the magnetospheric lobes is an indication of an increase in the cross tail current. Several satellite studies have used this result to demonstrate an intensification in the cross tail current in the late substorm growth phase [Birn and Hesse 2000].

### 1.11.2 Substorm expansion phase [intensification]

The subsequent northward turning of the IMF causes the solar wind dawn-dusk electric field across the polar cap to reduce so that the associated field-aligned currents, plasma sheet currents and electrojets also reduce. The CRB boundary may continue to expand equatorward after intensification but eventually reverses and moves poleward [Yeoman and Pinnock 1996]. At substorm onset there is rapid auroral intensification, a breakup of auroral forms into smaller filaments, a poleward expansion and a westward surge of the most intense auroral arcs. Ground magnetometer data often shows Pi2 oscillations at substorm onset.

The expansion phase of the substorm begins when a second field-aligned current system is switched on. This is referred to as the substorm current wedge circuit [Mc Pherron et al. 1973] and is depicted in Figure 1.13. The dawn-dusk cross-tail current at  $\sim 6 - 10R_E$  is diverted along field lines into a conducting channel in the ionosphere where it gives rise to a strong westward substorm electrojet that shows up in ground magnetograms as a negative substorm bay. The downward flowing currents are in the same sense as the Region 1 Birkeland currents shown in Figure 1.9, but are located at a more southerly latitude so that they map to a nightside distance of between 6 and  $25R_E$  on the equatorial plane [Lu 2000]. Another study [Birn and Hesse 2000] places them at a nightside distance of between 5 and  $13R_E$ . A feature of the substorm current wedge is that the region where electrons precipitate down to the ionosphere is located at the westward end of the substorm electrojet where auroral luminosity is higher, the far eastward end being associated with upward electron flow. The region of disruption together with associated field-aligned currents has been inferred as propagating away from the Earth [Jacquey 2000] which is consistent with the observation that substorm onset, as shown by negative deflection in ground magnetograms, proceeds from low to high latitude.

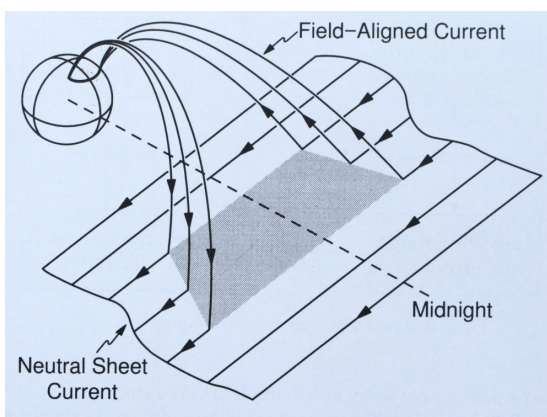


**Figure 1.13**

#### **Substorm current wedge**

When the nightside magnetospheric cross tail current circuit is interrupted field-aligned current is diverted through the ionosphere [Baumjohann and Treumann 2006].

A mechanism that could give rise to current disruption is localised anomalous resistivity caused by current-driven plasma instability resulting from the increasing cross-tail current. Magnetic reconnection is then triggered by a tailward propagating rarefaction wave [Lui 1996] [Hesse and Birn 2000]. The current density instability threshold may be of the form:  $j = \alpha n e v_{ti}$  where:  $\alpha$  is a parameter of the order of  $[m_e/m_i]^{1/2}$  and  $v_{ti}$  is the ion thermal velocity. Studies of this mechanism [Birn and Hesse 2000] however have suggested that the region of current diversion is not coincident with the region of anomalous resistivity, which acts only to divert the plasma flow.

Another theory [Baker et al. 1996] for the initiation of the substorm expansion phase is that Near-Earth Neutral Line [NENL] magnetic reconnection on closed field lines in the tail at  $\sim 20-30R_E$  is responsible for the processes leading to the diversion of current from  $\sim 6 - 10R_E$  to the ionosphere. This magnetic field configuration in the magnetotail is illustrated by the artist's impression shown in Figure 1.14 which dramatically emphasises the release of energy. At the time of writing it is not known what process triggers this magnetic reconnection but when reconnection occurs on closed field-lines some of the magnetic stresses in the tail are released and the magnetic field relaxes back Earthwards in a process referred to as dipolarization. This reconfiguration of the magnetic field could be a source of the fast mode waves described in Section A1.6.5 which may then couple their energy to oscillations on magnetic field lines in the PSBL region [Figure 1.16].

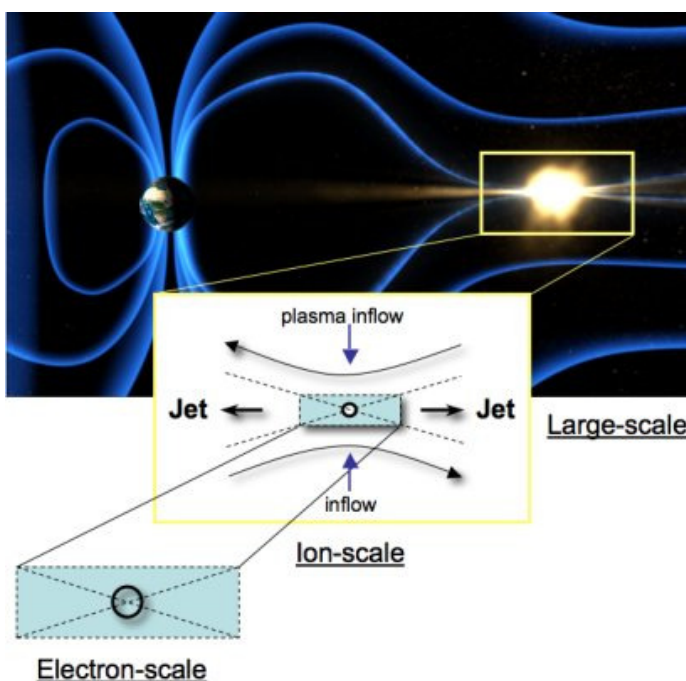


**Figure 1.14**  
**Magnetic reconnection in the magnetotail**

The important region in the magnetotail where magnetic reconnection on closed field lines gives rise to energy transfer is shown in this artistic impression at three different scales. [NASA Themis]

Tailward of the reconnection X-line a flux rope plasma structure called a plasmoid may be created which expands as it travels tail-wards away from the reconnection X-line at a speed of  $\sim 200 - 600 \text{ km s}^{-1}$  [Figure 1.15]. Its origin in the tail plasma sheet means that a plasmoid is a region of hot plasma [ $\beta \gg 1$ ]. Its magnetic structure is helical with a direction determined by the  $B_y$  component of the IMF and the plasmoid current direction is from dawn to dusk. The plasmoid is regarded as evidence that magnetic reconnection has taken place and its ejection is thought to precede events such as auroral brightening [Ieda et al. 2001] and magnetic substorms.

Earthward of the reconnection X-line Bursty Bulk plasma Flows [BBFs] have been observed. The resulting increasing magnetic field nearer the Earth induces a cross-tail current beyond geosynchronous orbit and the NENL model provides a source of energetic charged particles that travel along magnetic field lines to the ionosphere.

The THEMIS satellite mission was designed to study the sequence of events in order to determine the cause of substorm onset. The following sequence of events was described for the substorm on 2008-02-26 [Angelopoulos 2008]:

0450:03UT	magnetic reconnection inferred
0451:39UT	auroral intensification observed
0452:00UT	Pi2 onset in ground magnetometer data
0452:21UT	poleward expansion of aurora
0452:27UT	Earthward flow observed at $-11R_E$
0453:01UT	dipolarisation [arrival of reconnected flux] observed at $-11R_E$ arrival of Pi2s at mid latitude

The auroral intensification 21 seconds ahead of the Pi2s was attributed to the acceleration of the auroral electrons by [kinetic] Alfvén waves [Chaston 2006] which can travel up to  $\sqrt{2}$  times faster than the Pi2 Alfvén shear waves. This particular analysis concluded that magnetic reconnection was initiating the substorm sequence. A contributory factor, or possibly the cause of these mechanisms, is enhanced current as a result of inductance following the reduction in EMF across the polar cap when the IMF turns northward.

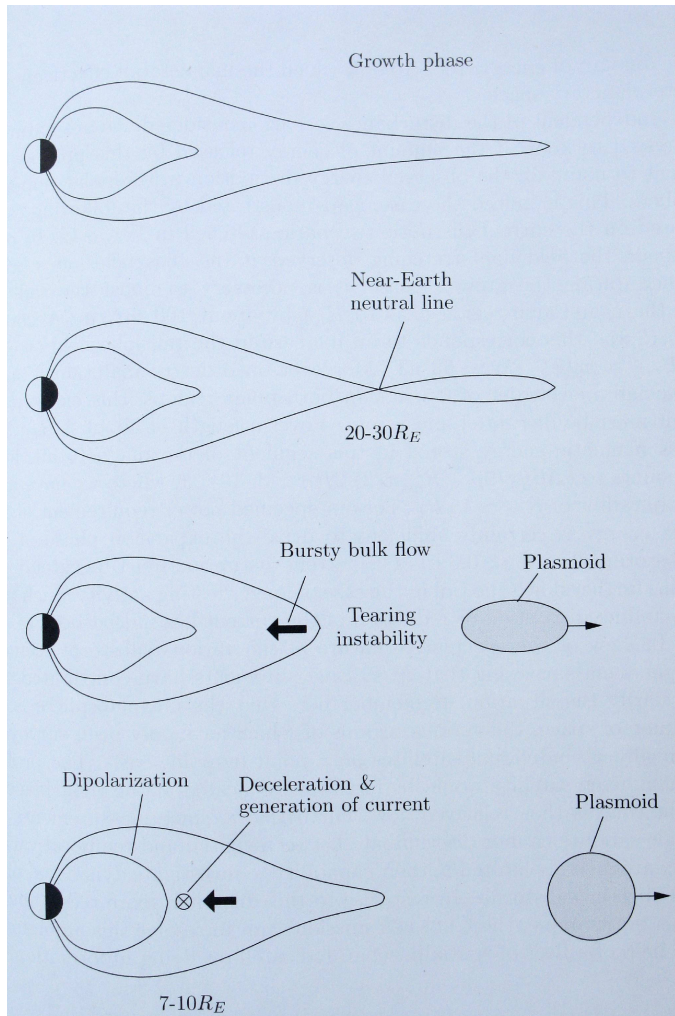


**Figure 1.15**  
**Near-Earth Neutral Line model**  
**of magnetic reconnection**

Increased pressure on closed field lines during substorm growth forces them closer together.

Magnetic reconnection gives rise to the formation of a plasmoid which travels tailward and to bursty bulk flows which travel earthward. Dipolarisation in the inner magnetosphere results in field lines, together with associated field-aligned currents, moving polewards [Pröls 2004].

### 1.11.3 Substorm recovery phase

Substorm expansion is followed by substorm recovery during which time the auroral arcs remain active at the poleward boundary of the auroral oval for several hours until they gradually reduce in intensity and move equatorward, often leading to another substorm sequence.

Ground magnetograms show that negative deflection associated with the substorm electrojet generally decreases during this phase.

Easterly travelling omega bands [Akasofu 1964] are a well established feature of the recovery phase of substorms. In a case study using the Finland CUTLASS radar [Wild et al. 2000] it was found that omega bands in the recovery phase of a substorm over Scandinavia were observed simultaneously with the expansion phase of a new substorm to the west from which it was inferred that substorm onset in the dusk sector can globally affect magnetospheric currents.

## 1.12 The ionosphere<sup>(1)</sup>

The approximate altitudes of the main regions of the ionosphere are:

D region 50km to 90km, E region 90km to 170km, F region 170km to 1000km and  
co-rotating plasmasphere 1000km to  $\sim 4R_E$

In space plasmas the particle density is often very low and the ions and electrons have sufficient thermal kinetic energy for recombination to be negligible. When space plasma encounters neutral matter this situation changes and collisions result in recombination. Collisions cause ions to decouple from the magnetic field in the E region allowing high currents to flow there: electrons only decouple from the magnetic field lines below  $\sim 80$ km.

In the ionosphere plasma is being created by ultraviolet radiation and by solar X-rays and at the same time being destroyed by dissociative recombination of molecular ions and by recombination of atomic ions, so that the actual amount is a dynamic balance between these processes of ionisation and recombination [Prölss 2004].

The ionosphere has a bearing on these studies in the following ways:

- (1) Particle fluxes entering the high atmosphere can give rise to enhanced ionisation in the ionosphere which can give rise to absorption of cosmic radio background and be detected in ground riometers.
- (2) Conductivity gradients created by precipitation can give rise to ionospheric shear flow and associated ground magnetometer deflections
- (3) ULF waves interact with the conducting ionosphere and may be reflected back along magnetic field lines giving rise to quadrature oscillations [Chapter 9].
- (4) ULF waves can give rise to ionospheric electric currents which in turn give rise to magnetic fields that deflect ground magnetometers.

### 1.12.1 Ionospheric Hall currents

The electron gyrofrequency  $\omega_g$  in a uniform magnetic field is:  $\omega_g = \frac{|e B|}{m_e}$  (1.11)

Electrons gyrate clockwise and positive ions gyrate anticlockwise when viewed in the direction along lines of magnetic field.

---

<sup>(1)</sup> In 1902 Arthur Kennelly and Oliver Heaviside independently postulated the existence of a highly electrically conducting ionosphere to explain Marconi's transatlantic radio transmissions although currents flowing in an electrically conducting strata of the upper atmosphere had been suggested earlier [Stewart 1861] to explain geomagnetic pulsations.

If the collision frequency is low a charged particle can perform many gyrocycles before suffering a collision. If an electric field  $\mathbf{E}$  is also present in this collisionless case both ions and electrons drift normal to the electric and magnetic field directions at velocity:

$$\mathbf{u} = \mathbf{E} \times \mathbf{B} / B^2 \quad (1.12)$$

However there is no net current because both the sign of the charges and the sense of gyration is opposite. In the upper ionosphere the ions suffer collisions with neutral particles more frequently than the electrons and the ion current has a component in the direction of the electric field and a reduced component in the direction of  $\mathbf{u}$  with the result that the electron drift current in that direction is no longer cancelled out. This gives rise to components of conductivity in the  $\mathbf{E}$  and  $\mathbf{u}$  directions which are termed the Pederson and Hall conductivities respectively. At an altitude below about 120 km the Hall conductivity dominates over the Pederson conductivity and then in the lower ionosphere both conductivities tend to zero because of recombination.

It has been found that the westward substorm related electrojet associated with the formation of the substorm current wedge is dominated by Hall currents with a magnitude of  $\sim 1\text{MA}$ :  $\sim 2\text{-}3$  times the magnitude of the Pederson current [Lu 2000].

### 1.12.2 Field-aligned currents

At high latitudes the precipitation of charged particles along magnetic field lines into the ionosphere makes an important contribution to the electron density and to ionospheric joule heating. These precipitating particles can have sufficient energy to ionise secondary electrons with sufficient energy to create further ionisation.

By taking the divergence of Ohm's Law [Kosch 2001] the field-aligned current density arising from precipitation  $\mathbf{j}_{\parallel}$  can be decomposed into the sum of three terms as:

$$\mathbf{j}_{\parallel} = \sum_p \nabla \cdot \mathbf{E} + \nabla \sum_p \rho \cdot \mathbf{E} + \nabla \sum_H \cdot (\hat{\mathbf{z}} \times \mathbf{E}) \quad (1.11)$$

where the first right hand side term is the contribution to the field aligned current density from the divergence in the electric field, the second the contribution from the gradient in the height integrated Pederson conductivity and the third the contribution from the gradient in the height integrated Hall conductivity.

Thus precipitation can create ionospheric channels of higher conductivity bounded by decreasing conductivity. This gives rise to the phenomena of ionospheric shear flow whereby currents flow in opposite directions. An example of this occurs in the region known as the Harang discontinuity [Figure 1.9] between the pre-midnight eastwards electrojet and

the post-midnight westwards electrojet [Amm et al. 2000]. This paper suggests that there are actually two field-aligned current sheets in the same sense separated by  $1-2^\circ$  of latitude with the equatorward one associated with the gradient terms and the poleward one with the divergence term in Equation 1.11. It is also suggested that these may originate in different plasma regimes in the magnetosphere. It is however difficult to directly observe the magnetic fields from field-aligned currents on the ground as explained by the well-known theorem [Fukushima 1976] that states:

*At all points below the ionosphere the magnetic field from field-aligned currents and the magnetic field from associated Pederson currents exactly cancel. It holds in any planar or spherical geometry provided that the field lines are vertical and that the ionospheric conductances are spatially uniform.*

The problem is that the anticlockwise magnetic field from the field-aligned current is exactly cancelled out by the clockwise magnetic field from the radial Pederson currents. Since a current sheet can be regarded as an infinite number of field-aligned currents the same problem arises in detecting the magnetic field of a current sheet on the ground. Another way of looking at this is to regard two current sheets closed through the ionosphere as part of a long solenoid with a field outside the solenoid near to zero. It is sometimes possible to detect high latitude field-aligned currents from inclined field lines that pass over using low latitude ground magnetometers because the ionospheric currents then have a horizontal component. However in the presence of an applied electric field a current sheet may also give rise to Hall currents which give rise to a magnetic field that can be detected on the ground.

### **1.13 The tail plasma sheet**

The tail current sheet structure lies in the geomagnetic equatorial region from the co-rotating plasma sphere and beyond in the dawn sector. In the dusk and midnight sectors the tail current sheet is separated from the co-rotating plasma sphere by a region of low plasma density called the plasma trough. The geostationary orbit at  $6.6R_E$  is near the plasma sheet inner edge and during quiet times geostationary spacecraft are Earthward of this edge but during geomagnetic storms dipolarisation of the field combined with the  $\pm 11^\circ$  variation in GSE coordinates means that they can be on field-lines that extend into the distant tail.

To the north and south of the tail plasma sheet is the Plasma Sheet Boundary Layer PSBL [Figure 1.16] which is threaded by magnetic field lines that map to the high-latitude region

of the auroral oval. Beyond the PSBL are the north and south magnetospheric lobes. The equatorial boundaries of the tail plasma sheet are referred to as the low-latitude boundary layer LLBL.

Plasma flows across field lines in the tail plasma sheet but along field lines in the PSBL where it can exhibit bursty flow with peak speeds of  $\sim 250\text{-}1000 \text{ km s}^{-1}$  [Lyons et al. 2000]. These bursty flows are associated with auroral poleward boundary intensifications [PBIs] and hence with significant field-aligned currents. The plasma sheet can exist in a stable state or in a turbulent state at the time of these PSBL bursty flows.

Processes in the magnetotail affect the PSBL which is crossed from south to north by the orbit of the Polar satellite. There have been some recent studies of Poynting flux measurements which have reported Alfvén shear waves in this region [Keiling et al. 2000 and 2002], [Dombeck Wygant and Cattell 2005] and a well-written review [Keiling 2008] describes many aspects of these Alfvén waves including their association with substorm onset and the carrying of field-aligned currents. Two papers also describe the association of substorms with mHz oscillations detected by the Polar satellite [Toivanen et al. 2002 and 2003].

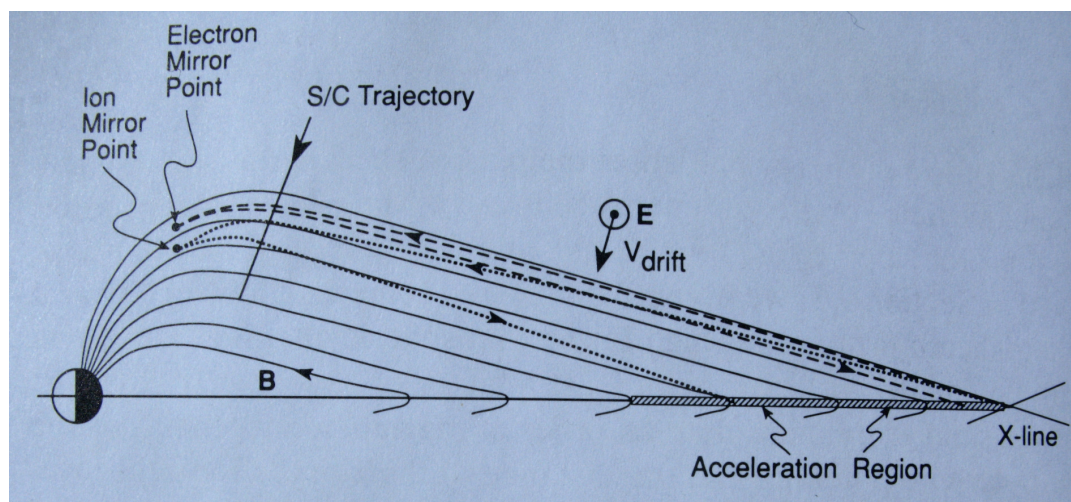


**Figure 1.16 Field-lines from the Earth to the tail plasma sheet**

This diagram shows how plasma drifts onto the high-latitude closed field lines that link the tail plasma sheet to the ionosphere. These thread the PSBL region and extend far out into the tail. In the situation depicted these closed field lines have reconnected along an X-line and are in the process of dipolarising. The Polar satellite orbit passes through this region of the magnetosphere. [Kivelson and Russell 1995]

## 1.14 Aurora

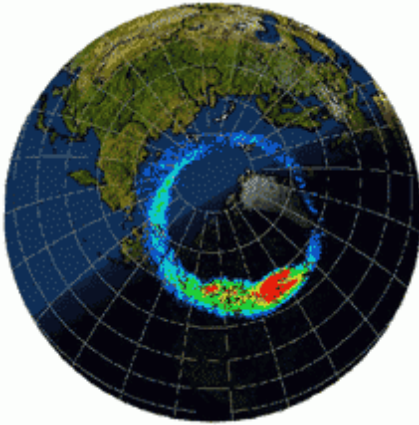


**Figure 1.17 Auroral oval**

The auroral oval is aligned with respect to the Earth-Sun line as a result of the solar wind distorting the terrestrial dipole field. The brightest aurora in this illustration was at midnight. [NASA Themis]

The two descriptions of aurora given in the historical footnotes<sup>(1)(2)</sup> below were made many thousands of years apart and illustrate the enduring fascination in this natural phenomena. A comprehensive review of auroral physics research has been written by David Stern [Stern 1996]. The greenish colour that is often seen is due to emission of the 557.7nm line of atomic oxygen from a long lived metastable state at altitudes of 100km-200km [Baumjohann and Treumann 1997]. However the energies of the charged particles that give rise to the aurora far exceed the energy required for visible emissions and only ~1% of the energy of the incoming particles is transferred to radiation – about 50% is converted to heat, ~30% to chemical potential energy and the remainder scattered back into the magnetosphere. An approximate estimate of the heating intensity is given as  $10^{-8} \text{ Wm}^{-3}$  [Prölss 2004]. Aurora also emit in the UV [atomic oxygen lines at 130.4nm and 135.6nm] and X ray emissions are detected by the Pixie instrument on the Polar satellite.

---

<sup>(1)</sup> After treading on frost we arrive(d) on strong ice. In front, aside, (all was) vastness. That which contains brightness (and to which) can be put questions (shows). (It is a) fastened-up bag. It does not drum, it does not expand. A yellow lower garment (shows). Dragons are fighting in sight. Their blood (is like) dark-purple and yellow rays.

Translation of the second I-Ching hexagram 坤 [kūn] by Z.D. Sung 1935 [Teboul 1985]

<sup>(2)</sup> In the evening, the aurora had a quiet, homogenous arc form while the aurora over the midnight sky was always very active. The morning sky was covered by patchy aurora. The Earth rotates once a day under such a fixed pattern. As a result, standing at a point on the Earth, the aurora appeared to undergo a daily variation, from a quiet homogenous arc, to active rayed arcs and finally to patchy auroras, as the Earth's rotation carries the observer under the fixed pattern.

Shun-ichi Akasofu

Auroral arcs have been classified in different ways and the paper entitled: Electron acceleration by Alfvén waves in the magnetosphere [Lui and Seyler 1992] subdivides discrete arcs with slightly peaked or flat electron distributions in the range 1 – 10keV into: *small scale discrete arcs* 1-10km with electron energies from 1 – 5keV – common in the evening and at dusk when the generator may be the interaction of the solar-wind with the LLBL although they are at times related to substorm events

*large scale arcs* ~100km width with electron energies from 5-10keV – the electron population is consistent with warm plasma sheet electrons 0.1-1keV accelerated through a potential drop of 5-10 keV.

Aurora form part of a magnetospheric current circuit in which the electron precipitation is equivalent to an upward field-aligned current. The general picture that emerges from rocket and low-altitude satellite studies, as in the examples in the footnotes<sup>(1) (2) (3)</sup> below, is that the ionospheric circuit is completed by a downward field-aligned current of electrons rising from the ionosphere equatorward of the luminous arc pre-midnight and poleward of the luminous arc post-midnight. This gives the direction of the auroral Pederson current through the ionosphere in the same sense as that shown by the red arrows between the Region I and Region II Birkeland current sheets in Figure 1.9. The auroral Hall electrojet is also eastwards pre-midnight and westwards post-midnight. However the picture may be more complex as a post-midnight flight of a Nike-Tomahawk rocket from Fort Churchill through a quiet auroral arc at 0945UT [Choy et al. 1971] showed that on the poleward side of the luminous arc there was a strong upward field-aligned current caused by low-energy downward precipitating electrons with a current density an order of magnitude greater than in the arc.

---

<sup>(1)</sup> A pre-midnight study of field-aligned currents inferred from magnetometer data from the Triad satellite [Armstrong, Akasofu and Rostoker 1975] found that the poleward discrete arc marked the poleward boundary of the upward Birkeland current flow in the evening sector with downward current further equatorward.

<sup>(2)</sup> A post-midnight Porcupine 4 rocket data study [Brünig and Goertz 1986] showed an upward current density of  $5 \pm 3 \mu\text{Am}^{-2}$  in the arc and a strong downward current density of 10 - 20  $\mu\text{Am}^{-2}$  poleward of the arc.

<sup>(3)</sup> A Turbulence II rocket launched from Poker Flats, Alaska at 0836UT [Danielides 1999] reported a triple field-aligned current signature comprising an upward current density of  $0.17 \mu\text{Am}^{-2}$  in the arc with downward current densities of  $0.12 \mu\text{Am}^{-2}$  poleward of the arc and  $0.05 \mu\text{A}^{-2}$  equatorward of the arc.

Auroral arcs are associated with the closed magnetic field lines linking the ionosphere to the tail plasma sheet or PSBL region of the magnetosphere [Figure 1.17]. To produce an aurora requires several processes to operate and changing any one of these conditions is likely to result in changes in the auroral parameters of which one is the visible intensity.

- (1) There needs to be a supply of charged particles which are thought to come from the vicinity of the equatorial tail plasma sheet
- (2) These particles need to acquire orbits around magnetic field lines and drifting motion on a shell that would take them to auroral latitudes
- (3) The pitch angle distribution of the charged particles needs to be modified by some mechanism such as VLF wave-particle interaction [Coroniti and Kennel 1970] so that a fraction of them have sufficiently low pitch angles to avoid magnetic mirroring in the increasing field strength towards the Earth.
- (4) The energy of the particles from the tail plasma sheet [ $\sim 1$ keV] needs to be increased to create discrete arcs. This enhancement is thought to come from electric fields with a component parallel to the magnetic field lines at an altitude of  $\sim 1 - 2 R_E$  in the auroral acceleration region [AAR]. Another theory is that  $E_{\parallel}$  is created by anomalous resistivity caused by plasma wave instabilities [Papadopoulos 1977]. This idea could account for the generation of the intense auroral kilometric radiation [AKR] [Gurnett 2008]. Plasma double layers and kinetic Alfvén waves [Block and Fälthammar 1990 and Lui and Seyler 1992] have also been put forward as possible generators of these parallel electric fields.

#### **1.14.1 Ionospheric auroral electric fields**

Ionospheric Pederson current flowing into the arc from one side [equatorward pre-midnight and poleward post-midnight] gives rise to an ionospheric electric field that is enhanced by low ionospheric Pederson conductivity. This region of enhanced perpendicular electric field displaced from the arc has often been detected in STARE coherent radar returns and has been referred to as *electric field overshoot* [Brünig and Goertz 1986]. EISCAT radar studies using phase modulated codes and short integration times [Opgehoorth et al. 1990] [Williams et al. 1990] have revealed enhancements on timescales similar to the Poynting flux Impulses [PFIs] described in Chapters 6 and 7. In these studies the EISCAT radar was operated in tristatic mode using ground stations at Tromsø, Kiruna and Sodankylä [Figure 1.18] to measure the component of electric field perpendicular to the field lines using the

relation:  $\mathbf{E} = -\mathbf{v} \times \mathbf{B}$ , where  $v$  is the ionospheric flow velocity determined from the Doppler shift in the radar return. In the upper E region and F region of the ionosphere between 125 and 270km the ion gyrofrequency is greater than the collision frequency and the strong electric field drives the ions through the neutral atmosphere where collisions give rise to ion heating. This ion heating was observed on all 27 occasions when the electric field exceeded  $50\text{mVm}^{-1}$ . Electron heating was also observed in the lower E region. An example of their observations on 2008-03-28 showed 4 major electric field spikes at 2009UT, 2023UT, 2028UT and 2049UT. At 2023UT the electric field changed from  $50\text{mVm}^{-1}$  to  $180\text{mVm}^{-1}$  and back within 3 minutes. Both the auroral electric field pulse signature and the pulse repetition timescale are similar to the pulsing of the Poynting flux impulses described in Section 6.5.3.



**Figure 1.18** EISCAT radar at Sodankylä

This antenna was used in the tristatic studies of auroral electric fields by Williams et al. 1990  
This photograph was taken on 2008-03-27 by the author.

## 2.0 ULF waves

### 2.1 Introduction

Oscillations about equilibrium arise when a mechanism exists that acts to restore equilibrium following a displacement of the system from equilibrium. For Alfvén waves in the context of this study the equilibrium state is the background level of the terrestrial magnetic field and the restoring mechanisms are the tendency of lines of magnetic fields to resist deformation together with the plasma *gas* pressure . Oscillations provide a way of transferring energy without transferring the particles involved. The Penguin Dictionary of Physics [Pitt 1975] defines a wave as a disturbance, either continuous or transient, travelling through a medium by virtue of the elastic and inertial factors of the medium, the resulting displacements of the medium being relatively small and returning to zero when the wave has passed. The displacements at each point in space couple to the surrounding points in a way that determines the subsequent temporal evolution of the wave [Ohanian 1994]. These are sometimes recognised as the classical patterns of reflection, refraction, interference and diffraction as in the study described in Chapter 5. ULF waves with frequencies in the milliHertz region are observed in many data sets including those from magnetometers, riometers, all-sky imagers, radars and satellite sensors. As ULF waves are of wide interest there are a number of review papers including those by [Allan and Poulter 1992], [Anderson 1994], [Hughes 1994], [Troitskaya 1994] and [Kivelson 2006]. Some notes on the early observations of geomagnetic oscillations are given in the historical footnote<sup>(1)</sup> below.

---

<sup>(1)</sup>A London instrument maker, George Graham, discovered that a compass needle is always in motion and this was confirmed in 1740 by Anders Celsius in Uppsala, Sweden whose observations were continued by Olof Hiorter [Kivelson and Russell 1995]. A link between the Sun and terrestrial geomagnetic activity was provided by Richard Carrington's observation on 1859-09-01 of a solar flare followed 18 hours later by a very strong magnetic storm. Observations of oscillations in the geomagnetic field were made by a photographic self recording three axis magnetometer at the Kew Observatory, London in the 19<sup>th</sup> century [Kivelson and Russell 1996], [Walker 2005] and pulsations during the time of 'a great magnetic disturbance' with periods of between half a minute [33mHz] and five minutes [3.3mHz] were described [Stewart 1861]. The connection between an electric current and a magnetic field had been made earlier in 1820 by the Danish scientist Hans Oersted and Stewart suggested that currents were flowing in an electrically conducting strata of the upper atmosphere many years before the ionosphere or the magnetosphere were postulated [Hughes 1994].

### 2.1.1 Classification of pulsations

IAGA Class	Period	Frequency	Notes
Pc1	0.2s – 5s	5Hz - 200mHz	EMIC instability generated by temperature anisotropies of protons in the energy range of a few keV to a few hundred keV [Erlandson et al. 1994] Can be modulated by Pc5 waves [Rasinkangus et al. 1994]
Pc2	5s – 10s	200mHz -100mHz	
Pc3	10s – 45s	100mHz - 22mHz	Related to activity in the solar wind upstream of the bow shock [Baker K.B. 1998], [Potapov 1994]- period $T(s) \sim 160/B(nT)$ [Troitskaya 1994] Period affected by magnitude of IMF - occurrence and power affected by IMF cone angle [Luhmann, Petrinec and Russell 1994]. Absent when cone angle $\sim 90^\circ$ [Takahashi 1994]
Pc4  Pg	45s – 150s	22mHz - 7mHz	Toroidal field line resonances at lower geomagnetic latitudes than Pc5 [Verö 1994] Plasmaspheric cavity modes and drift-bounce resonance with hot ring-current ions Giant pulsations observed just to the south of the auroral oval [Thompson and Kivelson 2001]
Pc5	150s – 600s	7mHz - 1.7mHz	Toroidal field line resonances at high geomagnetic latitudes Waveguide and cavity mode Magnetotail phenomena such as BBFs
Pc6*	>600s	< 1.7mHz	Waveguide and cavity mode
Pi1	1s – 40s	1Hz - 25mHz	Seldom mentioned
Pi2	40s – 150s	25mHz - 7mHz	Impulsive processes in the magnetotail [Luhmann 1994]. Defines the time of substorm onset. Frequency of occurrence approximately anti-correlated with sunspot number [Luhmann, Petrinec and Russell 1994] Correlated with $v_{sw}$ but less so with IMF orientation suggesting a velocity shear origin - associated with electron precipitation [Posch et al. 1999]

**Table 2.1 IAGA classification of ULF pulsations with additional notes**

In 1964 the International Association of Geomagnetism and Aeronomy [IAGA] recommended a classification scheme for what was then referred to as geomagnetic micropulsations. A distinction was made between continuous pulsations [Pc] and irregular pulsations [Pi]. At Hamburg in 1981 the Working Group on Geomagnetic Micropulsations recommended the general term ULF pulsations be used to describe the phenomena [Walker 2005] as it was by then clear that the oscillations were not just magnetic. Often the classification scheme is just used to refer to frequencies and occasionally unofficial reference [denoted by an asterisk] is also made to a lower frequency Pc6 band and to giant pulsations Pg.

A summary of the classification scheme together with notes is shown in Table 2.1.

### **2.1.2 Pc5 and Pi2 waves**

ULF waves with frequencies in the low mHz band are prevalent for much of the time in ground magnetometer data. On a magnetogram there is a difference in character between the wideband and irregular Pi2 waves and the narrowband and continuous Pc5 waves. However, the distinction is somewhat subjective and irregular oscillations with narrow bandwidth are sometimes referred to as Pc5. Pc5 waves may be generated by solar wind pressure pulses on the magnetosphere boundary. This interaction is stronger on the dayside magnetosphere and arises when either the speed or the density of the solar wind increases. Other mechanisms that generate predominantly dayside Pc5 waves may include magnetic reconnection on the dayside magnetosphere and the Kelvin- Helmholtz instability on the dayside magnetosphere boundary [Song 1994]. A comprehensive study of the characteristics of Pc5 waves is given by Baker et al. [2003] and this study clearly showed the predominantly dayside occurrence of these waves, a feature that could explain why it may be comparatively rare for Pc5 waves to be detected in the dusk-midnight sector. Pc5 wave parameters exhibit complex latitude dependence [Samson and Rostoker 1972].

Pi2 waves derive their irregular character from the presence of a range of frequencies, suggesting an impulsive origin.. They are often observed as a precursor to substorm activity and detecting their presence using wavelet processing has been developed to provide nowcasting of substorm onset [Nosé 2006]. In a study [Saka et al. 1999] which compared a low latitude ground magnetogram from Huancayo, Peru [geomagnetic latitude 1.44°N] with all-sky camera [ASC] images from Syowa Station, Antarctica [geomagnetic latitude 66.2°S] Pi2 waves were shown to correlate well with luminosity modulation following an auroral breakup event on 1986-06-16. Peru is too distant from Antarctica for the Pi2 waves to be

the ground signal of ionospheric currents associated with the auroral precipitation so this raises the question of where Pi2 signals are generated and one possibility is that they are the ionospheric signature of surface waves on the co-rotating plasmasphere set up by energy released from the magnetotail, although they may be generated by other mechanisms of an impulsive nature.

The dispersion relations for the different MHD modes, which define the relationship between angular frequency  $\omega$  and wavenumber  $k$  are summarised in Table 2.1. Because Pi2 oscillations contain a range of frequencies and hence wavelengths they propagate at the group velocity in the magnetosphere.

The group velocity differs from the phase velocity when the speed depends upon the wavelength and is given by:  $v_g = \frac{d\omega}{dk}$  Substituting  $\omega = v_p k$  and differentiating

$$\text{gives: } v_g = v_p + k \frac{dv_p}{dk} \text{ which can be rewritten: } v_g = v_p - \lambda \frac{dv_p}{d\lambda} \quad (2.1)$$

The group velocity is less than the phase velocity when the velocity of longer wavelengths is greater than that of shorter ones [Jenkins and White 1957].

Measuring the time interval between successive magnetogram peaks was found to be a simple and useful way of establishing whether the signals were monochromatic. In these studies pure monochromatic Pc5 oscillations were not encountered, although many signals in the Pc5 band with bandwidths of  $\sim 1$  MHz and upwards were observed.

## 2.2 Sources of ULF waves

Although no mechanism nor connection with terrestrial observation has been established it is of interest that the Sun itself has p modes of oscillation at mHz frequencies, a 4 mHz oscillation being one of the first to be discovered in Doppler studies of spectral lines in the early 1970s [Chaplin 2006].

The sources of ULF waves may be subdivided into those of external origin, such as solar wind impulses, Kelvin Helmholtz instability on the magnetopause and sources upstream of the bow shock and those of internal origin, such as drift-bounce resonance with ring current ions, magnetic reconnection and plasma flows into the magnetotail [bursty bulk flows] [Mann 2001]. However the solar wind is ultimately the driving mechanism behind all these sources of ULF waves [Luhmann, Petrineric and Russell 1994]. A diagram illustrating the different magnetospheric ULF waves is reproduced from [Allan and Poulter 1992] in

Figure 2.1

### 2.2.1 External excitation of ULF waves

Transient waves are generated when a system is subjected to an impulse, either internally or externally. An impulse that could act upon the terrestrial magnetosphere system could arise from a change in the solar wind parameters such as the speed, density, composition or magnetic field direction. Many studies have been carried out on ULF waves in ground magnetometer data with frequencies below 10mHz. They have been observed to be prevalent at varying levels for much of the time, particularly during the period from dawn until dusk. Daytime Pc5 waves have been associated with the interaction between the solar wind and the magnetopause [Mann and Wright 1999] [Engebretson et al. 1998]. In a study spanning a solar cycle [Mann, O' Brian and Milling 2004] a high rank order correlation coefficient of  $\sim 0.75$  was measured between the solar wind speed  $v_{sw}$  and ULF wave power on L shells from 3.1 to 6.6 during the declining phase of a solar cycle. The dawn and noon sectors showed the highest levels of correlation and the nightside the least, an observation attributed to the absence of any KHI-driven waves in the midnight local time [LT] sector.

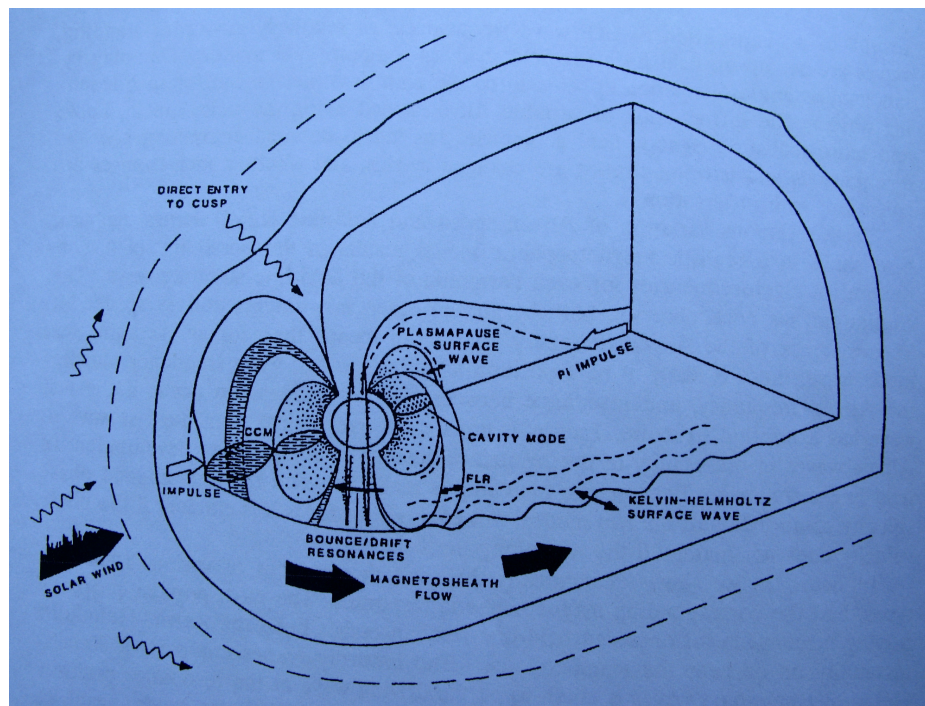


**Figure 2.1 Magnetospheric ULF waves** This sketch [reproduced from Allan and Poulter 1992] shows solar wind impulses generating magnetospheric oscillations, solar wind ULF waves entering the polar cusp, Kelvin-Helmholtz surface waves on the magnetopause and Pi2 impulses from the magnetotail.

These authors also noted that although the correlation did not depend upon L-shell the actual ULF wave power has been shown to increase significantly with L-shell [i.e. towards higher latitudes] in the morning sector [Mathie and Mann 2001]. Peak ULF wave power was observed during the declining phase of the solar cycle and this may be accounted for by the inclination of this current sheet over the solar cycle which would be expected to bring the higher latitude, higher speed solar wind to the ecliptic plane most often in the periods between sunspot maxima and minima [Luhmann, Petrinec and Russell 1994].

A high-latitude study [Menk et al. 2003] showed that a sharp decrease in solar wind dynamic pressure gave rise to 1.6 - 1.7 mHz pulsations and to a narrow field line resonance. Another study [Clemmons et al. 2000] showed Pc5 waves associated with the hole in a magnetic cloud.

The Kelvin-Helmholtz instability [KHI] on the magnetospheric boundary, whereby the solar wind brushes over the magnetosphere and sets up turbulent vortices is frequently cited as a source of ULF wave energy. ULF waves generated by KHI are generally associated with large spatial scales and hence high azimuthal m numbers as described below.

An analysis of a large number of Pc5 band pulsations [Baker et al. 2003] enabled a statistical approach to be used and this showed that there was a higher probability of observing pulsations during the morning sector. They suggested that these morning sector results were suggestive of Pc5 band power coupled onto closed field lines from disturbances on the dawnside magnetopause. Their study showed wave propagation from the east in the morning and from the west in the afternoon with the directional reversal taking place around the time of local noon. Their paper included maps of the location of ULF wave sources in the magnetosphere. In an earlier study [Mathie et al. 1999] also showed a variation in azimuthal wavenumber over the course of a day which corroborated with these propagation directions. The azimuthal wavenumber denoted m physically corresponds to the number of waves around the Earth at the geomagnetic latitude of the observing stations. If two magnetometers are at the same latitude  $\lambda$  and distance d apart it is possible to estimate from the phase difference  $\Delta\phi$  [in radians] how many waves would theoretically go around the Earth at that latitude: this is referred to as the azimuthal wavenumber and is denoted by m where:

$$m = \frac{2\pi r}{\lambda} = \frac{2\pi R_E \cos \Lambda}{2\pi d / \Delta\phi} = \frac{R_E \cos \Lambda \Delta\phi}{d} \quad (2.2)$$

The sign of m can be + or - depending upon the sign of  $\Delta\phi$

### 2.2.2 Internal excitation of ULF waves

Charged particles spiral around magnetic field lines and depending upon their pitch angle may mirror reflect as they encounter the increasing field strength towards the Earth. They are also able to drift across the field lines as a result of their gradient and curvature [Kivelson and Russell 1995] resulting in a westwards ring current.

The condition for ion cyclotron resonance between charged particles and the electric field of a ULF wave is that the particles encounter a coherent electric field in their frame of reference. If the particle drift frequency around the Earth is  $\omega_d$  and the frequency of a ULF travelling wave is  $\omega$  then the Doppler shifted ULF wave frequency in the particle frame of reference is :  $\omega - h_d \omega_d$  and the condition for cyclotron resonance with the bounce frequency  $\omega_b$  is:

$$\omega - h_d \omega_d = h_b \omega_b \quad (2.3)$$

where  $h_d$  and  $h_b$  are the harmonic numbers of the drift and bounce frequencies.

ULF waves either become stronger or weaker as a result of the exchange of energy. Resonance occurs with ring current ions with keV energies and may provide a means of transferring energy from the ring current to Pc4 band ULF waves.

Compressional waves with high m number associated with these wave-particle interactions have been observed in the dusk sector during magnetically disturbed conditions [Yeoman et al. 2000]. Another class of Pc5 oscillations which are thought to be generated by wave particle interactions are the giant pulsations denoted Pg which have been observed pre-noon [Chisham et al. 1994] in ground magnetometer and satellite data during geomagnetically quiet times. Cyclotron resonance with global toroidal Pc5 pulsations may provide a mechanism for accelerating electrons in the outer radiation belt to MeV energies. Particularly relevant to these studies is the possibility of ULF waves being internally generated as a result of reconfiguration of the magnetic field lines at substorm onset.

## 2.3 ULF wave phenomena

### 2.3.1 Polarisation of ULF waves

Polarisation is a way of describing the amplitude ratio and the phase-difference between monochromatic signals in two orthogonal channels, such as the horizontal H and D channels in ground magnetometer data.

If the H and D components of an oscillation have the same amplitude and are in phase [or in anti-phase] the signal is linearly polarised at 45°. If the D component lags the H component by  $\pi/2$  then the signal is said to be circularly polarised in the clockwise sense and if it leads

the H component by  $\pi/2$  it is said to be circularly polarised in the anticlockwise sense. Elliptical polarisation results when the phase-difference is between 0 and  $\pi/2$ .

The orientation of the major axis of the polarisation ellipse depends upon the relative amplitudes in the H and D channels and points in a direction orthogonal to the ionospheric current channel. Phase differences that give rise to circular or elliptic polarisation can have an origin in propagation time-differences between the orthogonal displacement directions, so if a field line is forced to oscillate in a direction with x and y field-aligned components it is possible that these components will propagate at different speeds because of different restoring forces in and across geomagnetic shells.

Although the polarisation of ULF waves was not studied here other studies have shown a reversal in the direction of circular polarisation in the horizontal components of ground magnetometer observations from anticlockwise to clockwise around the time of local noon [Samson, Jacobs and Rostoker 1971], [Samson and Rostoker 1972], [Samson 1972] and [Korotova and Sibeck 1994]. The opposite sense has been observed in the southern hemisphere [Itonga and Yumoto 1998]. A study of mid latitude Pi2 polarisation patterns in SAMNET data [Yeoman, Milling and Orr 1990] showed a reversal in polarisation sense across the plasmopause. The direction of circular polarisation has also been observed to reverse with latitude across a field line resonance although this is not always the case [Hughes and Southwood 1976] [Keiling 2001].

### **2.3.2 Interaction of ULF waves with the ionosphere**

The ionosphere is highly conducting and the electric field component of an incident electromagnetic wave will result in the motion of charged particles that sets up an electric field equal and opposite to the incident electric field. For a perfectly conducting ionosphere there would be a null in the electric field vector at the ionosphere, although in practice electric fields of  $50\text{mVm}^{-1}$  have been measured by radar. The oscillation of the charged particles in response to the incident wave gives rise to a secondary wave in anti-phase that cancels the incoming wave below the ionosphere. The secondary wave also travels back along the field line as a reflection. The non-zero ionospheric electric field drives a Pederson current which shields the magnetic field displacements from the ground. The components of this current can be detected in the Doppler shift in echoes from HF coherent scatter radars such as Super DARN [Super Dual Auroral Radar Network] [Greenwald et al. 1995] and coverage by more than one radar allows the Pederson current in the plane normal to the magnetic field to be determined. Coherent scatter radars rely on the presence of small-

scale, ionospheric, magnetic field-aligned irregularities which give rise to Bragg scattering [Lester 2000]. Direct backscatter requires the E field of the radio wave to be orthogonal to the magnetic field: at HF frequencies the natural refraction by the ionosphere allows this condition to be met for scattering off the E and F layers by high-latitude radars although the signal can be lost if there is enhanced ionisation in the D or E layers. This sometimes occur at substorm onset when there is increased precipitation.

For a toroidal mode ULF wave with the  $\mathbf{B}$  field oscillation tangential to a geomagnetic shell the Pederson current would be aligned approximately in the north-south direction at noon. The associated Hall current [Section 1.12.1] would then be aligned approximately east-west and the ground magnetometer signature of the Hall current strongest in the H [geomagnetic north] or X [geographic north] component.

For a poloidal mode ULF wave the ground magnetometer signature of the Hall current would be expected to be strongest in the D [geomagnetic east] or Y [geographic east] component.

The ionospheric magnetic field rotation by  $90^\circ$  is modified if there are gradients in the Pederson and Hall conductances [Orr 1984]. The ground signal from fast mode and Alfvén waves depends on the values of the Hall and Pederson conductances [Nishida 1964]. A fast mode wave propagating across field lines is not associated with a field-aligned current and sees the ionosphere as a thin sheet. The fast mode wave reflecting boundary is at the ground plane of the Earth [Allan and Poulter 1994].

### **2.3.3 Interaction of ULF waves with relativistic electrons**

Relativistic MeV electron fluxes have been associated with enhanced and sustained ULF pulsation activity, particularly in the declining phase of the solar cycle [Mann, O'Brien and Milling 2004]. The outer radiation belt containing these energetic electrons extends from  $3 R_E$  to  $10 R_E$  with the greatest intensity around  $4 R_E$  to  $5 R_E$ . Electrons are injected into the radiation belts from the tail plasma sheet during geomagnetic storms and energised by wave-particle interactions. The review by Scot R. Elkington describes ULF wave interactions with radiation belt electrons [Elkington 2006].

## **2.4 ULF resonance**

Physical systems have a natural frequency of oscillation as a result of their inertia and the strength of the restoring forces which may be of a mechanical or an electrical nature. The Fourier transform of an impulse is a spectrum containing all frequencies, so when a

resonant system is subjected to an impulse it responds by oscillating at its natural frequency. Mechanical examples of resonance are the pinging of a wine glass and the plucking of a guitar string. The natural resonance dies away as the kinetic and potential energy is transferred into other forms. Resonance can be sustained, amplified and modulated by providing a continual driving frequency and this is referred to as forced oscillation.

When a system is forced to oscillate well below its natural frequency the response is nearly in phase with the forcing signal and when it is driven well above its natural frequency the response lags  $180^\circ$  out of phase. When driven at its natural resonant frequency the system response lags the forcing signal by  $90^\circ$  [Jones 1965]. Thus phase differences can be used to determine the resonant frequency.

The maximum transfer of energy from the driving system to the natural oscillator occurs at the resonant frequency so that the amplitude response and the dissipation are a maximum there. If there is no dissipation a system would only respond at the resonant frequency and the amplitude response would be infinite. Dissipation increases the bandwidth of resonance and reduces the peak amplitude of the resonance so that the system responds with reduced amplitude to all frequencies. A useful dimensionless parameter is the Q of the resonance defined as the ratio of the resonant frequency to the bandwidth around the resonance as:

$$Q = f_0 / \Delta f \quad (2.4)$$

This is inversely proportional to the damping coefficient [Pain 1983] which can be measured from the time it takes a resonance to decay naturally to  $1/e$ .

The pioneering work of James Dungey [Dungey 1954] showed that transverse oscillations on magnetic field lines couple magnetically to compressional waves propagating across field lines for all non-zero values of the azimuthal wave-number  $m$ .

When  $m=0$  the Dungey equations describe a purely toroidal mode of magnetic oscillation in which the electric field is radial and the magnetic and plasma perturbations are azimuthal [ $E_x$ ,  $B_y$  and  $u_y$  components in the field-aligned coordinate system used in Chapters 6 - 8].

When  $m = \infty$  the Dungey equations describe the poloidal [magnetic field breathing] mode in which the electric field is azimuthal [ $E_y$  field-aligned coordinate system components] and the magnetic and plasma perturbations pulsate radially [ $B_x$  and  $u_x$  field-aligned coordinate system components]. For the fundamental and even modes the magnetic displacements at each end of a field line are out of phase for the toroidal mode and in-phase for the poloidal mode: for the odd harmonic modes the reverse is true.

Coupling between MHD modes is a form of interaction in which the component of the phase velocity of the fast mode wave matches the Alfvén phase speed along a field line. Because the fast mode propagates in three dimensions whereas the shear Alfvén mode is confined to the curved field lines this coupling condition is only met at one place along a field line and at other points along the field line the coupling is less efficient. In a cold plasma where the fast mode speed and the Alfvén speed are the same this coupling would therefore be expected to be strong where the fast mode waves were propagating along the magnetic field lines. Such a situation arises in the waveguide region around the Earth at high geomagnetic latitudes.

#### **2.4.1 Field line resonance**

Plasma loaded on geomagnetic field lines can oscillate in the toroidal mode with the restoring force provided by the tendency of a magnetic field line to resist bending. This is because the undeflected equilibrium position corresponds to a potential energy minimum in the magnetic field. Associated with the changing magnetic field is a changing electric field and if the field line is displaced by a bulk motion of the plasma or by coupling with a fast mode wave then Alfvén electromagnetic shear waves propagate in both directions to the ionospheres in the northern and southern hemispheres. The natural period of the field line resonance is the time it takes the Alfvén shear waves to travel to the ionosphere in the opposite hemisphere and return because then the two travelling waves are able to interfere constructively. At high geomagnetic latitudes the field line resonant frequency can be in the Pc5 band [Wild 2005]. For the fundamental mode the nodes in the electric fields at the ionospheres gives rise to an anti-node in the electric field near the geomagnetic equator and the anti-nodes in the magnetic field at the ionospheres gives rise to a node in the magnetic field near the geomagnetic equator. At this location a satellite magnetometer would not be expected to detect a magnetic field displacement in a fundamental mode standing wave oscillation. At other locations along the field line the ratio of electric to magnetic field amplitude varies. Harmonics of the field-line resonant frequency may also exist with their associated nodes and antinodes. Field line resonances have been the subject of a number of theoretical and observational studies: [Southwood 1974], [Chen and Hasegawa 1974], [Samson 1971], [Rae et al. 2005]. The phrase *field lines anchored at the ionospheres* is sometimes used in describing this propagation model. Field line resonances are associated with the toroidal oscillation mode which gives rise to  $E_x$  and  $B_y$  components of oscillations in field-aligned coordinates in the magnetosphere.

### 2.4.2 Cross phase technique

A fast mode impulse propagating into the magnetosphere would be expected to give rise to natural damped oscillations on field lines over a wide range of latitudes. These resonant frequencies would in general increase towards lower latitudes and because of the change in resonant frequency and because of the propagation delay in initiating the resonances a continuous phase change would be expected with latitude.

This is quite different to the situation that would arise with the forced resonance from a continuous fast or slow mode MHD compression wave propagating into the magnetosphere from a source such as Kelvin-Helmholtz instability on the magnetopause. This may couple energy to all the field lines, but will transfer most power to a field line that has the same natural frequency as itself. Field line resonances have been reported as being very narrow in the radial direction [typically 0.3 – 0.6 RE in the equatorial plane] [Samson and Rankin 1994].

On the ground a strong pulsation would be observed on the field line that was resonating and there would be a 180° phase-difference between magnetometers far to the north and the south of it. If a magnetometer was located on the resonating field line a phase lag of 90° with respect to the magnetometer in the far south would be expected. This phase-difference would change most rapidly around the resonance.

A way in which the technique can be implemented is to fast fourier transform [FFT] data from latitudinally spaced magnetometer pairings and to plot the phase-difference in colour on a background of frequency against time.

The field line resonant frequency is then read from the plot of the magnetometer pairing that yields the maximum phase-difference. The actual field line that is resonating is considered to be the one located in latitude at the mid-point between this magnetometer pairing. Given a model of the magnetic field strength along this particular field line and another model of the distribution of plasma it is then possible to infer the plasma density along the field line. The cross-phase technique is considered to be useful for the remote sensing of magnetospheric plasma densities at high latitudes using only a latitudinal array of ground magnetometers [Dent 2003]. At low latitudes it gives coupled magnetospheric-ionospheric plasma densities.

The actual frequency of a field line resonance depends upon the return length of the field line between the ionospheres in the two hemispheres and upon the integrated reciprocal of the local Alfvén shear speeds. At any point along a field line this local Alfvén speed depends

upon the local magnetic field and the local plasma mass density, which may be predominantly hydrogen ions or a mixture of hydrogen with oxygen and other species.

The first harmonic of the resonant frequency is the inverse of the integrated return time of flight of the waves along the field line. Some of the factors that influence the field line resonance frequency detected in ground magnetometer data are discussed and modelled by Wild, Yeoman and Waters [2005] and include:

- (1) The latitude of the observing station. In general the length of a magnetic field line increases with latitude so that if all other factors are unchanged the field line resonant frequency decreases with increasing latitude
- (2) The plasma loading on the field line. If this increases anywhere along the field line the Alfvén velocity decreases locally and the resonant frequency decreases
- (3) The magnetic local time MLT. The shape of a magnetic field line through a ground magnetometer station changes as the Earth rotates. At low latitudes, where field lines are approximately dipolar, the effect is smaller but at high latitudes the field lines are increasingly distended towards midnight with the result that other factors being equal the field line resonant frequency decreases as the evening progresses towards midnight
- (4) The  $D_{st}$  index. If the westward equatorial ring current increases as a result of geomagnetic activity the magnetic field strength at all latitudes is weakened and the above equation shows that the Alfvén velocity decreases. This in turn has the effect of decreasing the field line resonant frequency.
- (5) Solar wind dynamic ram-pressure. Pressure on the magnetosphere by the increased momentum of the solar wind distorts the field line geometry and may act to reduce the length of field lines through a magnetometer station on the dayside magnetosphere. All other factors being equal this would then increase the field line resonant frequency.
- (6) The clock angle of the solar wind magnetic field defined as:  $\arctan(B_y/B_z)$  where  $B_y$  and  $B_z$  are the components of the IMF.

A typical field line resonant frequency at the auroral latitude of the Sodankylä Geophysical Observatory in Finland [magnetic coordinates  $64.0^\circ$  N  $107.0^\circ$ E  $L=5.2$  ] is about 5 mHz during quiet times but decreasing with field line plasma loading, geomagnetic activity and MLT as the field lines distend.

### 2.4.3 Magnetospheric waveguide and cavity modes

In the Earth's complex three-dimensional magnetospheric cavity there is also the scope for ULF plasma waves to resonate in a way analogous to sound waves in a musical instrument such as an ocarina. The strong Alfvén speed gradient around the Earth gives rise to the idea of an inner turning point for incoming fast mode waves. The distance of this location from the Earth depends upon the angle of propagation relative to the magnetic field and does not exist if the wave is propagating normal to the field. The outer turning point for ULF waves is the magnetospheric boundary where there is a change in plasma properties and an electrically conducting current sheet. The resulting waveguide is in the form of the magnetosphere with a missing core. In the plane normal to the Sun - Earth line through the Earth the waveguide is annular and it would be possible to imagine fast mode standing wave modes across this region although wavevectors normal to the Alfvén gradient would only be weakly reflected. Fast mode standing waves around the annular structure may however be a possibility. This waveguide is open to the magnetotail so it may act as a spatial filter for both propagating fast mode and Alfvén shear waves. The resulting diffraction of fast mode waves was studied in Chapter 5 and waveguiding can be seen in the simulation movie that is included with this thesis.

The origin of this idea that compressional waves propagating between the magnetospheric boundary and the inner turning point might give rise to cavity modes of oscillation was attributed to two papers [Kivelson, Etcheto and Trotignon 1984] and [Kivelson and Southwood 1985] in a later review [Samson and Rankin 1994]. The magnetosphere was expected to support normal modes of oscillation that would couple to field lines so that field line resonance frequencies would also be the cavity frequencies [Harrold and Samson 1990]. Stable frequencies of 1.3mHz, 1.9mHz, 2.6mHz and 3.4mHz have been reported as being prevalent in field line resonances and therefore possible evidence for magnetospheric cavity modes [Samson et al. 1991, Mathie et al. 1999]. Further work has partially confirmed these observations [Ziesolleck and McDiarmid 1995] but this is an evolving field. In these studies a frequency of 3.3mHz was frequently observed in high latitude ground magnetometer data.

Another structure in the magnetosphere that is considered to support cavity modes is the co-rotating plasmasphere near the Earth. The outer region of rapidly decreasing plasma density  $\rho$  is termed the plasma trough and would give rise to an increase in the Alfvénic speed since :  $v_A \propto \rho^{-0.5}$  and hence to a critical angle of reflection. If fast mode wave resonances in the plasmasphere couple to give rise to field line resonances the ground

signature would be detected at lower latitudes in higher frequency bands. Excitation of these plasmaspheric modes could be by dipolarisation of the geomagnetic field following reconnection in the distant tail. Considerable work has been carried out on the cavity mode theory [Samson and Rankin 1994] and the cavity mode waveguide variation on it. If the magnetosphere supports multiple cavity/waveguide modes then simultaneous multiple field line resonances would be expected and indeed have been observed in ground magnetometer and radar data.

There are also observations of specific and stable [ $\sim 5 - 10\%$  over 3-4 hours] ULF frequencies such as 1.3, 1.9, 2.6 and 3.4 mHz in CANOPUS ground magnetometer data [Samson et al. 1991 and 1992]. These low frequencies may require higher plasma densities than had been thought to exist in the magnetosphere and the question has put: is there hidden cold dark matter in the magnetosphere [Mitchell et al. 1990]? A possible solution is the presence of undetected oxygen in the equatorial regions.

The picture that emerges from the waveguide model is of a magnetosphere with discrete field line resonances extending azimuthally on part or all of their geomagnetic shells. These shells have a radial thickness of the order of the field line resonance spatial width which would be expected to depend upon the amount of dissipation. Typically it might be  $\sim 0.5RE$  at the geomagnetic equator. The electric field associated with adjacent modal patterns reverses phase in the radial direction across the field line resonance [Samson and Rankin 1994] which means that on adjacent shells for the same mode order the electric fields are in opposition. This in turn has implications for current sheets between the shells and possibly therefore for multiple auroral arcs.

## 2.5 Poynting flux

### 2.5.1 Derivation of the Poynting flux theorem

The Poynting flux theorem combines Faraday's law and the Ampère – Maxwell law using the vector identity [Boas 1966] :

$$\nabla \cdot \mathbf{E} \times \mathbf{H} = \mathbf{H} \cdot \nabla \times \mathbf{E} - \mathbf{E} \cdot \nabla \times \mathbf{H} \quad (2.5)$$

substituting:  $\nabla \times \mathbf{E} = -\frac{\partial \mathbf{B}}{\partial t}$  [Faraday's Law] and  $\nabla \times \mathbf{B} = \frac{1}{c^2} \frac{\partial \mathbf{E}}{\partial t}$

which is the Ampère – Maxwell law with  $\mathbf{j} = 0$  into this vector identity to remove the curl on the rhs gives:

$$\nabla \cdot \mathbf{E} \times \mathbf{H} = -\mathbf{H} \cdot \frac{\partial \mathbf{B}}{\partial t} - \epsilon \mathbf{E} \cdot \frac{\partial \mathbf{E}}{\partial t} \quad (2.6)$$

If the electric and magnetic energy densities are denoted by  $u_E$  and  $u_B$  the two terms on the rhs are their rates of change since:

$$\mathbf{H} \cdot \frac{\partial \mathbf{B}}{\partial t} = \frac{1}{\mu} \mathbf{B} \cdot \frac{\partial \mathbf{B}}{\partial t} = \frac{1}{2\mu} \frac{\partial}{\partial t} \mathbf{B} \cdot \mathbf{B} = \frac{\partial}{\partial t} u_B$$

and: 
$$\epsilon \mathbf{E} \cdot \frac{\partial \mathbf{E}}{\partial t} = \frac{\epsilon}{2} \frac{\partial}{\partial t} \mathbf{E} \cdot \mathbf{E} = \frac{\partial}{\partial t} u_E$$

so that: 
$$\nabla \cdot \mathbf{E} \times \mathbf{H} = -\frac{\partial}{\partial t} (u_B + u_E) \quad (2.7)$$

Integrating both sides over a volume:

$$\begin{aligned} \iiint \nabla \cdot \mathbf{E} \times \mathbf{H} \, dv &= \iiint -\frac{\partial}{\partial t} (u_B + u_E) \, dv \\ &= -\frac{\partial}{\partial t} (U_B + U_E) \end{aligned} \quad (2.8)$$

where:  $U_E$  and  $U_B$  are the total electric and magnetic energies inside that region

Applying the divergence theorem: 
$$\iiint \nabla \cdot \mathbf{S} \, dv = \iint \mathbf{S} \cdot \mathbf{n} \, da$$

where:  $\mathbf{S} = \mathbf{E} \times \mathbf{H}$  gives the Poynting flux theorem:

$$\iint_{\text{surface}} \mathbf{E} \times \mathbf{H} \cdot \mathbf{n} \, da = -\frac{\partial}{\partial t} (U_B + U_E) \quad (2.9)$$

This says that the Poynting flux vector  $\mathbf{E} \times \mathbf{H}$  integrated over the surface of a region equals the rate of change with time of the electromagnetic energy inside that region [Poynting 1884].

The rhs of the Poynting flux theorem has units of watts, from which it follows that  $\mathbf{E} \times \mathbf{H}$  has units of  $\text{Wm}^{-2}$ , which is possibly why  $\mathbf{E} \times \mathbf{H}$  is often referred to as a Poynting flux, even though the gedanken experiment described below shows that there may not necessarily be any physical energy flowing into or out of the system.

### 2.5.2 Interpretation of $\mathbf{E} \times \mathbf{H}$

The converse of the above interpretation of the Poynting flux theorem is also true: if there is no change in the energy contained within a closed region [such as a geomagnetic shell] then the Poynting flux vector integrated over the surface of that region is zero. This does not mean that the value of  $\mathbf{E} \times \mathbf{H}$  is zero everywhere over that surface since positive and negative contributions to the surface integral can sum to zero.

A *gedanken* or thought experiment is one that you do in your mind. Schrödinger's cat in quantum mechanics is a good example of a *gedanken* experiment. The following *gedanken* experiment was devised by the author to illustrate this aspect:

*Imagine a charged sphere containing a bar magnet [Figure 2.2]. The electric field is zero everywhere inside the sphere so there is no electric energy stored inside the sphere. There is energy stored in the magnetic field but this remains constant. Now the Poynting flux theorem says that if  $\mathbf{E} \times \mathbf{H}$  is integrated over the surface of the sphere the result will be zero since the total energy inside the sphere is constant. In Figure 2.2 an imaginary Polar satellite orbiting around the sphere senses the electric and magnetic fields. Only where the electric and magnetic field vectors are parallel is the local value of  $\mathbf{E} \times \mathbf{H}$  equal to zero. This occurs everywhere along a horizontal axis through the centre of the sphere but nowhere else is  $\mathbf{E} \times \mathbf{H}$  equal to zero. In the upper half of the diagram  $\mathbf{E} \times \mathbf{H}$  is out of the page and in the lower half it is into the page. However by symmetry it can be seen that these contributions to  $\mathbf{E} \times \mathbf{H}$  are equal and opposite, thereby making the surface integral zero, as would be expected from conservation of energy considerations. In this configuration  $\mathbf{E} \times \mathbf{H}$  is directed toroidally around the bar magnet and has no radial component.*

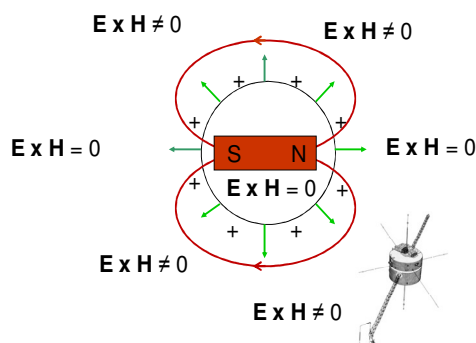


**Figure 2.2 Poynting flux theorem  
gedanken experiment**

The electric and magnetic fields associated with a bar magnet inside a charged sphere give rise to local non-zero values of Poynting flux even though there is no energy flux

$\mathbf{E} \times \mathbf{H}$  is a local measurement in a wider  $\mathbf{E} \times \mathbf{H}$  vector field and it is the surface integral over an enclosed region in that field that determines whether there is a net flux into, or emanating from that region.

An analogous situation arises if the Polar satellite is sensing the electric and magnetic fields outside a closed surface such as a magnetic flux tube – if energy is trapped by standing waves propagating inside the tube then the Poynting flux integrated over the surface of the tube should be zero. But it may still be possible for the Polar satellite to sense local non-zero values of  $\mathbf{E} \times \mathbf{H}$  and these local non-zero time series provided useful information on standing waves, including the fact that no energy was necessarily being lost from the tube as a whole.

If electromagnetic waves were propagating through the enclosed region without attenuation the Poynting flux surface integral would again be zero. This leads to a second *Gedanken experiment* where electromagnetic waves are imagined to be propagating through a thin sheet with the outwardly directed normals  $\hat{\mathbf{n}}$  in opposite directions on either side.  $\mathbf{E} \times \mathbf{H}$  is the same on both surfaces of the sheet because the direction of propagation is the same but the scalar product with  $\hat{\mathbf{n}}$  makes the sign different so that the Poynting surface integral is zero as would be expected. However if the Poynting integral is not carried out then  $\mathbf{E} \times \mathbf{H}$  for one side only gives the wave intensity. The conclusion this leads to is that if an electromagnetic wave is known *a priori* to be propagating then  $\mathbf{E} \times \mathbf{H}$  is a valid measurement. Clues as whether a wave is propagating can be found in the existence of a temporal variation and the in-phase nature of the electric and magnetic field oscillations.

Data from a single point spacecraft, such as the Polar satellite whose data was used in these studies, cannot be used to carry out a spatial integral of Poynting flux – however multisatellite data, such as from the CLUSTER mission, could provide several point observations of Poynting flux and provide useful information on the spatial integral.

### 2.5.3 Poynting flux vector for ULF oscillations

ULF oscillations generate AC electric and magnetic fields. This means that  $\mathbf{E} \times \mathbf{H}$  is time-varying. If the physics allows  $\mathbf{E} \times \mathbf{H}$  to be associated with an electromagnetic flux then that flux is not constant but varies with factors such as the phasing of the electric field relative to the magnetic field. This can give rise to pulsing of the Poynting flux.

If the AC components of the electric and magnetic fields are denoted by *tildes* then:

$$\tilde{\mathbf{S}} = \tilde{\mathbf{E}} \times \tilde{\mathbf{H}} = \frac{1}{\mu_0} \begin{vmatrix} \mathbf{i} & \mathbf{j} & \mathbf{k} \\ \tilde{E}_x & \tilde{E}_y & \tilde{E}_z \\ \tilde{B}_x & \tilde{B}_y & \tilde{B}_z \end{vmatrix} \quad (2.10)$$

Each component is a real signal, though they may each have a different spectral content.

The mathematical operation  $\tilde{\mathbf{E}} \times \tilde{\mathbf{H}}$  then generates Poynting flux components with a spectral content that depends upon the spectral content in the terms from which it was calculated. Imagine a series of observations over time in which the electric and magnetic fields have the same frequency [f] and are in-phase with each other. To further simplify things also imagine that the propagation is such that only  $\tilde{E}_x$  and  $\tilde{B}_y$  are non-zero.

$$\text{Then the above determinant representation reduces to: } \tilde{S}_z = \frac{1}{\mu_0} \tilde{E}_x \tilde{B}_y \quad (2.11)$$

The electric and magnetic component frequencies heterodyne to yield sum and difference frequencies of  $2f$  and zero respectively. The zero frequency is a DC offset that makes  $\tilde{S}_z$  positive at all times. If they were in anti-phase then  $\tilde{S}_z$  would be negative at all times: thus the phase difference determines whether the propagation is in the  $+z$  or in the  $-z$  direction. A particularly interesting case arises with standing electromagnetic waves when the phase difference between the electric and magnetic oscillations is  $90^\circ$  as a result of reflection from the ionospheres. The above operation would then only generate a frequency of  $2f$  in the  $\tilde{S}_z$  component. This zero mean signal shows that although energy is alternately propagating in the  $+z$  then the  $-z$  direction there is no resultant energy propagation. Thus the time varying nature of  $\tilde{\mathbf{E}} \times \tilde{\mathbf{H}}$  can be used to distinguish between electromagnetic propagating oscillations and electromagnetic standing oscillations and this was the basis of the classification scheme used in Chapter 6.

#### 2.5.4 Detection of electromagnetic waves

The operation  $\overline{\tilde{\mathbf{E}} \times \tilde{\mathbf{H}}}$ , where the bar denotes a time average, is a highly sensitive detector for the presence of *propagating* ULF electromagnetic waves. Effectively it performs a cross-correlation in time between the electric and magnetic fields. The result yields information on the strength and direction of propagation of the waves.

This operation rejects oscillations where there is only an electric field or only a magnetic field present and oscillations where the electric and magnetic fields have different frequencies. A non-zero result requires the electric and magnetic fields to maintain their phase relationship. However if this operation is carried out on standing waves the quadrature nature of the phase-difference will mean that the time average goes to zero since:  $\langle \sin \omega t \cos \omega t \rangle = 0$ . Thus even if quadrature oscillations were present they would remain undetected if a time average were to be used.

### 2.5.5 Poynting flux signature of electromagnetic standing waves

It is a matter of experience that the entire electromagnetic spectrum can be reflected by electrically conducting boundaries. An electric field incident on an electrically conducting medium such as the ionosphere will give rise to forces on the charged particles in that medium and these charges will then move until their collective electric field is of the same magnitude as the incident electric field but opposite in direction.

The resultant electric field on the boundary is then zero and a node in the electric field oscillation is created there. The oscillating anti-phase electric field of the charged particles is the source of an reflected electromagnetic wave that travels in the reverse direction in antiphase with the incident wave since:  $-\mathbf{E} \times \mathbf{H} = -\mathbf{S}$

The incident and reflected waves then interfere and the following proof shows that there is a  $90^\circ$  phase shift between the electric and the magnetic field displacements in an electromagnetic standing wave pattern such as might be encountered when an Alfvén shear mode wave is reflected between ionospheres in the northern and southern hemispheres. This important result is used in the classification scheme described in Chapter 6.

For the electric field components in a travelling wave there is a phase change on reflection at a conducting boundary of  $\pi$  and superposition occurs between the wave travelling in the  $+z$  direction and the  $-z$  direction. In the following proof the arrows above the electric field  $\mathbf{E}$  and magnetic field  $\mathbf{B}$  components denote the direction of propagation:  $k$  is the wavevector and  $\omega$  the angular velocity of the travelling wave.

The origin of the  $z$  direction is at the southern hemisphere ionosphere: for an origin at the northern hemisphere ionosphere  $kz$  is replaced by  $-kz$ .

The magnetic component is initially in phase with the electric field component: there is no phase change on reflection:

$$\vec{\mathbf{B}} = \mathbf{B}_0 \sin(kz - \omega t) = \mathbf{B}_0 \sin(kz) \cos(\omega t) - \mathbf{B}_0 \cos(kz) \sin(\omega t)$$

$$\overleftarrow{\mathbf{B}} = \mathbf{B}_0 \sin(kz + \omega t) = \mathbf{B}_0 \sin(kz) \cos(\omega t) + \mathbf{B}_0 \cos(kz) \sin(\omega t)$$

$$\text{Adding:} \quad \vec{\mathbf{B}} + \overleftarrow{\mathbf{B}} = 2\mathbf{B}_0 \sin(kz) \cos(\omega t) \quad (2.12)$$

The  $\vec{\mathbf{E}}$  travelling wave has a phase change of  $\pi$  as a result of reflection:

$$\begin{aligned} \vec{\mathbf{E}} &= \mathbf{E}_0 \sin(kz - \omega t + \pi) \\ &= -\mathbf{E}_0 \sin(kz - \omega t) = -\mathbf{E}_0 \sin(kz) \cos(\omega t) + \mathbf{E}_0 \cos(kz) \sin(\omega t) \end{aligned}$$

$$\overleftarrow{\mathbf{E}} = \mathbf{E}_0 \sin(kz + \omega t) = \mathbf{E}_0 \sin(kz) \cos(\omega t) + \mathbf{E}_0 \cos(kz) \sin(\omega t)$$

$$\text{Adding:} \quad \vec{\mathbf{E}} + \overleftarrow{\mathbf{E}} = 2\mathbf{E}_0 \cos(kz) \cos(\omega t) \quad (2.13)$$

Equations 2.12 and 2.13 show that, after reflection from the southern hemisphere ionosphere the magnetic field leads the electric field by  $\pi/2$ . This means that the Poynting flux:  $\mathbf{S} = \mathbf{E} \times \mathbf{H}$  contains the product of a time-varying sine function and a time-varying cosine function with the result that the Poynting flux also contains a time-varying sinusoidal signal but at twice the frequency of the electromagnetic wave since:  $2\sin\omega t \cos\omega t = \sin 2\omega t$ . The time average of the Poynting flux is zero, as would be expected for two travelling waves carrying energy in opposite directions, but in fact what is happening is that the energy in the standing wave pattern is fluctuating and flowing in one direction for a quarter cycle of the electromagnetic wave and in the opposite direction during the next quarter cycle.

The fundamental standing wave pattern set up on field lines by reflection from both ionospheres has an antinode in the electric field and a node in the magnetic field at the equator. At this node the sign of the magnetic field displacement reverses and the result is that the magnetic field lags the electric field by  $\pi/2$  in the northern hemisphere. This phasing effect was found to be the case in all the observations of standing waves.

The quadrature relationship between the electric and magnetic fields in a standing wave is valid in the central field line region but one of the effects of a finite ionospheric Pederson conductivity is to modify the phase difference towards 0 or  $180^\circ$  towards the ionosphere [Orr 1984]. Another effect is that there is a minimum, but not a node, in the magnetic field near the geomagnetic equator. A consequence of this is that the standing wave has more of the characteristics of a travelling wave near the ionosphere so that Poynting flux is transferred to joule heating in the ionosphere.

### **2.5.6 Ionospheric Poynting flux**

Because the latitudinal separation between shells converges towards the Earth and because the azimuthal distance around a shell decreases with decreasing distance from the Earth the Poynting flux in field-guided oscillations increases towards the ionosphere by the same factor as the magnetic field strength increases. However in this thesis only the value of the Poynting flux measured at the satellite location is cited.

### **3.0 Instrumentation and data processing**

This section provides further details about the ground-based and Polar satellite instruments used in these studies.

#### **3.1 Ground-based instruments**

The ground-based instruments used in these studies comprised fluxgate magnetometers in Canada, Greenland and Scandinavia, the IRIS riometer at Kilpisjärvi and the Sodankylä all-sky camera. The coordinates of all the magnetometers used are given in Appendix 5.

##### **3.1.1 Fluxgate magnetometers [FGM]**

A ground magnetometer detects magnetic fields from any source and changes in the ambient field caused by changes in those sources as well as changes in the magnetic environment. Oscillations observed in the magnetometer output may be attributed to ionospheric currents but it is always possible that they are caused by induced AC ground or sea currents or by man-made magnetic fields.

The ground magnetometer signature is the Biot-Savart integral of these ionospheric and non-ionospheric currents and a ground magnetometer responds to ionospheric currents over a large area since the magnetic field from each source region only falls off inversely with distance. This integrated output from a magnetometer may therefore include a significant contribution from distant signals. Sometimes great care is taken to orientate the magnetometers with true North using a theodolite, as at the BGS site at Lerwick, but this is not always the case and there may be uncertainties associated with the orientation.

The fluxgate magnetometer is ideal for the study of ULF waves since the sampling frequency of either 1 Hz or 0.1 Hz is at least an order of magnitude higher than the mHz frequencies of interest. A resolution of 1nT is usually adequate for detecting ULF waves on the ground.

Fluxgate magnetometers can be made very small and rugged for use on spacecraft.

A fluxgate magnetometer is a vector instrument that measures one component of the ambient magnetic field. The sensor element consists of an alloy core(s) with coils. Alloys such as Permalloy or Mumetal with very low coercivity [magnetisation can be changed by a weak magnetic field] and very high susceptibility [magnetisation can be saturated by a weak magnetic field] are used [Laurie 2004].

Designs vary but in the version constructed by the author [Tullet 1998] alternating current with a frequency of 10kHz energises the primary coil. In the presence of an ambient magnetic field which caused saturation of the core a second harmonic [20kHz] is induced in

the secondary sensing coil and this is rectified, low pass filtered and used to drive a direct current through the sensing coil to create a magnetic field to cancel out the ambient magnetic field component and hence the second harmonic - the magnetometer output is proportional to the current required to do this. The time constant of the low pass filter determines the high-frequency response – typically around 1Hz. The instrument is calibrated by orientating it normal to the Earth’s magnetic field and then using Helmholtz coils to provide a known ambient magnetic field. The output sensitivity was preset to  $1\text{mV nT}^{-1}$  and because the input to the analogue to digital converter was in the range  $\pm 1\text{V}$  it can measure changes of  $\pm 1000\text{nT}$ . A small permanent magnet placed  $\sim 50\text{mm}$  from the fluxgate sensor is used to cancel out the Earth’s quiet level of magnetic field.

With careful calibration a fluxgate magnetometer could be used to estimate the absolute strength of an ambient magnetic field component, but it is not perfectly stable over time because the output is affected by voltage supply variations, temperature and oscillator stability so where absolute measurements are required an instrument such as a proton magnetometer is used.

For scientific purposes it is highly desirable to site a magnetometer in a remote location where it is free from interference from induced currents and magnetic materials – this is extremely difficult. Figure 3.1 shows the magnetometer huts at Tähtelee, in Finland.



**Figure 3.1**  
**Magnetometer huts at**  
**Tähtelee, Finland**

Tähtelee means *the place of the stars*.

Snow clearing machinery was not allowed too close. Photo taken by author on 2008-03-27

Spikes do occur in magnetometer data, sometimes quite frequently, and when reading magnetometer files it is necessary to remove these if that has not already been done. Spikes and corrupted data were marked by NaN [not a number] in the SAMNET MIA MATLAB format and by the large value 9E99 in IMAGE data from the Finnish Meteorological Institute [FMI].

### 3.1.2 IMAGE chain

Observations made over a north-south chain of ground magnetometers are very useful for estimating the latitude of events such as electrojets and of phase-reversal in ULF oscillations.

Figure 3.2 shows a map of the 12 IMAGE [International Monitor for Auroral Geomagnetic Effects] [Lühr et al. 1998] ground magnetometers used in this study. The geomagnetic latitude range of this chain is from 75.25° N [NAL] to 54.47° N [TAR]

10 second readings of the X [geographically northwards], Y [geographically eastwards] and Z [vertically downward] components of IMAGE data were available in the IAGA ASCII format described in Appendix 4 with a resolution of 0.1nT from the FMI.

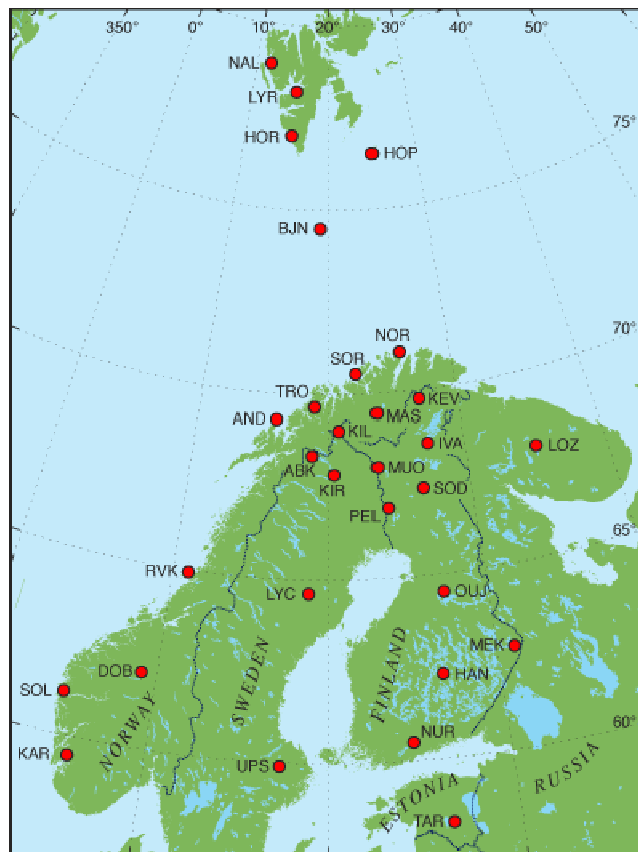


**Figure 3.2** Location of the IMAGE ground magnetometer network

This includes the north-south magnetometer chain NAL – TAR that was extensively used in these studies [FMI]

### 3.1.3 SAMNET

Data from SAMNET ground magnetometers was particularly used in the direction-finding study described in Chapter 4.

The SAMNET array of magnetometers includes 3 magnetometers [FAR, NOR and OUL] on L shell 4.3 and 3 magnetometers [GML, KVI and NUR] on L shell 3.2. Field lines from the former generally thread the plasma-trough region and field lines from the latter thread the plasma-sphere [Yeoman, Milling and Orr 1990].

The British Geological Survey operates three of the SAMNET magnetometers and publishes the data in a monthly bulletin. It is possible to construct a doglegged chain using the Greenland East coast magnetometers DMH DMB SCO HEL FAR together with the SAMNET magnetometers HLL , FAR and LER and data from these was used in the studies described in Chapters 7 and 8.

A map showing the location of the SAMNET ground magnetometers is given in Figure 3.3 below. 1 second readings of the H [horizontal magnetic northwards] D [horizontal magnetic eastwards ] and Z [vertically downwards ] components were available in ASCII format with 1nT resolution from Lancaster University.

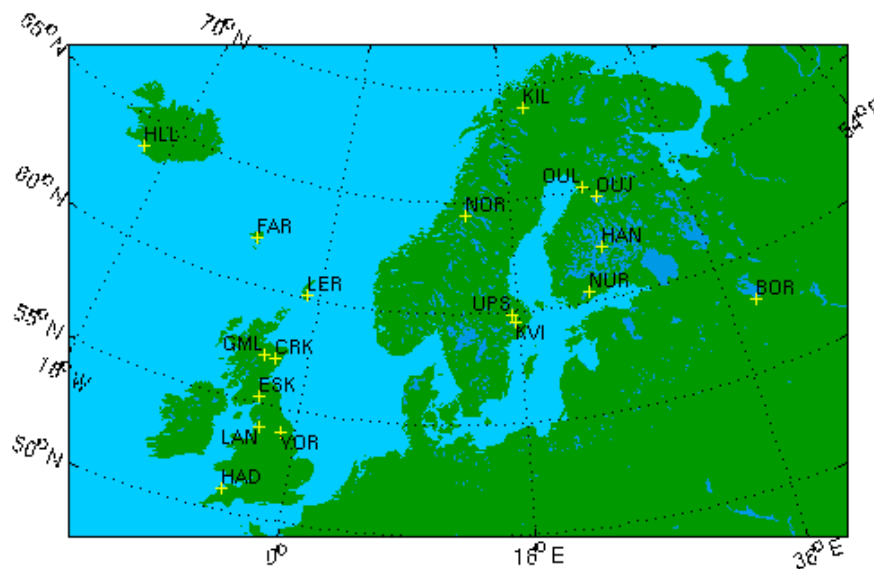


**Figure 3.3** Location of the SAMNET ground magnetometers

This network of ground magnetometers is operated by Lancaster University [Dr S Marple ]

### 3.1.4 Greenland magnetometers

The Greenland West coast magnetometer chain extended over a geomagnetic latitude range of 84.97°N [THL] to 65.85°N [NAQ]. For these studies it would have been very useful to extend this chain southwards by placing some additional magnetometers on the seabed. Figure 3.4 shows a map of the locations of the Greenland East and West coast magnetometers. 20s readings of the H [local horizontal magnetic north] E [local horizontal magnetic east] and Z [magnetic downwards] components were provided for these studies with a resolution of 0.01nT from the Danish Meteorological Institute.

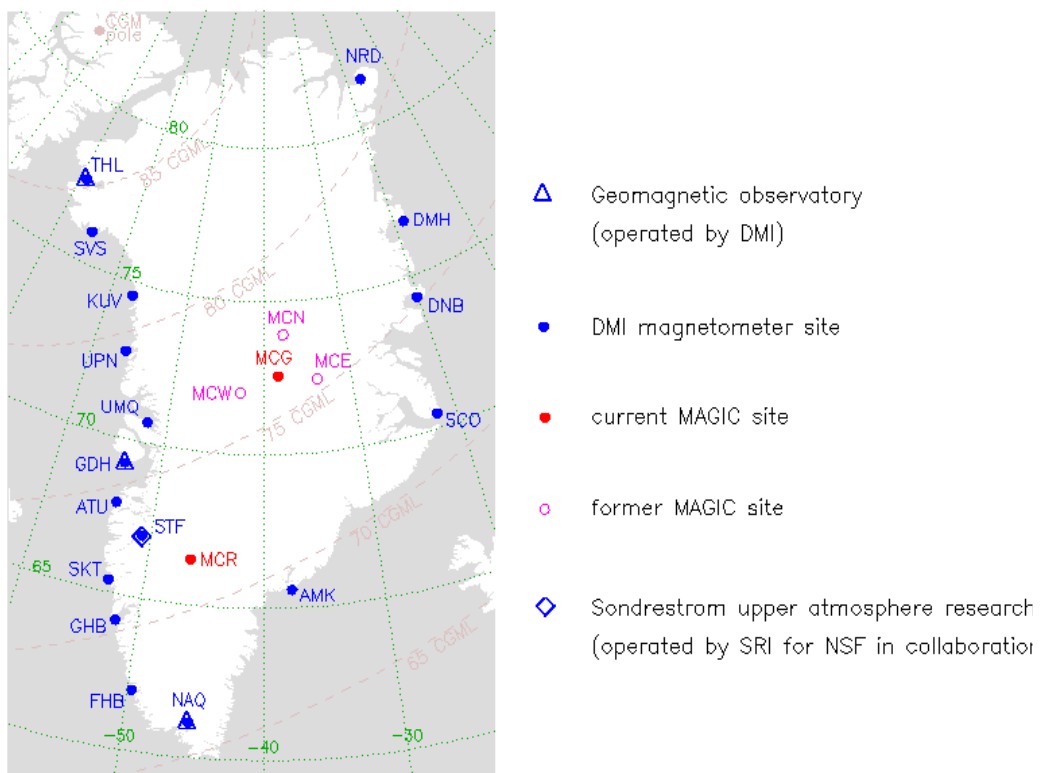


**Figure 3.4** Location of the Greenland ground magnetometers

[Danish Meteorological Institute]

### 3.1.5 Canadian CARISMA magnetometers

Stackplots from the Canadian CARISMA ground magnetometer chain from RANK to PINA were used in these studies. Figure 3.5 shows a map of the locations of these magnetometers.

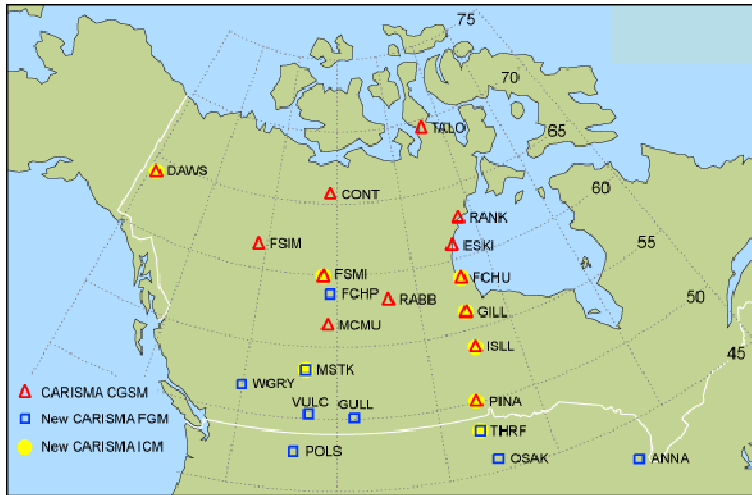


**Figure 3.5**  
**Location of the**  
**Canadian CARISMA**  
**magnetometers**  
 including the TALO –  
 OSAK north-south chain  
 [University of Alberta]

### 3.1.6 IRIS riometer

A riometer measures variations in cosmic radio noise caused by varying ionisation in the D region ionosphere [50km to 90km altitude] as a result of charged particle precipitation or solar particle events. The Imaging Riometer for Ionospheric Studies [IRIS] is located near Kilpisjärvi in northern Finland at 69.05°N 20.79°E geographic [65.83°N 104.41°E CGM] and is supervised by Lancaster University and operated in conjunction with the Sodankylä Geophysical Observatory. A photograph of the crossed dipole array is shown in Figure 3.6. The riometer is tuned to 38.2MHz and the array data beamformed to give 49 beams with widths of between 13° and 16° and a time resolution of 1s. These beams collectively have a footprint on the ionosphere measuring ~ 240km x 240km at an altitude of 90km.

Data from the IRIS riometer was used in the Poynting flux studies described in Chapters 6 to 8. Because it is unaffected by cloud cover it has a considerable advantage over optical instruments, although it responds to precipitation by higher energy particles that give rise to enhanced ionisation in the lower ionosphere.



**Figure 3.6**      **IRIS riometer**  
 The photograph shows the crossed  
 dipole aerial array at Kilpisjärvi  
 Finland . The site is loaned  
 by METLA, the Finnish Forest  
 Research Unit  
 [Lancaster University]

These studies made use of 21x23 grids of interpolated ionospheric absorption data which were available from Lancaster University. The ionospheric absorption is estimated by subtracting quiet day curves. Only the centre column of these data were used to plot IRIS keograms showing the absorption [in dB] over latitudes from 68°N to 70°N against UT with a time resolution of 1 minute.

### 3.2 Polar satellite instruments

The Polar satellite [Figure 3.7] was launched on 1996-02-24 and was operational until 2008-04-15. Its payload included the 11 instruments listed below, included three-axis electric field sensors and three-axis fluxgate magnetometers as well as a visible imager and a far UV imager .

- Plasma Waves Investigation (PWI)
- Magnetic Fields Experiment (MFE)
- Toroidal Imaging Mass-Angle Spectrograph (TIMAS)
- Electric Fields Investigation (EFI)
- Thermal Ion Dynamics Experiment (TIDE)
- Ultraviolet Imager (UVI) Images in the far UV 130nm -190nm
- Visible Imaging System (VIS)
- Polar Ionospheric X-Ray Imaging Experiment (PIXIE)<sup>(1)</sup>
- Charge and Mass Magnetospheric Ion Composition Experiment (CMMICE)
- Comprehensive Energetic-Particle Pitch-Angle Distribution-- Source/Loss Cone Energetic Particle Spectrometer (CEPPAD/SEPS)

Its highly elliptic orbit with apogee at  $\sim 9R_E$  and perigee at  $\sim 1.8R_E$  was designed to study the polar region magnetosphere. The inclination of the orbit was  $86^\circ$  to the plane of the ecliptic. The orbital period of  $\sim 17.5$  hours meant that the geomagnetic field line trace very approximately returned to the same longitude every three days, although at a slightly different latitude.

---

<sup>(1)</sup> Detects X-ray emission from aurora above 3keV from which the fluxes and energies of the parent electrons can be deduced

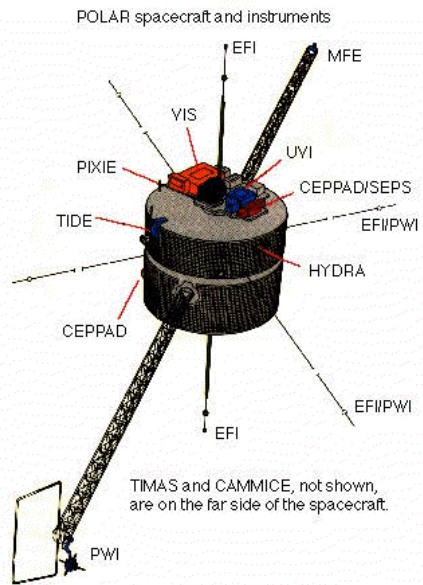


**Figure 3.7**  
**Polar spacecraft instruments**  
 [NASA]

The electric field instruments [EFI] [Harvey et al. 1995] were designed to measure the electric field components from the potential difference between spheres at the end of long probes. They can also be operated in a Langmuir probe mode to measure electron density. The booms for one of the two spin-plane sensors measured 130m tip to tip and the other measured 100m tip to tip. Those for the spin axis sensors were 13.8m from tip to tip.

In preliminary studies three axis electric field data from NASA Goddard was used. However, on the advice of the Principal Investigator [PI] for the Polar satellite electric field instrument polarefi data from Berkeley was used in all the observations described in this thesis. One reason for this change is that electric field data is affected by satellite operations and the polarefi data takes this into account by deleting unreliable data. The polarefi three axis electric field data in the spacecraft centred GSE frame of reference are synthesised from the two spin-plane sensors on the MHD assumption that the field-aligned electric field was zero. When transformations were performed on this data to display the electric field in field-aligned coordinates the component along the field lines come out as zero as expected. Spin data provided one data point at the spin rate of the satellite which was approximately every 6 seconds, and this data rate was adequate for these studies at ULF frequencies. All data was tagged with a time code and there were often gaps. The data format was: sample number, space, time in seconds, three data components, repeat...

Because the interest was in ULF frequencies where the periods were 100 seconds or longer the spin rate data was used throughout these studies linearly interpolated to an exact 6s rate.

The Polar satellite magnetic fields experiment [MFE] included three-axis fluxgate magnetometers. Time-tagged data was available from Berkeley either as: B\_GSE\_RTime or as B\_GSE\_Spin. The difference was that the RTime data provided a sample approximately every 0.12s [ $\sim 8$ Hz data rate] whereas the Spin data provided one sample at the spin rate of the satellite which was approximately every 6 seconds [ $\sim 167$  mHz data rate].

Magnetic field data was also available from NASA Goddard with a sample interval of 0.92 minute [18 mHz data rate]. Since the Nyquist frequency would then be at 9mHz this data rate is near to the limit for studies in the Pc5 band. However it was a reliable data source and was used for the Poynting flux studies described in Chapters 6 to 8 with linear interpolation to up-sample to the same exact 6s rate as the electric field data.

Figure 3.8 [left] shows a plot of electric field, magnetic field and Poynting flux components derived from Berkeley  $\sim 6$ s spin rate data and Figure 3.8 [right] with Goddard 0.92 minute magnetic field data. Both plots used the same electric field data from Berkeley.

As would be expected from the higher data rate there is slightly more detail in Figure 3.8a which affects the maximum and minimum values but not the time of events nor the phase difference between the electric and magnetic fields. These differences have no effect on the classification scheme in Chapter 6.

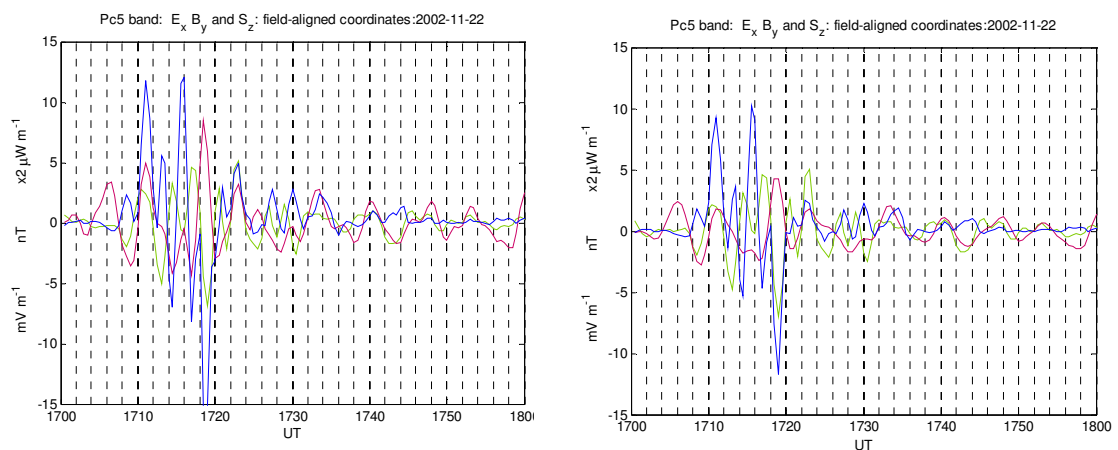


**Figure 3.8 Berkeley and Goddard magnetic field data**

These two diagrams show the difference between the processing of the 6s Berkeley data [left] and the Goddard 0.92 minute Polar electric field data [right]. The colours show the E<sub>x</sub> component of electric field, the B<sub>y</sub> component of magnetic field and the S<sub>z</sub> component of Poynting flux.

## **Part II**

## **Studies**

Nothing defines humans better than their willingness to do irrational things in the pursuit of phenomenally unlikely payoffs

Scott Adams

## 4.0 A null phase-difference technique for ULF wave direction-finding

### 4.1 Introduction

A method of estimating the mean direction of arrival of ULF waves at two ground magnetometers is described which has the useful feature that no prior knowledge of either the wave speed or the wavelength  $\lambda$  is required.

The phase difference  $\Delta\phi$  between two detectors separated by a position vector  $\mathbf{p}$  is:

$$\Delta\phi = 2\pi \frac{\mathbf{p} \cdot \hat{\mathbf{k}}}{\lambda} \quad \text{where } \hat{\mathbf{k}} \text{ is a unit vector normal to the wavefront.} \quad (5.1)$$

If  $\hat{\mathbf{k}}$  and  $\mathbf{p}$  remain constant relative to each other this phase-difference will also remain constant, but any change in relative orientation between them results in a change in this phase-difference. Usually the direction of  $\hat{\mathbf{k}}$  cannot be determined unless the wavelength  $\lambda$  is known. However if:  $\Delta\phi = 0$  either:  $\lambda = \infty$ , which is physically unlikely, or:  $\hat{\mathbf{k}} \perp \mathbf{p}$ . So if the signal is arriving from a constant direction in a frame of reference that is not co-rotating with the Earth, and the two detectors change their orientation  $\mathbf{p}$  relative to this source direction as a result of the rotation of the Earth, there should come a time when the signal is detected in-phase at both detectors. At this exact time the local direction of arrival must be in the plane orthogonal to the detector baseline and this would be true whatever the speed or wavelength of the signal.

The rotation of the Earth allows the time of the nulls to be found from a single pair of ground magnetometers – an alternative approach would be to use pairs of ground magnetometers with different baseline orientations to establish the direction of arrival.

In the context of this study the detectors were ground magnetometers in the Scandinavian sub-auroral magnetometer network [SAMNET] and the magnetometer baseline was chosen to be approximately geomagnetically east-west.

### 4.2 Ionospheric and ground magnetometer phase-difference

Ground magnetometers detect the integrated magnetic field of ionospheric currents from all directions above them and although they may be far apart they both respond [by Biot-Savart] to exactly the same ionospheric current systems. The difference between them though is that the local ionospheric currents above each magnetometer make a greater contribution to the signal from that magnetometer. However, provided that the ionospheric current system is of a large extent compared to the separation of the ground

magnetometers the amplitude weighting would be the same for both instruments with the result that the ionospheric phase-difference would also be measured in the ground magnetometer data. Furthermore the same phase-difference would be measured in the two horizontal channels of the vector magnetometers.

In the case of a uniform amplitude AC ionospheric current system with wavefronts rippling across the ionosphere in a direction with wavevector  $\hat{\mathbf{i}}$  the phase difference between any

two points in the ionosphere separated by  $\mathbf{p}$  is given by: 
$$\Delta\phi = 2\pi \frac{\mathbf{p} \cdot \hat{\mathbf{i}}}{\lambda} \quad (5.2)$$

The assumption that is sometimes made in connection with ground magnetometers is that they respond mainly to an area of ionosphere with a radius of 100km. This would mean that two ground magnetometers more than 100km apart would be quasi-independent. However whether or not this is a good assumption depends upon the kind of current systems being detected. To minimise some of these problems data was used from widely spaced ground magnetometers and phase-differences were averaged over sixty days. This had the effect of enhancing the persistent underlying signal and of minimising any swamping by local ionospheric currents. But the practical upper limit to ground magnetometer spacing was set by the need to avoid aliasing in the frequency domain processing used.

### 4.3 Frequency domain observations of phase-difference

Some studies have suggested that the ULF wave spectrum may contain particular frequencies [Ziesolleck and McDiarmid 1994, Menk et al. 2003]. But in general the spectrum of daytime ULF wave activity extends across a broad bandwidth. In this study the data was subjected to the series of narrowband filters provided by the DFT. This meant that in order to carry out averaging across a wide bandwidth the phase-differences had first to be converted to time-delays. The time-delay  $dt$  associated with a phase difference  $d\phi$  in a DFT

frequency bin centred on frequency  $f$  is given by: 
$$dt = \frac{d\phi}{2\pi f}$$

As well as averaging the data over the frequency band the considerable variation between geomagnetic pulsations suggested that it would also be necessary to average over time to derive any underlying pattern. In fact it was found that the degree of variability was so great that it was necessary to average over sixty days to obtain a reasonably clear diurnal time-delay signal that could be used for ULF wave direction-finding.

The method adopted was to carry out non-overlapping 1800 point DFTs on one second sampled magnetometer data from two SAMNET stations to provide spectra for cross-phase analysis every half-hour. Phase-differences were calculated on a cell by cell basis and then converted into time-delays, averaged across the bandwidth below the spatial aliasing frequency and plotted in colour-coded form in a day versus time-of-day plot. Finally the time-delays for each half hour in the day were averaged over the sixty days and displayed in the form of the bar graph.

An example of this processing for SAMNET ground stations NOR and OUL [Figure 3.3] is shown in Figure 4.1 for the sixty days from 2002-01-01 to 2002-03-01. The colour scale was truncated to +/-20s to enhance the negative time delays. Signals arrived at OUL before they arrived at NOR in the morning as shown by the broad blue vertical band at that time. After the time of local noon [at 1040UT] they reversed direction as shown by the vertical yellow band in the afternoon. Finally they reversed direction again in the evening sector. This observed variation in the average time-delay over the course of a day is referred to here as the diurnal time-delay signature and it contained information that was used to estimate both the direction of arrival and then the ionospheric phase speed of the ULF waves. The lower diagram in Figure 4.1 shows the diurnal time-delay signature obtained by averaging over the 60 days.

#### **4.4 Analysis in the Geocentric Solar Ecliptic [GSE] frame of reference**

The diurnal time-delay signature suggests that there is an underlying asymmetric pattern, with signals propagating across the ionosphere from east to west in the morning and again after dusk. Similar diurnal time-delay signatures were obtained using both the H and D channels from other pairs of SAMNET ground magnetometers. If the signals had been arriving from the sunward direction it would have been expected that they would have propagated from east to west in the morning and from west to east in the afternoon.

Nulls were observed at 1130UT and at 1600UT and these times were used through a series of coordinate transformations from Geographic coordinates [GEO] through Geocentric Ecliptic Inertial [GEI] coordinates to Geocentric Solar Ecliptic [GSE] coordinates, as described in Appendix 2, to determine the two planes in the GSE frame of reference broadside to the ground magnetometer baseline at those two times. On the assumption that the mean source remained constant in this frame of reference the far-field GSE latitude and longitude defining the source direction was found from the intersection of these two planes.

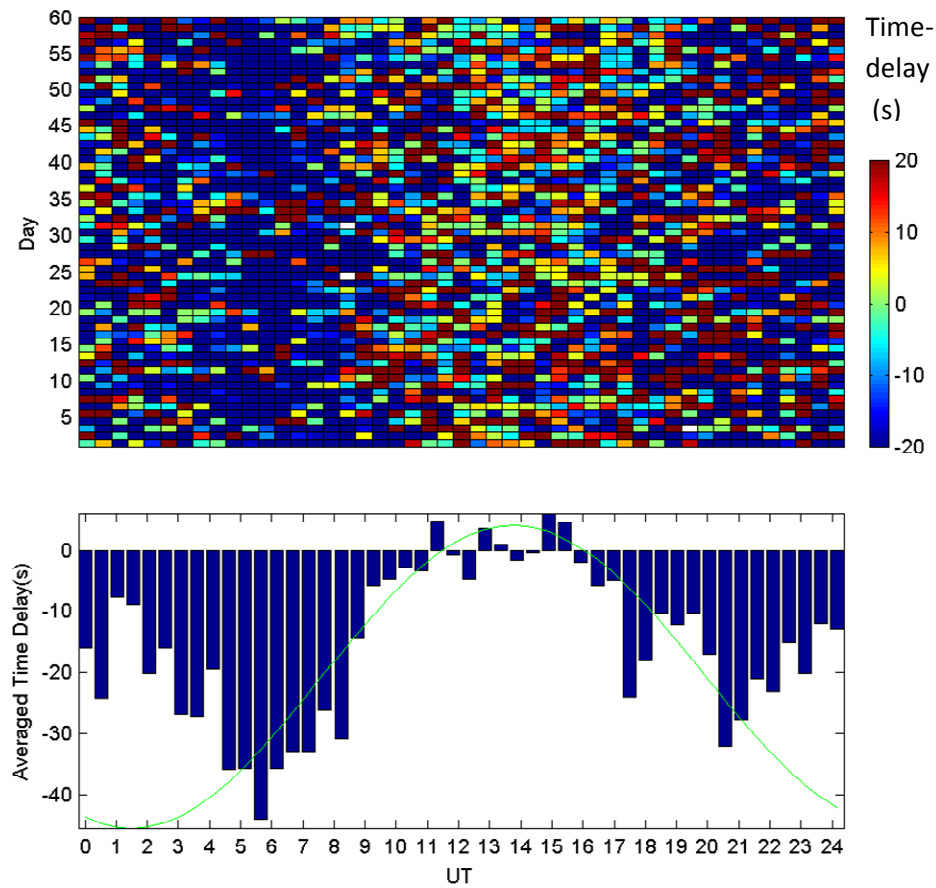


**Figure 4.1 Time-delay measurements from 2002-01-01 to 2002-03-01**

The pixels in the upper image are half hour averages of time-delays between the SAMNET Nordli and Oulu ground magnetometers in the 1 to 5mHz ULF band. The colour scale range shown on the right hand side is truncated to  $\pm 20$ s. The untruncated values of the half hour divisions of the day are summed over 60 days to give the bar graph shown below. In the text the envelope of this bar graph is referred to as the diurnal time-delay signature.

The green curve is the average diurnal time-delay signature that would be expected if the ULF waves arrived from a constant direction in the GSE frame of reference.

The source direction was found to be either from a high latitude sunwards of the pole in the northern hemisphere or antisunwards of the pole in the southern hemisphere. This ambiguity in the direction of arrival was resolved in favour of a northern hemisphere source using the additional observation that the signal arrived from the east in the morning sector. These GSE source directions are given in Table 4.1.

Once the source direction had been estimated then the same set of coordinate transforms were used in reverse to find the time-delay modulation that would be expected over 24

hours from a constant average direction source in the Geocentric Solar Ecliptic [GSE] frame of reference.

The green trace superimposed on the bar graph in Figure 4.1 is the pattern of time-delays that would arise from a signal from this particular high latitude source direction and, as would be expected, the reverse coordinate transform automatically means that the trace passed through the estimated times of the nulls. But it also has the desired feature that it gives rise to an asymmetric variation in diurnal time-delays. The matching of the trace to the observations is much better from dawn to dusk. In the dusk to dawn sector the green line does not show the observed return to zero time delays around midnight. It is possible that this is an incoherent effect since because, as mentioned in Chapter 2, the source of many ULF waves is associated with the region of interaction between the magnetosphere and the solar wind which is predominantly day-time. The extent to which the trace matches the observations during the daytime entirely depends upon whether the assumption of an underlying dayside average ULF wave source direction in the GSE frame of reference is valid.

In fact this simulated time-delay signature was found to be very sensitive to the arrival direction and changing this by  $\pm 5^\circ$  in either GSE latitude or longitude resulted in a noticeable degradation of agreement with the actual observations.

Estimates of mean source direction in the GSE frame of reference were made during five sixty day periods during 2002 when good data was available from the ground magnetometers. These are shown in Table 4.1 together with the GSE coordinates of the geographic pole at the mid-time of the sixty day observation. Although it is usual to use cartesian coordinates, GSE latitude and longitude coordinates were used here as the signal was assumed to have arrived from the far-field. Latitude was measured from the GSE x-y plane and longitude was measured clockwise around the GSE z direction from the GSE x axis. The source direction that gave the best match to the null observations consistently followed the geographic pole around the sky throughout the year, but always remained between  $-17^\circ$  and  $-23^\circ$  away from it in longitude, which meant that the mean source direction was always biased towards the morning side. The source latitude was at higher latitudes than the geographic pole in the winter and lower latitudes in the summer which meant that the mean source direction remained on the dayside of the geographic pole throughout the year. It was expected that the mean direction of arrival would really be related to a combination of the Sun-Earth direction and the geomagnetic pole direction. The dipole axis was tilted at  $10.3^\circ$  to the geographic axis in 2002 [Section 1.2.1] so the oscillatory tilting motion of the

geomagnetic pole relative to the geographic pole was insufficient to change the bias of the mean source direction towards the morning side. The variation by  $\pm 10.3^\circ$  over the course of a day in the GSE latitude of the geomagnetic pole relative to the geographic pole also does not change the finding that the mean source direction was also from high geomagnetic latitudes.

60 day start date	GSE mean source latitude	GSE mean source longitude	Geographic Pole latitude	Geographic Pole GSE longitude	Ionospheric phase speed
2002-01-01	80°N	120°E	66.6°N	138.6°E	13km s <sup>-1</sup>
2002-03-01	62°N	56°E	66.6°N	79.4°E	13km s <sup>-1</sup>
2002-07-01	60°N	-20°E	66.6°N	-38.1°E	13km s <sup>-1</sup>
2002-09-01	60°N	-80°E	66.6°N	-97.2°E	13km s <sup>-1</sup>
2002-11-01	72°N	-135°E	66.6°N	-158.1°E	12km s <sup>-1</sup>

**Table 4.1 GSE coordinates of the underlying ULF source direction**

#### 4.5 Ionospheric phase speed estimation

A feature of the null technique is that the estimate of source direction is completely independent of the unknown wave speed. Having found this direction the ionospheric speed could then be estimated, since it acts to scale the amplitude of the trace. In Figure 5.1 an ionospheric speed of 13 kms<sup>-1</sup> scaled the maximum in the green trace to the maximum time delay of 45s in the observations, although the times of minima differed by four hours.

The average ionospheric phase speed over the course of the year that was estimated by this method was found to be consistently around 13 kms<sup>-1</sup>. This value agrees with ionospheric phase speeds of 9 km s<sup>-1</sup> to 17 km s<sup>-1</sup> [Ziesolleck and McDiarmid 1994] and 14km s<sup>-1</sup> [Olson and Rostoker 1978], but is higher than the estimate of ionospheric phase speeds of 3 kms<sup>-1</sup> to 10 kms<sup>-1</sup> for the ground magnetometer signature of travelling convection vortices [Lühr and Blawert 1994].

#### 4.6 Discussion and conclusions

This rotation of the Earth effectively provides a scanning motion that enables a ground magnetometer baseline to search for an incoming ULF wave direction. A null direction-finding technique was developed that used the instants of time when the magnetometer baseline was scanning broadside to the incoming signal. This technique yielded estimates of an underlying sixty day average direction of arrival without the need for any prior knowledge about the speed or wavelength of the ULF waves.

Geomagnetic activity was observed to give rise to considerable variability in the time-delays between the arrival of signals at two SAMNET ground magnetometer stations situated at approximately the same geomagnetic latitude. This showed up clearly as background noise in Figure 4.1 and was entirely consistent with the magnetospheric source of individual ULF waves being dependent upon the natural variability in the solar wind. Nevertheless integration of these time-delays revealed an underlying diurnal time-delay modulation signature with signals arriving from the east [sunward direction] around dawn. A directional reversal was observed around the time of local noon, with signals coming from the west [also the sunward direction] for a few hours in the afternoon before reverting to the east again before dusk. This periodic diurnal time-delay modulation was attributed to the rotation of the Earth because it was shown that simulated signals from a constant high latitude direction in the GSE frame of reference [not co-rotating with the Earth] resulted in a pattern of time-delays that reproduced this observed asymmetry in the time-delay observations around noon. A low-latitude average source direction would not have given the short reversal period that were observed.

The conclusion therefore was that there was an underlying average direction of arrival of ULF waves from high geomagnetic latitudes which was biased from the Sun-Earth line towards the morning sector by about  $20^\circ$ . It is also possible that this technique was detecting the weak signature of magnetic reconnection in the polar cusp region [Section 1.9]. This study has subsequently been published [Tullet and Honary 2010].

## 5.0 Solving the Helmholtz equation for the magnetosphere

### 5.1 Introduction

This short study was motivated by an interest in the way that fast mode magnetosonic waves [Section A1.6.5] propagate into and through the magnetosphere from an upstream source. Diffraction of fast mode waves at the magnetopause [outer turning point] and by the Alfvén gradient around the Earth [inner turning point] gives rise to a waveguide region threaded by field lines onto which energy can be coupled and give rise to Alfvén shear waves and field-line resonances. The direction-finding study described in Chapter 4 had indicated a high latitude source of ULF waves and other studies have shown how pulsations are stronger at higher latitudes with a progressive decrease towards equatorial latitudes [Howard and Menk 2001]. This was also borne out by a L/MLT plot showing magnetospheric waves predominantly above  $L \sim 6$  [Anderson 1994]. Another aspect is how fast mode waves from a dayside source diffract in the magneto-tail region which includes the inner and outer radiation belts, the tail plasma sheet region and the LLBL. ULF wave activity has been correlated with the detection of relativistic electrons in the outer radiation belt between  $\sim 3R_E$  and  $\sim 10R_E$  [Mann, O'Brien, Milling 2004]. The higher plasma density in the tail plasma sheet gives rise to a lower Alfvén speed and hence a waveguide structure which entrains MHD energy. It was also thought that the diffraction of ULF wave energy into the tail plasma sheet may have a role in initiating or in modulating magnetic reconnection there. Since the classical propagation of waves, including electromagnetic and acoustic waves, is modelled by the Helmholtz equation the idea was to try to numerically solve the Helmholtz equation for an extended region of the magnetosphere. This was made possible by the availability of a multiphysics software package<sup>(1)</sup> which was designed for solving propagation in auditoria. It allowed simulated oscillations to be introduced, from either a point source or a line source on a boundary, onto a canvas of real data comprising a grid of propagation speeds. It is not known whether this approach has been tried before but the manufacturers were surprised by the 40000km x 25000km size of this magnetospheric auditorium. An outcome of this study was the creation of the real-time simulation movie that is included with this thesis showing the propagation of fast mode magnetosonic wavefronts through magnetospheric model data.

---

<sup>(1)</sup> The Swedish company COMSOL kindly supplied a software package for an evaluation period of a month, during which time these results were obtained.

## 5.2 Helmholtz equation

The time-independent Helmholtz equation can be obtained from the wave equation by the method of separation of variables [Boas 1996]. Given a parameter  $\mathbf{P}$  that varies with a position vector  $\mathbf{x}$ , time  $t$  and angular frequency  $\omega$  as:

$$\mathbf{P}(\mathbf{x}, t) = \mathbf{P}(\mathbf{x}) e^{-i\omega t} \quad (6.1)$$

$$\text{then: } \frac{\partial \mathbf{P}}{\partial t} = -i\omega \mathbf{P} \quad \text{and: } \frac{\partial^2 \mathbf{P}}{\partial t^2} = \omega^2 \mathbf{P}$$

Substituting these partial derivatives into the wave equation:

$$\frac{1}{\rho_0 c^2} \frac{\partial^2 \mathbf{P}}{\partial t^2} + \nabla \cdot \left( -\frac{1}{\rho_0} \right) \nabla \mathbf{P} = 0 \quad (6.2)$$

yields the Helmholtz equation:

$$\nabla^2 \mathbf{P} = -\frac{\omega^2}{c^2} \mathbf{P} \quad (6.3)$$

This equation naturally reproduces all the classical wave phenomena such as reflection, refraction, diffraction and interference. By way of example Figure 5.1 shows the two-dimensional solution to the Helmholtz equation obtained using the Multiphysics software for waves from a point source to the left of a narrow slit.

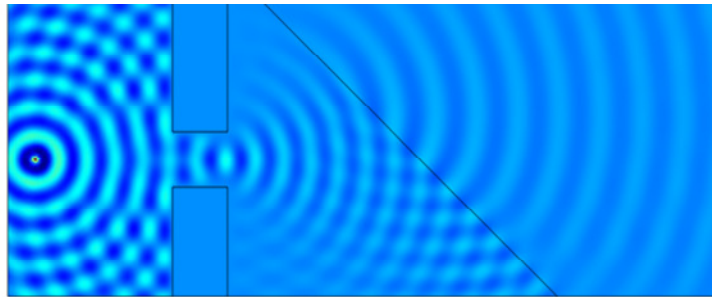


**Figure 5.1 Helmholtz equation solution for a laboratory ripple tank**

In this test of the Multiphysics software the speed of the waves increases by 50% beyond the  $45^\circ$  boundary. However there were no boundaries here in the usual sense, only sub-domains where the wave speed was different. Classical wave phenomena including reflection from a virtual image of the source, diffraction through the aperture and reflection and refraction at the  $45^\circ$  boundary are all visible in this numerically computed image and as the results are reminiscent of the patterns observed in a laboratory ripple tank it gives a measure of confidence in the method.

The restoring force for MHD waves in warm plasma is provided by the plasma pressure as well as by the magnetic field lines, which act to resist bending and tension. Fast mode magnetosonic wave propagate with a phase speed of:  $\frac{\omega}{k} = \sqrt{c_s^2 + v_A^2}$  in the direction perpendicular to the field lines and at the Alfvén speed along the field lines [Section A1.6.6]. In a cold plasma, where  $c_s = 0$ , the fast mode MHD waves propagate isotropically at the Alfvén speed. It was recognised from the outset that the anisotropic propagation of fast mode magnetosonic waves in warm plasma regions of the magnetosphere would create non-linearities in the Helmholtz equation so only an isotropic Alfvén speed was used. The plasma  $\beta$  parameter is approximately equal to the ratio:  $(c_s/v_A)^2$  and Figure 1.7 shows the logarithm to base 10 of  $\beta$  calculated using the VISAN magnetospheric model data for 1200UT on 2002-09-16 used throughout this study. This logarithmic ratio is zero where  $v_A = c_s$  so regions where fast mode waves propagate anisotropically and where approximations would inevitably arise are those shown in magenta.

### 5.3 Helmholtz equation solutions for idealised data

The multiphysics software was investigated to see whether it could generate solutions to the Helmholtz equation for the terrestrial magnetosphere. The physical scale turned out not to be a problem because a dense mesh for the numerical computation could be set up that far exceeded the resolution of available data. Three dimensional modelling was possible, although all these results were for the plane through  $y_{GSM} = 0$ . The software was designed for solving acoustic propagation in auditoria so the parameter P was pressure. Two sources of these pressure waves could be generated: plane parallel wave-fronts on the model boundary and waves from point sources within the sub-domains. A plane parallel source with an arbitrary amplitude of 2nPa was used for all the plots. Although this value is of the order of the solar wind momentum flux [Kivelson and Russell 1996] neither the value nor the units were of significance as these studies were concerned only with the propagation. Before using magnetospheric model data some results were obtained by drawing highly idealised magnetospheric sub-domains and giving them each a particular value of Alfvén speed. This illustrated some general features of wave propagation. The first of these idealised simulations was concerned with the Alfvén gradient around the Earth. Since the

near-Earth dipolar magnetic field falls off approximately as  $r^{-3}$  with equatorial distance  $r$  the Alfvén speed increases rapidly for fast mode magnetosonic waves

approaching the Earth. The multiphysics solution to the Helmholtz equation for a highly idealised strong Alfvén gradient consisting of a series of concentric rings with Alfvén speeds from  $100\text{kms}^{-1}$  to  $1000\text{kms}^{-1}$  around an imaginary Earth suggests that the Earth would act as a secondary source of ULF waves as shown in Figure 5.2.

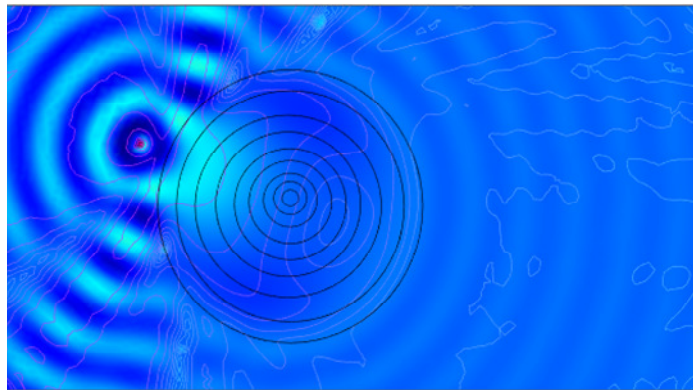


**Figure 5.2 Helmholtz equation solution for an Alfvén gradient**

The ULF waves from a point source are diffracted by a synthesised Alfvén gradient marked by concentric circles of increasing wave speed towards the centre. On the night-side the waves are an order of magnitude weaker than on the dayside. This may be another feature that explains the predominance of ULF wave observations on the dayside.

#### **5.4 Helmholtz equation solution for magnetospheric model data**

The magnetospheric model data used for these studies<sup>(1)</sup> had been generated by solving the MHD equations for the magnetosphere using the Block-Adaptive-Tree–Solarwind-Roe-Upstream-Scheme [Daum 2007 and 2009]. The input data was derived from ACE satellite data extended over the whole  $y$ - $z$  boundary plane upstream of the magnetosphere.

Data for 1200UT on 2002-09-16 was used and the associated  $K_p$  value was 3.

The model data were actually updated every 16 seconds, although in this study only one magnetospheric data set was used and the  $y_{\text{GSM}}=0$  plane through this was used as a canvas across which synthetic waves generated by the Multiphysics program propagated.

---

<sup>(1)</sup>The magnetospheric model data was kindly supplied by Dr P. Daum Lancaster University

The fundamental data required for numerically solving the Helmholtz equation was the Alfvén speed at points on a grid. The Alfvén speed:  $v_A = B (\mu_0 \rho_m)^{-0.5}$  is proportional to the magnetic field B strength and inversely proportional to the square root of the plasma density  $\rho$ . Values for these parameters are therefore required by the multiphysics software for a grid of points. It was however first necessary to convert Alfvén speed data derived from the magnetospheric model into the special .txt file format required by Multiphysics and a listing of a MATLAB function that was written to do this is given in Appendix 3. An interpolation function was then set up in the Multiphysics software to linearly interpolate between data grid points to get the Alfvén speed values required on the finite element mesh nodes.

A simulation movie showing the propagation of simulated 10mHz ULF waves through the MHD model data canvas is included with this thesis. Contours showing the wavefronts were added to show the propagation proceeding. It runs in real time and therefore accurately depicts the timescales for ULF wave propagation in the magnetosphere. Figure 5.3 shows the last frame of the movie with approximate locations of the magnetopause and the bow shock added. Some of the features that are shown in this still frame include:

- (1) Complex reflection and interference upstream of the bow shock [purple region on the far right]
- (2) Wave propagation through the magnetosheath region between the bow shock and the magnetopause [blue-purple structures]
- (3) Penetration of ULF waves into the northern hemisphere polar cusp region [purple circle near  $x_{GSM}=10, y_{GSM}=5$ ].
- (4) A region of high pressure in the dayside magnetosphere which turned from red to orange towards the Earth showing that dayside ULF fast mode waves are attenuated by  $\sim 10$ dB before they encounter the ionosphere.
- (5) Two strong first-order diffraction beams which can clearly be seen extending from the Earth at  $\sim 45^\circ$  into the tail [orange-brown regions].
- (6) Regions of very low ULF wave activity shown in cyan in the magnetotail.
- (7) A zeroth order diffraction beam near the tail current sheet region and fast mode magnetosonic waves propagating in the PSBL region.
- (8) Enhanced ULF wave activity and shorter wavelengths caused by slower propagation along the tail plasma sheet. Undulations in the tail plasma sheet are also visible.

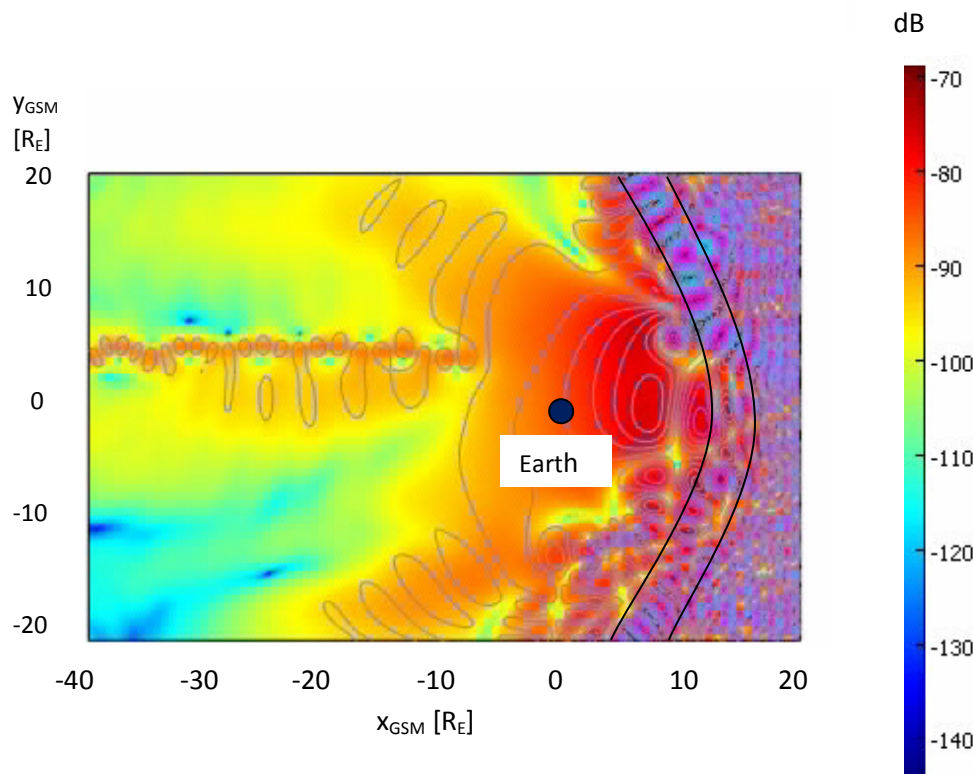


**Figure 5.3 The last frame from the Helmholtz equation simulation movie**

10mHz plane-parallel ULF waves propagate from a synthesised upstream source on the right hand boundary through the magnetospheric MHD data. The approximate positions of the bow shock and plasmapause are marked in black.

This frame shows the concentration of ULF waves on the dayside magnetosphere [red region], zeroth and first order ULF wave diffraction lobes in the magnetotail [orange] and the concentration of ULF wave energy in the tail plasma sheet beyond  $x_{\text{GSM}} = -10R_E$  [brown].

ULF activity is present in the radiation belt region but absent in the south lobe of the magnetosphere [cyan]. It is particularly strong in the polar cusp region around  $x_{\text{GSM}}=10$ ,  $y_{\text{GSM}}=5$  [purple].

MHD data for 1200UT on 2002-09-16 was used and the resolution of the MHD data grid was  $0.5 R_E$ .

## 5.5 Discussion and conclusions

The Helmholtz equation simulation movie shows that ULF waves from an upstream source diffract strongly through the magnetosheath where they may have a role in initiating the Kelvin-Helmholtz instability [KHI] which has been identified as one source of magnetospheric ULF waves [Section 2.2]. The results also explain why Pc5 band pulsations were observed coming from the high latitude dayside region in the direction-finding study described in Chapter 4. The region coloured red just inside the magnetopause shows that ULF activity was particularly strong there and as this region is threaded by high latitude field lines Alfvén shear waves could be set up and carry the wave energy to the high latitude ionosphere.

The high Alfvén speed close to the Earth clearly acted to diffract fast mode waves so that they became attenuated as they approached the Earth. However, despite this diffraction, fast mode wavefronts were observed reaching the Earth on the dayside. The simulation movie also showed these fast mode waves entering the polar cusp region at  $x_{\text{GSM}}=10$ ,  $y_{\text{GSM}}=5$  [purple] where they could interact with the polar cap ionosphere. This observation is in agreement with a study of Pc5-6 activity in the polar cap which showed noisy, but highly coherent activity along a magnetic meridian [Yagova et al. 2002].

A new result that emerged from this study was that the diffraction of fast mode waves by the Alfvén gradient around the Earth gave rise to first order diffraction lobe beams of enhanced wave amplitude at approximately  $45^\circ$  to the Sun-Earth line in the magnetotail. These are clearly shown in the simulation movie and in Figure 5.3. No reference to the existence of these beams has been encountered in the literature. It would be expected that the sine of the angle these diffraction beams make to the Sun-Earth line would depend upon the frequency, with lower ULF frequencies making greater angles. In three dimensions these lobes would be expected to be conical.

The zeroth order diffraction beam was near to the tail plasma sheet in the PSBL region so that constructive interference in the tail region acted to enhance the strength of ULF waves there. This region may be significant for the modulation of aurora at Pc5 frequencies [Section 9.2.1]. Diffraction along the tail plasma sheet can also be watched in the simulation movie and this was of particular interest as these waves may have a role in initiating or modulating magnetic reconnection in the distant tail [McLaughlin 2008]. Although the simulation shows the wave-fronts propagating towards the tail, waves from a source in the tail would equally well propagate Earthwards.

Figure 5.3 bears close resemblance to Figure 11 in the paper entitled: Source of Pc4 pulsations observed on the nightside [Takahashi et al. 2005]. Figure 5.4 shows a magnetic pressure profile along the Earth-Sun axis from  $x_{\text{GSM}} = -40R_E$  to  $x_{\text{GSM}} = +20R_E$  [ $y_{\text{GSM}} = 0; z_{\text{GSM}} = 0$ ] so the sunward direction is to the right. There is a pressure maxima in the dayside magnetosphere at  $8R_E$  and magnetic field lines that thread through this region would have a footprint at a geomagnetic latitude of  $\sim 70^\circ$ . The pressure on the nightside was an order of magnitude lower [ $0.2/1.6 = 0.125$ ], in agreement with their reported observations.

Although ULF waves were present in the outer radiation belt region from  $3 R_E$  to  $10 R_E$  on the nightside they were significantly stronger on the dayside. This would suggest that if ULF waves interact to enhance relativistic electron energies they could be more effective when the particles drift through the dayside region.

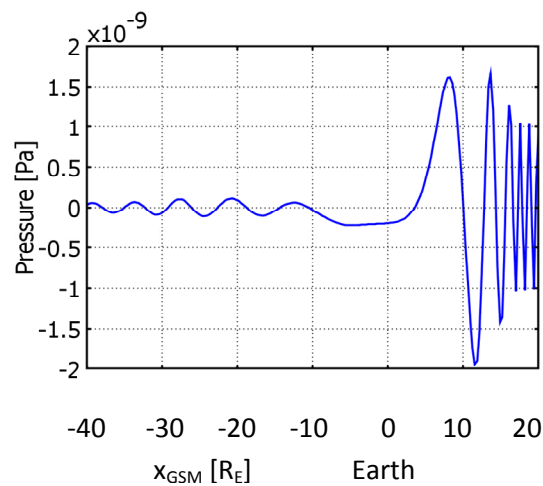


**Figure 5.4** ULF wave pressure profile along the Earth - Sun axis

The nightside ULF wave activity is an order of magnitude weaker than on the dayside. The source pressure was set to 2nPa for this run.

In conclusion it was shown that it was possible to achieve some useful insight into the propagation of ULF waves in the terrestrial magnetosphere by numerically solving the Helmholtz equation for synthetic fast mode waves propagating through MHD data.

Although it was not considered at the time of the original study, it may be possible to carry out a similar study on the propagation of ULF waves using the BATS-R-US software alone by artificially superimposing ULF oscillations on the ACE data input. This would modify the output matrices generated by the MHD model and one suggestion is that the dispersion of the ULF waves in the magnetosphere could then be found by subtracting the unmodified output.

## **6.0 Poynting flux classification of ULF oscillations**

### **6.1 Introduction**

Poynting fluxes in the ULF band calculated from Polar satellite data at high geomagnetic latitudes contain information on the direction of propagation and the intensity of energy flux in the terrestrial magnetosphere. Preliminary studies showed that in the evening sector at high geomagnetic latitudes there were some clear and interesting features. There was also an apparent coincidence between the signals that are referred to here as Poynting Flux Impulses [PFIs] and absorption spikes in IRIS riometer data.

Data cuts were selected when the Polar satellite field-line trace was over Scandinavia in the autumn evenings because all-sky camera imagers were operational then and because data was available from the IMAGE magnetometer chain. However because of frequent cloud cover at the times when signals were observed in the Polar satellite data the study eventually centred on IRIS riometer data rather than all-sky camera images. Data from 56 Finland-Greenland field-line transits of the Polar satellite were analysed from the autumn of 2002 and 40 from the autumn of 2003.

It was found that magnetospheric events could be detected on the ground over an extended region, so use was made of data from the SAMNET, Greenland and eventually Canadian ground magnetometers further to the west. These observations map out to the PSBL region of the magnetosphere [Figure 1.16] which is affected by processes such as magnetic reconnection occurring in the tail current sheet.

This chapter is concerned with the classification process and with some measurements of Poynting flux propagation in the 2 - 7mHz ULF Pc5 band : the temporal association with geomagnetic substorms is described in Chapter 7 and the observations of Group V quadrature events are discussed in Chapter 8.

### **6.2 Magnetospheric classification groups**

The first stage in making scientific deductions from the Polar satellite observations was to classify the observations into six magnetospheric groups designated Group I to Group VI on the basis of their electric field, magnetic field and Poynting flux characteristics as described in the following Section. Groups I and II were classified on the basis of the relative amplitude and Groups III to VI on the relative phasing of the electric and magnetic field oscillations.

Oscillations in the electric field associated with oscillations in the magnetic field give rise to electromagnetic waves. Theoretically their existence can be shown by taking the curl of both sides of the Faraday and the Ampère-Maxwell laws [Equations A1.11 and A1.12] and applying Gauss' law to yield wave equations for oscillations in the magnetic and electric fields with sinusoidally varying solutions [Fleisch 2008]. These oscillations couple into an electromagnetic wave because a sinusoidally varying electric field gives rise to a sinusoidally varying magnetic field and vice versa. It was found however that sometimes either the amplitude electric or the magnetic field oscillations were an order of magnitude stronger than the other and this feature defined magnetospheric Groups I and II. Figure 6.1 shows idealised mathematical function plots for Groups III to VI derived from the theoretical considerations described in Section 2.5.

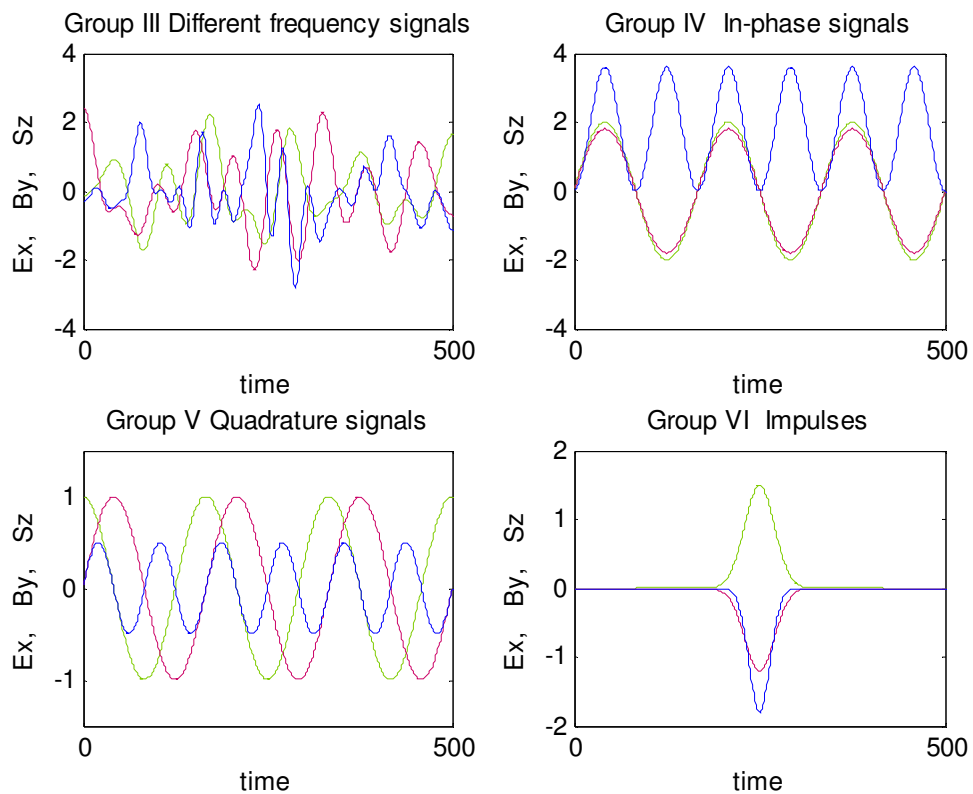


**Figure 6.1** Groups III to VI in the magnetospheric classification scheme.

These diagrams illustrate the relationship between the electric field, magnetic field and Poynting flux in four of the magnetospheric groupings.

**Group I** encompasses dominant electric field oscillations, although the explanation for this was uncertain. One possible explanation for the high ratio of electric field to magnetic field amplitude was that the waves in this group are propagating at high Alfvén speed [A1.6.7], a situation that would arise when the plasma mass density is low. For standing wave oscillations the magnetic field displacement would be expected to be low and the electric field displacements high near the nodal points.

**Group II** encompasses dominant magnetic field oscillations. A low E:B ratio could arise if the wave was propagating at low Alfvénic speed, which in turn would arise if the plasma density was high. For standing wave oscillations the magnetic field displacement would be expected to be high and the electric field displacements low near the anti-nodal points. Low electric fields can also arise where there is electrostatic screening.

**Group III** encompasses electric and magnetic field oscillations with different spectral components. Since the Poynting flux time series is an excellent detector of coherence in time between electric and magnetic oscillations a series of PFIs is observed when the fields are coherent. It is possible that these multiple PFIs are a generalisation of the single impulses classified as Group VI. Events in this group often displayed impulses with positive and negative signs of the  $S_z$  component of Poynting flux. As well as the above coherence effects such a situation could also arise from the superposition of PFI echoes.

**Group IV** comprises oscillations where the electric and magnetic fields are in phase [or in antiphase] as would be the case for a propagating electromagnetic wave. In this case calculation of the Poynting flux is analogous to heterodyning the electric and magnetic field components as described in Section 2.5.3 and gives rise to a Poynting flux oscillation at twice their common frequency. The sign of the Poynting flux oscillations are either positive or negative, although in practice there was sometimes an occasional PFI with the opposite sign which may have been a reflection.

**Group V** specifically describes standing waves where the electric and magnetic fields were in quadrature as described in Section 2.5.5 The electric field may be advanced or retarded by  $90^\circ$  relative to the magnetic field. The E:B ratio would depend upon the proximity of the Polar satellite to nodes or anti-nodes in the standing wave pattern.

**Group VI** consists of predominantly single PFI events where a simultaneous  $E_x$  electric field component and  $B_y$  magnetic field component have either the same or the opposite sign.

The above classification scheme is summarised as follows:

- Group I** AC electric fields with an ac magnetic field significantly weaker
- Group II** AC magnetic fields with an ac electric field significantly weaker
- Group III** ac signals where the electric fields and the magnetic fields had different frequency components and therefore PFIs of different signs.
- Group IV** AC signals where the electric and magnetic fields were in phase [or in anti-phase] and therefore with PFIs of mainly the same sign.
- Group V** AC signals where the electric and magnetic field oscillations were in quadrature
- Group VI** single impulses caused by momentary deflections of the electric and/or magnetic fields

### 6.3 The thirty-nine magnetospheric events

The events catalogued and described are those that had a possible counterpart in data from ground-based instruments. There were thirty-nine events where magnetospheric Poynting flux signals had a possible ground counterpart and these are summarised in Table 6.1 by chronological order within their magnetospheric group classification. Table 6.1 also includes the Polar satellite field-line trace geographical latitude and longitude to the ionosphere at an altitude of 100km. Tsyganenko 86 modelling was used with the listed Kp values. These planetary Kp indices had been calculated every three hours from ground magnetometer observations. Kp values of 50 or greater are an indicator of storm level activity, although many observations at high latitude showed substorms with lower Kp values. [Note that the second digit of 3, 0 or 7 is an alternative to the older Kp notation which used +, 0 or –]

The number of events classified into each group is depicted in Figure 6.2 . For a description of each event and the corresponding plots the reader is referred to Appendix 7. A Magnetic Local Time [MLT] clock diagram representing when these events were observed during the dusk-midnight sector that was selected is shown in Figure 6.3.

C1	C2	C3	C4	C5	C6	C7
Group Date Figure	Time UT	Poynting flux FAC $\mu\text{Wm}^{-2}$	E:B $\text{kms}^{-1}$	IRIS peak UT	Ground observations	Kp Polar trace Geographic
Group I		$S_x$ $S_y$ $S_z$				
2002-12-10 Figure A7.1	1830	$S_x$ $S_y$ ~4 to 12	$\sim 10^4$	-	Variable IRIS absorption 1810UT onwards	13 68°N -30°E
2002-12-17 Figure A7.2	1630	$S_x$ $S_y$ ~4 to 10	~2000	-	Variable IRIS absorption	03 70°N -6°E
2003-12-12 Figure A7.3	1630	$S_y$ ~4 to 20	Ex:Bz ~500	-	Variable IRIS absorption. Oscillations SOR- PEL	33 67°N 8°E
2003-12-28 Figure A7.4	1430	$S_y$ ~4 to 8	~1000	-	Variable IRIS absorption.	07 74°N 3°E
Group II		$S_x$ $S_y$ $S_z$				
2002-12-27 Figure A7.5		$S_x$ $S_y$ $S_z$ <4	<100	-	Oscillations in Greenland magnetometers	37 64°N 39°E
Group III		$S_x$ $S_y$ $S_z$				
2002-10-10 Figure A7.6	2301 2303 2305 2307 2309	+15 -5 +15 -20 +20 -15 <b>-20 -12 +31</b> -22 +12 +8 +6 0 -12	4000	-	Substorm onset 2302UT MUO PEL	30 65°N -24°E
2002-10-19 Figure A7.7	1926 1928 1934 1936	-5 0 -10 <b>+20 -4 +15</b> -5 -7 -5 0 +9 +9	-	-	Substorm onset 1932UT BJN OGMD BJN MUO 1938UT	37 72°N 8°E
2002-11-22 Figure A7.8	1711 1716 1719	+10 -5 +19 0 0 +20 <b>0 +32 -22</b>	1600	1719 68.6°N	Substorm onset 1710UT SOR-MUO	40 68°N 25°E

2003-09-26 Figure A7.9	2033	-3 -12 -10		2039	Substorm onset	43
	2035	0 +15 +10	-	70°N	2037UT BJN	71°N 12°E
	2038	+5 -5 -6				
2003-11-12 Figure A7.10	1857	0 -10 +16		1902	Substorm onset	50
	1858	-70 +25 -40		68°N	1853 MUO	65°N 0°E
	1859	+70 +80 +45	1500		OGMD MUO-PEL	
	1900	+40 -30 -70			1900UT	
	1901	-10 0 +20				
2003-11-22 Figure A7.11	1638	-15 -25 -15		1640	OGMD OUJ-HAN	47
	1641	+6 -25 -30	3000	68.3°N	1638UT	69°N 24°E
	1643	0 0 +30		1648		
	1650	0 0 -25		69.6°N		
	1651	0 0 +35				
2003-12-15 Figure A7.12	1650	-6 0 -6		-	Substorm onset	47
	1652	0 0 -8	2200		1646UT HOR BJN OGMD BJN-SOR 1651UT	72°N 17°E
Group IV		$S_x$ $S_y$ $S_z$				
2002-10-17 Figure A7.13	2212	0 +120 +180	2100	-	Substorm onset	20
	2216	+20 -40 +350	3000		~2212UT SOR MAS	68°N -15°E
2002-10-27 Figure A7.14	1806	+10 +10 +30	200	1811	OGMD PEL-OUJ	40
	1808	-14 -10 -18		68.8°N	1808UT	68°N 43°E
2003-10-16 Figure A7.15	2016	-10 +50 -50		-	Substorm onset at	40
	2019	0 -30 -85	3200		2022UT SOR-MUO	68°N -1°E
	2024	-5 +7 -25				
2003-11-09 Figure A7.16	1818	0 0 +18		1821	Substorm onset at	50
	1820	0 -20 +20		68.6°N	1819UT SOR-MAS	66°N 18°E
	1821	-38 -20 -39	85			
	1822	0 0 +12				
	1830	-40 0 +20				
2003-11-15 Figure A7.17	1634	0 +80 -140	2000	1630	Substorm onset at	53
	1639	-25 -150 -100	3000	69.3°N	1630UT MAS and 1634UT NAL-BJN OGMD PEL-OUJ	72°N 20°E

					1630UT	
Group V		$S_x$ $S_y$ $S_z$				
2002-10-26 Figure A7.18	1746- 1753	$S_z +90 -150$	-	-	Substorm onset SOR	43 73°N 35°E 72°N 30°E
2002-11-09 Figure A7.19	1850- 1916	$S_z +6 -4$	-	-	1850UT Half-cycle oscillations SOR- TAR	27 68°N 16°E 68°N 9°E
2002-12-24 Figure A7.20	1830- 1850	$S_z \pm 6$	-	-	Oscillations AMK	37 65°N -34°E 64°N -40°E
2003-10-10 Figure A7.21	2134- 2150	$S_z \pm 6$	-	-	Pi2 oscillations at SOR and MAS	17 67°N -3°E 66°N -10°E
2003-10-19 Figure A7.22	2122 2128- 2150	-8 +40 -115 $S_z +25 -50$	4000		Oscillations FAR Substorm onset 2122 SOR	53 65°N -23°E 63°N -29°E
2003-10-26 Figure A7.23	1905- 1925	$S_z +5 -3$	-	-	1909UT Half-cycle oscillations SOR - TAR	33 70°N 6°E 69°N 3°E
2003-11-09 Figure A7.24	1618- 1736	$S_z +5 -7$	-	-	1618UT $\pm 50$ nT oscillations SOR MAS	40 69°N 47°E 68°N 35°E
2003-11-18 Figure A7.25	1854- 1858	$S_z +4 -13$	-	-	-	33 68°N -15°E 67°N -18°E
2002-11-25 Figure A7.26	1722- 1732	$S_z \pm 30$	-	-	Oscillations MUO- PEL	33 70°N 3°E 69°N -1°E
2003-12-15 Figure A7.27	1400- 1410	$S_z +50 -120$	-	-	Oscillations SOR- PEL	47 72°N 17°E
2003-12-15		$S_z \pm 5$	-	-	Oscillations BJN-	37 73°N 18°E

Figure A7.28	1458- 1518					MUO	71°N 14°E
Group VI		$S_x$ $S_y$ $S_z$					
2002-09-11 Figure A7.29	2255	-45 +40 +68	3600			Substorm onset 2256UT SOR	47 67°N 14°E
2002-10-03 Figure A7.30	2231	+80 -1 -25	1200	2234 68°N		Substorm onset 2232UT MUO	63 63°N -10°E
2002-10-20 Figure A7.31	2144	+5 +25 +35	2000	2141 70°		Substorm onset 2144UT BJN	27 67°N -12°E
2002-12-14 Figure A7.32	1608 1631	+50 -30 -19 -5 0 +13	700 -	1609 1629 68.9°N		Weak substorm onset ~1628UT NAL	40 71°N 8°E
2003-09-30 Figure A7.33	1910	-12 +8 -8	-	-		OGMD BJN-MUO 1912UT	07 72°N 38°E
2003-10-03 Figure A7.34	1817	-21 +32 -27	1800	-		OGMD BJN-SOR 1811UT	30 74°N 47°E
2003-10-19 Figure A7.22	2122	-4 +10 -115	3600	-		Substorm onset 2121UT SOR-PEL	53 64°N -25°E
2003-10-20 Figure A7.35	1927	-4 +5 0	800	1933 69.4°N		Substorm onset 1933UT SOR	50 66°N 20°E
2003-10-26 Figure A7.36	2040	-15 +15 +11	1000	2039 68.6°N		OGMD MAS-MUO 2040UT	50 64°N -13°E
2003-11-25 Figure A7.37	1550 1604	0 +8 -16 -10 -25 -35	1000 1000	1601 70°N		Irregular oscillations SOR- PEL 1544UT	33 73°N 22°E
2003-12-12 Figure A7.38	1722	0 +45 -91	1200	-		OGMD PEL-OUJ 1722UT	33 66°N -5°E

**Table 6.1 The thirty-nine magnetospheric and terrestrial events**

These observations made during the autumn of 2002 and 2003 all appeared to have a terrestrial counterpart. Column numbers are denoted C1 to C7. The strongest Poynting flux components in a series are shown in red.

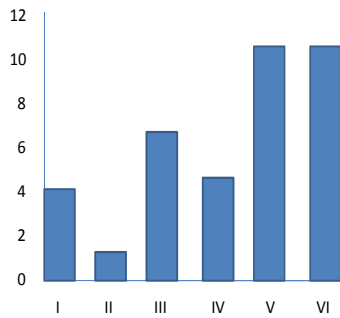


**Figure 6.2**  
**Number of events in each magnetospheric group**

This bar graph shows the distribution of the 39 events given in Table 6.1

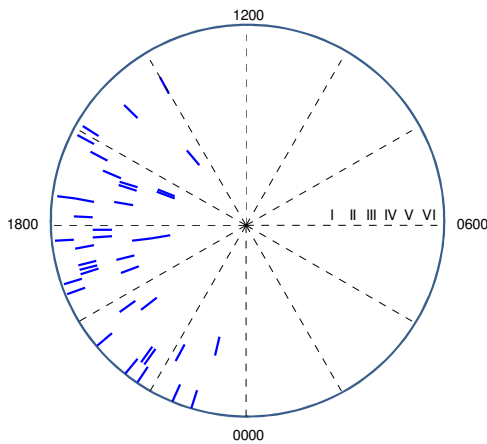


**Figure 6.3**  
**Clock diagram depicting MLT of the thirty-nine events**

Observations were mainly made in the dusk-midnight sector.

Magnetospheric Groups I to VI are shown with different radii as indicated by the annotation on the 0600 MLT axis.

### 6.3.1 Temporal coincidence

The temporal accuracy of the events shown in Table 6.1 was of the order of a  $\pm 1$  minute. Partly this was due to the 10mHz low-pass filtering of satellite data, which had a time-constant of around 1 minute, and partly it was due to the 1 minute resolution of the IRIS riometer keograms. Substorm onset was timed from the change in gradient in magnetograms and this could vary with latitude over timescales of several minutes.

The event times given in Columns 5 and 6 of Table 6.1 show a high occurrence of magnetospheric-terrestrial coincidences within  $\pm 6$  minutes. To illustrate this Figure 6.4 depicts the timing of all riometer absorption events over a time of  $\pm 60$  minutes relative to the time of the strongest Poynting flux impulse. Where there was more than one PFI in Groups III and IV the strongest was highlighted in red in Table 6.1 and the time of this signal was used, albeit with some uncertainty as to whether some weaker signal was associated with the ground event. These events were coloured light blue to distinguish them from the dark blue coloured single impulse events in Group VI.

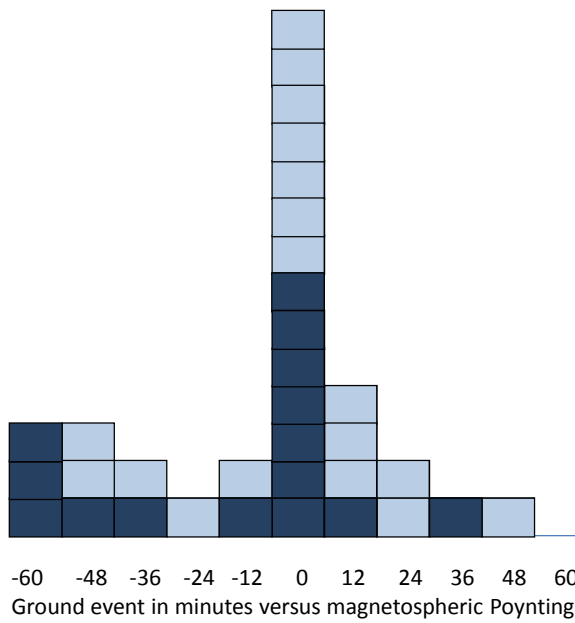


**Figure 6.4**

**Timing of IRIS riometer absorption events relative to PFIs**

This bar graph shows the terrestrial IRIS absorption events over a time interval of  $\pm 66$  minutes relative the time of the strongest magnetospheric Poynting flux. Times relative to the single PFI events in magnetospheric Group VI are shown in dark blue.

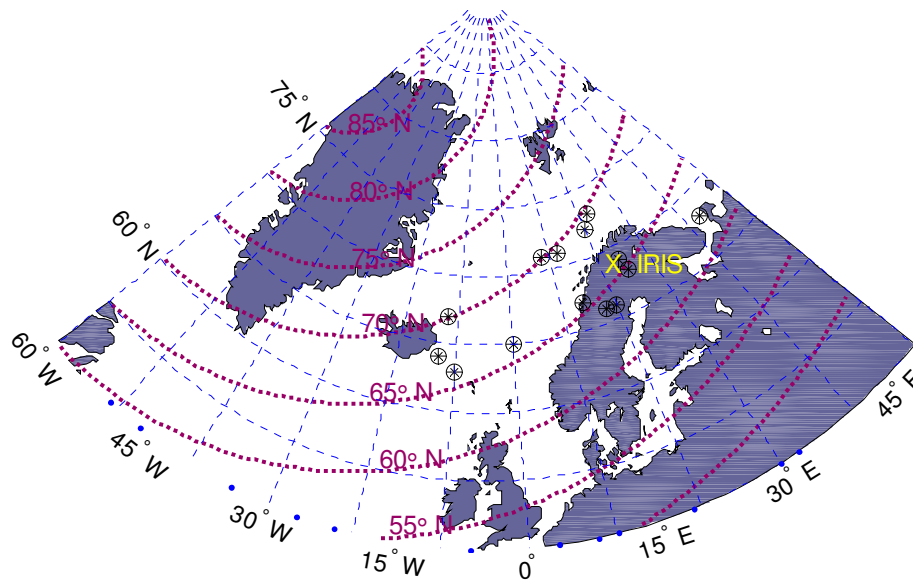


**Figure 6.5 Map of Polar satellite field-line traces**

Black stars indicate the Polar satellite field-line trace to the ionosphere at the times when enhanced absorption events in Groups III IV and VI were detected in the IRIS riometer within  $\pm 6$  minutes of the strongest magnetospheric PFI. The location of the IRIS riometer at Kilpisjärvi in Finland is marked by a yellow X.

### **6.3.2 Geographic separation of temporal coincidence**

Figure 6.5 shows a map on which was plotted the Polar satellite field-line trace to the ionosphere when enhanced absorption was observed in the IRIS riometer at the same time as the strongest Poynting flux impulses within  $\pm 6$  minutes. The events are up to  $4^\circ$  further to the north geomagnetically and up to  $35^\circ$  further to the west. The errors inherent in field line tracing are not known but may be of the order of a few degrees. This is less than the spatial separation of many of the coincidences.

### **6.3.3 Coincidence and association**

A relevant question is: when does an apparent coincidence between a magnetospheric and a terrestrial observations become an association? Although it may never be possible to be certain, given enough observations of the coincidences it may be possible to give a statistical estimate of the probability that they didn't arise by chance. In this study, events on the ground such as riometer spikes and substorm onsets, were sometimes detected around the times of PFIs in the magnetosphere. This led to a hypothesis that they were associated and a null hypothesis that the apparent temporal coincidences arose from chance alignment with a background of precipitation from other uncorrelated processes. It was always possible that events would be observed on the ground but not in Polar satellite data because the satellite was not at a location where it could detect the electromagnetic waves. Alternatively there are events observed in Polar satellite data but not on the ground because the charged particles for that event were not on field lines that reached the ionosphere over Kilpisjärvi. So it was not considered practical to calculate statistics from the continuous stream of magnetospheric and terrestrial signals throughout a season as was done in a study of substorm onset in relation to the northward turning of the IMF [Hsu and McPherron 2002, Morley and Freeman 2007]. However at the other extreme it was not felt necessary, nor was it practical, to only consider the rather short intervals when the Polar satellite field line trace was precisely connected to Kilpisjärvi since auroral arcs [Figure 1.3] suggest that precipitation can occur on current sheets very approximately aligned with geomagnetic latitude.

In order to get an idea of the probability that the observed pattern of magnetospheric and terrestrial coincidences arose by chance the following analysis was carried out.

All Polar satellite impulse events that also gave rise to a ground riometer absorption enhancement within  $\pm 6$  minutes were included in a possible association. This time window was chosen because standing wave oscillations with a frequency of around 3mHz were often observed at high latitudes and their period of 5.6 minutes would correspond approximately to the return propagation time along a high latitude field line.

A window of  $\pm 66$  minutes was taken around the time of the Polar satellite PFI and this was divided up into eleven  $\pm 6$  minute bins. Each keogram was then examined for absorption enhancement events in each bin and the total number N was accumulated.

The null hypothesis probability that the resulting number denoted X of events in the centre bin could have arisen by chance was estimated. If there was no association between spacecraft signals and ground signals then there was nothing special about the time origin for each keogram. Then the probability p that any event is successfully found in a particular bin was:  $p=1/11$  and the probability q that it would fail to be in that bin was:  $q=1-p = 10/11$ . The probability [Spiegel 1961] of finding X events in a particular bin out of N events in total

[X successes and N-X failures] is given as :

$$p(X) = {}_N C_X p^X q^{N-X} = \frac{N!}{X!(N-X)!} p^X q^{N-X}$$

If all the events from Groups III, IV and VI shown in Figure 6.4 were used then  $X=12$ ,  $N=32$ ,  $p=1/11$ ,  $q=10/11$  and  $p(X) = 9 \times 10^{-5}$ . If instead only the Group VI events for which there was no ambiguity in the reference time were used then  $X=6$ ,  $N=14$ ,  $p=1/11$ ,  $q=10/11$  and  $p(X) = 8 \times 10^{-4}$ . A window of  $\pm 66$  minutes may have meant that events were being detected in IRIS keograms that were not detectable by the Polar satellite because of its orbital motion: recalculating these probabilities for a window of  $\pm 42$  minutes gave the lower probabilities of  $3 \times 10^{-5}$  and  $1 \times 10^{-3}$  respectively.

Despite the geographical separation between Polar satellite field line traces and the IRIS riometer the lowest of these estimates suggested that the probability that the pattern of these coincidences arose by chance was of the order of 1 in 1000. This was only a statistical estimate and it remains the case that it is never possible to say definitely that any particular riometer signal is associated with a magnetospheric PFI.

#### 6.4 Poynting flux vectors

An initial clue about propagation was provided by the phasing of the electric and magnetic fields. They were expected to be in phase [or in anti-phase] for a propagating Alfvén wave and in quadrature for a non-propagating standing wave. From this it followed that signals in magnetospheric Group V were non-propagating resonances as discussed in Chapter 8.

Although the Polar satellite data was initially provided in the GSE frame of reference this was transformed to a spacecraft-centred field-aligned coordinate frame of reference [Section A2.8] so that the Poynting flux vector component along magnetic field lines [ $S_z$  component], in geomagnetic shells [ $S_y$   $S_z$  components], or obliquely across geomagnetic shells could be distinguished. In order to visualise the Poynting flux vectors relative to the magnetic field lines the field-aligned  $S_z$  component of the Poynting flux vector were plotted against the radial  $S_r$  component of Poynting flux, where:  $S_r = \sqrt{S_x^2 + S_y^2}$  in Figure 6.6 for magnetospheric Groups III, IV and VI. These plots suggested that nearly all the Pc5 band-limited signals had a component of their Poynting flux vectors across field lines, with the possible exception of two strong signals in Groups IV and VI.

Sunward-directed Poynting flux vectors could be seen when the Poynting flux vectors were projected onto the GSE x-y and x-z planes and clear examples of this orientation were observed on 2002-09-11, 2002-10-12, 2003-09-30, 2003-10-03, 2003-10-19 and 2003-11-25. It is possible that some of the signals with opposite directions of Poynting flux vectors were reflections.

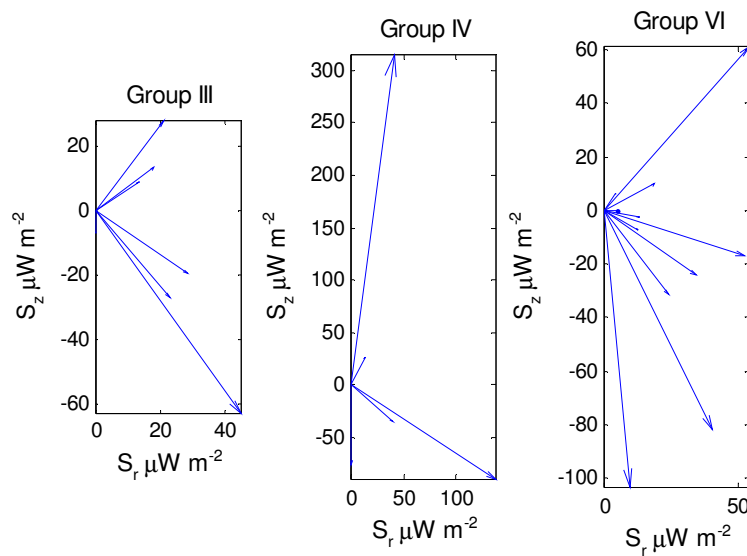


**Figure 6.6 Poynting flux vectors relative to the magnetic field**

Magnetospheric groups III, IV and VI in cylindrical coordinates.  $S_z$  is the Poynting flux component along the field line and  $S_r$  is the Poynting flux component normal to the field line direction. These diagrams suggest that the PFIs were sometimes observed propagating across magnetic field lines.

Always the meaning of the  $\mathbf{E} \times \mathbf{H}$  Poynting vector needs care in interpretation. But there is nevertheless a suggestion here that many of these events were electromagnetic impulses with an ultimate source in the magnetotail and the word *tailquake* for the source of these events in an AGU monograph [Engebretson 2006] seems a good description.

In field-aligned coordinates a negative  $S_z$  means a component of Poynting flux towards the ionosphere in the southern hemisphere. This was initially perplexing as many of the coincidences between PFIs and enhanced absorption in the IRIS riometer in the northern hemisphere were observed with negative  $S_z$  impulse. Finally it was realised that the sign of the Poynting flux field-aligned  $S_z$  component simply depended upon whether the Polar satellite was in the northern or the southern region of the magnetosphere as depicted in Figure 6.7. If it was in the northern region then a Poynting flux from a source near the geomagnetic equator would be detected with a  $+S_z$  component but if it was in the southern hemisphere then a Poynting flux from a source near the geomagnetic equator would be detected with a  $-S_z$  component. This would be true whether the PFI was propagating along or across field lines. The fact that only one exception to this [Figure A7.28] was observed in the thirty-nine events examined suggests that these PFIs generally had an origin very near to the geomagnetic equator.

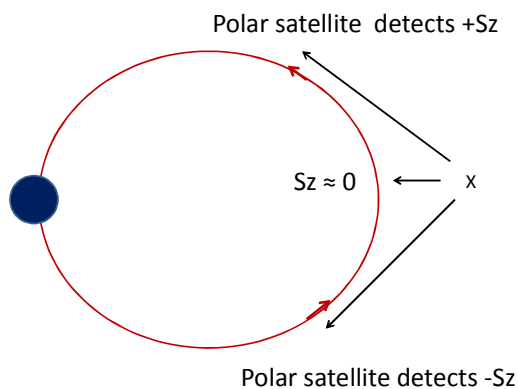


**Figure 6.7**

**Explanation of  $+S_z$  and  $-S_z$  signals in Polar satellite data**

The sketch illustrates PFI propagation across field lines from a source in the tail plasma sheet.

This interpretation of the sign of the Poynting flux  $S_z$  component is equally valid for field-guided signals.

Energy transfer between PFI s and precipitating electrons may involve a non-linear process whereby the speed of the PFIs, as estimated from their E:B ratio, would increase with their intensity in  $\mu\text{Wm}^{-2}$ . The transfer of energy from PFI to electrons would then cause a fast , intense wave to become weaker and slow down. Figure 6.8 shows a graph with all the signals for which an E:B ratio had been estimated in Table 6.1. Data for magnetospheric Groups III, IV and VI were coloured blue, red and black. The first order regression lines that

were plotted for each magnetospheric group did suggest that faster propagation might be associated with stronger PFIs, but the paucity of data may account for the considerable difference in gradient between the different groups.

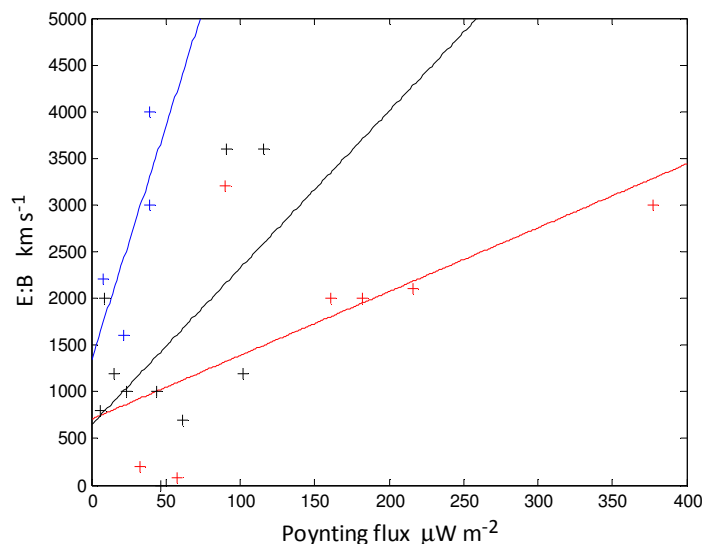


**Figure 6.8 E:B ratio versus Poynting flux intensity**

Estimates of the ratio of electric to magnetic field strength are plotted here for the PFIs in magnetospheric Groups III, IV and VI

An interesting mode of propagation arises if the geomagnetic shells act as waveguides. Table 6.2 gives the times and the magnetospheric groups when  $S_y$   $S_z$  Poynting vectors were observed. The angle across the geomagnetic shell relative to the magnetic field direction was designated as  $\theta$ . There is however insufficient evidence to be certain that this is a unique mode or just the chance alignment of oblique Poynting flux vectors.

Group	Date	Time UT	$S_y$ $\mu\text{Wm}^{-2}$	$S_z$ $\mu\text{Wm}^{-2}$	$\theta = \tan^{-1} \frac{S_y}{S_z}$
III Figure A7.9	2002-09-26	2035	+15	+10	$56^\circ$
IV Figure A7.15	2003-10-16	2019	51	-30	$-60^\circ$
VI Figure A7.38	2003-12-12	1722	+45	-91	$-26^\circ$

**Table 6.2 Observations of geomagnetic shell Poynting flux vectors**

These events suggested propagation tangential to the local geomagnetic shell

## 6.5 Examples of events in the magnetospheric groups

In the following subsections one representative example from each of the six magnetospheric groups is described. Notes and plots for these and all the other events in Table 6.1 are given in Appendix 7.

### 6.5.1 Magnetospheric Group I event 1600 - 1700UT on 2002-12-17

This group comprised signals where the  $E_x$  component of electric field strength in  $\text{mVm}^{-1}$  was significantly greater than the  $B_y$  component of magnetic field strength in nT. As a result there tended to be very low levels of the  $S_z$  component of field-aligned Poynting flux. The dominant  $S_x$  and  $S_y$  components of Poynting flux suggest that electromagnetic energy is propagating normal to the magnetic field lines.

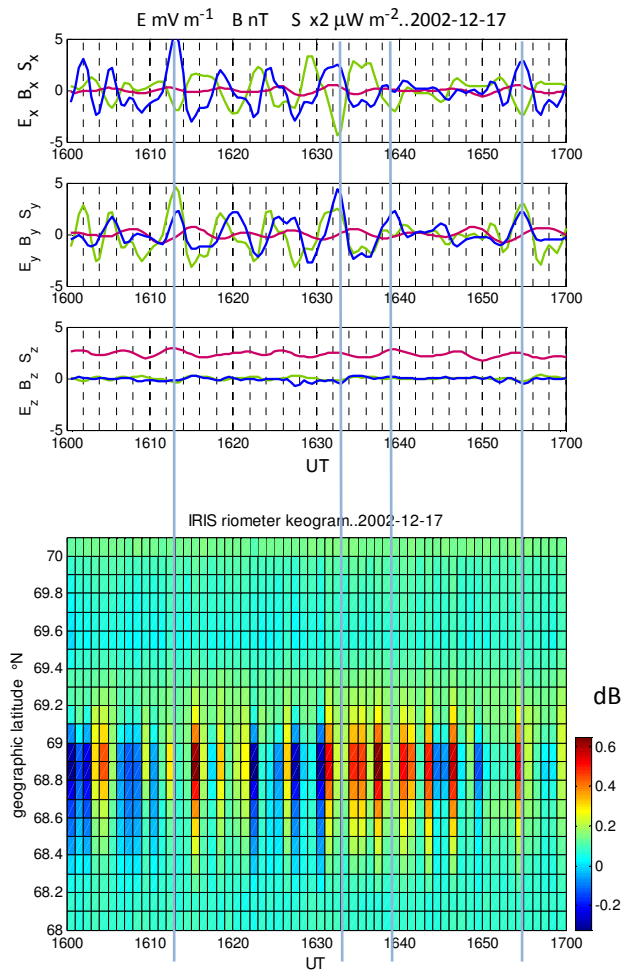
The character of the IRIS riometer keograms during these electric field oscillations suggested that the ionosphere was frequently receiving bursts of particles. It is not possible to show a 1:1 correspondence between the electric field displacements and the riometer enhancements, and also in these events the Polar satellite field-line trace was not to the riometer, but the existence of a possible association between the electric field deflections and enhanced absorption in the IRIS riometer cannot be altogether ruled out.

Figure 6.9 shows the components of the electric field, magnetic field and Poynting flux vectors together with the IRIS riometer keogram for 1600 - 1700UT on 2002-12-17.

$E_x$  and  $E_y$  oscillations with an frequency of 2.8mHz [6 minute period] were observed in Polar satellite data between 1600UT and 1640UT. At 1630UT the field-line trace was to  $70^\circ\text{N} -6^\circ\text{E}$ , which was over the Norwegian Sea and some  $27^\circ$  eastwards of the IRIS riometer. IMAGE ground magnetometers recorded very low amplitude [less than 2nT] oscillations with a frequency of 3.3mHz south of BJN between 1600UT and 1640UT which was reasonably close to the electric field oscillation frequency given the difference between field-line trace and magnetometer location.

The IRIS keogram showed approximately 10 enhancements in absorption between 1600UT and 1700UT at a latitude of  $69^\circ\text{N}$  giving a mean period of 6 minutes between these irregular enhancements, the same period as in the Polar satellite data.

Low values of magnetic field could arise near a standing wave node but here the phasing between the electric and magnetic oscillations was nearer to  $180^\circ$  rather than the quadrature signature of field-line resonance [Chapter 9]. Another unexplored phenomena that might explain these events is a higher Alfvén speed caused by low plasma density cavities.



**Figure 6.9 Group I  
1600 - 1700UT on 2002-12-17**

The upper diagram shows the components of the electric field, magnetic field and Poynting flux time series vectors and the lower diagram the IRIS riometer keogram.

Vertical lines indicate a possible association between electric field oscillations and riometer absorption.

Low amplitude oscillations in the IMAGE magnetograms are shown in Figure A7.2

### 6.5.2 Magnetospheric Group II event 1800 - 1900UT on 2002-12-27

This group was defined to comprise signals where the magnetic field in nT was significantly stronger than the electric field strength in  $\text{mV m}^{-1}$ . Only one example was encountered in these data, so compared to the other signals studied they may be a relatively rare phenomena. Some kind of electrostatic shielding may be a possible explanation for the absence of an electric field or alternatively the low E:B ratio may indicate a low Alfvén speed which could arise from a high plasma density. For the event on 2002-12-27 shown above in Figure 6.10, magnetic field oscillations with a frequency of 2.8mHz were observed in all three components between 1800UT and 1900UT, with the greatest amplitude of 9nT in the  $B_x$  component, suggesting that a ULF compression wave was propagating obliquely to the magnetic field. The Polar satellite field-line trace was to  $64^\circ\text{N} - 39^\circ\text{E}$  which placed it [within the accuracy of field -line tracing] near the Greenland ground magnetometer Tasiilaq [Ammassalik] [AMK] at  $65.6^\circ\text{N} - 37.6^\circ\text{E}$ . Magnetograms from the Greenland West Coast chain show that a substorm commenced at 1808UT which was the time when the 4 cycles of  $B_x$  oscillations began in the Polar satellite data suggesting that the substorm triggering and these compression waves are related.

The substorm was also observed further to the east in IMAGE magnetograms where there was a marked positive deflection at 1812UT as was seen in the Greenland plots.

The IRIS riometer keogram showed an increase in absorption at 1813UT but a stronger spike was observed far to the north at 1826UT, which was around the time when the  $B_x$  oscillations ceased. There was a faint indication of oscillations with an amplitude of 0.1dB and a frequency of approximately 4mHz in the IRIS riometer keogram at latitude 69°N during this time.

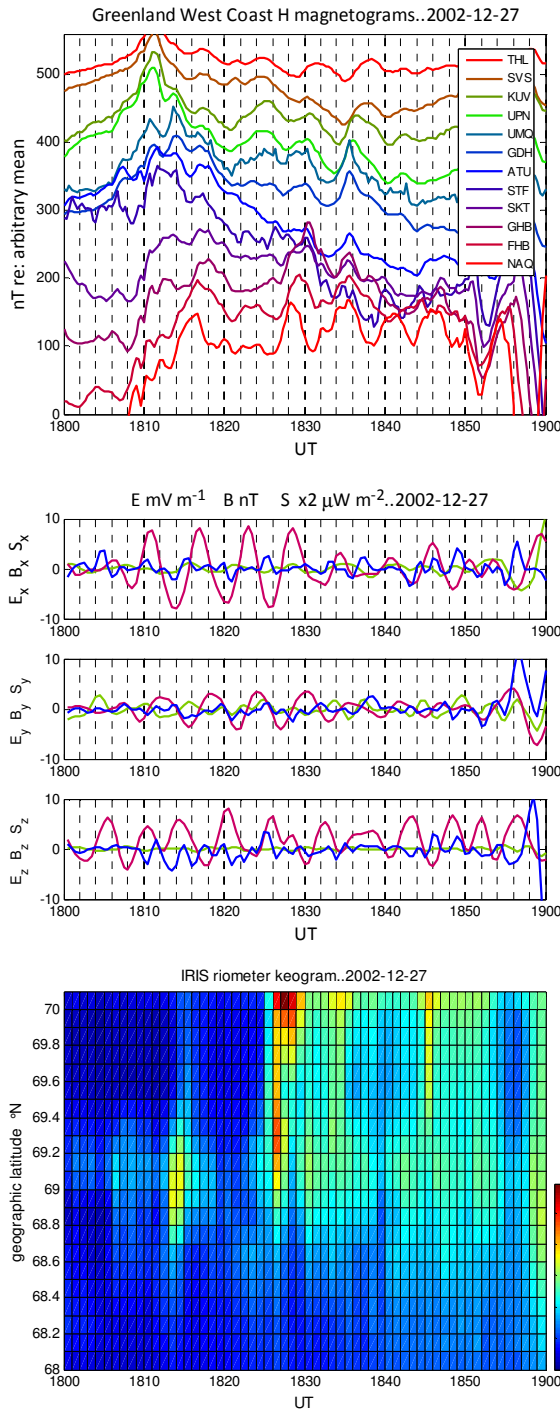


**Figure 6.10 Group II**  
**1800 - 1900UT on 2002-12-27**

These diagrams show the Greenland West Coast magnetograms, the components of the magnetospheric electric field, magnetic field and Poynting flux time series vectors and the IRIS riometer keogram.

### 6.5.3 Magnetospheric Group III event 1630-1730UT on 2003-11-22

This was the largest group identified in this sample so it could be said that electric and magnetic field deflections with different frequency components is a comparatively common phenomena in the magnetosphere.

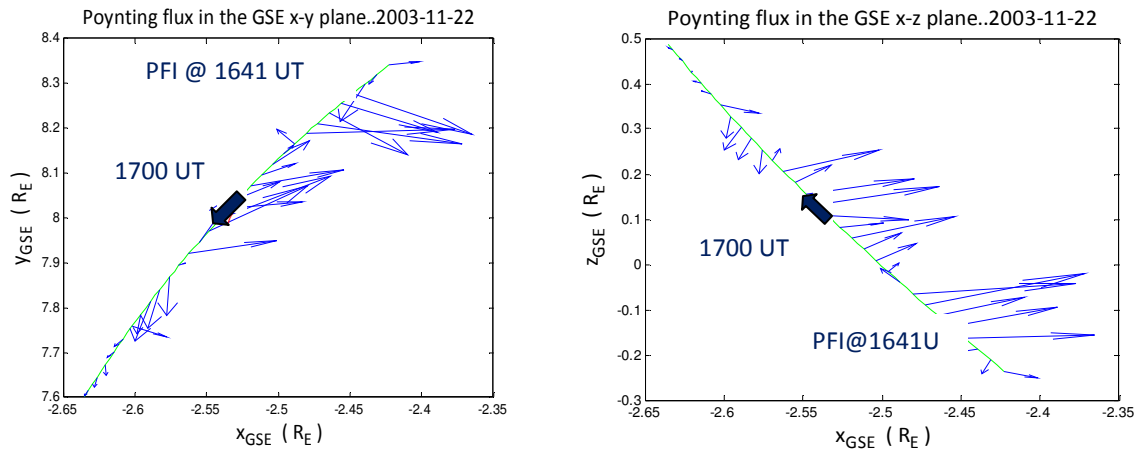


**Figure 6.11 Poynting vector quiver plots 1630 - 1730UT on 2003-11-22**

One hour of low-pass filtered Poynting flux vectors projected onto the GSE x-y and x-z planes showing the sunward PFI components at 1641UT. The green line shows the Polar satellite track and the heavy arrows mark the position of the Polar satellite at 1700UT. Poynting flux vectors are uncalibrated.

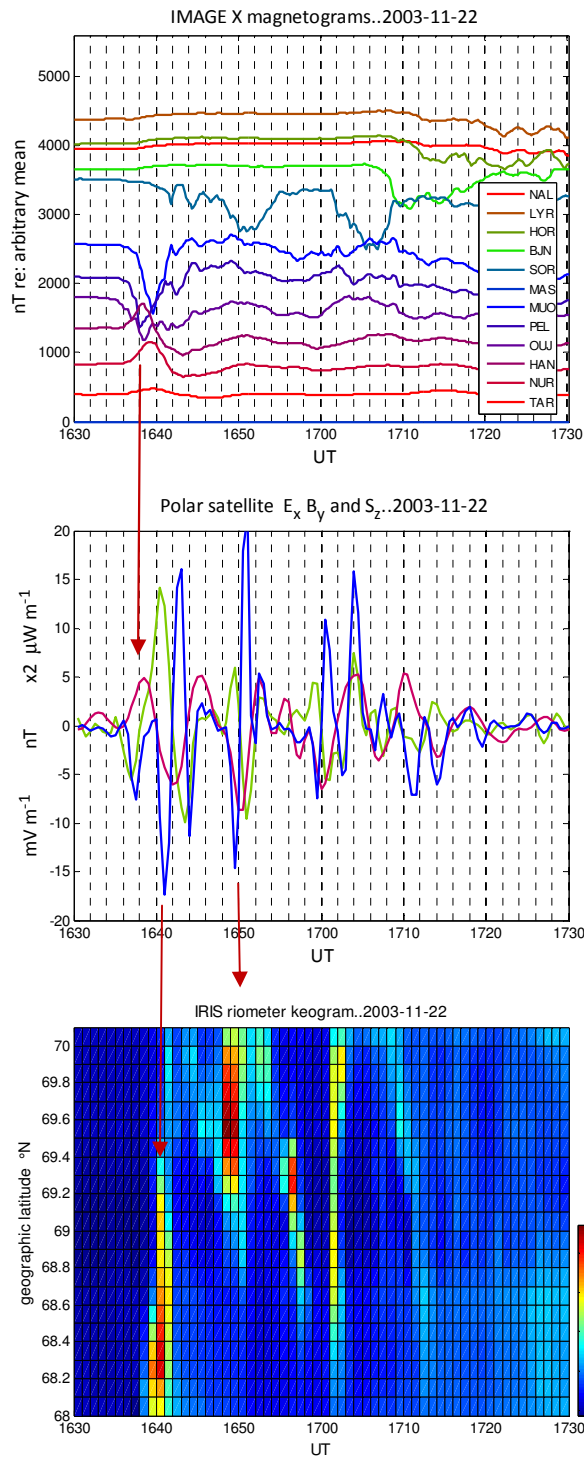
The above quiver plot projection of the Poynting flux vectors onto the GSE x-y and x-z planes [Figure 6.11] for the observations between 1630UT and 1730UT on 2003-11-22 showed a GSE/GSM  $+S_x$  component of propagation parallel to the Earth-Sun line.

Figure 6.12 showed that the strongest positive  $S_z$  impulses were seen at 1643UT and 1651UT. Enhanced absorption was observed in the IRIS riometer keogram at 1640UT and 1648UT and if these signals could be associated then the particle fluxes were reaching the ionosphere 3 minutes ahead of the oscillations crossing the Polar satellite at  $-2.5R_E$ .

What made this observation special was that the Polar satellite field line trace was to the same latitude as the IRIS riometer and only  $3^\circ E$  of it. The two strongest spikes were detected at latitudes of  $68.3^\circ N$  and  $69.6^\circ N$  respectively.

An opposing ground magnetometer deflection [OGMD] event which is described in Section 7.3.4 was observed in IMAGE magnetograms at 1638UT with a displacement of  $-500nT$  at OJJ [ $64.52^\circ N$ ] and  $+350nT$  at HAN [ $62.30^\circ N$ ] suggesting an ionospheric current system reversal to the south of the IRIS riometer. The large negative magnetometer deflection of

-1000nT at MUO [68.02°N] indicates that a strong ionospheric current was flowing from east to west further to the north of this reversal, however the ground magnetometer MAS which is at the same latitude as the IRIS riometer was not operational at the time.



**Figure 6.12 Group III**  
**1630 - 1730UT on 2003-11-22**

These diagrams show the IMAGE X-component magnetograms, the  $E_x$ ,  $B_y$  and  $S_z$  components of the electric field, magnetic field and Poynting flux time series vectors and the IRIS riometer keogram.

### 6.5.4 Magnetospheric Group IV event 1800–1900UT on 2003-11-09

There was not always a clear distinction between Groups III and IV but where the phase difference between the electric and magnetic field oscillations persisted over several cycles the result was a series of PFIs of one sign which were evenly spaced in time. Thus it was possible to measure a Poynting flux frequency which, when divided by two, gave an estimate of the frequencies of the quasi-coherent electric and magnetic field components. When the electric and magnetic fields were in phase the resulting PFIs were all positive [since  $+x + \Rightarrow +$  and  $-x - \Rightarrow +$ ]. If they were in anti-phase the PFIs were all negative [since  $+x - \Rightarrow -$ ]. As with Group III events the fact that these signals often occurred over extended timescales meant that it was not in general possible to associate any one ground signal with any one particular PFI. Table 6.1 shows that, these classes of signals often had significant  $S_x$  and  $S_z$  components, possibly indicating oblique propagation of the Pc5 band PFI component across geomagnetic shells.

A possible explanation for this group of observations was periodic electromagnetic impulses coming from an oscillatory process in the magnetotail. The round trip time for an echo off a dayside magnetosphere boundary would be of the order of a few minutes and it is very tentatively suggested that this could provide the feedback that sustains the oscillation. The quiver projection plot onto the GSE x-z plane shown below in Figure 6.13 for the Group IV event between 1816UT and 1836UT on 2003-11-09 showed a  $+S_x$  component of Poynting flux crossing the Polar satellite at  $-4.1R_E$ .

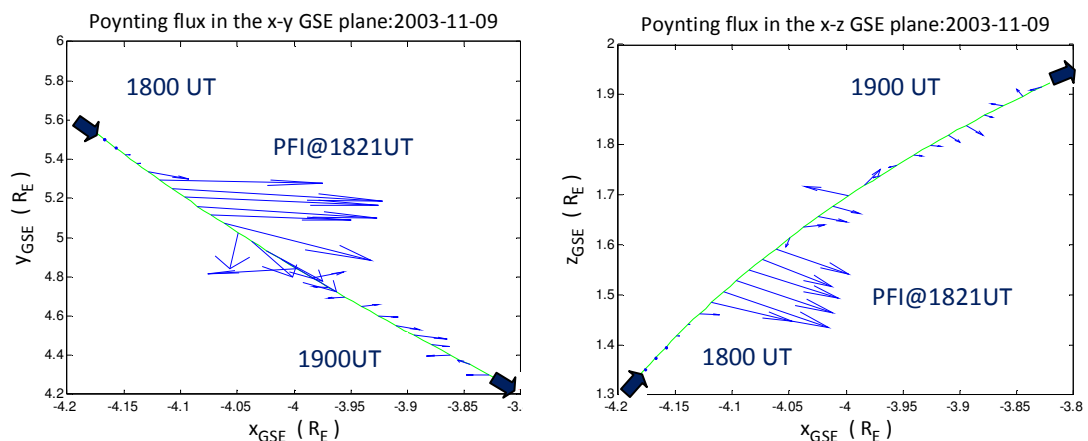


**Figure 6.13 Poynting vector quiver plot 1800 - 1900UT on 2003-11-09**

One hour of low-pass filtered Poynting flux vectors projected onto the GSE x-y and x-z planes showing the sunward PFI components at 1821UT. The green line shows the Polar satellite track and the heavy arrows the positions mark the satellite location at 1800UT and 1900UT. Poynting flux vectors are uncalibrated.

The IMAGE magnetograms shown in Figure 6.14 showed a substorm onset at 1818UT at SOR and 1819UT at MAS and then later again at 1821UT at BJN to the north. The onset at SOR coincided with the first PFI of  $+18 \mu\text{Wm}^{-2}$  at 1818UT. Further  $+S_z$  PFIs occurred at 1820UT, 1822UT, 1826UT, 1830UT and 1834UT giving a mean interval between positive impulses of 3.5 minutes [4.8 mHz].

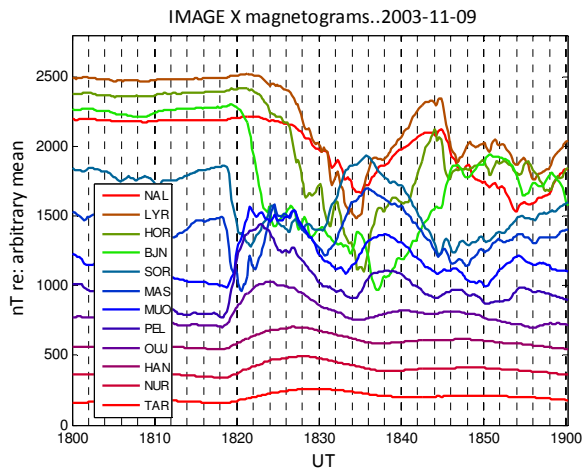
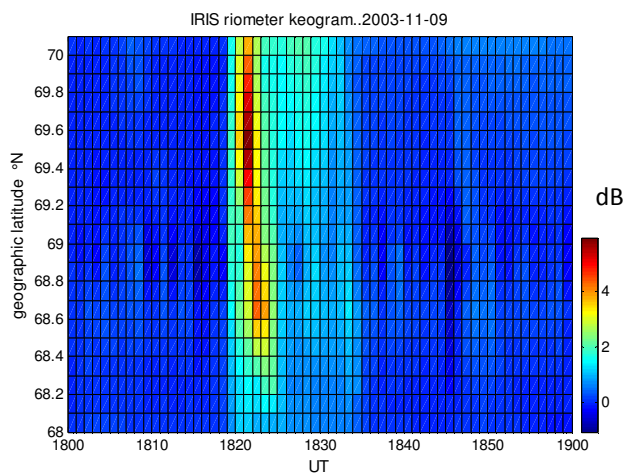
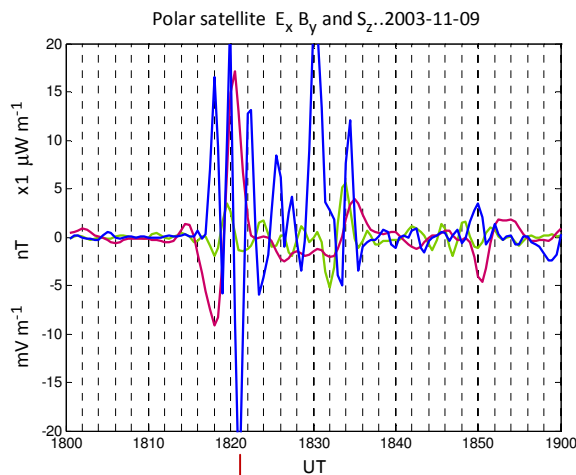


**Figure 6.14 Group IV**  
**1800 - 1900UT on 2003-11-09**

These diagrams show the IMAGE X-component magnetograms, the  $E_x$ ,  $B_y$  and  $S_z$  components of the electric field, magnetic field and Poynting flux time series vectors and the IRIS riometer keogram.



The process in the magnetotail that was launching these pulsed waves could also be powering the substorm because the substorm minima at 1834UT coincided with the last PFI. The IRIS riometer keogram showed 2dB of enhanced absorption between 1819UT and 1834UT which also coincided with the substorm expansion phase and was evidence of continued particle precipitation. The strongest PFI had a magnitude of  $58\mu\text{Wm}^{-2}$  and a negative  $S_z$  component of  $-39\mu\text{Wm}^{-2}$  which suggested propagation away from the Earth as the Polar satellite was in the northern magnetospheric lobe at the time. What is of interest is that a 6dB riometer spike occurred at the same time as this negative  $S_z$  impulse but what was surprising was that the latitude of the peak riometer absorption was  $69.6^\circ\text{N}$  whereas the Polar satellite field line trace was to  $66^\circ\text{N}$ . This may reflect errors in field line tracing or it may actually mean that the reflection was at a different latitude.

#### **6.5.5 Magnetospheric Group V event 2100 – 2200UT on 2003-10-19**

Quadrature oscillations are defined here as those where the electric and magnetic fields have the same frequency but with a phase difference between the electric and magnetic field of  $\sim 90^\circ$ . Poynting flux oscillations are a good detector of the presence of electromagnetic signals and when the electric and magnetic field oscillations are in quadrature the Poynting flux frequency is twice the frequency of the electric and magnetic components that gave rise to them [because  $\sin(2\omega t) = 2\sin(\omega t) \cos(\omega t)$ ]. Halving the Poynting flux oscillation frequency provides a good reference frequency from which to estimate the phase difference between the electric and magnetic fields from the phase angles calculated from complex FFT data. There is no DC offset when the phase difference is precisely  $90^\circ$  since the positive and negative displacements are then equal.

Quadrature oscillations are a distinctive class of signals that show up clearly when the  $E_x$  component of electric field is superimposed on the  $B_y$  component of the magnetic field. In every case that was observed the  $S_z$  [field-aligned] component of Poynting flux was the strongest. This component of Poynting flux was derived from both the  $E_x B_y$  and  $E_y B_x$  components in the vector cross product, but in the diagrams only the dominant  $E_x B_y$  and  $S_z$  components are shown. Most of these quadrature oscillations only lasted for one or two cycles of magnetic field oscillation which suggests that electromagnetic energy was being transferred from the resonance and giving rise to damped oscillations. Nevertheless this duration was too long to assign a particular time for the event in the way that was done with PFIs and IRIS riometer spikes in Groups III, IV and VI. An estimate of the start and end

times of these resonances was recorded in Table 8.1 and this was found useful when compared to substorm durations in Chapter 8.

An example of quadrature oscillations preceded by a strong PFI at 2122UT was observed on 2003-10-19. The only other example encountered of this phenomenon was on 2003-12-12 [Figure A7.37]. The quiver plot projection onto the GSE x-z plane [Figure 6.15] showed that this Poynting flux impulse was propagating earthward and although the  $S_z$  Poynting flux component was negative there was no inconsistency as the Polar satellite was in the southern lobe of the magnetosphere [Figure 6.7]. The E:B ratio suggested that the PFI had a high propagation speed of  $3600\text{kms}^{-1}$ . If this impulse initiated the following quadrature oscillations then the transient delay of  $\sim 16$  minutes between the initial impulse and the standing wave resonance may have been caused by the propagation time of Alfvén waves along magnetic field lines to the ionospheres. This would be analogous to striking a gong, when the initial, almost silent, impulse is followed by a gradual crescendo as waves reflected from the boundaries reinforce constructively. The Polar satellite field-line trace was initially  $1^\circ\text{N}$  and  $3^\circ\text{W}$  of ground magnetometer HEL but no ground signal was observed there at the time of the impulse. This placed it at a similar geomagnetic latitude to IMAGE ground magnetometer BJN. Far to the east however the IMAGE magnetograms [Figure 6.16] showed a substorm onset at 2120UT.

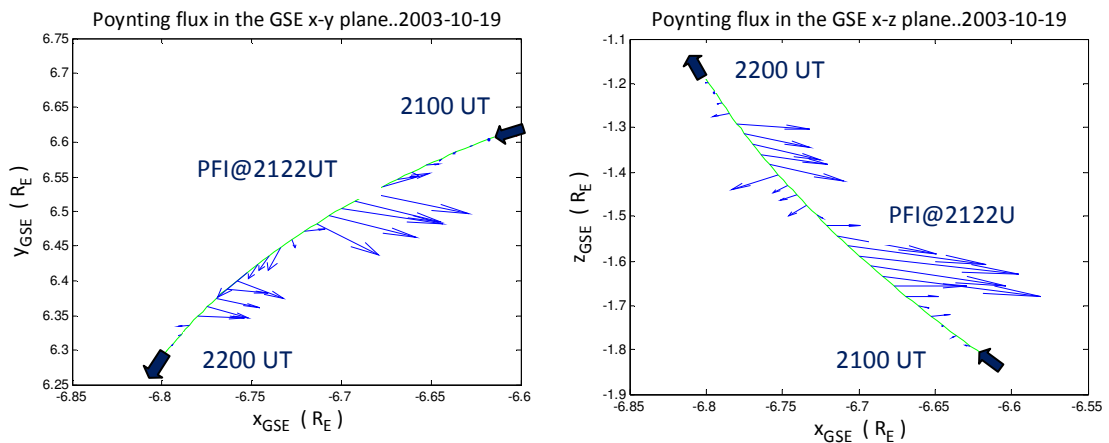


**Figure 6.15 Poynting vector quiver plot 2100 - 2200UT on 2003-10-19**

One hour of low-pass filtered Poynting flux vectors projected onto the GSE x-y and x-z planes showing the sunward components of the PFI at 2122UT that preceded the quadrature resonance. The green line shows the Polar satellite track and the heavy arrows the locations of the Polar satellite at 2100UT and 2200UT. Poynting flux vectors are uncalibrated.

The substorm developed in two stages, the first being initiated at the time of the impulse and the main expansion phase beginning at 2136UT, coincident with the time of the peak PFI in the quadrature resonance. Also the short substorm expansion phase ended around 2044UT at the same time as the quadrature event ended.

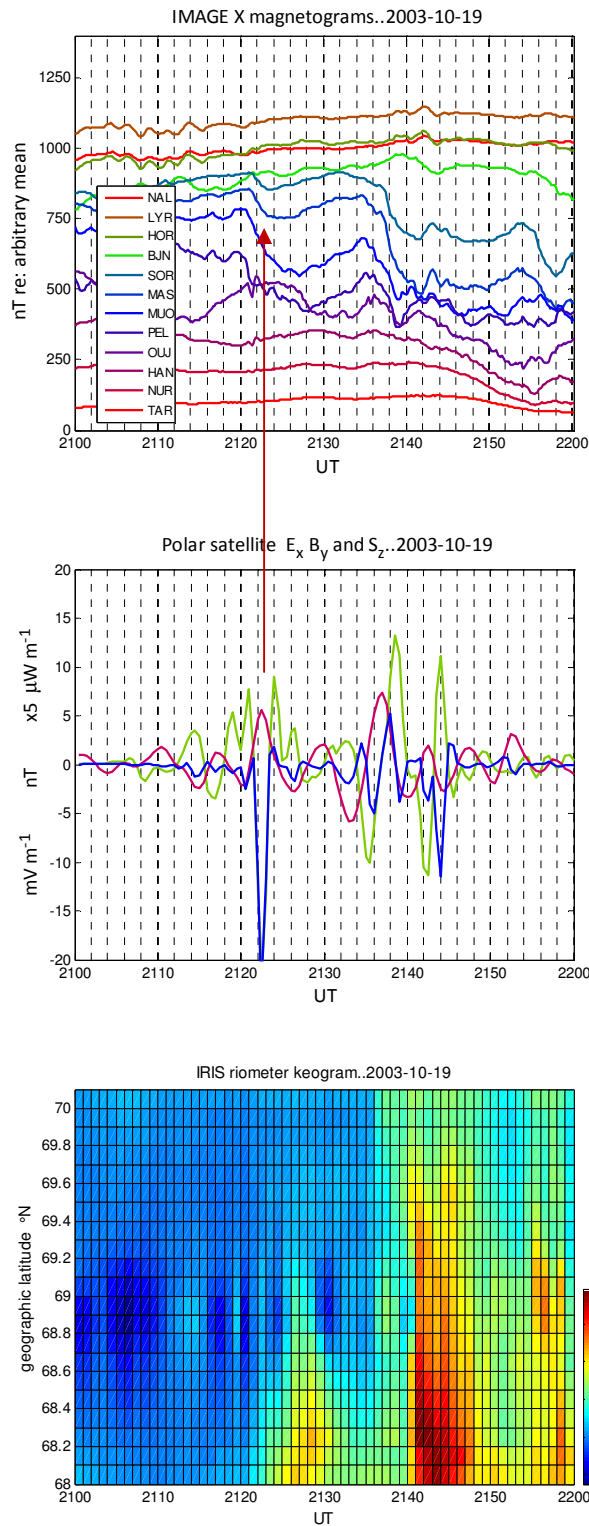


**Figure 6.16 Group V  
2100 – 2200UT on 2003-10-19**

These diagrams show the IMAGE X-component magnetograms, the  $E_x$ ,  $B_y$  and  $S_z$  components of the electric field, magnetic field and Poynting flux time series vectors and the IRIS riometer keogram.

No spike was seen in the IRIS riometer keogram at 2122UT but there was a 2dB absorption peak at 69.2°N at 2141UT during the main substorm expansion phase which then gradually weakened. The keogram has some of the characteristics of Group I because of the presence of electric field activity.

Chapter 8 describes the observations of these Group V signals and shows other examples where the quadrature signal was associated with the current flow to the ionosphere in the substorm expansion phase. However this was the only event where the quadrature signal was observed to be preceded by the arrival of a PFI.

### 6.5.6 Magnetospheric Group VI event 2200 – 2300UT on 2002-10-03

Single PFI signals are created either by sudden displacements in the electric and/or the magnetic field or by a short duration of temporal coherence between the electric and magnetic fields. The duration of a single impulse in Pc5 bandpass filtered Polar satellite data is typically about two minutes. They were often observed in association with  $E_x$  component electrical activity and the IRIS riometer keogram character then had the character of Group I events as shown for example in Figure A7.37. Isolated examples of Group VI events are shown in Figures A7.30, A7.31 and A7.38 and the first of these is described here.

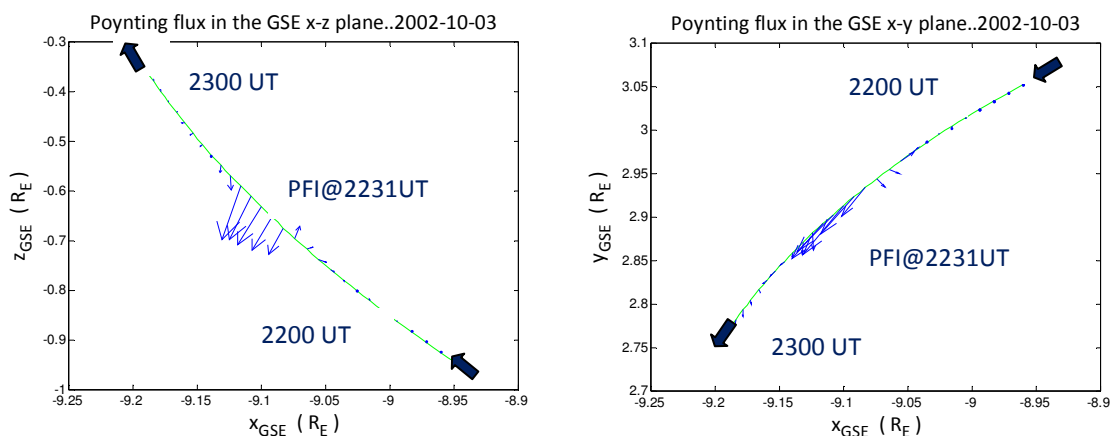


**Figure 6.17 Poynting vector quiver plot 2200 - 2300UT on 2002-10-03**

One hour of low-pass filtered Poynting flux vectors projected onto the GSE x-y and x-z planes showing the sunward PFI components at 2231UT. The green line shows the Polar satellite track and the heavy arrows the positions of the Polar satellite at 2200UT and 2300UT. Poynting flux vectors are uncalibrated.

The Polar satellite field line trace was over the Norwegian Sea when a strong  $+80\mu\text{Wm}^{-2}$  PFI was detected at 2231UT in the field-aligned  $S_x$  component. This was during a sequence of substorm onsets beginning at lower latitudes and progressing northward towards Bear Island. The IRIS riometer keogram showed enhanced absorption at 2234UT as a result of the substorm precipitation. Because of the location of the Polar satellite at GSM  $x = -9.1R_E$  the dominant  $+x$  field-aligned component implies anti-sunward propagation of this signal. It was unlikely to be a reflection because of the presence of only a single PFI.

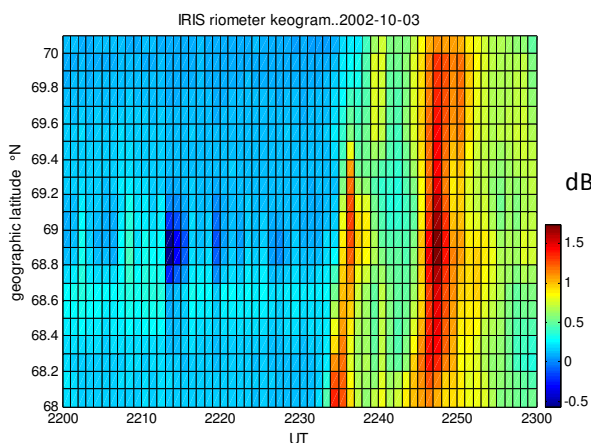
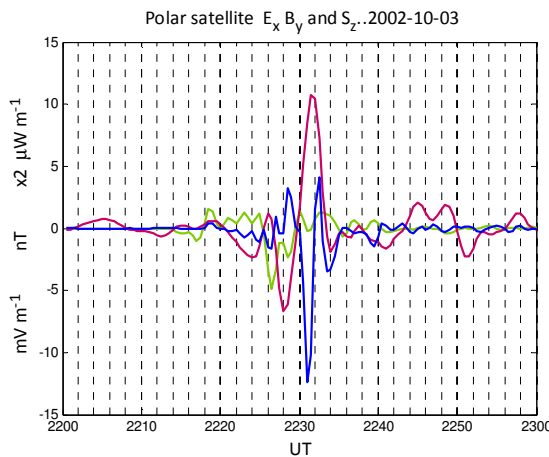
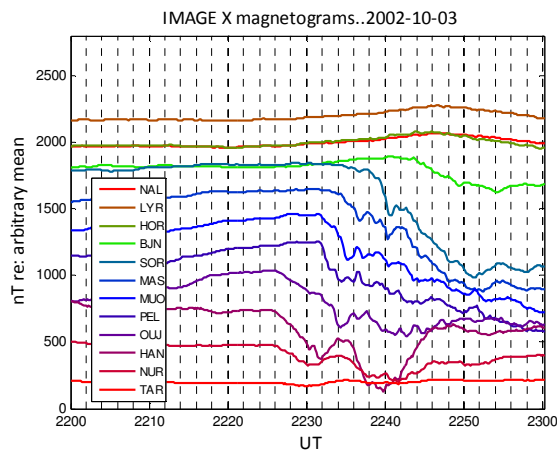


**Figure 6.18 Group VI**  
**2200 – 2300UT on 2002-10-03**

These diagrams show the IMAGE X-component magnetograms, the  $E_x$ ,  $B_y$  and  $S_z$  field-aligned components, the field-aligned  $x$ ,  $y$  and  $z$  components of the **electric field**, **magnetic field** and **Poynting flux** time series vectors and the IRIS riometer keogram.

These PFI vectors are shown projected onto the GSE x-y and x-z planes in Figure 6.17 and linear extrapolation suggests that the origin of the signal could have been from the dusk side plasma sheet at  $\sim$ GSE/GSM  $x = -8.9R_E$

The field line trace of the Polar satellite at 2230UT was to  $63^\circ\text{N } -10^\circ\text{E}$  which placed it south of the IRIS riometer and at approximately at the same geomagnetic latitude as IMAGE ground magnetometer MUO, although further to the west. The magnetograms in Figure 6.18 showed there was a distinct change of gradient associated with the onset of the substorm at MUO at 2232UT which was one minute after the magnetospheric PFI. An interpretation of these observations is that the PFI was launched from the same region and at the same time as the diversion of cross-tail current into a substorm current wedge [Figure 1.13] at around  $9R_E$ . The IRIS riometer keogram showed the onset of enhanced precipitation towards the south at 2034UT with a second pulse of enhanced precipitation at 2048UT near the time of substorm minimum. However no PFI was observed at this time.

## 6.6 Discussion and Conclusions

Classification of events is of considerable use when a diverse range of features is observed. Science abounds with examples such as the IAGA pulsation classification scheme described in Section 2.1.2. Even though any initial classification scheme is inevitably subjective it begins the process of organising the data so that patterns emerge. The scheme presented here is the first iteration of a classification scheme for PFI events in the magnetotail which includes some mathematical ideas about the effect of phase-differences on Poynting flux. Initially emphasis was placed on the field-aligned  $E_x$ ,  $B_y$  and  $S_z$  components. The classification of phenomena is not always definitive, so it would be understood if the reader would prefer to reclassify some of the events. In particular some of the Group VI events might be reclassified as Group IV and it is possible that the events classified as magnetospheric Groups III and IV are simply the general case of multiple oscillations of the single events classified as Group VI. The only difference between Groups III and IV may be that Group III includes the effect of interference from echoes and also, it is possible that the Group V quadrature resonance events include some Group VI signals reverberating along field lines between the ionosphere and the magnetotail.

With satellite data it is generally only possible to measure the  $\mathbf{E} \times \mathbf{H}$  vector from electric and magnetic field sensor data. Although this has the dimensions of intensity [ $\text{Wm}^{-2}$  in the bandwidth studied] it does not necessarily mean that energy is propagating. It is possible to devise static structures through which a satellite could pass that would yield a non-zero

value of  $\mathbf{E} \times \mathbf{H}$ . An abstract example is given in Section 2.5.2, but other examples could include electric fields around electrostatic charge structures and magnetic field from field-aligned currents. The Poynting flux theorem is concerned with the integration of  $\mathbf{E} \times \mathbf{H}$  over a surface to determine whether electromagnetic energy is increasing or decreasing within the enclosed volume [Equation 2.9] and the  $\mathbf{E} \times \mathbf{H}$  Poynting vector at a point may not physically correspond to the direction of energy flow. The direction of the  $\mathbf{E} \times \mathbf{H}$  vector also depends upon the phase difference between  $\mathbf{E}$  and  $\mathbf{H}$ : a good example of this occurs in the Group V quadrature resonance events where the phase-difference is  $90^\circ$  and there is no propagation. The Berkeley data used in these studies had the  $E_z$  component set to zero which would have affected the direction of the Poynting flux vector if that assumption was not valid. Another feature is that the signals that were studied were impulsive and therefore wideband so it is possible that if the Poynting vectors in all the bands were determined and vectorially added they would have yielded a field-aligned group velocity [Section 2.1.3]. However, despite these reservations it is not impossible that the observation of Poynting flux vectors oblique to field lines also imply PFI propagation across field lines but the balance of evidence from the IRIS riometer impulse timing [Figure 6.4], the substorm timing described in the next Chapter [Figure 6.1] and the ground map, allowing for errors in field line tracing, [Figure 6.5] is that the PFIs are field guided, with an oblique Poynting flux vector in the Pc5 band.

Figure 1.16 suggests that energy would propagate as Alfvén waves along field lines from the tail plasma sheet to the ionosphere, however the *primary* source that excites these waves may be a fast mode wave from the *tailquake* which then excites *secondary* field line oscillations. Whether the observed PFIs correspond to the *primary* or *secondary* signals in this model was not determined. Neither is it known exactly what the *tailquake* is, but possible mechanisms for the impulsive release of magnetic energy include magnetic annihilation, magnetic reconnection and plasma discharge as a result of the interruption of an inductive current path, whereby energy is stored in the associated magnetic field when the current is flowing and released when it is disrupted.

An alternative interpretation of the PFIs is that the magnetic field signal, which in the case of Group VI events was sometimes seen to have a dipolar signature [Figures A7.30, A7.31, and A7.32], was caused by relative motion between the Polar satellite and flux tubes or current sheets. The electric field associated with these structures is unclear but provided there is one, and that it is not parallel to the magnetic field, then a PFI would result. In particular if the electric field is normal to a current sheet on a geomagnetic shell the PFI vector would

point toroidally around the geomagnetic shell. Multiple PFIs could then be interpreted as Polar satellite crossing multiple current sheets of the kind that give rise to multiple auroral arcs [Figure 1.3] and the positively and negatively signed PFIs in Group III could be interpreted as Birkeland current sheets carrying current into and away from the ionosphere. However, the observation that needs to be explained is the temporal coincidence between PFIs and precipitation events which are described in the next Chapter and this favours the interpretation of PFIs as genuine electromagnetic wave propagation rather than current sheet crossings.

The association with ground events of  $+S_z$  PFIs when the Polar satellite was in the northern magnetosphere and of  $-S_z$  PFIs when it was in the southern hemisphere provide strong evidence for the source of PFIs near the geomagnetic equator. Since the Poynting flux vectors frequently had a sunward component when the Polar satellite was in the dusk sector the indications are that the source was located in the tail plasma sheet.

If the PFIs are interpreted in terms as propagating electromagnetic waves it means that impulsive disturbances take place in the magnetotail which transfer large amounts of [magnetic] energy into electromagnetic energy, as indicated by the Poynting flux values shown in Table 6.1.

Single PFIs were observed with Poynting fluxes up to  $350\mu\text{Wm}^{-2}$  [ $2.2 \times 10^{15} \text{eV s}^{-1} \text{m}^{-2}$ ]. If such a PFI transfers  $100\text{eV s}^{-1}$  to each electron in a plasma with a density of  $10^6 \text{m}^{-3}$  the PFI would be dissipated in a distance of  $3.4R_E$ . Then, if the PFI has a duration of 100s, the total heating of the electrons throughout this distance would be 10keV, which is of the order of the auroral electron energy and also the energy of electrons which give rise to spikes in IRIS riometer data. Furthermore, if there are several substorms a day and each has multiple PFIs associated with it then the total daily electron heating becomes a fraction of an MeV throughout this region. Thus it is possible that these PFIs could have an important role in increasing the energy of ions and electrons in the radiation belts. Since their propagation was often observed to be from the tail plasma sheet region they would be expected to preferentially heat the equatorial region of the radiation belts which is consistent with observations [Kivelson and Russell 1995].

Much theoretical work has been done on the subject of magnetic reconnection deep in the magnetotail and this is a physical process that has the potential to release both energetic waves and particles. The precise processes leading to the moment of initiation of magnetic reconnection are not known, although wave phenomena may have a role by disturbing the local fields and plasma. If this is the case then, once initiated, it is suggested that the

feedback necessary to sustain oscillatory magnetic reconnection in the magnetotail could be due to PFI reflection. The echo time for a PFI propagating at  $1000\text{kms}^{-1}$  to a boundary at a distance of  $20R_E$  would be 4 minutes and the Group IV event at 1818UT on 2003-11-09 described in Section 6.6.4 and depicted in Figure 6.14 showed multiple PFIs with a mean interval of 3.5 minutes [4.8 mHz].

The related topic of auroral optical modulation was studied whilst visiting the Sodankylä Geophysical Observatory in Finland. It has been consigned to future work in Section 9.2 because multiple PFIs and their ground signature in riometer and EISCAT data had not been identified at the time these measurements were made. However the measured frequencies shown in Table 9.1 were often a multiple of 1.6mHz so they may be related to the repetition frequency of multiple PFIs and it would be a straightforward study to confirm this.

The mechanism suggested for auroral modulation is that a PFI travelling along field lines towards the ionosphere [Figure 1.16] transfers energy to the electrons on the field lines. These electrons mirror bounce between the northern and southern ionospheres giving rise to an electron impulse response such that they do not all precipitate simultaneously. An observer therefore sees a gradual auroral intensification followed by a decay. The process repeats when the next PFI comes along. Effectively the precipitation process applies a low-pass transfer function to the PFI.

The Group I oscillations of electric field gave rise to a unique form of irregular oscillation of enhanced absorption in IRIS riometer keograms of which several examples were found. These electric field oscillations had field-aligned  $E_x$  and  $E_y$  components which mean that the electric field vector had a component that was oblique to the field lines. The  $E_z$  component along the field lines was not available because the Berkeley data was generated on the MHD assumption that this electric field strength component would be zero. A non-zero  $E_z$  component would mean that charged particles would be electrostatically accelerated along field lines and this could explain the precipitation and enhanced absorption in the riometer data. There was a suggestion that the number of oscillations of electric field in the magnetosphere matched the number of precipitation events but there was insufficient evidence to be sure of this. Transient electric field oscillations were often observed preceding a PFI [Figures A7.15, A7.19, A7.22, A7.34 and A7.37] so the deduction is that precipitation into the ionosphere over extended timescales can be associated with strong electric field oscillations alone, but often there are momentary magnetic field disturbances as well, which gives rise to magnetospheric PFIs and to precipitation spikes in ground riometer keograms.

## **7.0 Poynting flux impulses [PFIs] in the dusk sector auroral zone**

### **7.1 Introduction**

The observations described in this Chapter relate to sudden changes in ionospheric currents and hence ground magnetometer signatures at around the same time as electromagnetic Poynting flux impulses [PFIs] were observed far out in the dusk-midnight sector in Polar satellite data. Enhanced absorption spikes were also observed in IRIS riometer keograms near the time of these PFI events which implies that particle precipitation was present as well as oscillations in the electric and magnetic fields.

The connection between riometer spikes and substorms has been shown in a study that classified observations of 475 absorption spikes in the IRIS riometer between 1994 and 2001 into four types [Aminaei et al. 2006]. 80% of a particular class of spike that was followed by injection absorption was associated with the expansion phase. Interestingly, this study also showed that both the frequency of occurrence and the maximum intensity of absorption spikes was greatest in 1995 around the time of a solar minimum and least in 2001 around the time of a solar maximum.

Magnetospheric PFIs are associated here both with geomagnetic substorms in Section 7.2 and with a phenomena with a timescale an order of magnitude smaller referred to in Section 7.3 as opposing ground magnetometer deflections [OGMDs].

### **7.2 PFIs associated with geomagnetic substorms**

Some of the events identified and classified in Table 6.1 were observed at the same time as ground based observations of geomagnetic substorms. The reader is particularly referred back to Section 1.11.2 where some aspects of substorm onset are described. Two of the processes associated with substorm intensification are current disruption around 6 - 10  $R_E$  and magnetic reconnection in the NENL region around 20  $R_E$ . Although the transfer of magnetic potential energy to kinetic energy of charged particles is involved it is not known at the time of writing whether NENL magnetic reconnection processes precede [Baker 1996] or follow, current disruption [Lui 1996]. As the real-time movie in this thesis shows, the timescales for processes to be communicated between these regions by Alfvén waves is of the order of seconds rather than minutes so it is suggested by the author that the actual mechanism involves a mutual interaction. Both these processes could release the electromagnetic oscillations which give rise to the Poynting flux impulses that were detected.

Date Group Figure	IMAGE	Poynting flux			$E_x:B_y$ kms <sup>-1</sup>	IRIS	IRIS		
	onset	components $\mu\text{Wm}^{-2}$				onset	peak	dB geo. lat.	
	UT	UT	$S_x$	$S_y$	$S_z$	UT	UT		
2002-10-10 III A7.6	2302	2301	+15	-5	+15	4000	2312	2233	1.2 69°N
	MUO	2303	-20	+20	-15				
		<b>2305</b>	<b>-20</b>	<b>-12</b>	<b>+31</b>				
2002-11-22 III A7.8	1710	1711	+10	-5	+19	1600	1711	1719	2.2 68.6°N
	MAS	1716	0	0	+20				
		<b>1719</b>	<b>0</b>	<b>+32</b>	<b>-22</b>				
2003-09-26 III A7.9		2033	-3	-12	-10	3000	2038	2039	2.0 69.8°N
	2037	<b>2035</b>	<b>0</b>	<b>+15</b>	<b>+10</b>				
	BJN	2038	+5	-5	-6				
2003-11-12 III A7.10	1853	1857	0	-10	+16	1500	1856	1902	1.8 68.5°N
	MUO	1858	-70	+25	-40				
		1859	<b>+70</b>	<b>+80</b>	<b>+45</b>				
2002-10-17 IV A7.13	2212	2212	0	+120	+180	2100	2243	2248	1.2 68.9°N
	SOR	<b>2216</b>	<b>20</b>	<b>-40</b>	<b>+350</b>	3000			
2003-10-16 IV A7.15		2016	-10	+50	-50	6000	-	-	-
	2022	<b>2019</b>	<b>0</b>	<b>-30</b>	<b>-85</b>	3200			
	SOR	2024	-5	+7	-25	2500			
2003-11-09 IV A7.16	1819	1818	0	0	+18	200	1819	1821	6.0 69.6°N
	SOR	1820	0	-20	+20				
		<b>1821</b>	<b>-38</b>	<b>-20</b>	<b>-39</b>				
2003-10-19 V + VI A7.22	2121	2122	-8	+40	-115	3600	2122	2126	1.0 68°N
SOR									
2002-09-11 VI A7.29	2256	2255	-45	40	+68	3600	2255	2259	0.6 68.9°N
SOR									
2002-10-03 VI A7.30	2232	2231	15	-1	-3	1200	2234	2247	1.6 69°N
MUO									
2002-10-20 VI A7.31	2144	2144	+1	+5	+35	2000	2140	2141	0.7 70°N
BJN									

**Table 7.1 Events with ground substorm signatures**

The strongest PFIs in a set are highlighted in red

### 7.2.1 Events with substorm signatures

Current disruption across the tail diverts current along field lines into and out of the auroral ionosphere and the circuit is completed through the ionosphere in the form of an auroral electrojet with an order of magnitude of a million ampères. This circuit is known as a substorm current wedge [Figure 1.13] and the X [or H] component magnetograms then show a rapid decrease due to the increasing westward flowing ionospheric electrojet currents.

Table 7.1 gives a summary of the eleven magnetospheric observations when the Polar satellite field-line trace was between Finland and Greenland during the Autumn seasons in 2002 and 2003 and when a substorm bay was observed in IMAGE magnetograms. These form a subset of the thirty-nine events in Table 6.1. There were four PFIs in Group VI that provided an unambiguous reference to compare to substorm onset as defined by a change of gradient in IMAGE magnetogram data prior to the main expansion phase. For the other seven events in Groups III and IV either the initial PFI or the strongest PFI could be taken as the reference. In Figure 7.1 the substorm onset was plotted relative to the initial impulse for Groups III and IV. It can be seen that in nine out of the eleven observations the substorm onset in IMAGE magnetograms was within  $\pm 1$  minute of the magnetospheric PFI .

Substorm onset relative to magnetospheric Poynting flux impulses

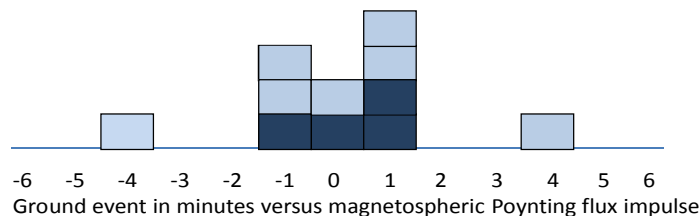


**Figure 7.1 Substorm onset times relative to Poynting flux impulses**

In Groups III and IV [light blue] the time of the initial PFI was taken as the reference. In Group VI [dark blue] there was no ambiguity.

A description of a substorm onset that was coincident with a single Group VI PFI was given in Section 6.6.5 where it was shown that quadrature resonance occurred during the substorm expansion phase. As shown in Table 7.1 this, together with the other examples from Group VI, where a single impulse was coincidence with the onset of a substorm can be seen in the plots in Figures A7.22, A7.29, A7.30 and A7.31. Examples where double or triple

PFI s were detected coincident with the onset of a substorm can be seen in Figures A7.6 and A7.9 [Group III] and in Figures A7.13 A7.15 and A7.16 [Group IV]. Also, in some cases, further PFI s were observed during the substorm, of which the event of 2003-11-09 [Figure A7.16] which is discussed in Section 7.6.4 is a particularly good example. Other examples are shown in Figures A7.8, A7.9, A7.15 and the first of these is described below.

### 7.2.2 Substorm at 1710UT on 2002-11-22

Figure A7.8 shows two  $+S_2$  PFI s at 1711UT and 1716UT followed by a stronger  $-S_2$  impulse at 1719UT. The IMAGE magnetograms show that substorm onset began at lower latitudes and propagated to higher latitudes, suggesting that current was being switched into the ionosphere sequentially from inner field lines to outer field lines. The first indication of an impending substorm was a change of gradient at SOR and MAS at 1710UT, although the main expansion phase did not begin until 1716UT when an OGMD event was observed between ground magnetometers PEL and OUJ.

The Poynting flux vector quiver plots in Figure 7.2 show that whilst the first two  $+S_2$  PFI s were propagating in the GSE/GSM  $+x$  direction across the Polar satellite at  $-4.3R_E$  the strongest PFI at 1719UT was propagating tailward. A possible explanation is that the second of these initial earthward impulses was being reflected from the dayside magnetosphere boundary such as the magnetopause or the bow shock. The E:B ratio suggests that the

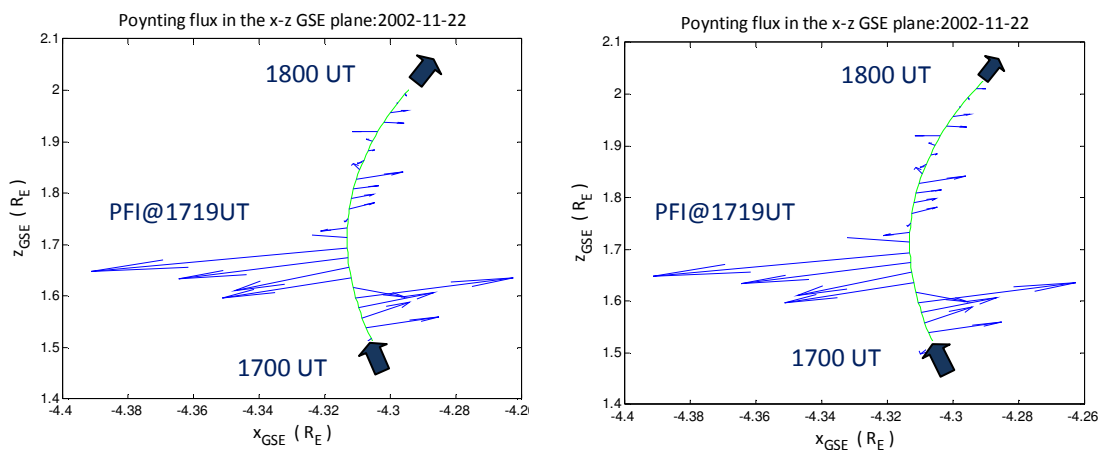


**Figure 7.2 Poynting vector quiver plot 1700 - 1800UT on 2002-11-22**

One hour of low-pass filtered Poynting flux vectors projected onto the GSE x-y and x-z planes showing the sunward PFI components at 1711UT and 1716UT and the anti-sunward PFI at 1719UT. The green line shows the Polar satellite track and the heavy arrows the satellite positions at 1700UT and 1800UT. Poynting flux vectors are uncalibrated.

propagation speed for the  $-S_2$  impulse was around  $1600\text{kms}^{-1}$ , which would give a round-trip time of 2-3 minutes from the Polar satellite to a dayside reflection boundary and back, and the observations showed a possible three minute echo. This is only a preliminary observation, but if this interpretation is correct then these impulses may have the ability to provide information of the dimensions of the magnetospheric cavity analogous to radar signals. The IRIS riometer keogram indicated an increase in absorption from 1711UT onwards, coincident with the time of the first PFI and the initial substorm onset. However the main riometer absorption spike at 1719UT was actually coincident with the  $-S_2$  impulse

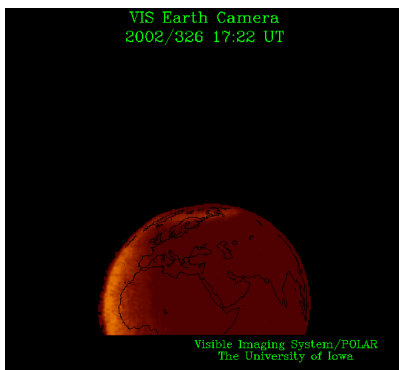


**Figure 7.3**

**Aurora at 1722UT on 2002-11-22**

Polar satellite visible light image of the aurora over Northern Finland at the time of the substorm expansion phase

[University of Iowa]

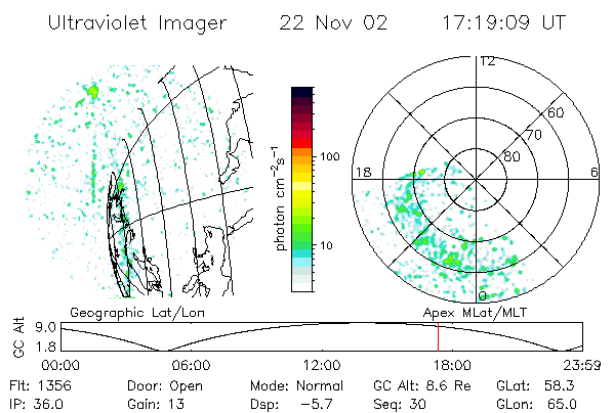


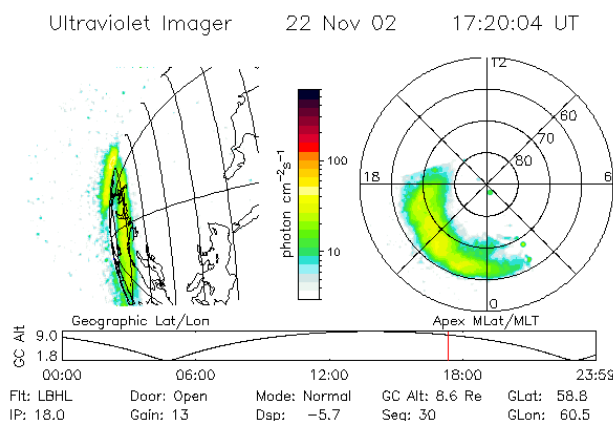
**Figure 7.4**

**Polar satellite UVI observations**

These two images were taken 55s apart and show the sudden brightening of the UV aurora around 1720UT on 2002-11-22.

The UV photon count on a polar plot of magnetic latitude against magnetic local time showed that the region of greatest UV light came from between  $19^\circ\text{E}$  and  $109^\circ\text{E}$ , which was over Finland and Russia.

[University of Iowa]



described above. The IRIS riometer was  $1^{\circ}\text{N}$  and  $4^{\circ}\text{E}$  of the Polar satellite field-line trace at this time.

The image shown in Figure 7.3 was taken in visible light by the Polar VIS instrument at 1722UT during the substorm expansion phase and showed an auroral substorm over Iceland, Finland and Russia. The sudden enhancement in ultraviolet auroral emissions is illustrated in the two consecutive images shown in Figure 7.4 taken by the Polar satellite UVI instrument at 1719:09 UT and then, 55 seconds later, at 1720:04 UT.

In the absence of any further data the median of these times at 1719:36UT was taken as an estimate of the onset of the UV light emitting precipitation into the ionosphere. Peak absorption in the IRIS riometer keogram also occurred at 1719UT and as mentioned above this was also the time of the strong  $-S_z$  PFI.

### **7.3 PFIs and opposing ground magnetometer deflection [OGMD] events**

In a geomagnetic substorm the westwards electrojet gives rise to a negative deflection in ground magnetometers over timescales of typically several tens of minutes. Another class of event was observed in these studies with a timescale an order of magnitude shorter. It was denoted *opposing ground magnetometer deflection* [OGMD] and given the symbol  $\updownarrow$  because X component magnetogram stackplots showed a negative deflection northwards of a particular latitude, and a positive deflection southwards of that latitude, which typically only lasted for around two minutes.

An example of an OGMD signal on 2003-11-22 between the SAMNET ground magnetometers HEL and FAR is shown in Figure 7.5. This event is further described and mapped below in Section 7.3.4. The ground signal implies a reversal in the ionospheric currents at a particular latitude. It is therefore reasoned that in-between the negative and positive deflecting magnetometers there must be a latitude at which the ground magnetometer deflection is zero, if only there had been a magnetometer there to observe it. These observations could be explained by electron precipitation in the form of an upward Birkeland current sheet with conventional Pederson currents flowing towards the current sheet from both the north and the south. The direction of Hall electric field, and hence the Hall current, to the north of the current sheet would be westwards [Section 1.13.1] and the converse would be true to the south of the current sheet, in agreement with the observations of ground magnetometer deflection.

Another possible explanation is that the ionospheric current system is caused by a reversal in the direction of magnetospheric convection which drives ionospheric currents which

reverse sign. When these currents become large ionospheric precipitation results from the upward field-aligned current along the shear line [Chui and Cornwall 1980].

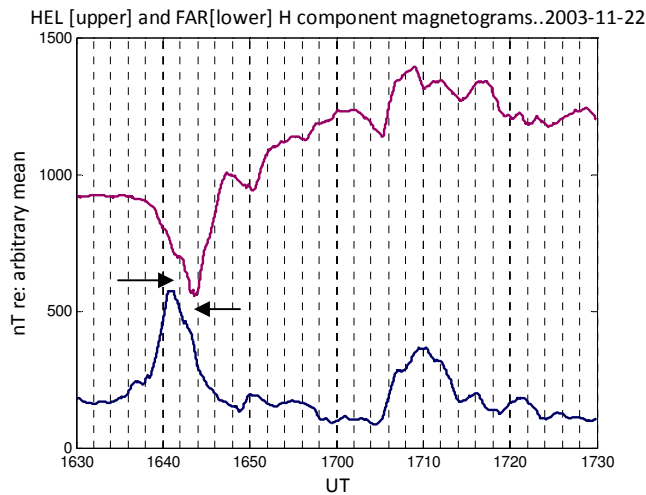


**Figure 7.5 HEL-FAR OGMD event at 1642UT on 2003-11-22**

Opposing H component ground magnetometer deflections suggest precipitation midway between the Faroe and Iceland stations. Arrows show that a time delay of  $\sim 3$  minutes was associated with the sequential polewards initiation of the ionospheric current system

By mapping this current sheet out to the magnetosphere it is possible to estimate the physical dimensions of the precipitation source.

An ionospheric current vortex around the precipitation can explain the observations at any one north-south chain of ground magnetometers. However it should be noted that in some cases the same ground signal appeared at around the same time over a very wide range of longitudes, as illustrated by the maps in Figures 7.8 and 7.9, suggesting an extended current sheet, similar to that of a quiet auroral arc. As with the onset of substorms, PFIs were often detected in Polar satellite data and absorption spikes were seen in the IRIS riometer keograms at the same time as these OGMD events.

### 7.3.1 Observations of opposing ground magnetometer deflections

Table 7.2 gives a summary of the eleven OGMD events observed when the Polar satellite field-line trace was between Finland and Greenland during the Autumn seasons in 2002 and 2003. These events are a subset of those in Table 6.1. Six of these events were classified magnetospherically as Group III, three as Group IV and two as Group VI.

Date Group Figure	Poynting flux UT	IMAGE UT	Iceland UT	Greenland UT
2002-10-19 III A7.7	1926 <b>1928</b> 1934 1936	↕1938 BJN-MUO	No signal	
2002-11-22 III A7.8	1711 1716 <b>1719</b>	↕1716 PEL-OIJ 66.1°N 25.1°E	↓1721SCO- ↑↓1721HEL 66.4°N -21.1°E	1700-1724 ↑FHB 200nT
2003-09-26 III A7.9	2033 <b>2035</b> 2038	↕2038 BJN-SOR 71.5°N 21.5°E	2034 North of HEL	No data
2003-11-12 III A7.10	1857 1858 1859 <b>1900</b> 1901	↕1900 MUO-PEL 69.5°N 23.7°E	1901HEL- 1902FAR 62.4°N -9.9°E	1904 FHB - 1250nT 1903 NAQ - 500nT ~59°N ~ -45.4°E
2003-11-22 III A7.11	1638 <b>1641</b> 1643 1651	↕1638 OUJ-HAN 64.1°N 27.1°E	1643HEL- 1641FAR 63.0°N -19.3°E	1638 ↑↓50nT NAQ 61.1°N -45.4°E
2003-12-15 III A7.12	<b>1650</b> 1652	↕1651		
2003-10-27 IV A7.14	<b>1806</b> 1808	↕1805	No signal	
2003-11-09 IV A7.16	1818 1820 <b>1821</b> 1822 1830	↕1822  ↕1835	No signal No signal	
2003-11-15 IV A7.17	1634 <b>1639</b>	↕1630 66.3°N 24.9°E	1633 200nT HEL No signal SCO	1618-1628 FHB ↓-500nT
2003-10-03 VI A7.34	<b>1817</b>	↕1811 BJN-SOR		
2003-12-12 VI A7.38	<b>1722</b>	↕1723		

**Table 7.2 Observations of OGMD events**

The strongest PFIs in a set are highlighted in red. OGMD events are denoted by ↕

Thus nine out of the eleven OGMD events involved multiple PFIs which inevitably makes the temporal association ambiguous.

Figure 7.6 shows the time of the OGMD events relative to the time of the strongest PFI for nine of the eleven events were within  $\pm 6$  minutes. It would often have been possible to pick one of the multiple PFIs nearer in time but this was felt to be too artificial. The temporal association between magnetospheric and terrestrial events is within  $\pm 1$  minute in five out of the eleven observations using this criteria.

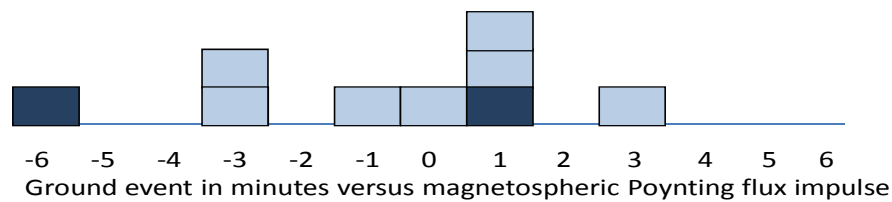


**Figure 7.6** OGMD times relative to Poynting flux impulses

Group III and IV events where there was a possible ambiguity in the reference time are shown in light blue and Group VI events, where there is no ambiguity, in dark blue.

### 7.3.2 Ionospheric mapping of the null deflection

In the two highlighted events in Table 7.2 a clear detection was made by all three north-south chains of ground magnetometers described below and this made it possible to map the signals. Where an OGMD signal was detected in three or more ground magnetometers along a north-south chain a cubic spline interpolation was used to estimate this latitude, but where there was a signal in only two ground magnetometers, as was sometimes the case with the widely spaced Iceland chain observations, linear interpolation was used. Once the latitude had been determined by either of these methods the longitude was estimated by linear interpolation between the same ground magnetometers.

An example of a cubic spline interpolation on X component data from the IMAGE ground magnetometer chain for the event at 1638UT on 2003-11-22 is shown in Figure 7.7. The geographic latitude of zero deflection was estimated as 64.1°N and then using linear interpolation between two magnetometer longitudes the geographic longitude was estimated as 27.1°E. When computing these cubic splines it was sometimes found necessary to make allowance for the fact that the peak deflection was often delayed towards higher latitudes. When examining Greenland data there was sometimes a negative deflection in ground magnetometers GHB, FHB and NAQ, suggesting that the zero was further to the

south – for these purposes it would have been useful to have had magnetometer data from under the Atlantic Ocean to the south of Narsarsuaq . In Figure 7.7 the zero was located approximately  $4^{\circ}$  to the south of the ground magnetometer with the greatest negative deflection. This empirical result could be used to provide a rough estimate of the latitude of a zero deflection to the south of Greenland where there is no ground magnetometer coverage.

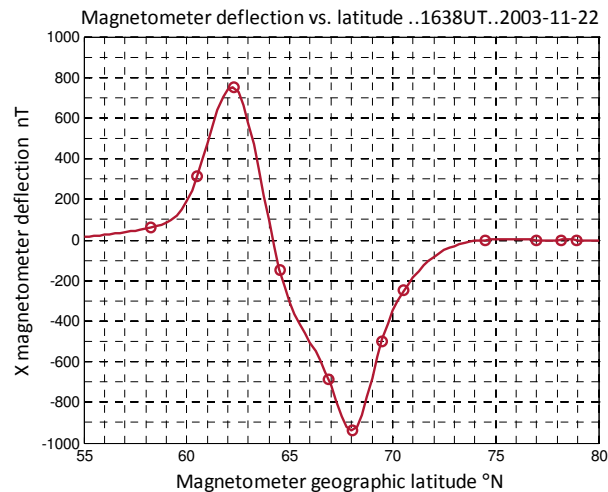


**Figure 7.7** OGMD event at 1638UT on 2003-11-22.

Graph of IMAGE ground magnetometer deflection [ nT ] versus IMAGE ground magnetometer geographic latitude. The latitude of zero deflection was estimated by fitting a cubic spline to the observations.

In order to map the event more than one pair of OGMDs was required and this in turn required the detection of the event by additional pairs of ground magnetometers. It was possible to construct a second magnetometer chain aligned approximately northwest-southeast geomagnetically from the SAMNET ground magnetometers HEL and FAR, together with the Greenland east coast magnetometers, and this is referred to here as the *Iceland chain*. A third ground magnetometer chain that was used in this study was the Greenland west coast chain referred to as simply the Greenland chain<sup>(1)</sup>. A MATLAB program was written to map the estimated ionospheric coordinates of the OGMD events and to display a cubic spline interpolation through them on a conic projection of part of the northern hemisphere.

---

<sup>(1)</sup> Dr Hans Gleisner at the DMI in Copenhagen kindly provided all the Greenland ground magnetometer data.

### 7.3.3 OGMD event at 1900UT on 2003-11-12

This event was observed across Finland, Iceland, Greenland and Canada over a longitude range of  $\sim 120^\circ$  and a map of the event is shown in Figure 7.8. The IMAGE magnetograms, Poynting flux oscillations and IRIS riometer keogram are shown in Figure A7.10. Ground magnetometers showed that the OGMD event was preceded by a substorm onset which occurred at 1852UT at PEL and progressively later towards higher latitudes, with onset at SOR at 1854UT.

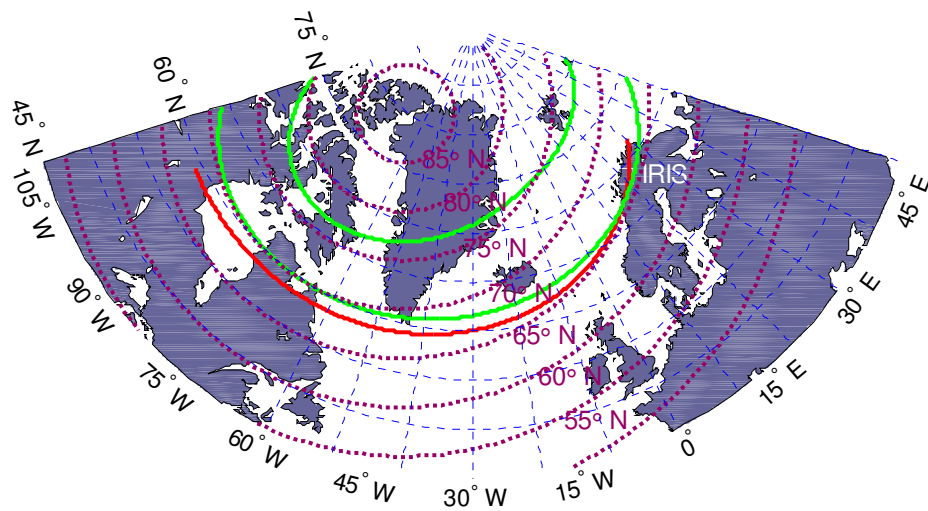


**Figure 7.8** Map of the OGMD event at 1900UT on 2003-11-12

The orange line shows the cubic spline interpolation on the estimated positions of the zero deflections in ground magnetometer data and the green lines the statistical boundaries of the auroral oval as described in the text.

The Poynting flux pulse comprised three cycles of oscillations and was classified as Group III. The first  $+S_z$  impulse occurred at 1857UT, three minutes after the substorm onset at SOR. The OGMD event occurred seven minutes after the substorm onset at MUO, and was coincident with the strongest  $-S_z$  Poynting flux impulse at 1900UT. Enhanced absorption in the IRIS riometer began at 1856UT and was probably related to precipitation during the expansion phase of the substorm. It persisted until around 1920UT, well into the substorm recovery phase. Any enhanced absorption due to the OGMD event was superimposed on this substorm background and may have been the 1.8dB peak that was observed at 1901UT, one minute after the  $-S_z$  Poynting flux impulse at 1900UT. The Polar satellite field line trace was  $4^\circ$  to the south and  $21^\circ$  to the west of the IRIS riometer but at the same geomagnetic latitude as the IRIS riometer.

The time sequence of the ground magnetometer OGMD events was 1900UT [MAS], 1901UT [HEL]-1902UT [FAR], 1903UT [NAQ]-1904UT [FHB] and 1906UT GIL - 1909UT [ESK].

This sequence clearly indicated that the event propagated from east to west across the ionosphere. In the magnetotail this corresponded to an event propagating from dawn towards dusk [assuming equal propagation times to the Earth].

A time difference of 9 minutes between the extremes of longitude of  $120^\circ$  at  $67^\circ\text{N}$  gave an estimate of the ionospheric phase speed as  $10\text{kms}^{-1}$ . This ionospheric phase speed estimate was similar to ionospheric phase speeds measured in the other studies that were referred to in Section 4.6.1 in connection with ULF waves.

The interpolated orange locus in Figure 7.8 may correspond to the intersection of a magnetospheric current sheet with the ionosphere and is described here as the ionospheric transcription line since it maps out to a magnetospheric source of charged particles such as those from a magnetic reconnection X-line. It tracks between geomagnetic parallels  $66^\circ\text{N}$  to  $68^\circ\text{N}$  [shown in purple in Figure 7.8] which for a dipole field would imply that the associated current sheet was on a geomagnetic shell of  $L=6.6$ . Multiplying the ionospheric phase speed by the L shell number would give a dawn-dusk magnetospheric propagation of  $66\text{ kms}^{-1}$  assuming a dipolar field but this is an underestimate as the magnetic field is highly distended in the tail.

Statistical limits of the auroral oval [Liou et al. 1997] derived from some 17,000 images of Lyman-Birge-Hopfield 170nm emissions recorded by the Polar satellite UVI detector have been added to Figure 7.8 as green lines. It can be seen that this OGMD event was near the lower boundary of the statistical auroral oval.

#### **7.3.4 OGMD event at 1638UT on 2003-11-22**

The reader is referred back to Section 6.6.3, Figures 6.11 and 6.12 and to Figure A7.11 for a description of the Poynting flux signals at the time of this particular OGMD event.

The OGMD at 1638UT in the IMAGE magnetograms was coincident with the first Poynting flux impulse. As in the above event on 2003-11-12 the OGMD propagated from east to west and Figure 7.5 showed that it reached the Iceland chain SAMNET magnetometers FAR and HEL between 1641UT and 1643UT. There was also a negative deflection at the southernmost Greenland ground magnetometer NAQ. Mapping of the event is shown in Figure 7.9 where the ionospheric transcription of the event was estimated to extend over a longitude of  $\sim 70^\circ$  in the ionosphere. Again, the event was observed near the southern

statistical boundary of the auroral oval, but from the available data, it although it did not follow the geomagnetic field lines as closely as in the previous event.

An east-west ionospheric phase speed of  $15\text{kms}^{-1}$  was estimated from the IMAGE OIJ-HAN OGMD at 1638UT and the FAR-HEL OGMD at 1642UT.

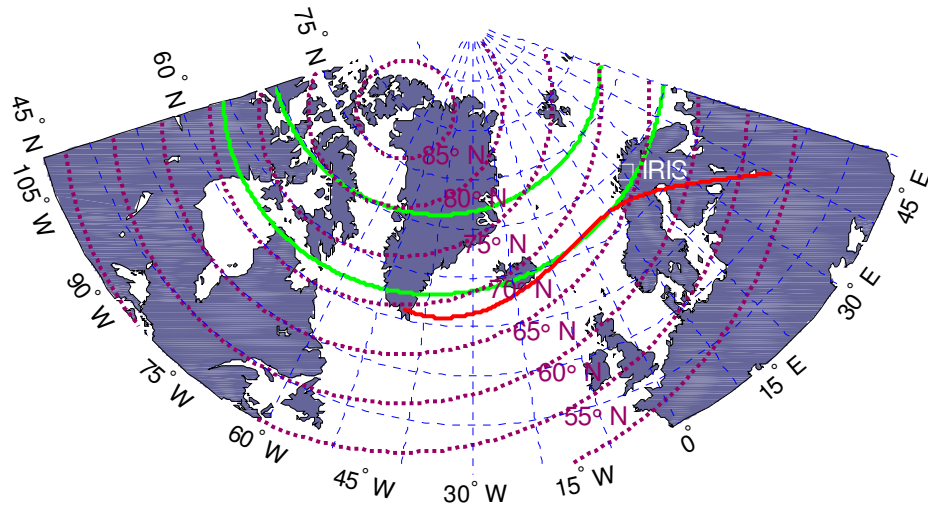


**Figure 7.9 Map of the OGMD event at 1638UT on 2003-11-22**

The orange line shows the cubic spline interpolation on the estimated positions of the zero deflections in ground magnetometer data and the green lines the statistical boundaries of the auroral oval as described in the text.

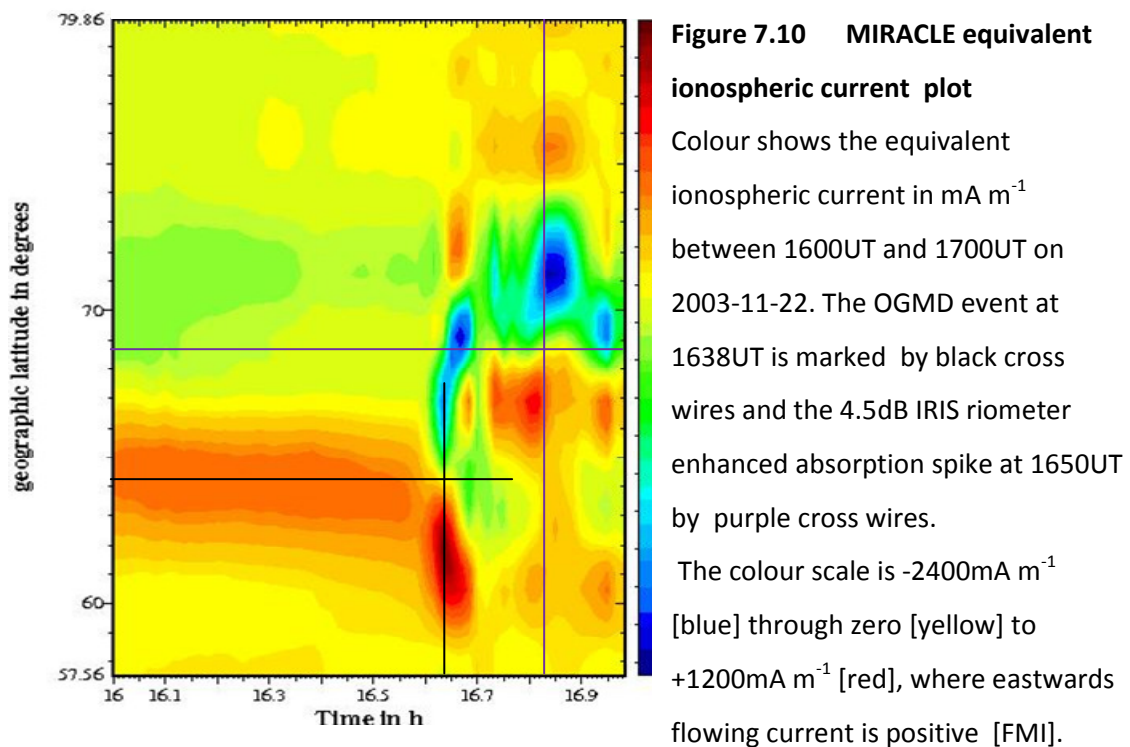
The MIRACLE data analysis software was used to estimate the equivalent ionospheric currents at an altitude of 100km that would give rise to the ground signal observed in the IMAGE magnetometers. The results are plotted in various ways, including the plots of geographic latitude versus time and of integrated eastwards and westwards ionospheric current densities and equivalent east and west current versus time.

Figure 7.10 shows the eastwards [red] and westwards [blue] integrated ionospheric currents flowing over a latitude range of the order of  $5^\circ$ , with the peak current densities approximately  $\pm 3^\circ$  in latitude either side of the null. Although they only flowed for a few minutes the equivalent Hall currents during this event were  $\sim 0.5\text{MA}$  eastwards and  $\sim 1\text{MA}$  westwards respectively. This is understood to be of the same order of magnitude as the auroral electrojet.

A close agreement was found between the latitude of zero deflection estimated from a cubic spline interpolation on IMAGE magnetometer data [ $64.1^\circ\text{N}$ ] and the latitude for which the MIRACLE software gave the equivalent ionospheric current density as zero [ $64.2^\circ\text{N}$ ].

There is also good agreement between the latitude of the peak absorption spike in the IRIS riometer keogram at 1650UT [69.0°N] and the latitude for which the MIRACLE software gave the equivalent ionospheric current density as zero [68.8°N].

Four enhanced absorption events are visible in the IRIS riometer keogram [Figure 6.12], of which the first peak of 4dB at 1640UT was two minutes after the IMAGE OIJ-HAN OGMD. At the time of these observations the Polar satellite field-line trace was at the same latitude as the IRIS riometer and only 3° east of it.



#### 7.4 Discussion and conclusions

Enhanced absorption in IRIS riometer keograms, substorm expansion, aurora and OGMD events all involve the precipitation of charged particles into the ionosphere. Observations were made over a sector of the Polar satellite orbit with field-line mapping between Finland and Greenland, but it seems possible that events associated with precipitation over Finland can be detected by their Poynting flux signature over a far wider sector of the magnetosphere by any satellite with electric and magnetic field sensors.

Changes in ground magnetograms reflect changes in ionospheric currents, and this in turn implies a change in the supply of charge or in the EMF that drives these currents. One way that the supply of charge to the ionosphere can change is by precipitation from the magnetosphere along field lines.

Substorm onset can be marked by Pi2 oscillations and by a change of gradient in H component ground magnetograms as east-west Hall currents are switched on in the ionosphere. In these studies the change of gradient was used as the marker of substorm onset. An important point is that the onset of substorm precipitation occurs first at lower latitude then propagates towards higher latitudes. As an example of this, Figure A7.6 shows a twelve minute delay between substorm onsets at IMAGE ground magnetometers MUO at 68.0°N and BJN at 74.5°N. This range in the onset time is significantly longer than the  $\pm 1$  minute accuracy with which PFIs and substorm onsets were determined in this study. It was found [in nine times out of eleven] that, provided the time of substorm onset was taken at the geomagnetic latitude of the Polar satellite field line trace, there was agreement within  $\pm 1$  minute between the time of substorm onset and the time of the magnetospheric PFI. These substorm studies therefore suggest that PFIs mark the time when this precipitation is switched onto the Polar satellite field lines. Switching in this context refers to the redirection of charged particles towards the Earth.

If even more accurate measurements are required then the association of magnetospheric PFIs with enhanced absorption in IRIS riometer keograms described in Chapter 6 provides a way of overcoming the limitations of field line tracing, since the riometer event gives the precipitation latitude and both the keogram and the magnetogram from the same site give the time of onset of precipitation. In fact the reverse approach, using PFIs to mark the satellite location and an imaging riometer to detect the precipitation location provides a precise way of verifying the accuracy of field line tracing.

Eleven examples were found of a class of terrestrial phenomena with a magnetospheric counterpart referred to here as opposing ground magnetometer deflections [OGMDs] which appeared to be due to precipitation into the ionosphere at a particular latitude. They had two interesting properties: firstly this latitude could be estimated, which meant that they could be mapped, and secondly their peak time of occurrence could be estimated, which meant they could be tracked.

In the small sample detected they were more often associated with multiple PFIs which leads to ambiguity in relating their times to PFIs. However what was remarkable was that the Polar satellite data did show PFIs within  $\pm 6$  minutes of OGMD events, even though the satellite field line trace was generally at a different geomagnetic latitude. This would not

have been expected on the basis of the substorm observations, where the PFI marked the time the charged particles were redirected onto the Polar satellite field line.

In two of the examples shown here, the OGMD precipitation extended over longitudes of  $120^\circ$  and  $75^\circ$  at auroral latitudes. Furthermore the time of these OGMD events showed that they propagated from east to west across the ionosphere. The estimates of ionospheric propagation speed were  $10\text{kms}^{-1}$  and  $15\text{kms}^{-1}$  which is in the same region as the ionospheric phase speeds that have been estimated for ULF waves [Chapter 4]. If these OGMD distances and times are projected out into the magnetosphere on their geomagnetic shells it suggests an [underestimated] dawn to dusk propagation of magnetospheric current switching at a speed of  $\sim 100\text{kms}^{-1}$ .

Whereas the OGMD observations suggested that the current switching sequence was from dawn to dusk across the magnetosphere the substorm onsets were always from low to high geomagnetic latitudes. This low to high latitude effect could be explained if current was switched at the same time at all latitudes, but then reached the Earth earlier because of the shorter distance along these field lines. Another explanation is that the switching actually occurred first at low latitudes and then propagated tailwards and hence to higher geomagnetic latitudes. In this scenario both the switching propagation and the longer field line propagation would contribute to the observed time delay between low and high latitudes. Yet another possibility is that the switching sequence propagated from the tail but the particle propagation delay along the longer field lines was the dominant effect.

This study does not distinguish between these ideas but it does show that the time of the PFI is closely linked to the time of particle precipitation which means that PFIs are initiated at the time and the magnetospheric location where the current is switched onto a particular field line.

Further studies are needed, but it is suggested on the basis of the substorm and OGMD events that the switching process does not occur simultaneously everywhere but propagates from east to west and from south to north. This could happen if the sequential switching onto field lines propagated away from a point on the dawn side of the magnetosphere. These observations also have implications for predicting space weather since a magnetospheric PFI signature could imply an impending substorm or OGMD event and also give the latitude of that precipitation into the ionosphere.

## 8.0 Polar satellite observations of Group V quadrature events

### 8.1 Introduction

The subject of ULF resonance was introduced in Section 2.4. It can arise when Alfvén shear waves are guided by the magnetic field in the same way as displacements are guided along a guitar string. The fundamental [first harmonic] period of the resonance is the time it takes the wave to propagate from one reflecting boundary to the other and back again. Since the Alfvén speed depends upon both the local magnetic field strength and the local plasma density it varies along the field line, and since the frequency is constant the wavelength also varies with location. It was shown in Section 2.5.5 that a phase change by  $\pi$  in the electric field as a result of reflection by a perfectly conducting boundary would result in a phase difference of  $\pi/2$  between the electric and magnetic field oscillations in the resulting standing wave. This is referred to here as a quadrature oscillation and observations of the phenomena in Polar satellite data were classified as magnetospheric Group V in Section 6.2. Oscillations between ionospheres are termed field line resonances [FLRs] but it may be that one of the boundaries is an ionosphere and the other a structure in the magnetotail giving rise to a tail line resonance [TLR]. Because of this possibility the events described here are just referred to as Group V quadrature oscillations.

The quadrature nature of the electric and magnetic field oscillations gives rise to a theoretical Poynting flux signature which is a symmetrical oscillation about zero displacement at twice the frequency of the electric and magnetic fields. Because the Poynting flux signal responds to the temporal coherence between the electric and magnetic fields it can sometimes, but not always, provide a more accurate way of determining the frequency of the resonance than estimating the frequency of the electric and magnetic fields alone. Once this frequency is known the phase-difference between the electric and magnetic fields can be estimated and this was done here by cross-spectral analysis. In practice the reflection phase changes may not be exactly  $\pi$  and the reflection coefficients may not be unity. However despite these natural sources of variability the average magnitude of the phase difference for these eleven observations is  $93^\circ$ , which is close to quadrature.

A question that arises in connection with resonances is how they are initiated. In one scenario *compressional impulses* propagate across the field lines and initiate resonance at their own natural frequency, analogous to strumming a glissando on a harp. This gives rise

to a pattern of increasing resonant frequency with decreasing geomagnetic latitude. There is also a progressive time-delay with latitude caused by a combination of the moment of initiation and the time it takes for constructive interference to build up between waves propagating in both directions along increasingly long field lines.

In another scenario a *continuous compression wave* forces all the field lines to oscillate so that resonance is only strong on the field line that has the same natural frequency as the incoming wave. Forced oscillation [Jones 1965] then predicts a phase change of  $\pi$  between low and high latitudes and a phase change of  $\pi/2$  at the resonant latitude compared to a low latitude reference.

It was always found that the magnetic field led the electric field when the Polar satellite was in the southern hemisphere and the electric field led the magnetic field when it was in the northern hemisphere.

Two examples of magnetospheric quadrature resonance were observed on 2003-12-15 [Figures A7.27 and A7.28] that were coincident with large amplitude oscillations in ground magnetograms and these may have been initiated by compression wave pulses that also reached the ionosphere. There were also three examples encountered where the ground magnetogram signal could be described as a distinctive V-shaped notch [Figures A7.19, A7.23 and A7.24] which had all the characteristics of impulsive initiation.

It was thought that the PFIs that were studied in Chapter 8 in connection with substorm activity and OGMD events could give rise to quadrature oscillations and two examples were observed on 2003-10-19 [Figure A7.22] and on 2003-11-25 [Figure A7.37] when this appeared to happen. It is possible that many of these observations of quadrature oscillation were either initiated by *tailquakes* or by currents flowing along flux tubes.

Another question about quadrature oscillations is their role in ionospheric precipitation. Alfvén shear waves do not have a field-aligned component of electric field which would drive a current, but the existence of other phenomena that give rise to a field-aligned component of electric field cannot be ruled out, since no information was available in the Berkeley data regarding the  $E_z$  component of electric field. Three of the events described here [Figures A7.18, A7.21 and A7.22] were coincident with the expansion phase of substorms, where enhanced precipitation resulted in westward substorm electrojets through the ionosphere. The inference is that these resonating field lines were carrying a field-aligned current and that there probably was a non-zero  $E_z$  component.

## 8.2 Observations of Group V quadrature oscillations

Figures A7.18 to A7.28 in Appendix 7 show the spectra of the electric field, magnetic field and Poynting flux, the Polar satellite time-series data and the ground magnetograms and the accompanying notes provide a summary of each resonance event.

Column 1 in Table 8.1 shows the times when quadrature oscillations were detected during the transits of the Polar satellite field line trace between Finland and Greenland in the Autumn seasons of 2002 and 2003. These eleven observations are a subset of those in Table 6.1. The annotation SM [NM] means that the Polar satellite was in the southern [northern] magnetosphere when the resonance was observed.

Column 2 in Table 8.1 indicates the start and end of the resonance in the Polar satellite data. The average duration of a resonance was 17 minutes, although it is possible that the Polar satellite was only able to observe the resonance whilst its orbit crossed the oscillating field lines. Counting the number of oscillations gives the average duration for these eleven observations as five cycles. Only the observation on 2003-10-10 [Figure A7.21] approximated an exponentially damped oscillation and a resonating pulse would be a more apt description for the seven observations on 2002-11-09 [Figure A7.19], 2002-12-24 [Figure A7.20], 2003-10-26 [Figure A7.23], 2003-11-09 [Figure A7.24], 2003-11-18 [Figure A7.25], 2003-11-25 [Figure A7.26] and 2003-12-15 [Figure A7.28]. The frequency of the Poynting flux oscillations during quadrature resonances was estimated from the spectra shown in Figures A7.18 to A7.28. Often the Poynting flux spectra had a well-defined peak from which the electric and magnetic field frequencies could be determined by dividing the  $S_z$  component of Poynting flux frequency by two. In the events studied here the  $E_x$  and  $B_y$  components were dominant which means that the magnetic field displacement was toroidal and the electric field displacement was poloidal. However the calculation of the  $S_z$  Poynting flux component also takes into account the information in the  $E_x B_y$  and  $E_y B_x$  components, which suggests that it may give a more reliable estimate of the resonant frequency than in the  $E_x$  and  $B_y$  components alone.

Column 3 in Table 8.1 shows the frequencies measured on Polar satellite data, the peak displacement and the phase-difference of the electric field relative to the magnetic field at the resonant frequency. The Poynting flux frequency ranged from 4.2mHz to 7.2mHz with an average of 5.3mHz. Dividing this by two meant that the average electric and magnetic field oscillation frequency for the Group V quadrature oscillations that were observed in this high latitude study was 2.6mHz.

C1	C2	C3	C4	C5	C6
Date Figure	Quadrature signal UT	Frequency Peak $\Delta\phi$	Geographic Polar trace at start and end of resonance	Ground magnetometer	Observations
2002-10-26 A7.18 SM	1746-1753	$S_z$ 4.2mHz $-150 \mu\text{Wm}^{-2}$ $\Delta\phi$ $-59^\circ$	73°N 35°E 72°N 30°E Barents Sea	BJN 74.5°N 19.2°E	Substorm 1746UT SOR
2002-11-09 A7.19 NM	1850-1916	$S_z$ 4.4mHz $6 \mu\text{Wm}^{-2}$ $\Delta\phi$ $94^\circ$	68°N 16°E 68°N 9°E Lofoten Islands	KIL 69.0°N 20.8°E	Notch 1853UT 2mHz SOR
2002-12-24 A7.20 NM	1830-1850	$S_z$ 4.4mHz $E_x$ 1.9mHz $-7 \mu\text{Wm}^{-2}$ $\Delta\phi$ $96^\circ$	65°N -34°E 64°N -40°E Greenland	AMK 65.6°N -37.6°E	1.7mHz AMK
2003-10-10 A7.21 NM	2134-2150	$S_z$ 4.4mHz $-7 \mu\text{Wm}^{-2}$ $\Delta\phi$ $90^\circ$	67°N -3°E 66°N -10°E Norwegian Sea	FAR 62.1°N -7.0°E	Substorm 2132UT BJN Pi2 SOR MAS
2003-10-19 A7.22 SM	2128-2150	$S_z$ 4.5mHz $E_x$ 2.8mHz $-50 \mu\text{Wm}^{-2}$ $\Delta\phi$ $-68^\circ$	65°N -23°E 63°N -29°E Iceland	HEL 63.8°N -20.6°E	Substorm 2121UT SOR Impulse2122 2.8mHz FAR
2003-10-26 A7.23 SM	1905-1925	$S_z$ 6.7mHz $4 \mu\text{Wm}^{-2}$ $\Delta\phi$ $-103^\circ$	70°N 6°E 69°N 3°E Norwegian Sea	SOR 70.5°N 22.2°E	Notch 1711UT 3.3mHz SOR
2003-11-09 A7.24 SM	1618-1746	$S_z$ 4.2mHz $-7 \mu\text{Wm}^{-2}$ $\Delta\phi$ $-93^\circ$	69°N 47°E 68°N 35°E Barents Sea	MAS 69.5°N 23.7°E	Notch 1628UT 2.1mHz MAS
2003-11-18 A7.25 SM	1844-1858	$S_z$ 6.7mHz $-16 \mu\text{Wm}^{-2}$ $\Delta\phi$ $-123^\circ$	68°N -15°E 67°N -18°E Greenland Sea	SCO 70.5°N -22.0°E	No Greenland data
2003-11-25 A7.26 SM	1722-1732	$S_z$ 6.7mHz $12 \mu\text{Wm}^{-2}$ $\Delta\phi$ $-80^\circ$	70°N 3°E 69°N -1°E Norwegian Sea	KIL 69.02°N 20.8°E	3mHz MUO
2003-12-15 A7.27 SM	1400-1410	$S_z$ 7.5mHz $E_x$ 3.5mHz $120 \mu\text{Wm}^{-2}$ $\Delta\phi$ $-119^\circ$	72°N 17°E Norwegian Sea	KIL 69.02°N 20.8°E	3.2mHz MAS MUO
2003-12-15 A7.28 SM	1458-1518	$S_z$ 7.2mHz $E_x$ 3.5mHz $5 \mu\text{Wm}^{-2}$ $\Delta\phi$ $-94^\circ$	73°N 18°E 71°N 14°E Barents Sea	SOR 70.5°N 22.2°E	3.5mHz SOR

**Table 8.1 Observations of Group V quadrature oscillations**

The columns are denoted C1 to C6. SM [NM] denotes the location of the Polar satellite in the southern [northern] magnetosphere. Locations of ground magnetometers are shown in green if they are within  $\pm 2^\circ$  of the Polar satellite field line trace.

A positive phase-difference meant that the electric field was leading the magnetic field. The magnitude of the phase difference varied between  $59^\circ$  and  $123^\circ$  with an average of  $93^\circ$  and Figure 8.1 shows this variability on a phasor diagram. Because the strength of the Poynting flux varied by two orders of magnitude the logarithm to base 10 of the resonant amplitude was plotted radially.

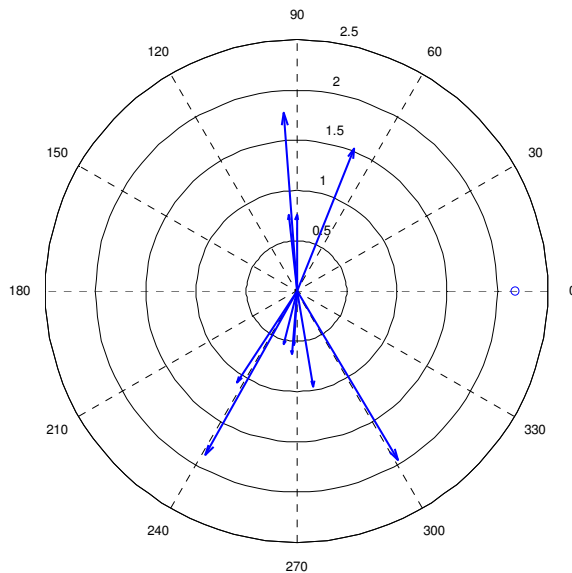


**Figure 8.1**

**Quadrature oscillation  
phasor diagram**

This diagram shows the phase of the electric field relative to the magnetic field for each quadrature resonance event. Zero phase difference means that the oscillations are in phase. [Logarithm to base 10 of amplitude plotted radially].

Column 4 shows the Polar satellite field line trace to the northern hemisphere ionosphere given by Tsyganenko 89c with observed Kp values. Only in two cases was it possible to locate a ground magnetometer within  $\pm 2^\circ$  in both latitude and longitude of this trace location. However it was often possible to locate a ground magnetometer at a geographic latitude within  $\pm 2^\circ$  and where this was possible the trace coordinates are highlighted in green.

**8.3 Magnetogram oscillations preceding magnetospheric resonance**

The two events an hour apart on 2003-12-15 were coincident with strong oscillations in IMAGE X-component magnetograms [Figures A7.27 and A7.28]. The quadrature oscillation between 1458UT and 1518UT in the Polar satellite data was preceded by ground oscillations with a frequency of 3.5mHz from SOR to OUJ as shown in Figure 8.2. The greatest amplitude of this pulse was observed at 1500UT at SOR and although the amplitude decreased with decreasing latitude the frequency remained approximately the same over the full range of latitudes. The magnetospheric resonance frequency in the  $E_x$  and  $B_y$  components was also estimated from the  $E_x$  and  $B_y$  spectra as 3.5mHz . These observations

therefore suggest that the ground signal may have been that of a compression wave that initiated the resonance as discussed theoretically in Section 2.4.

For the earlier event at 1400UT on 2003-12-15 the ground signal also had the strongest amplitude at the time the magnetospheric resonance was initiated. Ground oscillations with a more irregular character were observed at the time of the resonances on 2002-12-24 at Greenland station AMK [Figure A7.20] and on 2003-11-25 at IMAGE station MUO [Figure A7.26].

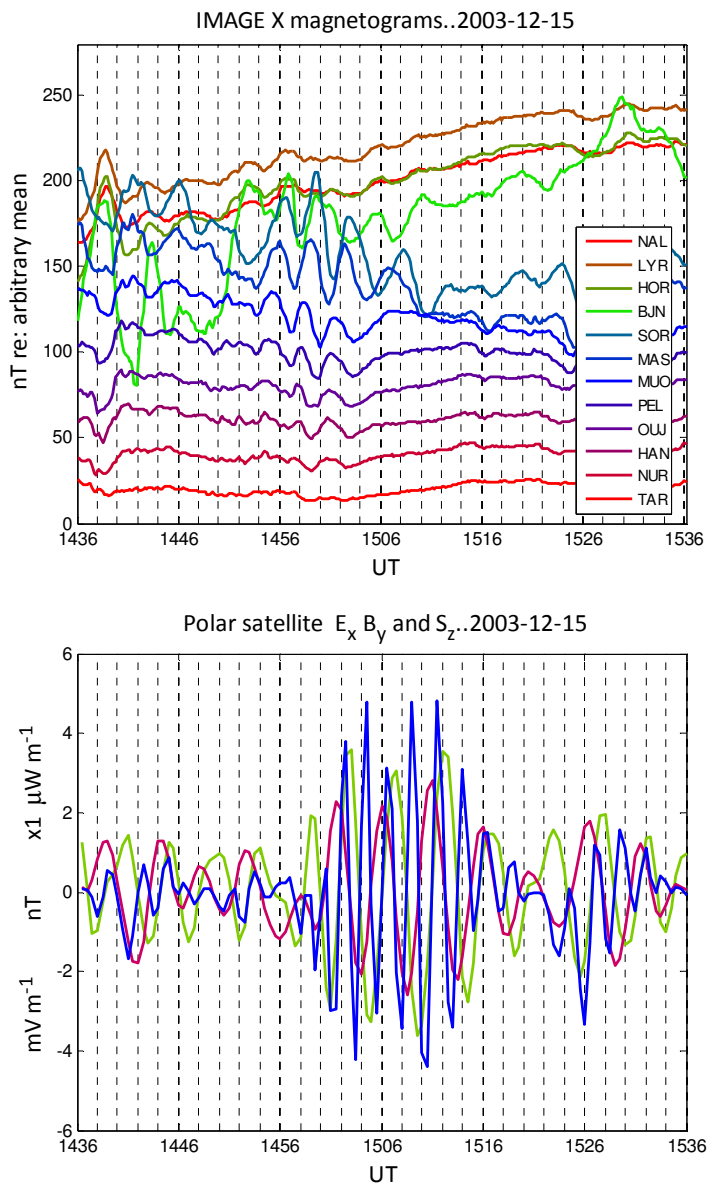


**Figure 8.2**      **Quadrature oscillation at 1458UT on 2003-12-15**

The upper diagram shows the IMAGE magnetograms and the lower diagram the  $E_x$ ,  $B_y$  and  $S_z$  magnetospheric quadrature resonance components.

#### 8.4 Group V quadrature oscillations associated with substorms

The events on 2002-10-26 [Figure A7.18] and 2003-10-10 [Figure A7.21] were associated with substorm activity in the IMAGE magnetogram stackplots. In addition a third event on 2003-10-19 [Figure A7.22] was of particular interest as it was preceded by a Poynting flux impulse of the kind associated with the onset of substorms described in Chapter 7. An overview of this event was described in Section 6.6.5.

Although for these three events the Polar satellite field line trace was to the Barents Sea, the Norwegian Sea and to Iceland, rather than the IMAGE ground magnetometers where the substorm was observed, the time of substorm onset at SOR, which was approximately at the same geomagnetic latitude for all three events, was used to provide a time origin.

Figure 8.3 shows the time-alignment between the presence of a quadrature signal in Polar satellite data and the substorm expansion phase observed in the SOR magnetograms.

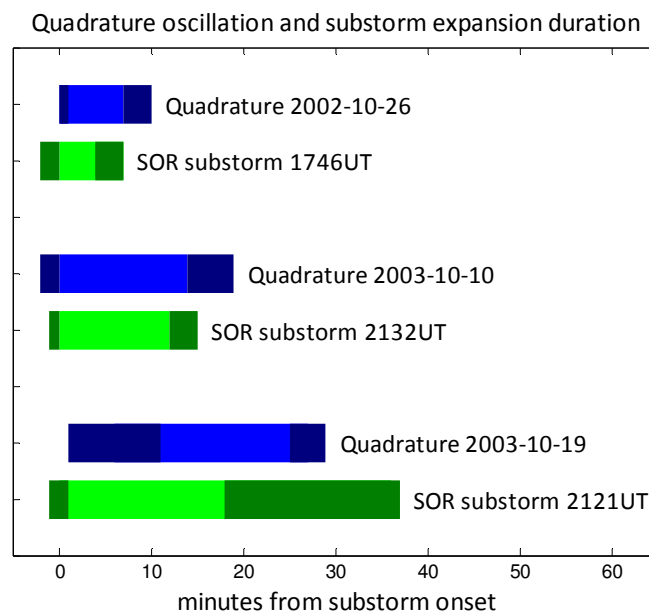


**Figure 8.3** Quadrature oscillations and substorm expansion

The time of substorm onset observed in the X component SOR magnetogram was used as the reference time. The duration of the quadrature resonance is shown in blue and the substorm expansion phase in green. Uncertainties in the start and end times of the quadrature resonance are shown by darker blue shading at the ends of the bars and uncertainties in the start and end times of the substorm by darker green shading at the end of the bars.

There was always some uncertainty in estimating the start and end times and these are shown in a darker shade at the ends of the bars. For the Polar satellite data the beginning and end of a Poynting flux oscillation was used as the main indication of the duration of the quadrature resonance but this was supplemented by an examination of the phase of the electric and magnetic field displacements. The uncertainty in the time of substorm onset from the negative deflection in X-component magnetogram data was generally of the order of two minutes or less. The greatest uncertainty was in estimating the end of the substorm expansion phase associated with the event on 2003-10-19.

These three observations suggested that the substorm expansion phase approximately matched the duration of the quadrature resonances and that when these ended by de-phasing of the electric and magnetic field oscillations the substorm expansion phase also ended. Substorm expansion meant that an ever-increasing current was flowing through the ionosphere and this would require either an increasing supply of charge or an increasing potential. It is therefore suggested that the resonating field lines on the Polar satellite orbit were either contributing to the supply of charge during the substorm expansion phase or that the PFI associated with the switching on the current was also causing the resonance.

### **8.5 Quadrature oscillations associated with magnetogram notches**

The terrestrial signals at the time of the three quadrature resonance observations on 2002-11-09 [Figure A7.19], 2003-10-26 [Figure A7.23] and 2003-11-09 [Figure A7.24] showed a signature which incorporated a distinctive V-shaped notch. These magnetospheric resonances all have the character of a pulse, rather than a decaying exponential, and the notch in the ground data coincided approximately with the time of the first strong magnetospheric magnetic deflection.

Verified level 2 data was examined from the Advanced Composition Explorer [ACE] satellite which is in a Lissajous orbit around the L1 Sun-Earth Lagrangian point and it seems likely that the first of these quadrature resonance events was associated with the increase in solar wind magnetic field strength, speed and density shown and described in Figure 8.4 . These factors would have increased the solar wind dynamic ram pressure and given rise to a fast mode compression wave in the magnetosphere that could have coupled to Alfvén shear waves on magnetic field lines. The ACE data showed similar, but smaller, increases in the same solar wind parameters that could have been associated with the second resonance and notch event but not for the third.

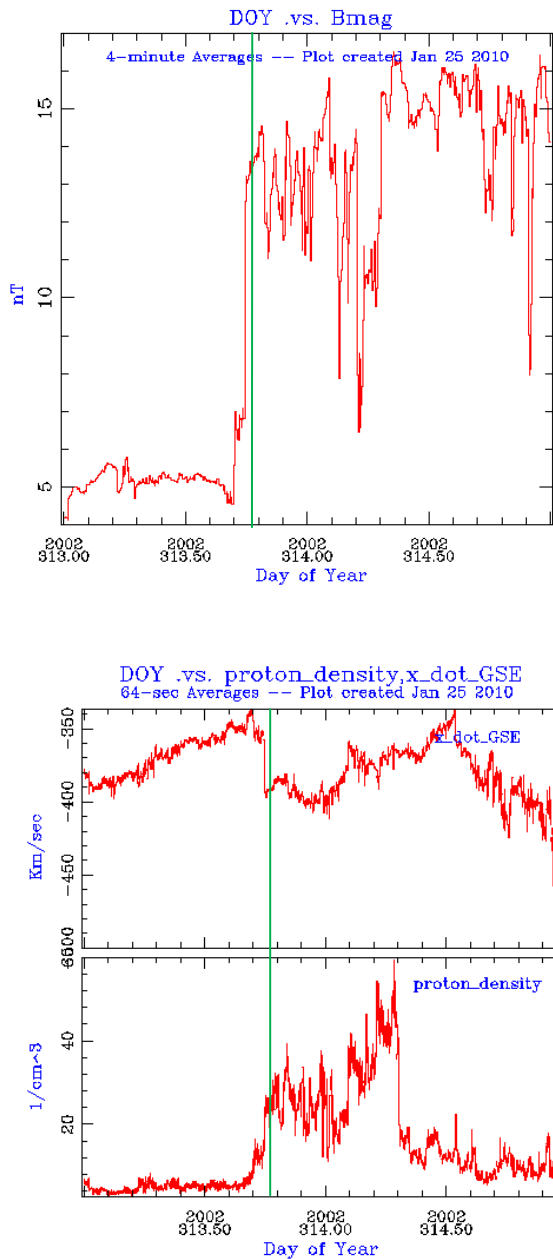


**Figure 8.4** ACE satellite plots of solar wind parameters

These verified level 2 plots show the increase in the solar wind magnetic field strength, speed and density that occurred on 2002-11-09 [Day 313]. The abscissa marks are at 0.1 day. The instant of the notch event at 1853UT [0.7868 decimal day] that was observed in the IMAGE magnetograms is marked by the green lines. The ACE satellite was near the L1 Sun-Earth Lagrangian point and the transit time from there to the magnetosphere at  $400\text{kms}^{-1}$  is approximately one hour [0.042 decimal day] which suggests that this quadrature resonance was initiated by the impact of the solar wind on the magnetosphere. [ACE SWEPAM instrument team and ACE Science Center]

### 8.5.1 Notch event at 1911UT on 2003-10-26

IMAGE magnetograms and Polar satellite signals are shown in Figure 8.5 for the notch event at 1911UT on 2003-10-26. The magnetic latitude of the Polar satellite field line trace was  $69.6^\circ\text{N}$  which was to the north of SOR [ $67.3^\circ\text{N}$ ] and possibly close to the open-closed field line boundary. The Polar satellite data showed quadrature oscillations with a phase difference of  $-103^\circ$  and a frequency that was estimated at 3.3MHz by dividing the Poynting flux frequency by two.

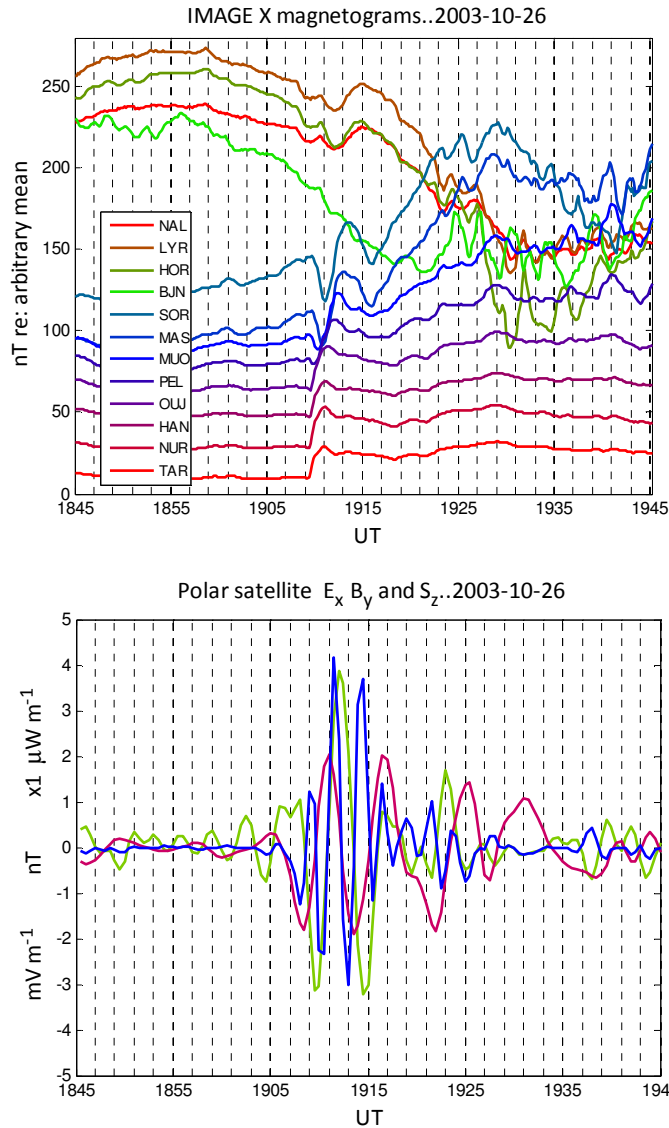


**Figure 8.5**  
**Magnetogram notch at**  
**1911UT 2003-10-26**

The upper diagram shows the notch feature in IMAGE ground magnetograms at 1911UT. Towards lower latitudes it morphs into a step feature.

The lower diagram shows the  $E_x$ ,  $B_y$  and  $S_z$  components of the magnetospheric quadrature resonance with the peak deflection at the same time as the notch minimum.

The notch feature was observed in magnetograms from SOR, MAS and MUO at 1911UT which gradually morphed into a step function with an increasingly earlier time of onset towards lower latitudes. The terrestrial notch minimum at SOR at 1911UT coincided with a magnetospheric +2nT  $B_y$  deflection.

Although multiple cycles of oscillation were not seen in the ground data it was thought that it might still be possible to make an estimate of the magnetospheric resonant frequency by interpreting these notches as the negative part of a half-cycle oscillation. A notch frequency was therefore defined as the reciprocal of twice the time between the notch minima and the following positive maxima. These notch frequencies were then plotted against the magnetic latitude of the ground magnetometer in Figure 8.6 and a first order regression line added. The circle shows the Polar satellite magnetic latitude trace and the frequency of the magnetospheric quadrature oscillation .

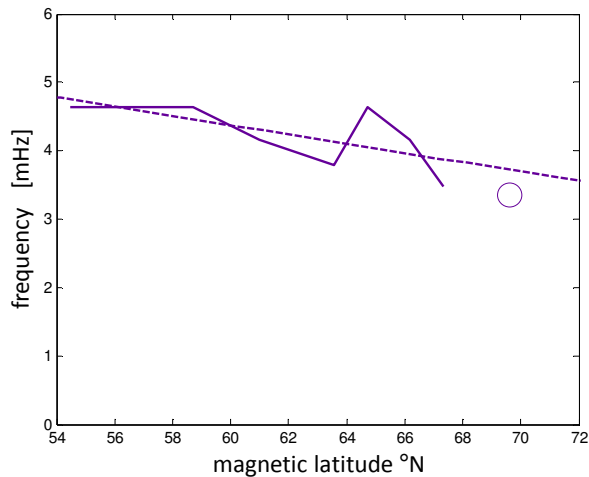


**Figure 8.6 Notch frequency versus latitude at 1911UT on 2003-10-26**

Estimates of resonant frequency derived from half cycle notches are plotted against the magnetic latitude of the ground magnetometer. The Polar satellite field line trace magnetic latitude and magnetospheric resonant frequency is shown by the circle.

It can be seen that the notch frequency estimate trend was a decrease towards higher latitudes as would be expected if the quadrature resonances were initiated by an impulse propagating into the magnetosphere. The suggestion is therefore that there may be a connection between these notch frequencies and the magnetospheric frequencies. In the absence of several cycles of oscillation in ground-based magnetograms this technique may therefore provide an approximate estimate of the magnetospheric quadrature resonant frequency.

Another feature of these notches and steps is that they occur at earlier times at lower latitudes, as with the substorm onsets and the OGMD events described in Chapter 8. This situation would arise if the process was initiated at the same time on all field lines but propagated to the Earth faster on the shorter low-latitude field lines. As with the observations of quadrature resonances in the expansion phase of substorms the existence of notches and steps provided yet another indication that Group V quadrature oscillations may be associated with the flow of current to the ionosphere.

## 8.6 Discussion and conclusions

For standing waves on magnetic field lines created by the perfect reflection of Alfvén shear waves the electric and magnetic fields would be expected to be in quadrature [Section 2.5.5]. This made for a recognisable signature in Polar satellite data and these quadrature signals were classified as magnetospheric Group V. Although there was considerable variability in the phase-angle between the magnetospheric electric and magnetic fields as shown in Figure 8.1, the average magnitude of the phase angle came to  $93^\circ$  for the eleven magnetospheric resonance events that were observed in this study.

Resonance occurs when a system is excited at its natural frequency. Lines of magnetic field or segments of a geomagnetic shell have a natural frequency determined by a combination of factors including magnetic field strength, plasma density and the length of the field line between the reflecting boundaries. The high latitude field lines tend to have a lower resonant frequency because they are longer and thread through regions of lower magnetic field strength.

Oscillations decay as energy is transferred to the surroundings and three of the observations of quadrature resonance exhibited this effect [2002-10-26 Figure A7.1, 2003-10-10 Figure A7.21 and 2003-12-15 A7.27]. The other eight events had the character of a pulse resonance which persisted over several cycles before decaying. This would suggest that a source of power was there to sustain the resonance. Because data was selected from Polar satellite field line traces to high latitudes it is possible that the reflecting boundary at one end of the field line may be in the magnetotail for some of these resonating pulses rather than the conjugate ionosphere. It would be expected that imperfect reflection from the PSBL region could account for the wide variation of phase-differences that were observed and the term *tail line resonance* [TLR] is suggested for this phenomena.

Two events were observed [both on 2003-12-15] where the ground magnetograms showed strong oscillations at the time the magnetospheric quadrature oscillations appeared. These may be compression waves propagating through the magnetosphere and coupling some of their energy to field lines, as described in Section 2.4.

Three examples were seen where the duration of the magnetospheric quadrature resonances corresponded to the expansion phase of a substorm [Figure 8.2]. During this phase the cross-tail current is thought to be diverted onto field lines in the form of a substorm current wedge [Figure 1.15]. It could therefore be that field-aligned currents were

flowing on the resonating field lines and an unresolved question is whether this was the power source that caused them to sustain their resonance. It may be significant in this respect that two of the three strongest resonances observed, with amplitudes of  $150 \mu\text{Wm}^{-2}$  and  $50 \mu\text{Wm}^{-2}$ , were associated with the high ionospheric currents in these substorm expansions.

Three other examples were seen where a phenomena described as a magnetogram notch was observed. This was found to be a half-cycle oscillation of ionospheric current with a minima at the time of the first strong magnetic field deflection in the magnetospheric data. In the event described in Section 8.4.1 it was shown that the notch frequency estimated from these half-cycle magnetometer deflections decreased with increasing latitude and tended towards the magnetospheric estimate of frequency in Polar satellite data [Figure 8.4]. At lower latitudes the notch feature morphed into a magnetogram step corresponding to a west-east flow of ionospheric current. This was another example where quadrature resonances could have been associated with the precipitation of charged particles and where it was possible that the quadrature resonance was being sustained by the current on the field lines. A possible form of plasma instability that would give rise to transverse plasma oscillations is the diocotron instability caused by two sheets of charge in relative motion. This is analogous to the Kelvin-Helmholtz instability [Knauer 1966].

To summarise these observations of magnetospheric resonance, two examples were encountered where the quadrature event may have been initiated by a quasi-continuous compression wave oscillation propagating through the magnetosphere, three where it may have been caused by a magnetospheric impulse so that the resonant frequency varied with latitude and three where they were associated with the expansion phase of a substorm. In one of these substorm observations the resonance may have been initiated by a PFI from the magnetotail.

In both the substorm and the magnetospheric notch events there was the suggestion that the resonance may have been sustained by field-aligned currents flowing from the ionosphere with a possible sink in the tail plasma sheet.

## 9.0 Concluding remarks

### 9.1 Narrative Summary

This thesis is concerned with the propagation and phenomena associated with ULF oscillations in the terrestrial magnetosphere. Propagation was studied in three ways: by estimating time-delays in ground magnetometer data, by solving the classical Helmholtz equation and by measuring Poynting fluxes on Polar satellite data. The phenomena that were related to these ULF oscillations were field-line resonances, auroral optical intensity modulation, geomagnetic substorms and the closely related phenomena referred to herein as opposing ground magnetometer deflections [OGMD events].

The direction of arrival of a wave is often estimated from measurements of time-delays, or of phase-difference between sensors. This works when: (a) the wave is spatially coherent (b) aliasing is avoided and (c) either the velocity or the wavelength is known. However with ground magnetometer data only the frequency could be measured, so a novel technique was developed which enabled an estimate of direction to be made without the need to know either the velocity or the wavelength. This consisted of regarding the Earth as a scanning platform and estimating the times when the signal was incident broadside to the ground magnetometer baseline so there were no time-delays or phase-differences. The direction of arrival was the one that gave the observed time-delays in a frame of reference that was not co-rotating with the Earth. ULF waves arrive at the ionosphere from many directions, but by coherently integrating the time-delays over 60 days a clear underlying diurnal pattern was observed with waves arriving from the east in the morning and again in the late afternoon with only a few hours around the time of local noon when they arrived from the west. Waves from the sunward direction would not have been expected to give this pattern but the null technique was able to explain it by showing that the signals were arriving from a high latitude dayside source direction that was biased by about  $20^\circ$  towards the morning sector. This meant either that the waves were field-guided along high latitude field lines from the dayside magnetosphere or they were propagating across field lines from high latitudes.

This technique would also be of general application to any situation where there are two or more sensors but where the velocity and wavelength are unknown.

To understand these high latitude observations, and to gain a broader understanding of how fast mode MHD waves propagate in the magnetosphere, the classical Helmholtz equation

was solved numerically for the magnetosphere. This was made possible by interfacing a Multiphysics software package<sup>(1)</sup> to MHD data derived from satellite observations<sup>(2)</sup> using the MATLAB software described in Appendix 4. Because ion cyclotron resonance is thought to be a source of ULF waves upstream of the bow shock the dayside boundary was set to give a plane-parallel source of 20 mHz oscillations and the other boundaries were set to radiate so that there were no internal reflections. The solution to the Helmholtz equation that is included with this thesis shows ULF wave propagation in real time so that it conveys an idea of the timescales involved in Alfvén wave speed propagation over these large distances.

ULF waves are diffracted by the Alfvén gradient around the Earth through the region threaded by high latitude field lines. Thus it was reasoned that magnetic coupling between fast mode waves and Alfvén shear waves would allow these oscillations to reach the high latitude ionosphere across which they would propagate. The Alfvén gradient around the Earth was also found to be responsible for the creation of ULF diffraction lobes in the tail as a result of the division of the wavefront. In three dimensions it would be expected that these diffraction lobes become cones of enhanced ULF wave amplitude in the radiation belt region. ULF waves were also diffracted into the tail plasma sheet which is the source region for the Poynting flux impulses [PFIs] that were the subject of the following studies. Here they propagate at a slower speed, and hence with shorter wavelengths, than in the adjacent PSBL regions. ULF wave energy from the solar wind is therefore concentrated in the tail plasma sheet region of the magnetosphere where it may have a role in auroral modulation and in initiating, and possibly modulating, magnetic reconnection.

Since both the direction-finding study and the Helmholtz equation propagation study had suggested that ULF waves would be strongest at high latitudes the next step was to identify a suitable satellite with electric and magnetic field sensors so that Poynting flux vectors could be calculated. The Polar satellite was in a high latitude orbit and had three-axis electric field sensors, but in these studies only electric field data derived from spin-plane sensors was used<sup>(3)</sup> to remove the problem of possible corruption of EFI data by satellite operations.

---

<sup>(1)</sup> The Swedish company COMSOL provided an evaluation copy of their Multiphysics software

<sup>(2)</sup> Patrick Daum kindly provided a  $60R_E \times 40R_E \times 40R_E$  MHD dataset with a resolution of  $0.5R_E$

<sup>(3)</sup> The Polar satellite EFI Principal Investigator Professor Mozer advised on using verified data

Poynting fluxes are a highly sensitive detector of electromagnetic waves when combined with low-pass filtering because the  $\overline{\tilde{\mathbf{E}} \times \tilde{\mathbf{H}}}$  operation then takes the form of a cross-correlation between the different electric and magnetic field components. When this operation was applied to Polar satellite data earthward fluxes were frequently observed at auroral latitudes as in other studies [Keiling 2002]. It was found useful to transform the Poynting flux components to field-aligned coordinates so that the orientation of the Poynting vector relative to the field lines could be used to try to relate these magnetospheric observations to terrestrial observations..

The ready availability of SAMNET and IMAGE ground magnetometer data suggested that observations should be made approximately every three days when the ~18 hour Polar satellite orbit brought it to geomagnetic field lines over Finland. To begin with all-sky camera images were examined for auroral brightening at the time of magnetospheric events and several examples were encountered, but the association of these events required the Polar satellite field-line trace to be over Finland when the weather was clear, when there was auroral activity and when validated electric field data was available. This was somewhat restrictive so attention was turned to IRIS riometer data because, although enhanced radio frequency absorption requires higher energy precipitation to reach the D layer in the ionosphere, the riometer operation at 38.2 MHz means that observations can be made through cloud. It was then immediately apparent that ionospheric precipitation is often coincident with magnetospheric PFIs.

Thirty-nine magnetospheric events were identified that had a possible terrestrial association and a classification scheme was devised which put these events into six magnetospheric groups of which three are concerned specifically with PFIs. In fourteen of these events enhanced absorption in IRIS riometer keograms was seen within  $\pm 6$  minutes of a Poynting flux impulse and when the Polar satellite field line traces were plotted on a map [Figure 7.5] it was found that there was up to four degrees of separation in geomagnetic latitude and up to thirty-five degrees of separation in longitude with three examples where the Polar satellite field line trace was almost to Iceland.

This led to consideration of the question: when is a coincidence an association? The hypothesis was that the satellite and riometer observations had a common cause and the null hypothesis was that they arose by chance. It was not possible to prove an association but the high improbability of this pattern of events coinciding by chance helped. Also in this case, the physics of the situation suggested that magnetotail annihilation or reconnection

could be a source of MHD waves. These could arise as a result of the reconfiguration of the magnetic field which could deflect lines of magnetic field and launch Alfvén waves on field lines as well as fast mode waves across field lines. These could be detected by the electric and magnetic field instruments on the Polar satellite. Magnetic field reconnection could also give rise to jets of charged particles which would spiral around field lines to the ionosphere above the IRIS riometer and result in the enhanced absorption spikes seen in the IRIS keograms.

The latitude displacement and the orientation of the Poynting flux vectors initially suggested that the PFIs were propagating across field lines, but this may not have been the case.

The observation that enhanced absorption was often detected in the IRIS riometer keograms when the PFIs had a  $-S_z$  component was initially a puzzle whose resolution [Figure 7.7] provided useful evidence that the source of the PFIs was on, or near to, the geomagnetic equator. Poynting flux vectors often had a dominant GSE/GSM  $x$  component which was taken together with the above deduction to infer that the source was often in the tail plasma sheet.

A study of the association between the times of substorm onset relative to the magnetospheric PFI showed that in nine events out of eleven substorm onset, as detected by a change of gradient in ground magnetograms, was coincident within  $\pm 1$  minute. As the IMAGE magnetograms showed that substorm onsets propagate northward over timescales of several minutes it was seen that the Polar satellite instruments were detecting the PFIs on the same geomagnetic field lines and near the same moment as the charged particle precipitation was initiated. This meant that both the PFIs and the charged particles were on the same field lines, which means that they had a common source which had been deduced to be near the geomagnetic equator. It also meant that the PFI marked the instant at which the charged particles were redirected towards the earth. Multiple PFIs were sometimes seen during the substorm expansion phase and this suggests that the redirection of charged particles was repeated.

Closely related to substorms was another feature in ground magnetometer data referred to here as OGMD events. Whereas the east-west substorm electrojet gives rise to a substorm bay signature over a wide range of latitudes these OGMD events had a well-defined latitude that could be estimated by interpolation between ground magnetometers. They could therefore be associated with ionospheric precipitation by a single current sheet. This current sheet was inferred to have considerable longitudinal extent with one example mapping

from Finland to Canada. As well as good spatial localisation, which meant they could be mapped, they also had good temporal resolution, which meant that they could be tracked. For two events it was estimated that the OGMD events propagated east to west with speeds of  $10\text{kms}^{-1}$  and  $15\text{kms}^{-1}$ . These propagation speeds were of a similar order to the ionospheric phase speed estimated in the earlier direction-finding study [ $\sim 13\text{kms}^{-1}$ ]. Mapping the ionospheric precipitation out to the magnetosphere suggested that the precipitation was initiated near the dawn side and propagated across towards the dusk side at an [underestimated] speed of  $\sim 100\text{km s}^{-1}$ .

It was possible to make a temporal association between PFIs and substorm onset because the substorm onset propagates northwards and eventually reaches the geomagnetic latitude of the Polar satellite. This is not the case for the OGMD events which are only observed at a particular latitude which is generally not the latitude of the Polar satellite. But nevertheless PFIs were still observed within  $\pm 6$  minutes of an OGMD event. This suggests either that PFIs propagate across field lines or that the switching process continues to proceed northwards, as in substorms, even though there is no current to switch.

The sequential sequence of east-west and south north switching suggests that it proceeds from a point on the dawn side of the magnetosphere.

Another feature of the PFIs was that there was a suggestion that the propagation speed, as determined from the E:B ratio, increased with the Poynting flux intensity [Figure 7.8] which suggests it may be possible for energy to be transferred from the PFI to charged particles, with the result that the PFI is attenuated and slows down.

PFIs carry a considerable amount of energy. It is estimated that if a strong PFI has a duration of 100s and transfers  $100\text{eV s}^{-1}$  to each electron in a plasma with a density of  $10^6\text{ m}^{-3}$  the PFI would be dissipated in a distance of  $\sim 3R_E$  and heat the electrons throughout this distance by 10keV, which is of the order of the auroral electron energy and also the energy of electrons which give rise to spikes in IRIS riometer data.

Another interesting observation was that multiple PFIs were sometimes detected in Polar satellite transits through the tail current sheet and PSBL region. This means that the magnetotail is a source of pulsed energy.

The observations of multiple pulsed PFIs with a mHz repetition rate leads to some further deductions about energy transfer. If there are several substorm or OGMD events a day and each has multiple PFIs then the daily transfer of solar wind energy to a population of trapped electrons is a fraction of a MeV. This transfer would be expected to occur in the

geomagnetic equatorial region is agreement with the observed distribution of energetic radiation belt particles. The mechanism by which a PFI could transfer energy to electrons however was not part of this study.

Another feature of multiple PFIs is that, if they are able to transfer their energy to auroral electrons, then mHz optical modulation of auroral intensity would result. The mirroring of auroral electrons on field lines give rise to an impulse response so that although the PFI is of short duration the resulting auroral activity is spread over time. Some measurements were made of mHz auroral modulation at the Sodankylä Geophysical Observatory in Finland, although at the time these multiple PFIs had not been seen. This is therefore an interesting topic for a further work and is discussed below.

The classification of the Poynting flux signals yielded eleven examples of resonances which were identified by the quadrature phase-difference between their electric and magnetic field time-series. There were three kinds of terrestrial signal coincident with these particular magnetospheric observations: substorm expansion, oscillations preceding the resonance and a phenomena described as a magnetogram notch which was identified as a half cycle oscillation coincident with the first strong Poynting flux deflection in the resonance. It was thought that the resonance could have been initiated by an impulse that gave rise to this notch signature or by earlier magnetospheric oscillations. There were also two events where the quadrature resonance was preceded by a PFI, but the interesting thing was that there was not always an explanation for their initiation. Because of the association of field line resonance with ionospheric precipitation it is suggested that field lines might oscillate as a result of plasma instabilities associated with field-aligned currents flowing along the resonating flux tubes.

This has been an amazing journey of discovery but there is much remaining to be explored.

**P F Tullet      Cranbrook      16<sup>th</sup> October 2009**

## 9.2 Future Work



**Figure 9.1 Quiet auroral arc**

This photograph was taken from the frozen Kittila River in Finnish Lapland on 2008-03-28 by the author.

The lights of the town of Sodankylä to the north can be seen in the lower right.

### 9.2.1 Auroral arc optical modulation in relation to PFIs.

During the course of these studies some measurements were made of the frequency of the optical modulation of quiet auroral arcs prior to substorms. These are given in Table 9.1.

Events were selected by watching the SGO archived ASC .mpg movies that had been generated for clear observing nights and identifying from these the times when quiet auroral arcs were overhead at Sodankylä.

It can be seen that all these frequencies are in, or near, the 2 - 7mHz Pc5 band and several of them are close multiples of 1.6mHz. The frequency of 3.3mHz, which was often seen in high latitude magnetograms was also present. The SGO is located at 64°N 107°E geomagnetic corresponding to L=5.2 The field line resonance frequency depends upon the path of the field line through the magnetospheric plasma which in turn depends upon MLT and magnetospheric distribution.

Date	Time (UT)	Frequency [period]
2002-10-16	1800 - 1830	1.9mHz [8.8 minutes]
2002-12-19	1600 - 1630	3.3mHz [5 minutes]
2002-12-24	1800 - 1830	3.3mHz [5 minutes]
2003-01-10	2100 - 2130	3.7mHz [4.5 minutes]
2003-01-29	1900 - 1930	1.6mHz [10.4 minutes]
2003-01-30	1600 - 1630	5.0mHz [3.3 minutes]
2003-03-20	2100 - 2130	5.0mHz [3.3minutes]
2003-03-27	1900 - 1930	2.2mhz [7.6 minutes]

**Table 9.1 Auroral optical modulation frequencies**

A revised time-of-flight study [Wild et al. 2005] suggests that these periods at the SGO magnetic latitude are not inconsistent with field line resonance. The author believes that another factor that needs to be taken into account in associating auroral modulation with field line resonance is the increased plasma loading that is associated with the precipitation that would have the effect of increasing the resonance period.

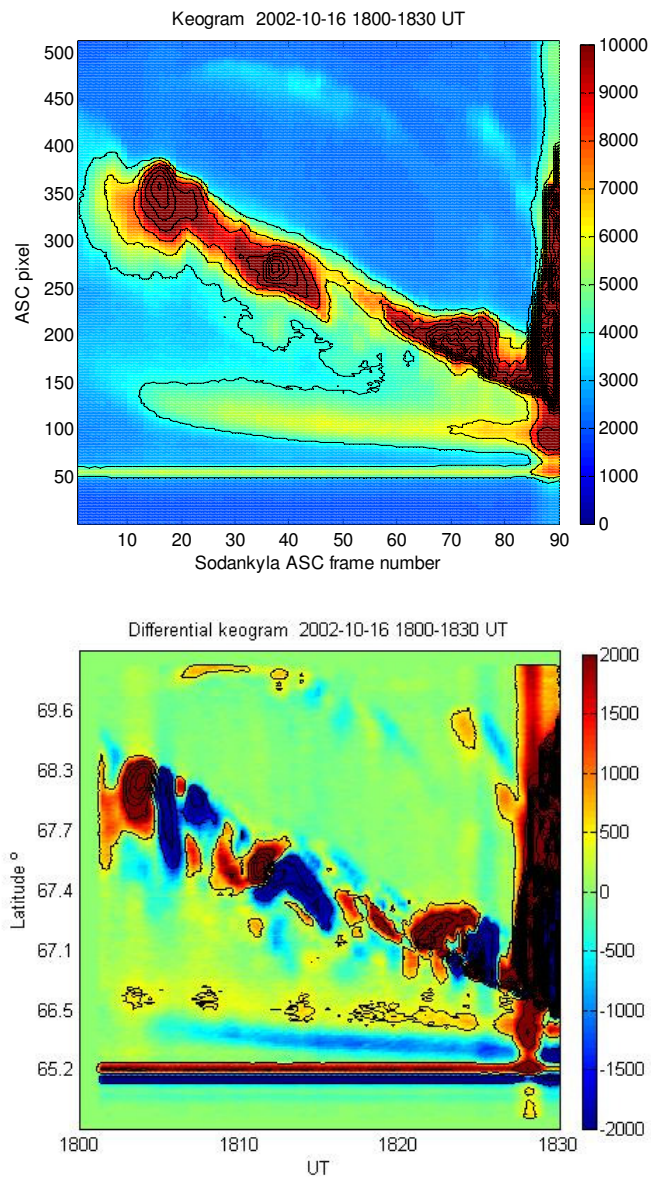


**Figure 9.2 Keogram and differential keogram 1800-1830UT 2002-10-16**

These images were generated using the processing method described in the text. Differential keograms are particularly sensitive to possible auroral modulation by PFIs.

As PFIs were observed coincident with the onset and expansion phase of geomagnetic substorms it would not be expected that they would be present at the time a quiet arc was

moving equatorwards, but there may be a possible association between the auroral modulation frequency determined in the quiet time prior to a substorm and multiple PFIs during the substorm. It is therefore suggested that a future study could be to determine whether the frequency of auroral modulation before a substorm was related to the repetition frequency of multiple PFIs during the substorm.

As well as magnetospheric detection these studies have shown that multiple PFIs are sometimes detected within approximately one minute in riometer keograms. Other studies [Williams et al. 1990, Opgenoorth et al. 1990] have suggested that they are also present in EISCAT radar data with short integration times. Thus these ground-based instruments could be used to place markers on all-sky camera differential keograms created as described below to relate magnetospheric PFIs to auroral modulation by inference.

An example of a keogram derived from all-sky camera images and the corresponding differential keogram in Figure 9.2. The 512x512 pixel mages were taken every 20s through a 557.7nm filter and the keogram was constructed by summing row pixels within  $\pm 100$  pixels of the meridian. The differential keogram was constructed by differencing pixels parallel to the auroral arc. This differentiation removes the mean level from all pixels in the keogram and leaves only the temporal changes, which can be positive or negative. This resulting differential keogram was visually amplified simply by reducing the dynamic range of the pixel-difference colour scale shown on the right hand side of the image. Three ULF optical pulsations showed up as red [increasing intensity] and blue [decreasing intensity] regions and the optical modulation frequency was estimated as 1.9mHz. The keogram shows the presence of a second auroral arc to the south and the differential keogram shows that this was also modulating in intensity. The auroral substorm appeared to begin when these arcs merged.

Figure 9.3 shows the IRIS riometer keogram between 1800UT and 1900UT on 2002-10-16. Strong enhanced absorption was seen during the time of the substorm and the absorption bands around 1834UT and 1844UT have approximately the same period as the quiet arc modulation peaks.

Any study that related these optical frequencies to PFIs would need to first identify the times when the Polar satellite was on, or close to the auroral field lines, when valid EFI data was available, when the observing conditions were favourable and when quiet auroral arcs

were present. This would probably mean looking through several winters of observation and data.

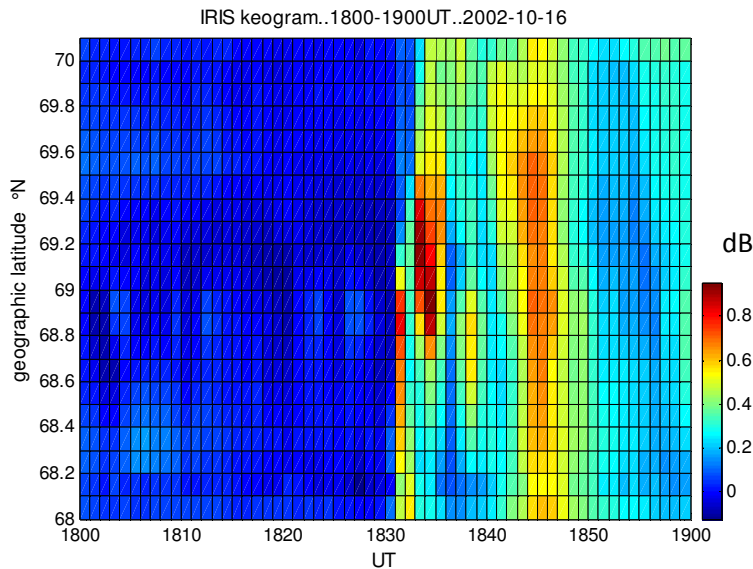


**Figure 9.3 IRIS riometer keogram 1800-1900UT on 2002-10-16**

The Sodankylä all-sky camera images in Figure 9.3 showed that an auroral substorm began at 1828UT. This IRIS riometer keogram from Kilpisjärvi showed enhanced absorption in the ionosphere after 1831UT during the substorm expansion phase.

### 9.2.2 PFI source location

It was found in these studies that PFIs were often observed to be propagating from a source region in the magnetotail. They may have also been reflected before being detected by the Polar satellite. The work described in Chapter 7 suggests that they come from the tail plasma sheet equatorial region and probably propagate along field lines. The ground-based observations also suggest that there is a dawn-dusk component associated with the source. Multiple observations of the Poynting flux direction from satellites crossing the geomagnetic equator may provide an indication of the source location.

### 9.2.3 Magnetospheric cavity oscillations

Alternating Poynting fluxes were observed in Polar satellite data with frequencies below 1mHz and at a strength of  $\sim 10^{-7} \mu\text{Wm}^{-2}$ , which is around two orders of magnitude weaker than most of the events described in Chapter 6. Figure 9.4 shows a Poynting flux vector quiver plot superimposed upon the Polar satellite orbit projected onto the GSE x-z plane between 0530UT and 0930UT on 2002-03-19. One hour marks are shown in red and suggest a period of  $\sim 35$  minutes [ $\sim 0.5$ mHz] if these fluxes are a temporal, rather than a spatial

phenomena. These oscillations might be the often-mentioned magnetospheric cavity-mode standing waves and it is suggested that a future investigation should use multisatellite data [such as CLUSTER] to distinguish between temporal or spatial effects. Measurements of the low-frequency phase-difference between the electric and magnetic fields could be made to determine whether these oscillations exhibit the quadrature signature of resonance.

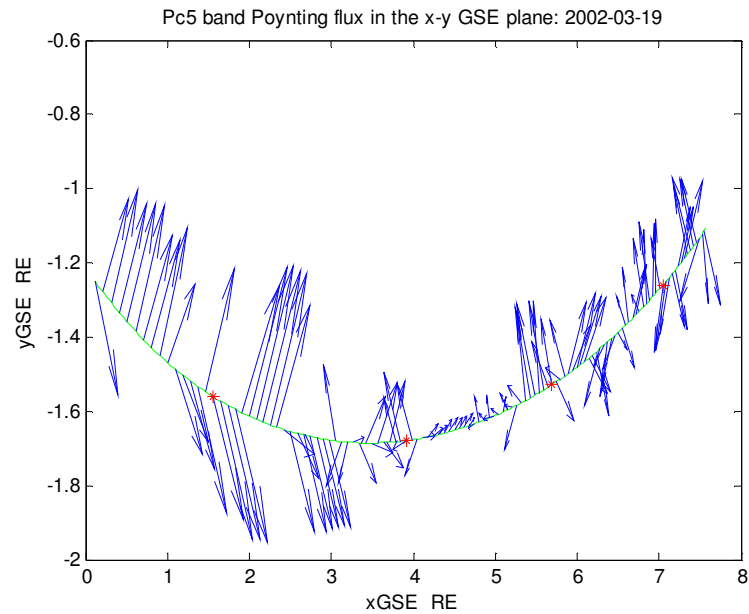


**Figure 9.4 Poynting flux bands in the dayside magnetosphere**

This MATLAB generated uncalibrated quiver plot shows the components of ULF magnetospheric Poynting flux vectors at a level of  $\sim 10^{-7} \text{ Wm}^{-2}$  detected in Polar satellite data and projected onto the GSE x-y plane. The observation was made in the morning sector between 0530UT [left] and 0930UT [right] when the Polar satellite was outward and sunward bound in the southern dayside magnetosphere so that the orbital path shown by the green line is from left to right in the Figure.

The four red time-stamp markers show the position of the Polar satellite from left to right at 0600UT, 0700UT, 0800UT and 0900 UT.

With observations from a single satellite it is not possible to determine whether this is a spatial or a temporal phenomena but it is quite possible that these fluxes correspond to ULF magnetospheric cavity wave oscillations.

## Appendix 1 Magnetohydrodynamics [MHD]

### A1.1 General background

Much of this material was derived from the plasma physics course given at QMW [Schwartz 2004]. Additional material has also been included from some of the many textbooks on plasma physics [Baumjohann 1997], [Choudhuri 1998], [Dendy 1993], [Jacobs 1970], [Kivelson and Russell 1995], [Ohanian 1988], [Parks 1991], [Pröls 2004] and [Sturrock 1994]. The chapters on vector algebra in the outstanding mathematics textbook by Mary Boas [Boas 1966] were also found to be most useful. From general considerations the governing equations of magnetohydrodynamics are given and these are then used to derive a perturbation equation whose solutions yield the four ULF wave modes, pure acoustic, slow and fast mode magnetosonic and electromagnetic Alfvén waves. It is the last two of these that are thought to be particularly relevant to the observations.

### A1.2 Electron Plasma Frequency

A disturbance in a plasma gives rise to electric fields which displaces the charged particles - they then move to restore the neutrality. Overshooting sets the electrons in oscillation giving rise to an important natural frequency of a plasma called the electron plasma frequency denoted  $\omega_p$ . Consider a slab of plasma of unit area and thickness  $L$  in which the ions are regarded as being essentially at rest, since their inertia is much less than that of the electrons. If the electron number density is  $n_e$  then an electron displacement  $\Delta x$  gives rise to two parallel sheets of net positive and negative charge with charge per unit area:

$$\sigma = n_e e \Delta x \quad \text{and an electric field between them of magnitude : } E = \frac{\sigma}{\epsilon}$$

The plasma inside the slab has a charge of:  $n_e e L$  and experiences a restoring force per

$$\text{unit displacement of: } \frac{F}{\Delta x} = \frac{q E}{\Delta x} = \frac{n_e e L}{\Delta x} \frac{n_e e \Delta x}{\epsilon} = \frac{n_e^2 e^2 L}{\epsilon}$$

The electron mass inside the slab is:  $n_e m_e L$  so it oscillates in SHM with the electron

$$\text{plasma frequency : } \omega_p = \sqrt{\frac{n_e e^2}{\epsilon m_e}} \quad (\text{A1.1})$$

This frequency is important for the propagation of HF radio, since if the radio frequency is higher than the plasma frequency the electrons will have insufficient time to respond and the HF signal will propagate. If the electron number density increases, then the plasma frequency increases and HF propagation may be affected.

### A1.3 Debye length

The electrons and ions in a plasma have random thermal motion which can violate the quasi-neutrality over distances less than the Debye length. In order to calculate this length it is assumed that the electrons have an average thermal kinetic energy component of  $\frac{1}{2} kT$  in the x direction where k is Boltzmann's constant. If the electrons are then displaced on average by a distance equal to the Debye length  $\lambda_D$  in the x direction as a result of their thermal motion it creates an average electric field of:

$$E_x = \frac{e n_e \lambda_D}{2 \epsilon_0} \quad (A1.2)$$

The average work done against this electric field by the thermal motion is:

$$e E_x \lambda_D \rightarrow e \frac{e n_e \lambda_D}{2 \epsilon_0} \lambda_D \quad \text{and equating this to: } \frac{1}{2} k T \quad \text{gives the Debye length of:}$$

$$\lambda_D = \sqrt{\frac{\epsilon_0 k T}{e^2 n_e}} \quad (A1.3)$$

The assumption of quasi charge neutrality is violated within this distance. A Debye sphere is a plasma volume of radius equal to the Debye length.

### A1.4 Maxwell's equations

Maxwell's equations [Fleisch 2008] in differential form [Equations A1.4, A1.10, A1.11 and A1.12] are based upon the early experimental work in electromagnetism.

#### A1.4.1 Gauss's law

$$\nabla \cdot \mathbf{E} = \frac{\rho_q}{\epsilon_0} \quad (A1.4)$$

where:  $\rho_q$  is a charge density within a region and  $\nabla \cdot \mathbf{E}$  describes the flux of electric field from that region.

This equation is a consequence of Coulomb's Law of electrostatics for the electric field a

$$\text{distance } r \text{ from a point charge } q \text{ at the origin: } \mathbf{E} = \frac{q}{4\pi \epsilon_0 r^2} \mathbf{e}_r \quad (A1.5)$$

where:  $\mathbf{e}_r$  is a unit vector in the radial direction.

Substituting the electric displacement vector  $\mathbf{D}$  defined as:  $\mathbf{D} = \epsilon_0 \mathbf{E}$

$$\text{gives: } \mathbf{D} = \frac{q}{4\pi r^2} \mathbf{e}_r \quad (A1.6)$$

If the charge is surrounded by a closed surface  $\sigma$  that encloses a volume, then Gauss's law

[Boas 1966] gives: 
$$\iint_{\text{closed surface}} \mathbf{D} \cdot \mathbf{n} \, d\sigma = q \quad (\text{A1.7})$$

However if there are many charges inside the volume then the single charge is replaced by

$$\iiint_{\text{volume}} \rho_q \, d\tau \text{ and Gauss's law becomes: } \iint_{\text{closed surface}} \mathbf{D} \cdot \mathbf{n} \, d\sigma = \iiint_{\text{volume}} \rho_q \, d\tau \quad (\text{A1.8})$$

The divergence theorem, which relates a surface integral to a volume integral:

$$\iint_{\text{closed surface}} \mathbf{D} \cdot \mathbf{n} \, d\sigma = \iiint_{\text{volume}} \nabla \cdot \mathbf{D} \, d\tau \quad (\text{A1.9})$$

can then be used to write Gauss's law as: 
$$\iiint_{\text{volume}} \nabla \cdot \mathbf{D} \, d\tau = \iiint_{\text{volume}} \rho_q \, d\tau$$

from which it follows that:  $\nabla \cdot \mathbf{D} = \rho_q$  which is equivalent to Equation A1.4.

#### A1.4.2 No magnetic monopoles

$$\nabla \cdot \mathbf{B} = 0 \quad (\text{A1.10})$$

If a volume of space contains positive electric charge the field lines diverge outwards from that volume element to negative charges beyond, or to infinity. However magnetic field lines always form closed loops and so return to the volume element. As a result the divergence of the magnetic field is always zero.

This lack of symmetry in Maxwell's equations would not be the case if there were magnetic monopoles. The field lines of a magnetic monopole are approximated by those emerging from one end of an infinitely long and infinitely thin solenoid. This is the idea behind the Dirac string [Ohanian 1988]. Searches for magnetic monopoles have not yet proved successful.

#### A1.4.3 Faraday's law

$$\nabla \times \mathbf{E} = -\frac{\partial \mathbf{B}}{\partial t} \quad (\text{A1.11})$$

Michael Faraday's experiments at the Royal Institution around 1831 showed that a current is induced in a conductor as a result of a changing magnetic field. More generally, a changing magnetic field gives rise to an electric field.

The minus sign is sometimes referred to as Lenz's Law or Faraday's Second Law of electromagnetic induction [the direction of the induced EMF is such as to oppose the change to which it is due] and is a statement of the conservation of energy.

#### A1.4.4 Ampère-Maxwell law

$$\nabla \times \mathbf{B} = \mu_0 \mathbf{j} + \frac{1}{c^2} \frac{\partial \mathbf{E}}{\partial t} \quad \text{where: } \frac{1}{c^2} = \mu_0 \epsilon_0 \quad (\text{A1.12})$$

Both steady currents as well as changing electric fields create magnetic fields - a changing or an alternating electric field gives rise to a kind of current called a displacement current.

The second term on the right hand side is a consequence of electromagnetic induction and the first term is a consequence of Ampère's Circuital Law as follows:

$$\oint_{\text{closed loop}} \mathbf{H} \cdot d\mathbf{r} = I \quad (\text{A1.13})$$

If  $\mathbf{j}$  is the current density then the current across an element  $d\sigma$  of a surface with normal vector  $\hat{\mathbf{n}}$  is:  $\mathbf{j} \cdot \hat{\mathbf{n}} d\sigma$  and the total current flowing through the surface enclosed by the closed loop is:

$$\iint_{\text{surface}} \mathbf{j} \cdot \mathbf{n} d\sigma \quad \text{so Ampère's law becomes: } \oint_{\text{closed loop}} \mathbf{H} \cdot d\mathbf{r} = \iint_{\text{surface}} \mathbf{j} \cdot \mathbf{n} d\sigma \quad (\text{A1.14})$$

Stoke's [butterfly net] theorem relates an integral over an open surface to the line integral around a curve bounding that surface:

$$\oint_{\text{closed loop}} \mathbf{H} \cdot d\mathbf{r} = \iint_{\text{surface}} (\nabla \times \mathbf{H}) \cdot \mathbf{n} d\sigma \quad (\text{A1.15})$$

$$\text{We then have: } \iint_{\text{surface}} (\nabla \times \mathbf{H}) \cdot \mathbf{n} d\sigma = \iint_{\text{surface}} \mathbf{j} \cdot \mathbf{n} d\sigma$$

from which it follows that :

$$\nabla \times \mathbf{H} = \mathbf{j} \quad \text{which is the same as: } \nabla \times \mathbf{B} = \mu_0 \mathbf{j} \quad (\text{A1.16})$$

A tetrahedral curlometer arrangement of 4 triaxial matching magnetometers [a reference + 3 components] can be used to find curl  $\mathbf{B}$  from the various field gradients and hence the current density.

### A1.5 The governing equations of magnetohydrodynamics

Magnetohydrodynamics [MHD] is a low frequency approximation to a plasma in which the plasma is treated as a highly conducting fluid. At these low frequencies the electrons have time to respond to the applied electric field and act so as to reduce it to zero in the frame of reference of the plasma - thus terms of the kind:  $\frac{\partial \mathbf{E}}{\partial t}$  which give rise to a displacement current are set to zero. A consequence of this is that a plasma is considered as having a very low AC electrical conductivity in the direction of an applied electric field. Another consequence, which is described below, is that magnetic field lines are said to be 'frozen' into the plasma – they convect with the plasma motion or conversely the plasma convects with the field lines as in the solar wind and the Earth's plasmasphere. Subscripts are used in the following to distinguish between mass density  $\rho_m$  and charge density  $\rho_q$ .

#### A1.5.1 Conservation of electric charge

The flux of current density out of a volume equals the rate of change with time of the electric charge in that volume so that:

$$\nabla \cdot \mathbf{j} = -\frac{\partial \rho_q}{\partial t} \quad (\text{A1.17})$$

#### A1.5.2 Conservation of mass

The flux of matter out of a volume equals the rate of change with time of the matter in that

volume:

$$\nabla \cdot (\rho_m \mathbf{v}) = -\frac{\partial \rho_m}{\partial t} \quad (\text{A1.18})$$

#### A1.5.3 Conservation of momentum

[The rate of change of momentum is equal to the sum of all forces acting - Newton]

$$\rho_m \left[ \frac{\partial}{\partial t} + \mathbf{v} \cdot \nabla \right] \mathbf{v} = -\nabla p + \mathbf{j} \times \mathbf{B} + \rho \mathbf{g} \quad (\text{A1.19})$$

where the term in square brackets is known as the convective derivative.

Note that the force associated with  $\frac{\partial \mathbf{E}}{\partial t}$  is not included in the low-frequency MHD approximation.

#### A1.5.4 Adiabatic equation of state

$$\left[ \frac{\partial}{\partial t} + \mathbf{v} \cdot \nabla \right] \rho \rho^{-\gamma} = 0 \quad (\text{A1.20})$$

#### A1.5.5 Ohm's Law for a plasma

In the frame of reference of the plasma:  $\mathbf{E}_{\text{plasma}} = \frac{\mathbf{j}}{\sigma}$  (A1.21)

In a frame of reference for which  $v \ll c$  substitution into Equation 1.2 gives:

$$\mathbf{E} + \mathbf{v} \times \mathbf{B} = \frac{\mathbf{j}}{\sigma} \quad \text{or:} \quad \mathbf{E} = \frac{\mathbf{j}}{\sigma} - \mathbf{v} \times \mathbf{B} \quad (\text{A1.22})$$

The second term on the right hand side, which is observed in a rest frame through which the plasma is moving, is referred to as the convection electric field.

If the conductivity is infinite, as in a collisionless plasma, then the first term on the right is zero and there is only the convection electric field [ but no current].

#### A1.5.6 Induction equation

This is derived from Ohm's law for a plasma. In the low frequency MHD approximation:

$$\frac{\partial \mathbf{E}}{\partial t} = 0 \quad \text{so Ampère's Law: } \nabla \times \mathbf{B} = \mu_0 \mathbf{j} + \frac{1}{c^2} \frac{\partial \mathbf{E}}{\partial t} \quad \text{reduces to:}$$

$$\nabla \times \mathbf{B} = \mu_0 \mathbf{j} \quad \text{which can be rearranged as: } \mathbf{j} = \frac{\nabla \times \mathbf{B}}{\mu_0} \quad (\text{A1.23})$$

Substitution of this result into Ohm's law for a plasma [A1.22] gives:

$$\mathbf{E} = -\mathbf{v} \times \mathbf{B} + \frac{\nabla \times \mathbf{B}}{\mu_0 \sigma} \quad (\text{A1.24})$$

$$\text{Taking the curl of both sides: } \nabla \times \mathbf{E} = -\nabla \times \mathbf{v} \times \mathbf{B} + \frac{\nabla \times \nabla \times \mathbf{B}}{\mu_0 \sigma} \quad (\text{A1.25})$$

$$\text{The useful vector identity: } \nabla \times \nabla \times \mathbf{B} = [\nabla(\nabla \cdot \mathbf{B}) - \nabla^2 \mathbf{B}] \quad (\text{A1.26})$$

$$\text{simplifies here to: } \nabla \times \nabla \times \mathbf{B} = -\nabla^2 \mathbf{B} \quad \text{because: } \nabla \cdot \mathbf{B} = 0$$

Substituting this result into the right hand side of Equation A1.25 and Faraday's law [Equation A1.11] into the left hand side then gives the very useful MHD induction equation:

$$\frac{\partial \mathbf{B}}{\partial t} = \nabla \times [\mathbf{v} \times \mathbf{B}] + \frac{\nabla^2 \mathbf{B}}{\mu_0 \sigma} \quad (\text{A1.27})$$

The induction equation describes how the magnetic field propagates in time. The first term on the right describes the convection of the magnetic field with the plasma flow and the second term on the right describes diffusion of the magnetic field through the plasma. Diffusion arises when particles in the plasma collide and are scattered

### A1.5.7 Diffusion of electric and magnetic fields through a plasma

A highly conducting plasma tends to retain any magnetic and electric fields that are present since decreasing say the magnetic field would induce an electric field that would cause currents to flow that would act to increase the magnetic field

The vector operator:  $\nabla \triangleq \mathbf{i} \frac{\partial}{\partial \mathbf{x}} + \mathbf{j} \frac{\partial}{\partial \mathbf{y}} + \mathbf{k} \frac{\partial}{\partial \mathbf{z}}$  is a measure of the rate of change over

distance. If the parameter L defines the scale size of the system such that:  $\mathbf{L} \sim \mathbf{x} \sim \mathbf{y} \sim \mathbf{z}$

then:  $|\nabla| \sim \frac{1}{L}$

In the induction equation [A1.27] the convection term has magnitude:

$$\nabla \times [\mathbf{v} \times \mathbf{B}] \sim \frac{v\mathbf{B}}{L}$$

and the diffusion term has magnitude:  $\frac{\nabla^2 \mathbf{B}}{\mu_0 \sigma} \sim \frac{B}{\mu_0 \sigma L^2}$

The ratio of the convection magnitude to the diffusion magnitude is called the Magnetic Reynold's [or Lundquist] number  $R_m$  :

$$R_m = \mu_0 \sigma v L \quad (\text{A1.28})$$

If  $R_m \gg 1$  then the diffusion term is relatively unimportant compared to the convection term and the magnetic field lines are convected with the plasma. This is the concept of *frozen in* lines of magnetic flux. However where the scale size L is comparatively small, such as within the thickness of current sheets, then the *Magnetic Reynold's number* is smaller and the diffusion of plasma across field lines becomes important .

## A1.6 Magnetohydrodynamic waves

### A1.6.1 Magnetic pressure and tension on a flux tube

In a cold plasma where there is no appreciable *gas* pressure arising from the motion of the particles the magnetic pressure is the only pressure. As in the derivation of the induction

equation the low frequency MHD approximation  $\frac{\partial \mathbf{E}}{\partial t} = 0$  means that:

$$\nabla \times \mathbf{B} = \mu_0 \mathbf{j} + \frac{1}{c^2} \frac{\partial \mathbf{E}}{\partial t} \quad \text{reduces to: } \nabla \times \mathbf{B} = \mu_0 \mathbf{j} \quad \text{or: } \mathbf{j} = \frac{\nabla \times \mathbf{B}}{\mu_0}$$

The magnetic force:  $\mathbf{F}_m = \mathbf{j} \times \mathbf{B}$  then becomes:

$$\mathbf{F}_m = \frac{(\nabla \times \mathbf{B}) \times \mathbf{B}}{\mu_0} = -\frac{\mathbf{B} \times (\nabla \times \mathbf{B})}{\mu_0} = \frac{-\nabla B^2}{2\mu_0} + \frac{(\mathbf{B} \cdot \nabla) \mathbf{B}}{\mu_0} \quad (\text{A1.29})$$

$$\text{where use has been made of the vector identities: } \mathbf{A} \times \mathbf{B} = -\mathbf{B} \times \mathbf{A} \quad (\text{A1.30})$$

$$\text{and: } \nabla(\mathbf{A} \cdot \mathbf{B}) = (\mathbf{B} \cdot \nabla) \mathbf{A} + (\mathbf{A} \cdot \nabla) \mathbf{B} + \mathbf{B} \times (\nabla \times \mathbf{A}) + \mathbf{A} \times (\nabla \times \mathbf{B}) \quad (\text{A1.31})$$

$$\text{which becomes: } \nabla(B^2) = 2(\mathbf{B} \cdot \nabla) \mathbf{B} + 2\mathbf{B} \times (\nabla \times \mathbf{B}) \quad \text{when: } \mathbf{A} = \mathbf{B} \quad (\text{A1.32})$$

$$\text{so that: } \mathbf{B} \times (\nabla \times \mathbf{B}) = \frac{\nabla(B^2)}{2} - (\mathbf{B} \cdot \nabla) \mathbf{B} \quad (\text{A1.33})$$

The magnetic force  $\mathbf{F}_m$  on a flux tube can be resolved into two components, a tension along the tube and a lateral compression. In the frame of reference of the magnetic field a unit vector along the direction of the field line is defined here as  $\hat{\mathbf{b}}$  so that  $\mathbf{B} = B \hat{\mathbf{b}}$ . The scalar product  $\hat{\mathbf{b}} \cdot \nabla$  is then the projection of the spatial derivatives along the field line and as it is a scalar quantity can be written as:  $\hat{\mathbf{b}} \cdot \nabla = \frac{\partial}{\partial s}$  where  $s$  is a distance measured along the field line.

$$(\mathbf{B} \cdot \nabla) \mathbf{B} = B \frac{\partial(B \hat{\mathbf{b}})}{\partial s} = B \hat{\mathbf{b}} \frac{\partial B}{\partial s} + B^2 \frac{\partial \hat{\mathbf{b}}}{\partial s} = \hat{\mathbf{b}} \frac{\partial}{\partial s} \left( \frac{B^2}{2} \right) + B^2 \frac{\mathbf{R}_c}{R_c^2} \quad (\text{A1.34})$$

where:  $\mathbf{R}_c$  is the radius of curvature vector shown in Figure A1.1

The spatial gradient operator can be written as the sum of two components:

$$\nabla = \nabla_{\perp} + \nabla_{\parallel} = \nabla_{\perp} + \hat{\mathbf{b}} \frac{\partial}{\partial s} \quad (\text{A1.35})$$

$$\begin{aligned} \mathbf{F}_m &= -\nabla_{\perp} \left( \frac{B^2}{2\mu_0} \right) - \hat{\mathbf{b}} \frac{\partial}{\partial s} \left( \frac{B^2}{2\mu_0} \right) + \hat{\mathbf{b}} \frac{\partial}{\partial s} \left( \frac{B^2}{2\mu_0} \right) + \frac{B^2 \mathbf{R}_c}{\mu_0 R_c^2} \\ &= -\nabla_{\perp} \left( \frac{B^2}{2\mu_0} \right) + \frac{B^2 \mathbf{R}_c}{\mu_0 R_c^2} \end{aligned} \quad (\text{A1.36})$$

The first term on the right hand side of Equation A1.36 is a compression force which resists field lines being forced together and the second term a tension which resists the field lines being bent as illustrated in Figure A1.1.

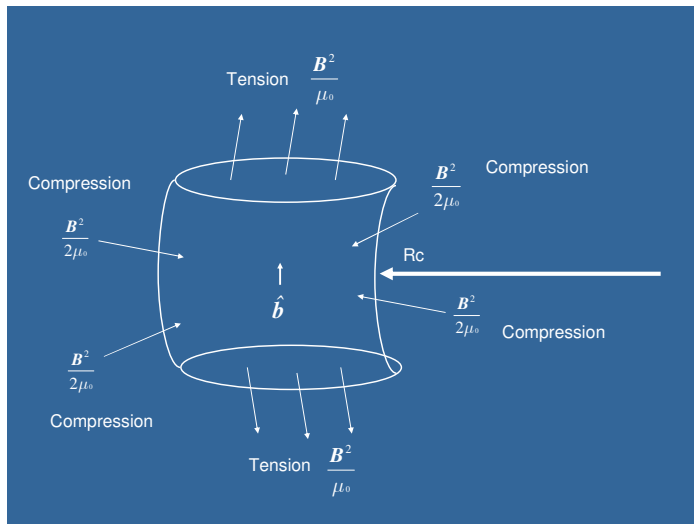


**Figure A1.1**

**Magnetic forces on an element of a magnetic flux tube.**

This diagram shows how an element of a magnetic flux tube is able to resist:

tension forces of  $\frac{B^2}{\mu_0}$  and  
 compression forces of  $\frac{B^2}{2\mu_0}$

**A1.6.2 Alfvén shear and compressional waves**

The importance of these compression and tension forces is that they provide the restoring forces for plasma oscillations. The inertia that allows waves to propagate is provided by the mass of the plasma. For transverse Alfvén waves the restoring force is provided only by the tension in the field lines and there is no compression of the plasma within the flux tube. All field line  $\mathbf{b}$  and plasma displacements  $\mathbf{u}$  are parallel and normal to  $\mathbf{B}$  and the flux tubes all oscillate together so that the distances between the waves on adjacent flux tubes remains constant. Because the plasma is displaced, but not compressed, an Alfvén wave is often described as a shear wave. Since the restoring force for an Alfvén wave is provided by the magnetic field lines and not by any plasma compression it is unaffected by the thermal pressure in a warm plasma and therefore is independent of the plasma  $\beta$  parameter.

Compression of the magnetic field allows waves to propagate across field lines and a combination of compression and tension forces allows propagation at arbitrary angles. In these *compressional waves* the wavevector  $\mathbf{k}$  and hence the wavefronts can be oriented at some angle to the field lines so that the displacements between adjacent flux tubes can be staggered as depicted in the lower diagram in Figure A1.2. The upper diagram shows the relationship between the wavevector  $\mathbf{k}$  and a unit vector  $\hat{\mathbf{b}}$  in the local magnetic field direction with Alfvén shear waves that propagate along the direction of the magnetic field.

For Alfvén waves the displacement of the magnetic field is transverse to  $\hat{\mathbf{b}}$  and the wavevector  $\mathbf{k}$  is normal the direction of the plasma displacement. These waves do not compress the plasma and alter its pressure and density. The lower diagram shows the same vectors for the fast and slow mode compressional waves.

Because for compressional waves the displacement of the magnetic field  $\hat{\mathbf{b}}$  is in the plane of the wavevector  $\mathbf{k}$  and the magnetic field  $\mathbf{B}$ , it was possible to represent these plasma compression waves in two dimensions.

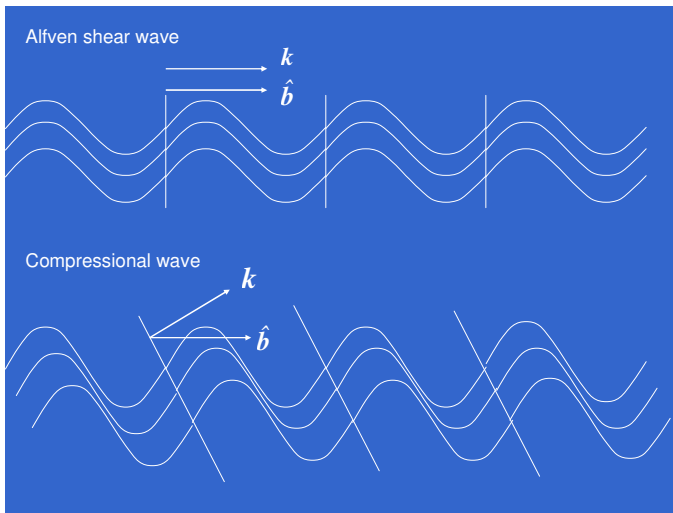


**Figure A1.2**  
**Alfvén shear and compressional wave wavefronts**

The unit vector in the direction of the local magnetic field is denoted by  $\hat{\mathbf{b}}$  and the wavevector by  $\mathbf{k}$

### A1.6.3 Derivation of magnetohydrodynamic wave dispersion

The following derivation of the MHD wave dispersion relationships is for small perturbations only. In equilibrium the plasma parameters are constants and are denoted with a subscript of zero. Small time varying perturbations around these equilibrium values are denoted with a subscript of unity. Thus the magnetic field strength, plasma velocity, mass density and scalar magnetic pressure are:

$$\mathbf{B} = \mathbf{B}_0 + \mathbf{B}_1 \quad (\text{A1.37})$$

$$\mathbf{v} = \mathbf{v}_0 + \mathbf{v}_1 \quad \text{In the frame of reference of the plasma } \mathbf{v}_0 = 0 \quad (\text{A1.38})$$

$$\rho_m = \rho_0 + \rho_1 \quad (\text{A1.39})$$

$$p_m = p_0 + p_1 \quad (\text{A1.40})$$

If  $\gamma = 1$  the equation for the speed of sound in a gas under adiabatic conditions:

$$c_s^2 = \frac{\gamma p_m}{\rho_m} \quad \text{means that:} \quad p_1 = c^2 \rho_1 \quad (\text{A1.41})$$

As equilibrium values differentiate to zero over time the conservation of mass equation

[Equation A1.18] rearranged as:  $\frac{\partial \rho_m}{\partial t} + \nabla \cdot (\rho_m \mathbf{v}) = 0$  becomes:

$$\frac{\partial \rho_1}{\partial t} + \rho_0 \nabla \cdot \mathbf{v}_1 = 0 \quad (\text{A1.42})$$

and the conservation of momentum equation [Equation A1.19]:

$$\rho_m \left[ \frac{\partial}{\partial t} + \mathbf{v} \cdot \nabla \right] \mathbf{v} = -\nabla p + \mathbf{j} \times \mathbf{B} + \rho \mathbf{g} \quad \text{becomes:}$$

$$\rho_0 \frac{\partial \mathbf{v}_1}{\partial t} = -\nabla p_1 + \frac{(\nabla \times \mathbf{B}_1) \times \mathbf{B}_0}{\mu_0} \quad (\text{A1.43})$$

In the MHD limit of large electrical conductivity Ohm's law for a plasma [Equation A1.22]:

$\mathbf{E} + \mathbf{v} \times \mathbf{B} = \frac{\mathbf{j}}{\sigma}$  becomes:  $\mathbf{E} = -\mathbf{v} \times \mathbf{B}$  and taking the curl of both sides gives:

$$\nabla \times \mathbf{E} = -\nabla \times (\mathbf{v} \times \mathbf{B})$$

Equating this to Faraday's law [Equation A1.11]:  $\nabla \times \mathbf{E} = -\frac{\partial \mathbf{B}}{\partial t}$  then yields:

$$\frac{\partial \mathbf{B}_1}{\partial t} = \nabla \times (\mathbf{v}_1 \times \mathbf{B}_0) \quad (\text{A1.44})$$

Plane wave solutions to Equations A1.37 – A1.40 are of the general form:

$$\xi_1 = \delta \xi \exp(i(\mathbf{k} \cdot \mathbf{x} - \omega t + \phi)) \quad (\text{A1.45})$$

where:  $\xi$  stands for any one of the perturbed plasma parameters  $\mathbf{B}$ ,  $\mathbf{v}$ ,  $\rho_m$  or  $p_m$

The phase velocity of these plane wave solutions is:  $\mathbf{v}_{\text{phase}} = \frac{\omega}{k} \hat{\mathbf{k}}$  where:  $\mathbf{k} = k \hat{\mathbf{k}}$  and

the dispersion relations describe how  $\omega$  depends upon  $k$ .

$$\frac{\partial \xi_1}{\partial t} = -i \omega \delta \xi \exp(i(\mathbf{k} \cdot \mathbf{x} - \omega t + \phi))$$

so that after dividing the right hand side by:  $-i \exp(i(\mathbf{k} \cdot \mathbf{x} - \omega t + \phi))$

$$\frac{\partial \xi_1}{\partial t} \rightarrow -\omega \delta \xi$$

If the wave is considered as travelling in the x direction:

$$\nabla \cdot \mathbf{v} \rightarrow \frac{\partial v_1}{\partial x} = i \mathbf{k} \cdot \mathbf{dv} \exp(i(\mathbf{k} \cdot \mathbf{x} - \omega t + \phi)) \quad (\text{A1.46})$$

Making these substitutions in the revised conservation of mass equation [Equation A1.42] gives:

$$-i \omega \delta \rho \exp(i(\mathbf{k} \cdot \mathbf{x} - \omega t + \phi)) + i \rho_0 \mathbf{k} \cdot \mathbf{dv} \exp(i(\mathbf{k} \cdot \mathbf{x} - \omega t + \phi)) = 0$$

$$\text{which reduces to:} \quad -\omega \delta \rho + \rho_0 \mathbf{k} \cdot \mathbf{dv} = 0 \quad (\text{A1.47})$$

The last term in the conservation of momentum equation [Equation A1.43] can be expanded using the vector identities:

$$\mathbf{A} \times \mathbf{B} = -\mathbf{B} \times \mathbf{A} \quad (\text{A1.48})$$

$$\nabla(\mathbf{A} \cdot \mathbf{B}) = (\mathbf{B} \cdot \nabla)\mathbf{A} + (\mathbf{A} \cdot \nabla)\mathbf{B} + \mathbf{B} \times (\nabla \times \mathbf{A}) + \mathbf{A} \times (\nabla \times \mathbf{B}) \quad (\text{A1.49})$$

so that:

$$(\nabla \times \mathbf{B}_1) \times \mathbf{B}_0 = -\mathbf{B}_0 \times (\nabla \times \mathbf{B}_1) = \nabla(\mathbf{B}_0 \cdot \mathbf{B}_1) - (\mathbf{B}_1 \cdot \nabla)\mathbf{B}_0 - (\mathbf{B}_0 \cdot \nabla)\mathbf{B}_1 - \mathbf{B}_1 \times (\nabla \times \mathbf{B}_0) \quad (\text{A1.50})$$

However the last two spatial derivative terms in:  $\mathbf{B}_0 \cdot \nabla$  and  $\nabla \times \mathbf{B}_0$  are both zero as  $\mathbf{B}_0$  is regarded as being constant in space.

With:  $\frac{\partial \mathbf{v}_1}{\partial t} \rightarrow -\omega \delta \mathbf{v}$   $\nabla p \rightarrow -k \delta p$  and  $\mathbf{B}_1 \rightarrow \delta \mathbf{B}$  the conservation of momentum

equation becomes:

$$-\rho_0 \omega \delta \mathbf{v} = -k \delta p + \frac{(\mathbf{k} \cdot \mathbf{B}_0) \delta \mathbf{B}}{\mu_0} - \frac{(\delta \mathbf{B} \cdot \mathbf{B}_0) \mathbf{k}}{\mu_0} \quad (\text{A1.51})$$

The right hand side of the MHD formulation of Ohm's Law [Equation A1.44] can be expanded using the vector identity:

$$\nabla \times (\mathbf{A} \times \mathbf{B}) = (\mathbf{B} \cdot \nabla)\mathbf{A} - \mathbf{B}(\nabla \cdot \mathbf{A}) - (\mathbf{A} \cdot \nabla)\mathbf{B} + \mathbf{A}(\nabla \cdot \mathbf{B}) \quad (\text{A1.52})$$

$$\text{so that: } \nabla \times (\mathbf{v}_1 \times \mathbf{B}_0) = (\mathbf{B}_0 \cdot \nabla)\mathbf{v}_1 - \mathbf{B}_0(\nabla \cdot \mathbf{v}_1) - (\mathbf{v}_1 \cdot \nabla)\mathbf{B}_0 + \mathbf{v}_1(\nabla \cdot \mathbf{B}_0) \quad (\text{A1.53})$$

The first and last derivatives of  $\mathbf{B}_0$  are zero so that Equation A1.44 can be written as:

$$\frac{\partial \mathbf{B}_1}{\partial t} = -\mathbf{B}_0(\nabla \cdot \mathbf{v}_1) - (\mathbf{v}_1 \cdot \nabla)\mathbf{B}_0 \quad (\text{A1.54})$$

With:  $\frac{\partial \mathbf{B}_1}{\partial t} \rightarrow -\omega \delta \mathbf{B}$  and  $\nabla \cdot \mathbf{v} \rightarrow \mathbf{k} \cdot \delta \mathbf{v}$  the MHD formulation of Ohm's law

$$\text{becomes:} \quad -\omega \delta \mathbf{B} = (\mathbf{k} \cdot \mathbf{B}_0) \delta \mathbf{v} - (\mathbf{k} \cdot \delta \mathbf{v}) \mathbf{B}_0 \quad (\text{A1.55})$$

Finally the adiabatic sound speed equation [Equation 1.41] becomes:

$$\delta p = c^2 \delta \rho \quad (\text{A1.56})$$

To summarise therefore, there are 4 perturbation equations in the 4 unknowns

$\delta \mathbf{B}$   $\delta \mathbf{v}$   $\delta p$   $\delta \rho$  which are as follows:

$$-\omega \delta \rho + \rho_0 \mathbf{k} \cdot \delta \mathbf{v} = 0 \quad (\text{A1.57})$$

$$-\rho_0 \omega \delta \mathbf{v} = -\mathbf{k} \delta p + \frac{(\mathbf{k} \cdot \mathbf{B}_0) \delta \mathbf{B}}{\mu_0} - \frac{(\delta \mathbf{B} \cdot \mathbf{B}_0) \mathbf{k}}{\mu_0} \quad (\text{A1.58})$$

$$-\omega \delta \mathbf{B} = (\mathbf{k} \cdot \mathbf{B}_0) \delta \mathbf{v} - (\mathbf{k} \cdot \delta \mathbf{v}) \mathbf{B}_0 \quad (\text{A1.59})$$

$$\delta p = c_s^2 \delta \rho \quad (\text{A1.60})$$

$$\text{Combining Equation A1.57 with Equation A1.60 gives: } \delta p = \frac{\rho_0 c_s^2}{\omega} \mathbf{k} \cdot \delta \mathbf{v} \quad (\text{A1.61})$$

and finally substituting Equation A1.59 and Equation A1.61 into Equation A1.58 gives:

$$\begin{aligned} -\rho_0 \omega \delta \mathbf{v} = & -\frac{\rho_0 c_s^2}{\omega} (\mathbf{k} \cdot \delta \mathbf{v}) \mathbf{k} - \frac{(\mathbf{k} \cdot \mathbf{B}_0)}{\mu_0 \omega} [(\mathbf{k} \cdot \mathbf{B}_0) \delta \mathbf{v} - (\mathbf{k} \cdot \delta \mathbf{v}) \mathbf{B}_0] \\ & + \frac{1}{\mu_0 \omega} [(\mathbf{k} \cdot \mathbf{B}_0)(\mathbf{B}_0 \cdot \delta \mathbf{v}) \mathbf{k} - (\mathbf{k} \cdot \delta \mathbf{v}) B_0^2 \mathbf{k}] \end{aligned} \quad (\text{A1.62})$$

Equation A1.62 contains all the information about Alfvén waves. Their phase speed depends upon the angle between the magnetic field and the wavevector, the sound speed and the Alfvén speed. The solutions give the dispersion relationships for the four kinds of MHD waves:

$$\text{Acoustic wave: } \omega^2 = c_s^2 k^2 \quad (\text{A1.63})$$

$$\text{Alfvén [shear] wave: } \omega^2 = k^2 v_A^2 \cos^2 \theta \quad c_s = 0 \quad (\text{A1.64})$$

Fast mode [+sign] and slow mode [-sign] magnetosonic [compressional] waves:

$$\omega^2 = k^2 \frac{(c_s^2 + v_A^2)}{2} \left[ 1 \pm \sqrt{1 - \frac{4 c_s^2 v_A^2 \cos^2 \theta}{(c_s^2 + v_A^2)^2}} \right] \quad (\text{A1.65 and A1.66})$$

If  $c_s = 0$  these last equations reduce to:  $\omega^2 = k^2 v_A^2$  as would be the case if there was negligible plasma pressure.

The Alfvén speed  $v_A$  is given by: 
$$v_A^2 = \frac{B^2}{\mu_0 \rho_m} \quad (\text{A1.67})$$

#### A1.6.4 Waves propagating parallel to the field lines

**Acoustic waves** Plasma displacements  $\delta \mathbf{v}_{\parallel}$  along the direction of the field lines give rise to purely acoustic waves as there is no shear component. Since:  $(\mathbf{k} \cdot \mathbf{B}_0) \delta \mathbf{v}_{\parallel} = (\mathbf{k} \cdot \delta \mathbf{v}_{\parallel}) \mathbf{B}_0$  only the first term survives giving:

$$-\rho_0 \omega \delta \mathbf{v}_{\parallel} = -\frac{\rho_0 c_s^2}{\omega} (\mathbf{k} \cdot \delta \mathbf{v}_{\parallel}) \mathbf{k} \quad \text{which reduces to: } \omega^2 = k^2 c_s^2 \quad (\text{A1.68})$$

This is an interesting result as it implies that field line disturbances also create acoustic waves that travel down towards the Earth, particularly at Northern latitudes where their momentum is transferred to the ionosphere and then to the atmosphere where they might be detected as micro-barometric fluctuations.

**Alfvén shear waves** Plasma displacement at right angles to the field lines  $\delta \mathbf{v}_{\perp}$  gives rise to Alfvén shear waves. If  $\mathbf{k}_{\parallel}$  is along the field line and  $\delta \mathbf{v}_{\perp}$  is at right angles then:  $\mathbf{k}_{\parallel} \cdot \delta \mathbf{v}_{\perp} = 0$  and only the first half of the second term survives giving:

$$-\rho_0 \omega \delta \mathbf{v}_{\perp} = -\frac{(\mathbf{k}_{\parallel} \cdot \mathbf{B}_0)}{\mu_0} \left[ \frac{(\mathbf{k}_{\parallel} \cdot \mathbf{B}_0) \delta \mathbf{v}_{\perp}}{\omega} \right]$$

which reduces to:  $\omega^2 = k^2 v_A^2 \quad (\text{A1.69})$

Alfvén shear waves are field guided even though the wave vector  $\mathbf{k}$  may be at some oblique angle to the field lines. Alfvén waves do not propagate in the direction of the wave vector and its only effect is to determine the speed of travel along the field lines. If the field lines curve Alfvén shear waves continue to follow the field lines.

### A1.6.5 Waves propagating obliquely to the field lines

Magnetosonic waves travel across field lines in the direction of the wavevector  $\mathbf{k}$ . If the field lines curve then the angle that these waves makes to the field lines changes.

**Fast mode magnetosonic waves** If  $\mathbf{k}_\perp$  is perpendicular to the field line and  $\delta\mathbf{v}_\parallel = 0$  is at right angles then:  $\mathbf{k}_\parallel \cdot \delta\mathbf{v}_\perp = 0$  and  $\mathbf{k}_\perp \cdot \mathbf{B} = 0$  so that only terms containing  $\mathbf{k}_\perp \cdot \delta\mathbf{v}_\perp$  survive giving:

$$-\rho_0 \omega \delta\mathbf{v}_\perp = -\frac{\rho_0 c_s^2}{\omega} (\mathbf{k}_\perp \cdot \delta\mathbf{v}_\perp) \mathbf{k}_\perp - \frac{(\mathbf{k}_\perp \cdot \delta\mathbf{v}_\perp) B_0^2 \mathbf{k}_\perp}{\mu_0 \omega} \quad (\text{A1.70})$$

Substituting the Alfvén speed relation:  $v_A^2 = \frac{B^2}{\mu_0 \rho_m}$  gives the dispersion relation for fast

$$\text{mode waves as:} \quad \omega^2 = k^2 (c_s^2 + v_A^2) \quad (\text{A1.71})$$

Thus the fast mode magnetosonic wave propagates with a phase speed of:

$$v_{\text{fast}} = \frac{\omega}{k} = \sqrt{(c_s^2 + v_A^2)} \quad \text{in the direction perpendicular to the field lines.}$$

In cold plasma [Section 1.7.1] where:  $c_s = 0$  this equation just reduces to the Alfvén speed and the fast mode wave propagates isotropically.

In the fast mode the plasma is compressed so that  $\delta\mathbf{p} \neq 0$  and  $\delta\rho \neq 0$ .

The magnetic field strength also changes so that  $\delta\mathbf{B} \neq 0$  and the changes in magnetic field strength and plasma pressure are in phase as shown in the upper trace in Figure A1.3.

The fast mode wave has a component of  $\mathbf{b} \cdot \hat{\mathbf{b}}$  along the magnetic field which allows it to transmit plasma pressure variations. The group velocity and hence the energy propagation is always parallel to the phase velocity. No field-aligned current is carried because  $\mathbf{j} \cdot \mathbf{B}$  is zero.

**Slow mode magnetosonic waves** These are similar to the fast mode waves except that the changes in pressure are  $180^\circ$  out of phase with changes in the magnetic field strength as shown in the lower trace in Figure A1.3.

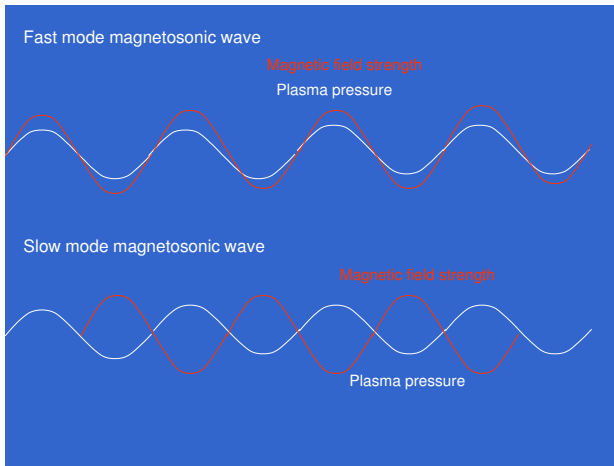


**Figure A1.3**

**Magnetic field and plasma pressure displacements.**

In the fast mode the magnetic field strength is in-phase with the plasma pressure whilst in the slow mode it is in anti-phase.

**A1.6.6 Friedrich diagram**

The way in which the phase speed varies with the angle between the wave-vector and the magnetic field direction can be represented in the form of a Friedrich polar plot diagram of which an example is shown in Figure A1.4 where  $v_A > c_s$

In the case of the Alfvén waves the propagation direction is always along the field lines. In a warm plasma the fast mode [green] is able to propagate across field lines with a phase speed faster than the Alfvén speed [except along the field lines] because plasma compression increases the restoring force.

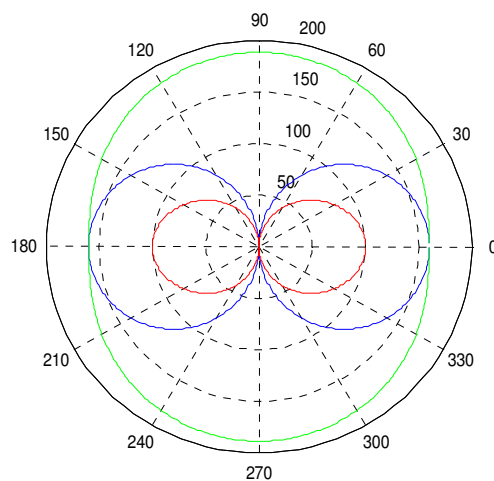


**Figure A1.4 Friedrich polar plot of phase velocity**

The phase speed [in  $\text{kms}^{-1}$ ] is shown in blue for Alfvén shear waves, in green for fast mode waves and in red for slow mode waves.

Plasma parameters for this plot were:  $B=40\text{nT}$   $p=0.5\text{nPa}$   $\rho_m=30 \text{amu cm}^{-3}$  and  $\beta=0.8$

### A1.6.7 E:B ratio for Alfvén waves

The above derivation of Alfvén waves is concerned with displacements in the magnetic field. But there are also associated oscillations in the electric field which have the dispersion

$$\text{relation: } v_A = \frac{\omega_E}{k_E} = \frac{\omega_B}{k_B} \quad [\text{Keller, Getty and Skove 1993}] \quad (\text{A1.72})$$

This allows for the frequency  $\omega$  and wavenumber  $k$  to be different for the electric and magnetic fields as denoted by subscripts.

Orthogonal plane wave displacements in the magnetic and electric fields are of the form:

$$B_y = B_0 \sin(k_B x - \omega_B t) \quad (\text{A1.73})$$

$$E_z = E_0 \sin(k_E x - \omega_E t + \phi) \quad (\text{A1.74})$$

where  $\phi$  allows for a possible phase shift between the electric and magnetic fields .

Differentiating Equation A1.73 w.r.t.  $t$  and Equation A1.74 w.r.t.  $x$  gives:

$$\frac{\partial B_y}{\partial t} = -\omega_B B_0 \cos(k_B x - \omega_B t) \quad (\text{A1.75})$$

$$\text{and: } \frac{\partial E_z}{\partial x} = k_E E_0 \cos(k_E x - \omega_E t + \phi) \quad (\text{A1.76})$$

Equations A1.75 and A1.76 can be equated using Faraday's Law for a plane wave:

$$\frac{\partial E_z}{\partial x} = - \frac{\partial B_y}{\partial t}$$

$$\text{so that: } k_E E_0 \cos(k_E x - \omega_E t + \phi) = \omega_B B_0 \cos(k_B x - \omega_B t)$$

which can be written using Equation A1.72 as:

$$k_E E_0 \cos(k_E x - \omega_E t + \phi) = v_A k_B B_0 \cos(k_B x - \omega_B t) \quad (\text{A1.77})$$

To satisfy this equality for all  $x$  and  $t$  requires that:  $k_E = k_B$   $\omega_E = \omega_B$   $\phi = 2\pi n$

so that the suffixes can be dropped to give:

$$k E_0 \cos(k x - \omega t + 2\pi n) = v_A k B_0 \cos(k x - \omega t) \quad (\text{A1.78})$$

$$\text{from which it follows that: } v_A = \frac{E_0}{B_0} \quad (\text{A1.79})$$

For an electromagnetic wave in free space this ratio is the speed of light  $c$  which can be written as:  $c = 300 \text{mV m}^{-1} \text{nT}^{-1}$

The Alfvén waves encountered in these studies however had speeds around 300 times lower so that:  $v_A \sim 1 \text{mV m}^{-1} \text{nT}^{-1}$

### A1.6.8 Summary

The four kinds of magnetohydrodynamic waves described here are all mechanisms by which ULF wave energy can be transmitted from a magnetospheric disturbance to a satellite or to the ionosphere. Table A1.1 summarises the dispersion relationships for the different modes.

Note however that these modes were derived on the assumption of small perturbations.

Mode	Dispersion relation	Notes
Sound wave	$\omega^2 = c_s^2 k^2$	$c_s^2 = \frac{\gamma p_m}{\rho_m}$
Alfvén shear wave	$\omega^2 = k^2 v_A^2 \cos^2 \theta$	Propagation along magnetic field lines $v_A^2 = \frac{B^2}{\mu_0 \rho_m}$
Fast mode magnetosonic wave	$\omega^2 = k^2 \frac{(c_s^2 + v_A^2)}{2} \left[ 1 + \sqrt{1 - \frac{4 c_s^2 v_A^2 \cos^2 \theta}{(c_s^2 + v_A^2)^2}} \right]$	Propagation along wave-vector k
Slow mode magnetosonic wave	$\omega^2 = k^2 \frac{(c_s^2 + v_A^2)}{2} \left[ 1 - \sqrt{1 - \frac{4 c_s^2 v_A^2 \cos^2 \theta}{(c_s^2 + v_A^2)^2}} \right]$	

**Table A1.1 Summary of dispersion relationships**

The fast mode magnetosonic modes are important because they are able to propagate across the magnetic field lines and the Alfvén shear waves are important because they direct wave energy to the ionosphere. In cold plasma the fast mode waves propagate across the field lines at the Alfvén speed but in warm plasma the speed across the field lines is faster. Coupling between these modes is discussed in Section 2.4.

### A1.7 The existence of electromagnetic-hydrodynamic waves

Hannes Alfvén published a one column paper in the journal Nature [Alfvén 1942] that showed the existence of electromagnetic-hydrodynamic waves in plasma. In view of the historical importance of this work it was thought worthwhile following through the mathematics. At the time he seems to have been interested in the plasma in mercury arc rectifiers and in the migration of sunspots. This section should be read with reference to the original paper which contains the statement:

$$\text{by elementary calculation we obtain } \frac{\partial^2 H_x}{\partial z^2} = \frac{4\pi\rho}{H_z^2} \left( \frac{\partial^2 H_x}{\partial t^2} \right) \quad (\text{A1.72})$$

Although SI units are used here cgs units were originally used. However the use of the magnetising intensity  $\mathbf{H}$  has been preserved, in line with the original manuscript.

$$\text{The Ampère-Maxwell law is: } \nabla \times \mathbf{B} = \mu_0 \mathbf{j} + \frac{1}{c^2} \frac{\partial \mathbf{E}}{\partial t} \quad (\text{A1.73})$$

but in a highly conducting medium the second term can be neglected because at low frequencies the electric field  $\mathbf{E}$  will have time to act on the charges to create a space field that cancels the original time-varying electric field.

With:  $\mathbf{B} = \mu_0 \mathbf{H}$  the Ampère-Maxwell law can then be rewritten as:

$$\nabla \times \mathbf{H} = \mathbf{j} \quad (\text{A1.74})$$

$$\text{Faraday's Law is: } \nabla \times \mathbf{E} = -\frac{\partial \mathbf{B}}{\partial t}$$

$$\text{or: } \nabla \times \mathbf{E} = -\mu_0 \frac{\partial \mathbf{H}}{\partial t} \quad (\text{A1.75})$$

$$\text{and Ohm's Law for a plasma is: } \mathbf{E} = \frac{\mathbf{j}}{\sigma} - \mathbf{v} \times \mathbf{B}$$

where the right hand term is the conduction electric field observed in a frame of reference through which the plasma is in motion.

If the electrical conductivity is sufficiently high the resistive term can be neglected to give

$$\text{the convection electric field as: } \mathbf{E} = -\mu_0 (\mathbf{v} \times \mathbf{H}_z) \quad (\text{A1.76})$$

where the z subscript was introduced because the convection electric field was assumed to be created by the motion of plasma through a magnetic field along the z direction.

Newton's second equation of motion for a fluid can be written:  $\rho \frac{\partial \mathbf{v}}{\partial t} = (\mathbf{j} \times \mathbf{B}) - \nabla P$

but in the absence of a pressure gradient it reduces to:  $\rho \frac{\partial \mathbf{v}}{\partial t} = \mathbf{j} \times \mathbf{B}$

which can be rearranged as:  $\frac{\partial \mathbf{v}}{\partial t} = \frac{\mu_0}{\rho} (\mathbf{j} \times \mathbf{H})$  (A1.77)

Equation A1.74 into Equation A1.77 gives:  $\frac{\partial \mathbf{v}}{\partial t} = \frac{\mu_0}{\rho} \left( (\nabla \times \mathbf{H}) \times \mathbf{H} \right)$  (A1.78)

Differentiating Equation A1.75 with respect to time:  $\nabla \times \frac{\partial \mathbf{E}}{\partial t} = -\mu_0 \frac{\partial^2 \mathbf{H}}{\partial t^2}$  (A1.79)

and also Equation A1.26 with respect to time:  $\frac{\partial \mathbf{E}}{\partial t} = -\mu_0 \left( \frac{\partial \mathbf{v}}{\partial t} \times \mathbf{H}_z \right)$  (A1.80)

Substituting Equation A1.80 into Equation A1.79:  $\nabla \times \left( \frac{\partial \mathbf{v}}{\partial t} \times \mathbf{H}_z \right) = \frac{\partial^2 \mathbf{H}}{\partial t^2}$  (A1.81)

and substituting Equation A1.78 into Equation A1.81 yields:

$$\nabla \times \left( \left( (\nabla \times \mathbf{H}) \times \mathbf{H} \right) \times \mathbf{H}_z \right) = \frac{\rho}{\mu_0} \frac{\partial^2 \mathbf{H}}{\partial t^2} \quad (\text{A1.82})$$

Equation A1.82 is in the form of a wave equation because of the two spatial derivative operators. Expanding the left hand side term:

$$\nabla \times \mathbf{H} = \begin{vmatrix} \mathbf{i} & \mathbf{j} & \mathbf{k} \\ \frac{\partial}{\partial x} & \frac{\partial}{\partial y} & \frac{\partial}{\partial z} \\ H_x & H_y & H_z \end{vmatrix} = \mathbf{i} \left( \frac{\partial H_z}{\partial y} - \frac{\partial H_y}{\partial z} \right) - \mathbf{j} \left( \frac{\partial H_z}{\partial x} - \frac{\partial H_x}{\partial z} \right) + \mathbf{k} \left( \frac{\partial H_y}{\partial x} - \frac{\partial H_x}{\partial y} \right)$$

But if the applied magnetic field is only along the z direction then:

$$\frac{\partial H_z}{\partial x} = 0 \quad \text{and} \quad \frac{\partial H_z}{\partial y} = 0 \quad \text{and if:} \quad \frac{\partial H_y}{\partial x} = 0 \quad \frac{\partial H_x}{\partial y} = 0$$

$$\text{and:} \quad \nabla \times \mathbf{H} = \mathbf{i} \left( -\frac{\partial H_y}{\partial z} \right) + \mathbf{j} \left( \frac{\partial H_x}{\partial z} \right)$$

$$(\nabla \times \mathbf{H}) \times \mathbf{H} = \begin{vmatrix} \mathbf{i} & \mathbf{j} & \mathbf{k} \\ -\frac{\partial H_y}{\partial z} & \frac{\partial H_x}{\partial z} & 0 \\ H_x & H_y & H_z \end{vmatrix} = \mathbf{i} H_z \frac{\partial H_x}{\partial z} + \mathbf{j} H_z \frac{\partial H_y}{\partial z} + \mathbf{k} \left( -H_y \frac{\partial H_y}{\partial z} - H_x \frac{\partial H_x}{\partial z} \right)$$

$$\begin{aligned} \left( (\nabla \times \mathbf{H}) \times \mathbf{H} \right) \times H_z &= \begin{vmatrix} \mathbf{i} & \mathbf{j} & \mathbf{k} \\ H_z \frac{\partial H_x}{\partial z} & H_z \frac{\partial H_y}{\partial z} & -H_y \frac{\partial H_y}{\partial z} - H_x \frac{\partial H_x}{\partial z} \\ 0 & 0 & H_z \end{vmatrix} \\ &= \mathbf{i} H_z^2 \frac{\partial H_y}{\partial z} - \mathbf{j} H_z^2 \frac{\partial H_x}{\partial z} \end{aligned}$$

Finally the left hand side of Equation A1.82 becomes:

$$\begin{aligned} \nabla \times \left( \left( (\nabla \times \mathbf{H}) \times \mathbf{H} \right) \times H_z \right) &= \begin{vmatrix} \mathbf{i} & \mathbf{j} & \mathbf{k} \\ \frac{\partial}{\partial x} & \frac{\partial}{\partial y} & \frac{\partial}{\partial z} \\ H_z^2 \frac{\partial H_y}{\partial z} & -H_z^2 \frac{\partial H_x}{\partial z} & 0 \end{vmatrix} \\ &= \mathbf{i} H_z^2 \frac{\partial^2 H_x}{\partial z^2} + \mathbf{j} H_z^2 \frac{\partial^2 H_y}{\partial z^2} \end{aligned}$$

and the right hand side is:  $\frac{\rho}{\mu_0} \left( \mathbf{i} \frac{\partial^2 H_x}{\partial t^2} + \mathbf{j} \frac{\partial^2 H_y}{\partial t^2} + \mathbf{k} \frac{\partial^2 H_z}{\partial t^2} \right)$

but the last term in  $\mathbf{k}$  must be zero to preserve the vector equality sign, so Equation A1.82 now becomes:

$$\mathbf{i} H_z^2 \frac{\partial^2 H_x}{\partial z^2} + \mathbf{j} H_z^2 \frac{\partial^2 H_y}{\partial z^2} = \frac{\rho}{\mu_0} \left( \mathbf{i} \frac{\partial^2 H_x}{\partial t^2} + \mathbf{j} \frac{\partial^2 H_y}{\partial t^2} \right) \quad (\text{A1.83})$$

If the perturbed magnetic field is only in the x direction then the wave equation becomes:

$$\frac{\partial^2 H_x}{\partial z^2} = \frac{\rho}{\mu_0 H_z^2} \left( \frac{\partial^2 H_x}{\partial t^2} \right) \quad (\text{A1.84})$$

Reverting back to cgs units by writing  $H_x$  in cgs units as:  $\frac{H_x}{\sqrt{4\pi\mu_0}}$  finally gives the equation in the original paper:

$$\frac{\partial^2 H_x}{\partial z^2} = \frac{4\pi\rho}{H_z^2} \left( \frac{\partial^2 H_x}{\partial t^2} \right) \quad (\text{A1.85})$$

This equation may be compared to the general form of the wave equation:

$$\frac{\partial^2 \phi}{\partial z^2} = \frac{1}{c^2} \left( \frac{\partial^2 \phi}{\partial t^2} \right) \quad (\text{A1.86})$$

to which a solution is a wave plane parallel wave of the form:  $H_x \propto e^{-i\omega t + i\mathbf{k} \cdot \mathbf{z}}$  travelling in the  $z$  direction.

If the wave-vector  $\mathbf{k}$  makes an angle  $\theta$  to the magnetic field in the  $z$  direction the wave travels in the  $z$  direction with a speed [in cgs units] of:

$$V_A = \frac{H_z}{\sqrt{4\pi\rho}} \cos\theta \quad (\text{A1.87})$$

These Alfvén shear waves were first observed experimentally in liquid mercury metal [Lundquist 1947]. This mode of electromagnetic propagation depends upon the existence of a magnetic field in the electrically conducting medium. This equation is referred to in *Cosmical Electrodynamics* [Alfvén 1950].

Table A1.2 reproduces an extract from the lecture that Hannes Alfvén gave, many years later, when he received the Nobel Prize on December 11<sup>th</sup> 1970 [Alfvén 1970]. It recognises that, although MHD is an elegant theory, space plasma is more complex and one should not be surprised if observations show phenomena that would not be expected in MHD.

First approach	Second approach
Homogenous models	Space plasmas often have a complicated inhomogenous structure
Conductivity: $\sigma = \infty$ Electric field $\mathbf{E}_{\parallel} = 0$	$\sigma$ depends on current and often suddenly becomes 0, $\mathbf{E}_{\parallel}$ often $\neq 0$
Magnetic field lines are frozen in and move with the plasma	Frozen in picture often completely misleading
Electromagnetic conditions illustrated by magnetic field line picture	It is equally important to draw the current lines and discuss the electric circuit
Electrostatic double layers neglected	Electrostatic double layers are of decisive importance in low density plasmas
Filamentary structures and current sheets neglected or treated inadequately	Currents produce filaments or flow in thin sheets
Theories mathematically elegant and very developed	Theories still not very well developed well and partly phenomenological

**Table A1.2** Extract from Alfvén's Nobel Prize lecture [Nobel museum Stockholm]

## Appendix 2                      Coordinate system transformations

Physical phenomena are usually more easily understood when the results are transformed into a particular coordinate system [Hapgood 1992]. Use is made in this study of the terrestrial geomagnetic [MAG] system, the geocentric solar ecliptic [GSE] system, the geocentric solar magnetospheric system [GSM], the geocentric equatorial inertial system [GEI] and the field aligned coordinate system.

Transformations between the systems consist of expressing the coordinates in any system as an  $x, y, z$  cartesian vector denoted  $\mathbf{x}_1$  and pre-multiplying by the appropriate rotation matrix  $\mathbf{R}$  to get the  $x, y, z$  cartesian vector of the new system denoted  $\mathbf{x}_2$ .

A useful result is that because the rotation matrix is Hermitean the transformation in the opposite direction is achieved by pre-multiplying by the transposed rotation matrix [Kivelson and Russell 1995]. Thus:  $\mathbf{x}_2 = \mathbf{R} \mathbf{x}_1$  and  $\mathbf{x}_1 = \mathbf{R}' \mathbf{x}_2$

The only problem is to derive the elements of these matrices and this is discussed as follows:

Rotation of the  $x$ - $y$  coordinate axes around the  $z$  axis has the effect of changing the coordinates of a point so that:  $x' = x \cos(\theta) + y \sin(\theta)$  and  $y' = -x \sin(\theta) + y \cos(\theta)$

Clockwise rotation by angle  $\theta_x$  around the  $x$  axis results has no effect upon the  $x$  component but the  $y$  and  $z$  components are rotated by angle  $\theta_x$  in the direction from  $y$  to  $z$ .

The desired result is that:  $y' = y \cos(\theta) + z \sin(\theta)$  and  $z' = -y \sin(\theta) + z \cos(\theta)$

and the rotation matrix is:

$$\mathbf{R}_x = \begin{bmatrix} 1 & 0 & 0 \\ 0 & \cos(\theta_y) & \sin(\theta_y) \\ 0 & -\sin(\theta_y) & \cos(\theta_y) \end{bmatrix}$$

Similarly, clockwise rotation by angle  $\theta_y$  around the  $y$  axis results has no effect upon the  $y$  component but the  $x$  and  $z$  components are rotated by angle  $\theta_y$  in the direction from  $x$  to  $z$ .

The desired result is that:  $z' = z \cos(\theta) + x \sin(\theta)$  and  $x' = -z \sin(\theta) + x \cos(\theta)$  which is more logically written as:  $x' = x \cos(\theta) - z \sin(\theta)$  and  $z' = x \sin(\theta) + z \cos(\theta)$

This rearrangement accounts for why the form of the rotation matrix appears at first sight to be at odds with the others:

$$\mathbf{R}_y = \begin{bmatrix} \cos(\theta_y) & 0 & -\sin(\theta_y) \\ 0 & 1 & 0 \\ \sin(\theta_y) & 0 & \cos(\theta_y) \end{bmatrix}$$

Finally, clockwise rotation by angle  $\theta_z$  around the z axis results has no effect upon the y component but the x and z components are rotated by angle  $\theta_z$  in the direction from x to y.

The desired result is that:  $x' = x \cos(\theta) + y \sin(\theta)$  and  $y' = -x \sin(\theta) + y \cos(\theta)$

and the rotation matrix is:

$$\mathbf{R}_z = \begin{bmatrix} \cos(\theta_x) & \sin(\theta_x) & 0 \\ -\sin(\theta_x) & \cos(\theta_x) & 0 \\ 0 & 0 & 1 \end{bmatrix}$$

The transformation from one frame of reference to another can always be carried out by a rotation around one axis followed in some cases by a rotation around one of the new axes created by the first rotation.

Where two stages of rotation are required a single rotation matrix may be created by multiplying together the individual rotation matrices in the required order. For example a rotation around the x axis followed by a rotation around the y axis would result in a combined rotation matrix given by:  $\mathbf{R}_{xy} = \mathbf{R}_y \mathbf{R}_x$

### A 2.1 Universal time [UT] and Julian day [JD]

In the MATLAB coordinate transformation software UT needs to be expressed as decimal time. For example 1030UT would be written as 10.5

The Julian day number is the integer number of days that have elapsed since noon UT on Monday January 1<sup>st</sup> 4713 BC. The very first Julian day from noon UT on Sunday to noon UT on the Monday was day 0 so if the Julian day number is divisible by 7 it is a Monday. Julian day calculators return the Julian day number for the morning even though this increments at noon UT. The algorithm in the coordinate transform allows for this.

## **A2.2 Geographic coordinates [GEO]**

The geographic frame of reference is a position referenced to the crust of the Earth. It can be extended to altitude if required. Ground magnetometer coordinates are essentially constant in time in this system. The GEO x axis passes through the equator at 0° longitude, the GEO y axis through the equator at 90° longitude and the GEO z axis through the North geographic pole.

## **A 2.3 Geomagnetic coordinates [MAG]**

The terrestrial magnetic field is variable spatially and temporally on all timescales. The International Geomagnetic Reference Field [IGRF] models the Earth's magnetic field as the negative gradient of a scalar potential which is a function of  $r$ ,  $\theta$ ,  $\lambda$  and  $t$  and from this is derived a dipole axis that provides a reference for the geomagnetic coordinate system. Geomagnetic coordinates depend upon which IGRF model was used – the 10<sup>th</sup> generation model [IGRF-10] was revised in 2005.

The transformation from geographic to geomagnetic coordinates consists of a clockwise rotation about the GEO z axis by the IGRF-10 longitude of the geomagnetic dipole axis [ $\sim -79^\circ$ ] so that the MAG x axis is in the dipole meridian, followed by a clockwise rotation about the new MAG y axis by the IGRF-10 dipole co-latitude [ $\sim 10^\circ$ ] so that the MAG z axis is along the dipole axis.

In general a compass will still not point precisely to North in this system because a magnetic dipole is only an approximation to the Earth's magnetic field. The dipole approximation becomes even less valid at increasing distance from the Earth because of the interaction with the solar wind.

## **A 2.4 Geocentric Ecliptic Inertial [GEI] coordinates**

This coordinate system has the x axis in the direction of the first point of Aries [ $\gamma$ ], which is the direction of the intersection of the Earth's equatorial plane with the plane of the ecliptic. This locks the frame of reference onto the distant stars.

The z axis is in the direction of the spin axis of the Earth and the y axis, as well as the x axis, is in the Earth's equatorial plane.

A satellite that was subject only to the gravitational field of the Earth would have constant orbital parameters in this system.

The transformation from GEO to GEI coordinates consists of a single clockwise rotation about the GEO z axis by the angle  $\theta$  in the Earth's equator between the Greenwich meridian and  $\gamma$ .  $\theta$  depends upon the Julian day and the Universal Time.

To find angle  $\theta$  the modified Julian day [MJD] is first calculated as:

$$\text{MJD} = \text{JD} - 2400000.5$$

then the time [T] in Julian centuries from 1200UT on 2000-01-01 to the previous midnight is found using:

$$T = (\text{MJD} - 51544.5) / 365.25$$

The required angle in degrees is then given by the equation:

$$\theta = 100.461 + 36000.770 * T + 15.04107 * UT$$

### **A 2.5 Geocentric Solar Ecliptic [GSE] coordinates**

The x axis is along the Earth-Sun line, the y axis is in the plane of the ecliptic and the z axis is normal to the plane of the ecliptic.

The transformation from GEI to GSE coordinates first requires a rotation about the GEI x axis to place the y axis in the plane of the ecliptic and the z axis normal to it. This angle is known as the obliquity of the ecliptic [ $\epsilon$ ] and is calculated as:

$$\epsilon = 23.439 - 0.013 * T$$

This is followed by a rotation around the new GSE z axis by the angle  $\lambda$  between  $\gamma$  and the Earth-Sun line.

First the Sun's mean anomaly [M] is calculated as:

$$M = 357.528 + 35999.050 * T + 0.04197 * UT$$

Then the Sun's mean longitude [L] is given by:

$$L = 280.460 + 36000.772 + 0.04107 * UT$$

Finally  $\lambda$  is given by:

$$\lambda = L + (1.915 - 0.0048 * T)\sin(M) + 0.020 * \sin(2M)$$

Both  $\epsilon$  and  $\lambda$  depend upon the Julian day and the Universal Time.

### **A 2.6 Geocentric Solar Magnetospheric [GSM]**

The difference between the GSE and GSM coordinate systems is a rotation around the GSE x axis [which points towards the Sun] so that the geomagnetic dipole axis is in the GSM x-z plane at  $y_{\text{GSM}}=0$ . The required rotation angle  $\theta_x$  between the dipole axis and the GSM x-z

plane [not the y axis] can be found from the y and z coordinates of the dipole axis in the GSE frame of reference for the appropriate JD and UT as:  $\theta_x = \tan^{-1}(y_{GSE} / z_{GSE})$

and a clockwise rotation is performed around the x axis by  $-\theta_x$

Relative to the GSE system the GSM frame rocks around the x axis during the course of a day.

### A 2.7 Solar Magnetic [SM] coordinates

The difference between the GSM system the SM coordinate systems is a rotation around the GSM y axis so that the SM z axis is aligned along the geomagnetic dipole. A consequence of this is that the Earth-Sun line is in the SM x-z plane but not along the SM x axis.

The required clockwise rotation angle  $\theta_y$  between the GSM dipole axis and the GSM z axis can be found from the z and x coordinates of the dipole axis in the GSM frame of reference for the appropriate JD and UT as:

$$\theta_y = \tan^{-1}(x_{GSM} / z_{GSM})$$

### A 2.8 Spacecraft-centred field-aligned coordinates [S/C FAC]

In the Poynting flux studies the local direction of propagation of electromagnetic waves relative to the magnetic field lines was of interest. This involved transforming the Poynting flux vector from spacecraft centred GSE coordinates to a spacecraft centred field-aligned coordinate system in which the z direction was along the local magnetic field line, the y direction was normal to the position vector of the spacecraft from the Earth and the x direction was out of the magnetosphere. The unit vectors in this local coordinate system are denoted as:  $\hat{x}$   $\hat{y}$   $\hat{z}$  and have components in the GSE frame of:

$$\hat{x} = \hat{x}_x \mathbf{i} + \hat{x}_y \mathbf{j} + \hat{x}_z \mathbf{k}$$

$$\hat{y} = \hat{y}_x \mathbf{i} + \hat{y}_y \mathbf{j} + \hat{y}_z \mathbf{k}$$

$$\hat{z} = \hat{z}_x \mathbf{i} + \hat{z}_y \mathbf{j} + \hat{z}_z \mathbf{k}$$

The local magnetic field fluctuates because of the presence of the presence of a *magnetic field of external origin* oscillations and to estimate the mean local direction the magnetometer components were low pass filtered.

The local unit vector in this smoothed direction was then calculated as:

$$\hat{\mathbf{z}} = \frac{\mathbf{z}}{|\mathbf{z}|}$$

If the position vector of the satellite from the Earth in GSE coordinates is  $\mathbf{p}$  then a local unit vector in this direction can be defined as:  $\hat{\mathbf{p}} = \frac{\mathbf{p}}{|\mathbf{p}|}$

The y direction was defined to be normal to the plane of  $\hat{\mathbf{z}}$  and  $\hat{\mathbf{p}}$  and a local unit vector in the y direction was calculated as:

$$\hat{\mathbf{y}} = \hat{\mathbf{z}} \times \hat{\mathbf{p}}$$

The ordering was chosen so that a local unit vector in the x direction was directed *outwards* from the magnetosphere [in both hemispheres]:

$$\hat{\mathbf{x}} = \hat{\mathbf{y}} \times \hat{\mathbf{z}}$$

In the particular case of a dipolar magnetic field then  $\hat{\mathbf{y}}$  would be tangential to the geomagnetic shell and  $\hat{\mathbf{x}}$  would be normal to it, but the extent to which this is the case varies with the spacecraft position. Irrespective of the magnetic field configuration  $\hat{\mathbf{z}}$  should always be along the direction of the local magnetic field

A vector [ $\mathbf{E}$ ,  $\mathbf{B}$  or  $\mathbf{S}$ ] in spacecraft centred GSE coordinates is projected onto the spacecraft centred field-aligned coordinates by multiplying it by the matrix  $\mathbf{R}$

The elements of  $\mathbf{R}$  are the components of the field-aligned unit vectors in the GSE frame or they can be regarded as the direction cosines between the field-aligned axes and the GSE axes as:

$$\mathbf{R} = \begin{bmatrix} \hat{\mathbf{x}}_x & \hat{\mathbf{x}}_y & \hat{\mathbf{x}}_z \\ \hat{\mathbf{y}}_x & \hat{\mathbf{y}}_y & \hat{\mathbf{y}}_z \\ \hat{\mathbf{z}}_x & \hat{\mathbf{z}}_y & \hat{\mathbf{z}}_z \end{bmatrix}$$

## Appendix 3                      Multiphysics

Note that the interpolation function named *va* had to be referenced as *va (x,y)* wherever use was made of it, such as in defining expressions or in specifying sub-domain settings.

### A 3.1    MATLAB to .txt file conversion

This is required when using Multiphysics with external data. One way of reading in external data is described in: Help>Index>Interpolated data,using functions..

A separate .txt file is created with numbers separated by spaces for each of the required parameters such as Bx By vA cs

It looks like this for a 2D array:

```
%grid
1 2 3 4 ... 121
1 2 3 4 ... 81
%data
Bx11 Bx12 Bx 13 Bx14 ...
Bx21 Bx22 Bx 23 Bx 24...
Bx 31 Bx32 bx 33 Bx34...
etc
```

Save as: eg Bx.txt

Repeat process for By vA cs etc to create files By.txt vA.txt cs.txt etc

In the Acoustics Pressure titlebar go to:

Options>Functions>New

Enter function name such as Bx but without any parentheses

Select interpolation blob

Use data from: file

Browse to locate filename

OK

Interpolation method: linear

Apply

OK

Then go to:

Options

Expressions

Subdomain expressions

Select subdomain number

Enter name: eg patrick\_function

Enter expression: eg  $\sqrt{Bx(x,y)^2}$

OK

Finally go to:

Physics>Subdomain Settings

Select subdomain number

Enter in cs box expression for speed of sound eg  $vA(x,y)*patrick\_function$

```
function y=MATtoTXT(a)
```

```
%MATtoTXT changes the file format of MATLAB array a to the .txt format required by Multiphysics
```

```
ix=size(a,1); iy=size(a,2);
```

```
fid=fopen('testdata.txt','w'); %text file called testdata
```

```
text='%grid';
```

```
fprintf(fid,'% .10s\n\r',text);
```

```
fprintf(fid,'\n\r');
```

```
x=(1:ix); y=(1:iy);
```

```
for n=1:ix
```

```
    fprintf(fid,'% .0f\t',x(n));
```

```
end
```

```
fprintf(fid,'\n\r'); fprintf(fid,'\n\r');
```

```
for n=1:iy
```

```
    fprintf(fid,'% .0f\t',y(n));
```

```
end
```

```
fprintf(fid,'\n\r'); fprintf(fid,'\n\r');
```

```
text='%data';
```

```
fprintf(fid,'% .10s\n\r',text);
```

```
fprintf(fid,'\n\r');
```

```
for n=1:iy
```

```
    for m=1:ix
```

```
        fprintf(fid,'% .5e\t',a(m,n));
```

```
    end
```

```
    fprintf(fid,'\n\r');
```

```
    fprintf(fid,'\n\r');
```

```
end
```

```
fclose(fid);
```

### A 3.2 Using Multiphysics with magnetospheric data

Model Navigator > New Tab > Space Dimension: 2D

Application Modes > Acoustics Module > Pressure Acoustics

Options > Axes /Grid Settings > [x y plane]

Axis Tab: xmin: 0 xmax: 120 ymin: 0 ymax: 80 > OK

Grid Tab > untick Auto > xspacing: 1 yspacing: 1

Options > Functions > New... > Function name: vA > Interpolation >

Use data from: File > Browse .> [select file of Alfvén data in .txt format] > OK > OK

Draw > Draw Objects > Rectangle/Square [Draw rectangle 120 x 79 so edges show]

Physics > Subdomain Settings > Subdomain Tag > [Select 1]>

Change cs to:  $vA(x,y)/(384e6/120)$  > OK [see below for non-linear function]

Physics > Boundary condition > Radiation condition

Select 1 > Boundary condition > Radiation condition

Select 2 > Boundary condition > Radiation condition

Select 3 > Boundary condition > Radiation condition

Select 4 > Boundary condition > pressure >  $P_0$  >  $1e-9$  > OK

Physics > Scalar Variables > freq\_acpr > 0.010 Hz > OK

Mesh > Initialise Mesh > Refine Mesh > Refine Mesh > (Refine Mesh)

Solve > =

#### Parametric solution

Options > Expressions > Subdomain Expressions > Name: alpha > OK

Options > Functions [define Bx]

Options > Functions [define By]

Options > Functions [define f1]

Options > Functions [define f2]

Physics > Subdomain Settings > Subdomain Tag > [Select 1]> Change cs to:  $(vA(x,y)/(384e6/120))*(1+alpha*f(x,y)*(1-(Bx(x,y)*px+By(x,y)*py)))$  > OK

Solve > Solver Parameters > Parameter > General Tab > name of parameter: alpha

List of parameter values 0;1e-3;1

Stationary Tab > Maximum number of iterations: 100 >

Tick Highly nonlinear problem > OK

Solve =

## Appendix 4 IAGA data format

This is the format of data from the IMAGE ground magnetometers

IAGA file format for one minute or denser values:

- Record Length 4 characters (1440)
- Length of one record 3 in minutes
- Type of data 2 00 = observatory; 01 = temporary st.;
- Station Identification 6 (e.g. 3 numbers, 3 letters)
- Geographic latitude 5 in 0.01 degrees (space or sign and 4 digits)
- Geographic longitude 5 in 0.01 degrees East
- Free 23
- Year 4
- Month 2
- Day 2
- Hour 2 00...23 UT
- Minute 2 00...59. The first minute of record.
- Interval between datapoints 2 in seconds
- How produced 1 0 = digital recording;; 1 = digitized from primary recordings;  
2 = digitized from supplementary recordings;  
9 = unknown.
- Filter breakpoint 4 0000 if values are means between data points.  
Otherwise period in seconds at which low pass filter is 3 db down (0.7 amplitude).  
9999 if no filtering was employed.
- Filter slope 2 db per octave, i.e. 6, 12, 18 db/octave  
or measured equivalent for numerical filter.
- Baseline information 1 = final data, absolute baseline, accuracy 1 nT;  
2 = final data but no absolute measurements;  
3 = preliminary data;  
4 = data relative to quiet day night values.
- Probable baseline change  
in 24 hours 2 in 0.1 nT
- Components 1 1 = X,Y,Z;  
2 = H,D (0.1'),Z;

3 = A,B,Z;

4 = H,d (0.1nT),Z

5 = H,E,Z

(note, 4 & 5 is a Leicester adopted convention)

- Character of day	1	0 = normal, 1 = one of the 5 international quietest days; 2 = one of the 5 international most disturbed days.
- Free	85	
- X1,Y1,Z1	7 x 180	values in 0.1 nT units (0.1' if D).
X2,Y2,Z2		The first character at left is the sign, which is a space for positive values and minus for negative values.
X60,Y60,Z60		
- Hourly mean of X	7	000000 if not the last part of hour
- Hourly mean of Y	7	000000 if not the last part of hour
- Hourly mean of Z	7	000000 if not the last part of hour

The value for an interval is its mean. For example the value of the first minute of an hour is the mean value from XXh 00 min 00 s to XXh 01 min 00 s, etc. The values are given in units 0.1 nT. One record contains 1440 characters. Missing values are marked 999999. For merged tapes the stations follow each other by record. Leading zeros have to be used for fields that are too long. One record = one hour in the case of one-minute values, or part of an hour in the case of denser values. CODE : ASCII.

## Appendix 5 Location of ground magnetometers

In this study data was processed from a number of fluxgate magnetometer stations including those listed. For some of the Greenland stations the alternative or the former name is also given.

Name		geogr. lat	geogr. long	CGM lat.	CGM long
<b>IMAGE</b>					
Ny Ålesund	NAL	78.92°N	11.95°E	75.25°N	112.08°E
Longyearbyen	LYR	78.20°N	15.82°E	75.12°N	113.00°E
Hornsund	HOR	77.00°N	15.60°E	74.13°N	109.59°E
Bear Island	BJN	74.50°N	19.20°E	71.45°N	108.07°E
Sørøya	SOR	70.54°N	22.22°E	67.34°N	106.17°E
Masi	MAS	69.46°N	23.70°E	66.18°N	106.42°E
Muonio	MUO	68.02°N	23.53°E	64.72°N	105.22°E
Pello	PEL	66.90°N	24.08°E	63.55°N	104.92°E
Oulujärvi	OIJ	64.52°N	27.23°E	60.99°N	106.14°E
Hankasalmi	HAN	62.30°N	26.65°E	58.71°N	104.61°E
Nurmijärvi	NUR	60.50°N	24.65°E	56.89°N	102.18°E
Tartu	TAR	58.26°N	26.46°E	54.47°N	102.89°E
<b>SAMNET</b>					
Oulu, Finland	OUL	65.10°N	25.85°E		
Nordli, Norway	NOR	64.37°N	13.36°E		
Hella, Iceland	HLL	63.77°N	-20.56°E		
Faroes	FAR	62.05°N	-7.02°E		
<b>Greenland East Coast</b>					
Nord	NRD	81.60°N	343.33°E	81.11°N	103.14°E
Danmarkshavn	DMH	76.77°N	341.37°E	77.27°N	85.00°E
Daneborg	DNB	74.30°N	339.78°E	75.13°N	78.64°E
Ittoqqortoormiit	SCO	70.48°N	338.03°E	71.50°N	71.73°E
Scoresbysund					

Tasiilaq Ammassalik	AMK	65.60°N	322.37°E	68.99°N	53.39°E
<b>Greenland West Coast</b>					
Qaanaaq Thule	THL	77.47°N	290.77°E	84.97°N	29.68
Savissivik	SVS	76.02°N	294.90°E	83.24°N	33.04°E
Kullorsuaq	KUV	74.57°N	302.82°E	80.87°N	42.04°E
Upernavik	UPN	72.78°N	303.85°E	79.12°N	40.01°E
Uummannaq Umanaq	UMQ	70.68°N	307.87°E	76.53°N	42.26°E
Qeqertarsuaq Godhavn	GDH	69.25°N	306.47°E	75.40°N	38.93°E
Kangerlussuaq Sondre Stromfjord	STF	67.02°N	309.28°E	72.73°N	40.51°E
Maniitsoq Sukkertoppen	SKT	65.42°N	307.10°E	71.55°N	36.87°E
Nuuk Godthab	GHB	64.17°N	308.27°E	70.11°N	37.50°E
Paamiut Frederikshab	FHB	62.00°N	310.32°E	67.56°N	38.72°E
Narsarsuaq	NAQ	61.16°N	314.56°E	65.85°N	42.97°E
<b>CARISMA</b>					
Back	BACK	57.72°N	265.83 °E		
Contwoyto	CONT	65.75°N	248.74 °E		
Dawson	DAWS	64.05°N	220.89 °E		
Eskimo Point	ESKI	61.11°N	265.95 °E		
Fort Churchill	FCHU	58.76°N	265.91 °E		
Fort Simpson	FSIM	61.76°N	238.77°E		
Fort Smith	FSMI	60.03°N	248.07°E		
Gull Lake	GULL	50.06°N	251.74°E		

Gillam	GILL	56.38°N	265.36°E		
Island Lake	ISLL	53.86°N	265.34°E		
Fort McMurray	MCMU	56.65°N	248.79°E		
Ministik Lake	MSTK	53.35°N	247.03°E		
Pinawa	PINA	50.20°N	263.96°E		
Rabbit Lake	RABB	58.23°N	256.32 °E		
Rankin Inlet	RANK	62.82°N	267.89°E		
Taloyoak	TALO	69.54°N	266.44 °E		

**Table A5.1      Location of ground magnetometers**

## Appendix 6 Processing of Polar satellite data

These studies were concerned with data in the frequency band below 10MHz. This meant that digital data with a low sampling frequency could be used with the computational advantages of low memory requirements and efficient processing on a 3GHz machine.

Where required the MATLAB filter design tool was used to generate the coefficients for finite impulse response [FIR] filters. These symmetric FIR filters had the advantage of being phase-linear, which meant that they introduced a constant time delay at all frequencies. This delay was then corrected by time-aligning the filtered data. Filter stop-bands were set to -60dB to minimise aliasing when sub-sampling the data rate.

An overview of the core processing is as follows:

- (1) Read a 1 day file of polarefi Edot0\_GSE\_Spin data from Berkeley together with time tags. The components of electric field were in the S/C GSE frame of reference and the data was sampled at the satellite spin rate [approximately 6seconds].
- (2) Select the data point nearest to an exact 6s rate starting at time zero to give electric field data components at 0, 6, 12...seconds.
- (3) FIR filter, time-align and subsample the electric field data to a 30s data rate
- (4) Either: read a 1 day file of Berkeley magnetometer data and process exactly as for the electric field data or: read a 1 day file of Goddard magnetometer data together with time codes. The components of magnetic field are in the S/C GSE frame of reference and the data is sampled at a 0.92 minute rate. Linearly interpolate the data components to an exact 6s rate starting at time zero to give magnetic field data components at 0, 6, 12...seconds
- (5) Calculate the Poynting flux vectors in the GSE frame of reference
- (6) Low-pass filter and time align the magnetic field data to define the z direction for the field-aligned coordinate frame of reference.
- (7) Read a 1 day file of Polar satellite position data and linearly interpolate it to the 30s rate of the magnetic field
- (8) Calculate the coordinate transform matrices for S/C GSE to S/C field-aligned
- (9) Coordinate transform the electric field, magnetic field and Poynting flux vectors data to field-aligned coordinates as described in Appendix 2. Display the components of electric field, magnetic field and Poynting flux. Where electric field, magnetic field and Poynting flux were plotted on the same graph the annotation on the y axis refers to  $\text{mVm}^{-1}$  and nT. It may need to be multiplied by the indicated scale factor eg  $\times 10$  to give the Poynting flux in  $\mu\text{Wm}^{-2}$

## Appendix 7

## Figures for Poynting flux studies

Events are listed by Group and then chronologically, as in Table 6.1. Polar satellite plots are colour coded as: **electric field strength [green]**; **magnetic field strength [red]** and **Poynting flux [blue]**. The Polar satellite position is given for the time of the strongest PFI or the mid-time of the duration of the resonance event in the case of Group V.

### Group I

### Figure A7.1

#### 1800 - 1900UT on 2002-12-10

Polar GSE [0.7 8.5 -2.4]  $R_E$

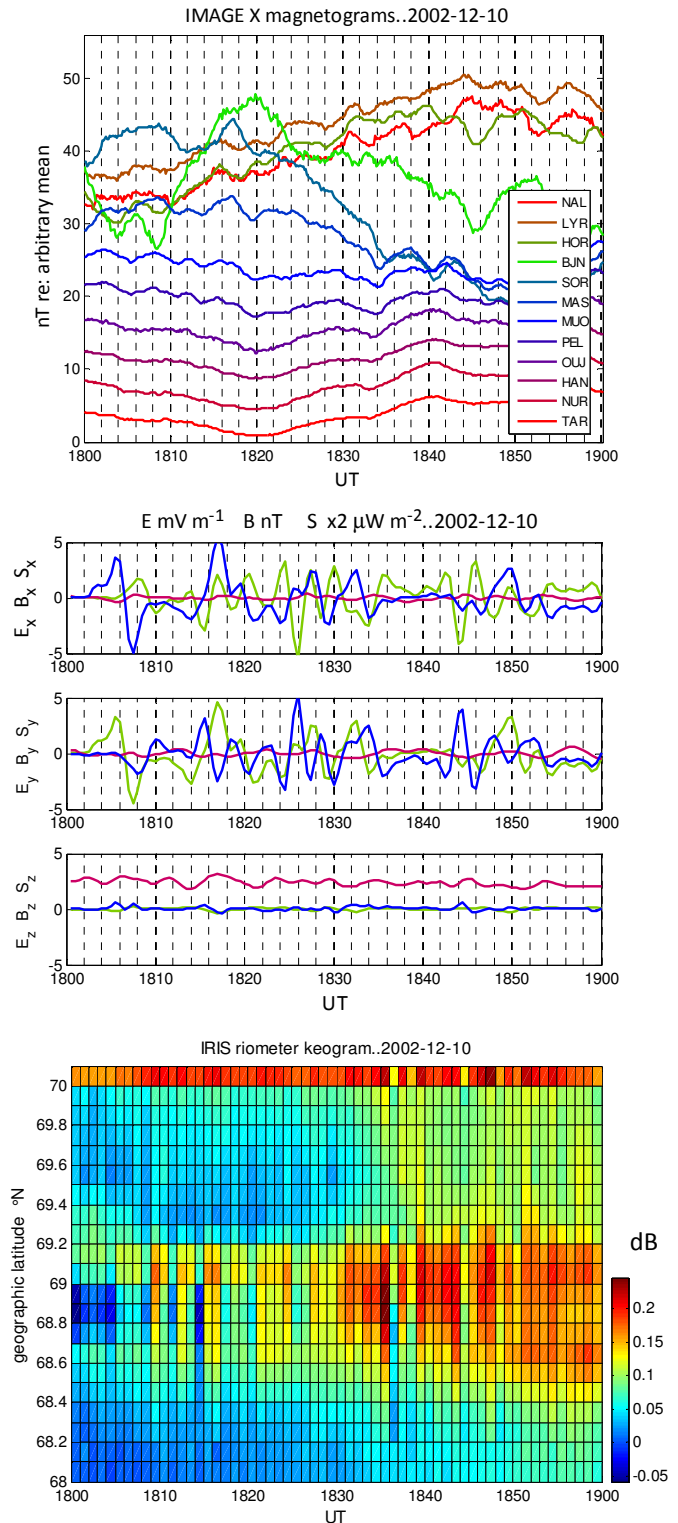
Polar GSM [0.7 8.5 -2.4]  $R_E$

Polar trace at 1830UT 68°N -30°E

The Polar satellite field line trace was far to the west of the IRIS riometer but nevertheless the characteristic pattern of fluctuating enhanced absorption was observed that is associated with magnetospheric Group I electric field oscillations.

The Polar satellite detected the electric field oscillations in the field-aligned x and y components, normal and tangential to the geomagnetic shell.

The data was derived from the spin-plane sensors on the MHD assumption of zero field-aligned electric field at low frequency and so the near-zero  $E_z$  component provides a useful cross-check on the coordinate transforms used.



**Group I Figure A7.2**  
**1600 - 1700UT on 2002-12-17**

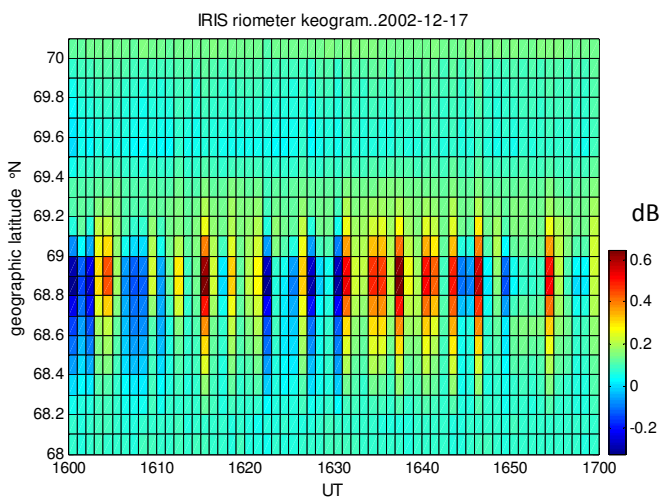
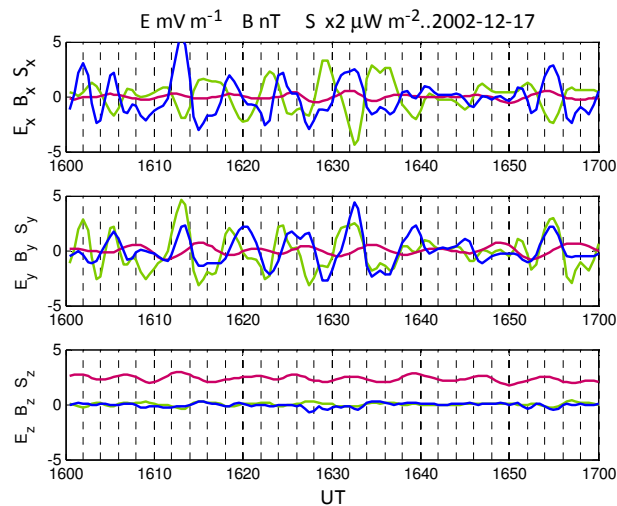
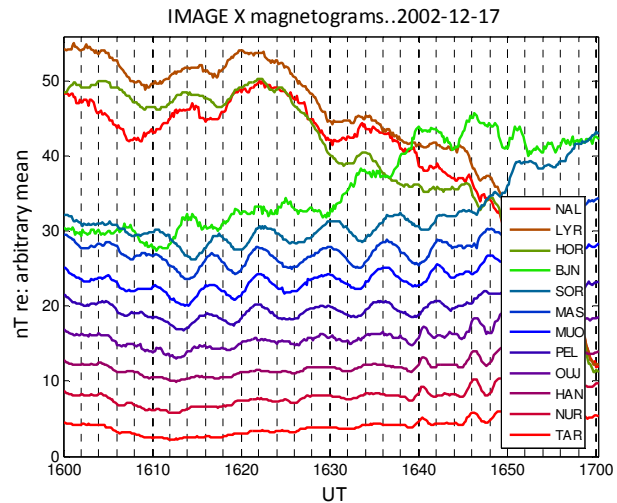
Polar GSE [1.4 9.0 -1.8]  $R_E$   
 Polar GSM [1.4 8.9 -2.2]  $R_E$   
 Polar trace at 1630UT 70°N -6°E

The Polar satellite field line trace was over the Norwegian Sea.  $E_x$  and  $E_y$  oscillations with a frequency of 2.8mHz were observed in Polar satellite data between 1600UT and 1640UT.

IMAGE ground magnetometers recorded very low amplitude [less than 2nT] coherent oscillations with a frequency of 2.5mHz south of BJN between 1600UT and 1640UT.

The IRIS riometer keogram showed the characteristic pattern of fluctuating enhanced absorption that is associated with magnetospheric Group I electric field oscillations.

Approximately 9 enhancements in absorption were seen between 1600UT and 1700UT and this matched the number of  $E_x$  and  $E_y$  displacements as described in Section 6.5.1 and Figure 6.9. The electric field oscillations have an irregular character implying a wideband spectrum.



**Group I      Figure A7.3**

**1600 - 1700UT on 2003-12-12**

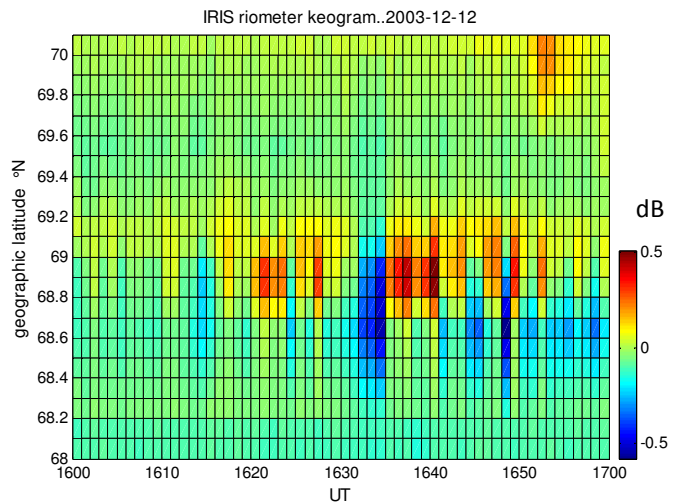
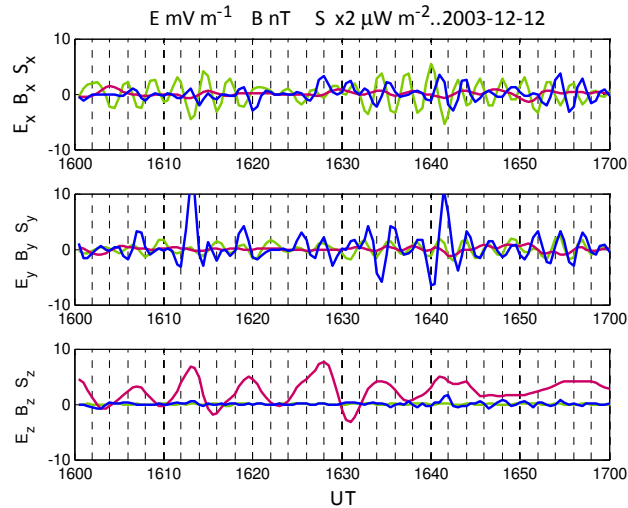
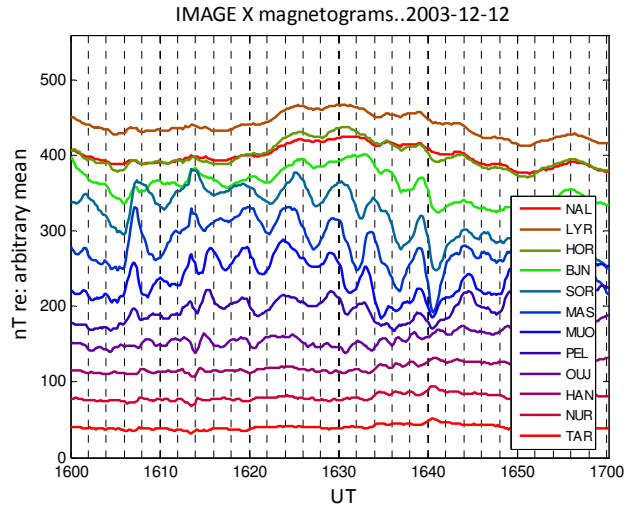
Polar GSE [-0.2 7.1 1.1]  $R_E$

Polar GSM [-0.2 7.2 0.5]  $R_E$

Polar trace at 1630UT 67°N 8°E

The Polar satellite trace was to the west of the IMAGE magnetometer chain.

Magnetospheric  $E_x$  and  $B_z$  oscillations were observed which gave rise to  $S_y$  Poynting oscillations normal to field lines and tangential to the geomagnetic shell. They were incoherent with the  $B_z$  compression wave oscillations which had a frequency of approximately 2.5mHz, the same as the oscillations observed in the X component IMAGE magnetograms. The IRIS riometer keogram showed the characteristic pattern of fluctuating enhanced absorption associated with magnetospheric Group I electric field oscillations.



**Group I      Figure A7.4**

**1400 - 1500UT on 2003-12-28**

Polar GSE [4.3 8.2 -2.0] R<sub>E</sub>

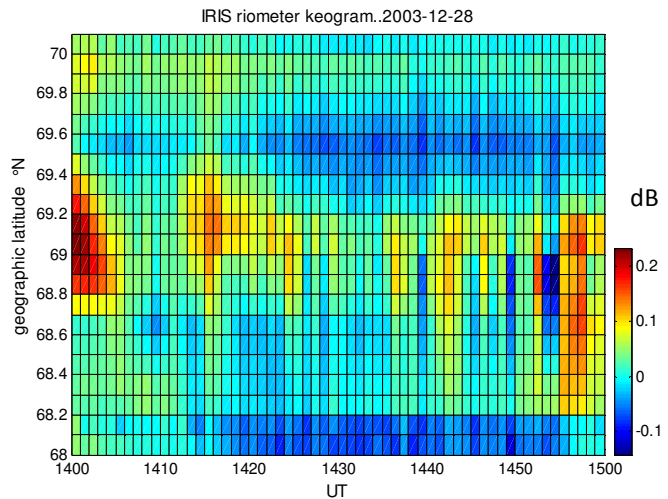
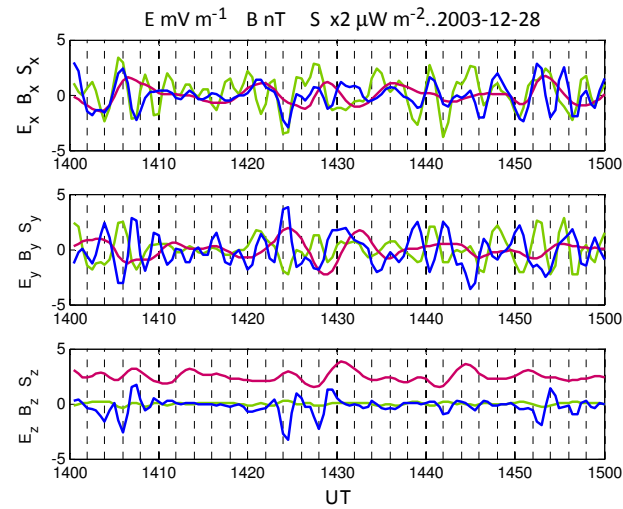
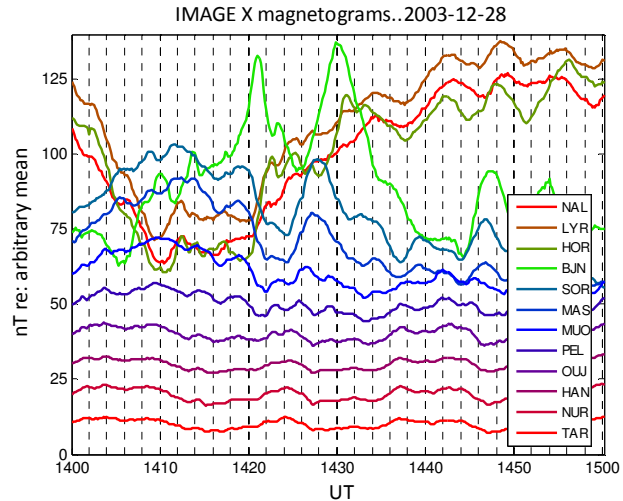
Polar GSM [4.2 8.1 -2.4] R<sub>E</sub>

Polar trace at 1430UT 74°N 3°E

The high-latitude Polar satellite trace was to the west of IMAGE ground magnetometer BJN [74.5°N 19.2°E].

Irregular Ex and Ey oscillations of magnetospheric electric field were observed with an approximate frequency of 5mHz and these were incoherent with the magnetic field fluctuations.

The IRIS riometer keogram showed the characteristic pattern of fluctuating enhanced absorption that is associated with magnetospheric Group I electric field oscillations although it was well to the south.



**Group II Figure A7.5**

**1800 - 1900UT on 2002-12-27**

Polar GSE [1.7 9.1 0.6]  $R_E$

Polar GSM [1.6 9.0 1.7]  $R_E$

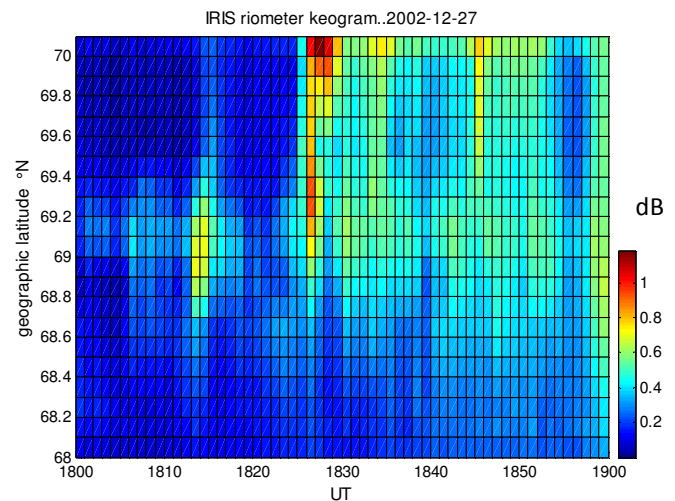
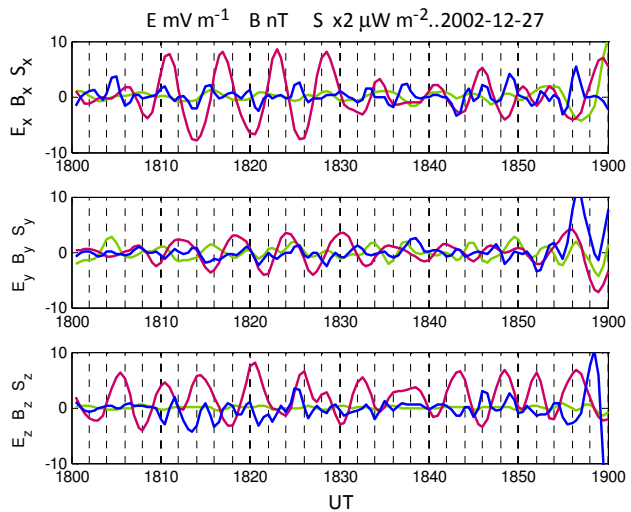
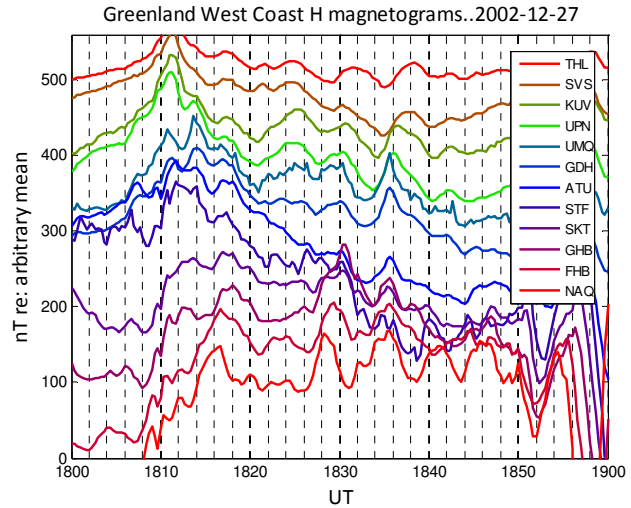
Polar trace at 1830UT 64°N 39°E

The Polar satellite trace was to the east of the IMAGE chain and at the latitude of ground magnetometer MUO.

Magnetospheric magnetic field oscillations were observed in all three field-aligned components with a well-defined frequency of 2.8mHz. The strongest  $B_y$  component had an amplitude of 9nT.

The IMAGE magnetograms showed strong but irregular fluctuations which were unlike the magnetospheric oscillations.

The IRIS riometer keogram showed a high-latitude enhanced absorption spike at 1828UT but this was not observed in the Polar satellite data probably because the field line trace was well to the south of Kilpisjärvi.



**Group III Figure A7.6**

**2236 - 2336UT on 2002-10-10**

Polar GSE [-8.4 2.4 1.6] R<sub>E</sub>

Polar GSM [-8.4 2.7 1.1] R<sub>E</sub>

Polar trace at 2300UT 65°N -24°E

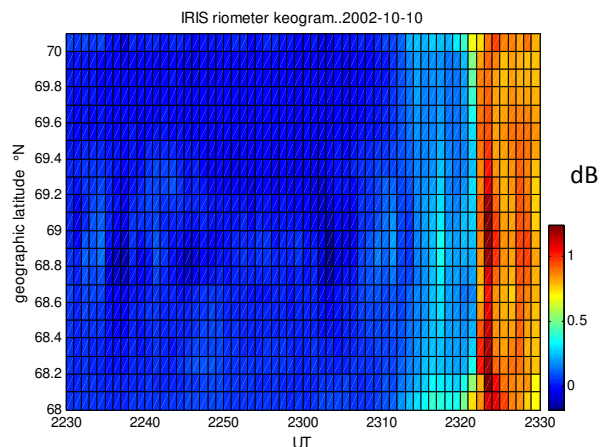
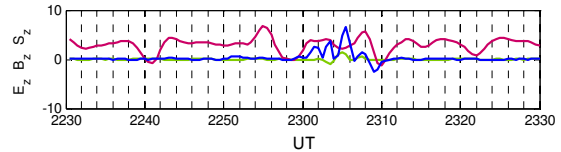
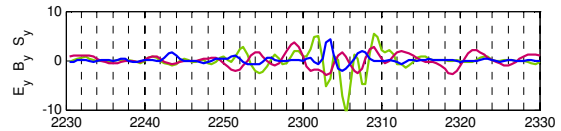
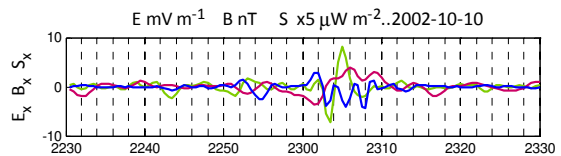
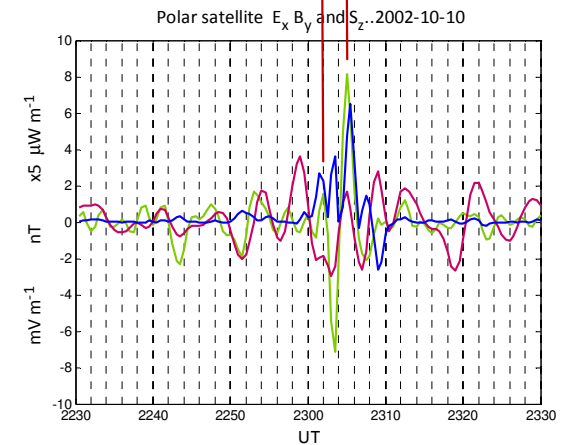
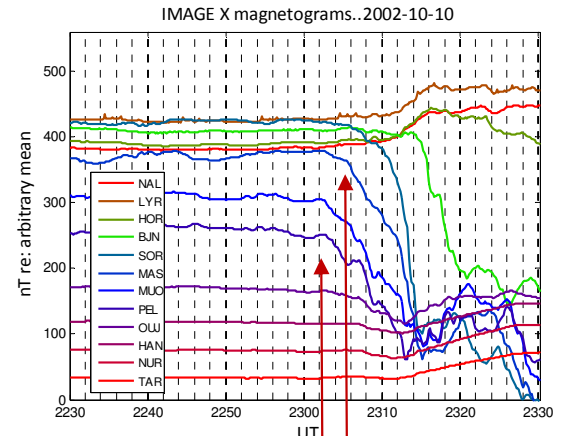
The Polar satellite trace was to Iceland at a similar geomagnetic latitude to IMAGE magnetometer BJN.

Substorm precipitation, as marked by a change of gradient in the IMAGE magnetograms, began at 2302UT at MUO at the same time as the initial magnetospheric PFI.

The substorm onset then propagated northwards and occurred about three minutes later between SOR and BJN when a 31 μWm<sup>-2</sup> magnetospheric PFI was detected at 2305UT. The positive S<sub>z</sub> component was consistent with the Polar satellite being in the northern magnetosphere.

The electric and magnetic fields were partially coherent, but the negative PFI at 2309UT suggested that they had some different frequency components which explains why this event was classified as magnetospheric Group III.

No enhanced absorption was seen in the IRIS riometer keogram at substorm onset. The PFI vector at 2305UT was in the GSM +x -y -z direction which suggests that the source may have been just tailward of GSM x = -8.4 R<sub>E</sub>



**Group III      Figure A7.7**  
**1900 - 2000UT on 2002-10-19**

Polar GSE [-5.4 5.3 -2.8] R<sub>E</sub>  
 Polar GSM [-5.4 3.3 -4.0] R<sub>E</sub>  
 Polar trace at 1930UT 72°N 8°E

The Polar field line trace was to the north of Norway at a similar geomagnetic latitude to IMAGE magnetometer BJN. Since the Polar satellite was in the southern magnetosphere negative S<sub>z</sub> PFIs would be expected to relate to terrestrial events in Scandinavia.

The second negative PFI coincided with a negative magnetometer deflection at BJN.

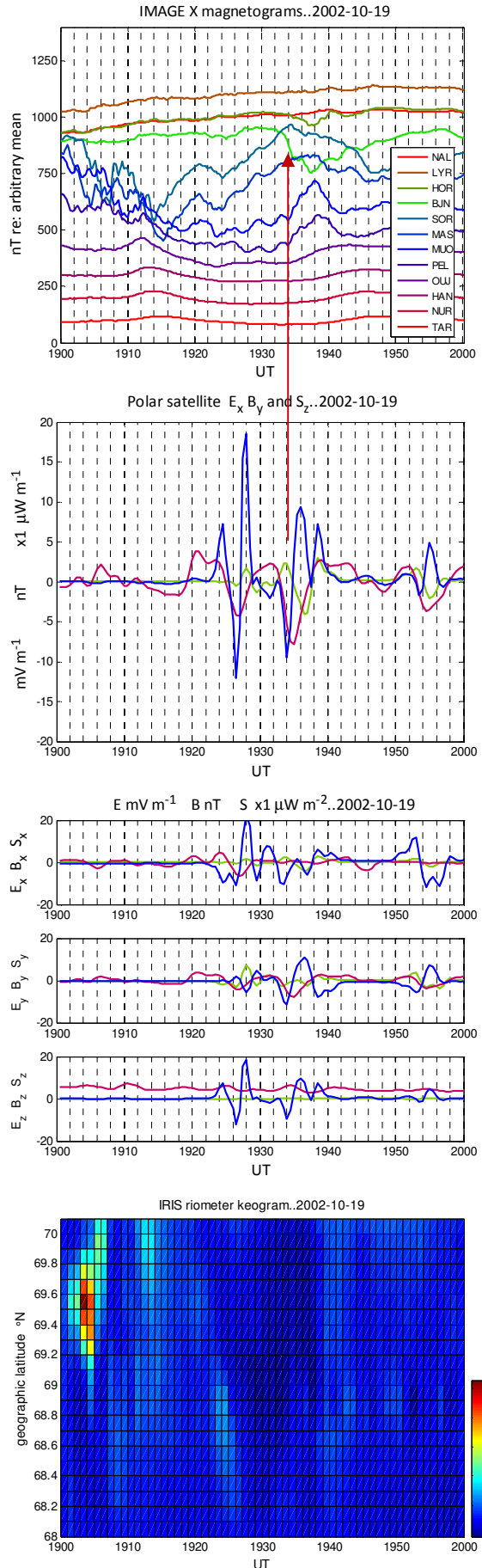
The strongest +S<sub>z</sub> PFI occurred at 1928UT, 4 minutes before the substorm onset at BJN at 1932UT. The PFI vector was predominantly S<sub>x</sub> S<sub>z</sub> normal to the geomagnetic shell.

The next strongest +S<sub>z</sub> PFI was observed at 1936UT which was 2 minutes before an OGMD event at 1938UT between BJN and MUO.

Here the vector was predominantly S<sub>y</sub> S<sub>z</sub> which is tangential to the geomagnetic shell.

No enhanced absorption was observed in the IRIS riometer keogram but this was probably because the substorm and OGMD event were too far to the north.

The PFI vector at 1928UT was in the unusual GSM +y -z direction.



**Group III      Figure A7.8**

**1700 - 1800UT on 2002-11-22**

Polar GSE [-4.3 7.4 1.6]  $R_E$

Polar GSM [-4.3 7.6 0.2]  $R_E$

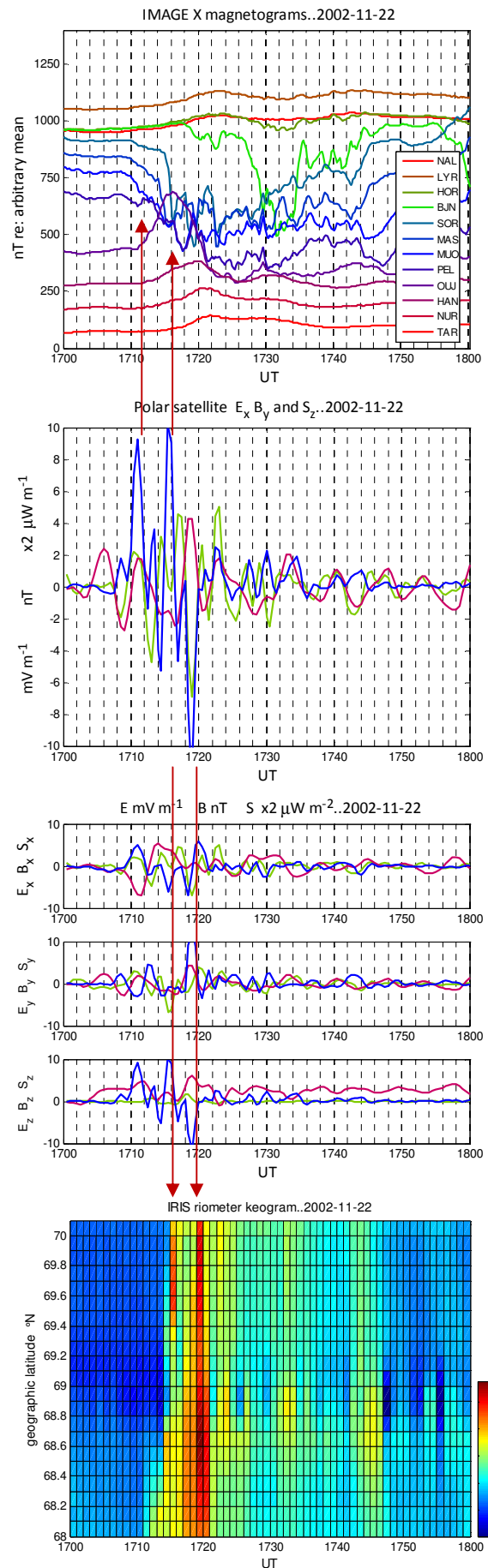
Polar trace at 1710UT 68°N 25°E

The Polar satellite was near the geomagnetic equator, so either sign of  $S_z$  may be significant, and the field line trace was close to IMAGE ground magnetometer MUO and to the IRIS riometer. A gradual decrease in the magnetic field began at 1710UT at SOR, MAS and MUO and a strong  $+S_z$  impulse was detected in the magnetosphere at 1711UT, which suggests that it was associated with the substorm onset. A strong  $+S_z$  PFI coincided with the main substorm expansion at 1716UT at SOR.

The IRIS riometer keogram showed enhanced absorption peaks at 1715UT and 1719UT and this latter 2.2dB absorption peak coincided exactly with the time of the strongest  $+S_y$   $-S_z$  geomagnetic shell PFI.

The PFI vectors at 1711UT and 1716UT were in the GSM  $+x$  direction but the PFI vector at 1719UT was in the GSM  $-x$  direction which suggests that it may have been a reflection.

Some additional notes on this event are given in Section 7.2.2



**Group III      Figure A7.9**  
**2018 - 2118UT on 2003-09-26**

Polar GSE [-8.6 3.7 -2.2]  $R_E$   
 Polar GSM [-8.6 3.0 -3.1]  $R_E$   
 Polar trace at 2036UT 71°N 12°E

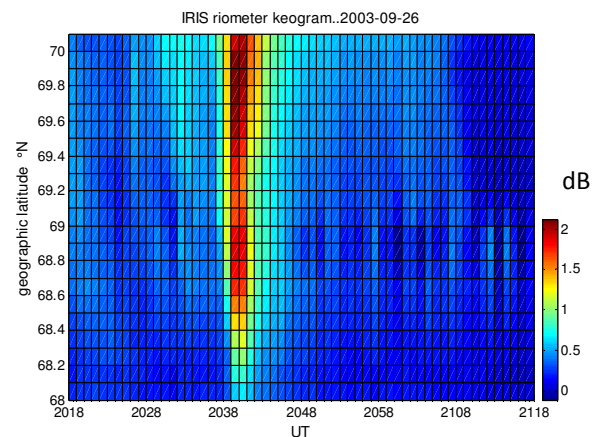
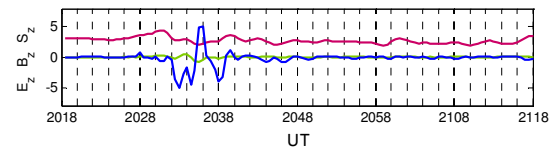
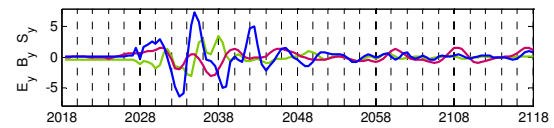
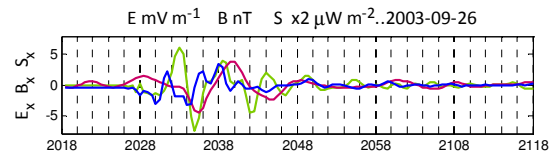
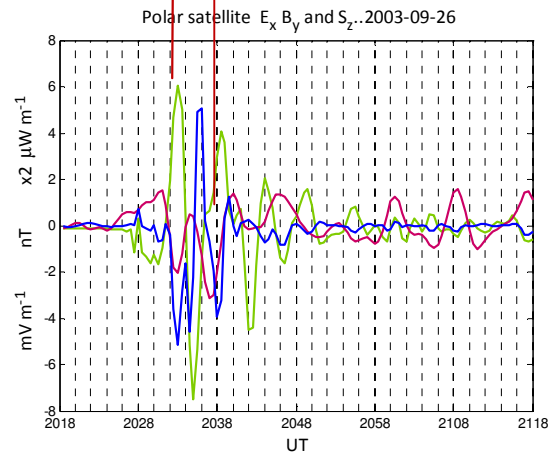
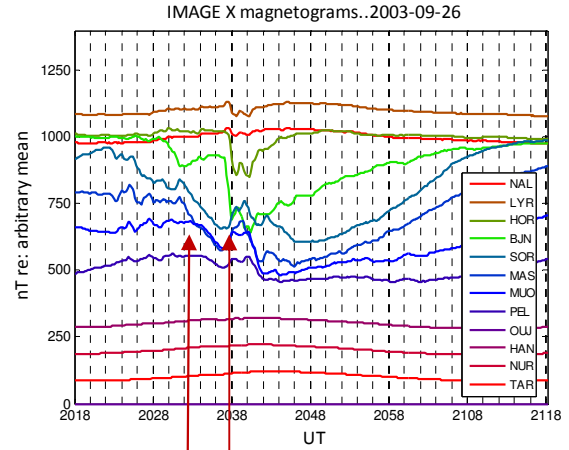
The Polar satellite was in the southern magnetosphere and the field line trace was to the Norwegian sea at a geomagnetic latitude between BJN and SOR

The first  $-S_z$  PFI of  $-10\mu W m^{-2}$  was at 2033UT and this was followed by a stronger  $+S_y +S_z$  geomagnetic shell PFI at 2036UT.

Substorm expansion at BJN commenced at 2037UT one minute after a  $+S_z$  PFI and one minute before a  $-S_z$  PFI. An OGMD event was observed between BJN and SOR at 2039UT, which illustrates the connection with substorm and OGMD phenomena.

High latitude absorption started to increase in the IRIS riometer keogram at 2038UT and reached a peak of 2dB at 2039UT indicating that precipitation was associated with these PFI events.

The PFI vector at 2033UT was in the GSM +x direction so the PFI at 2036UT could have been a reflection.



**Group III Figure A7.10**

**1830 - 1930UT on 2003-11-12**

Polar GSE [-3.9 6.5 0.9] R<sub>E</sub>

Polar GSM [-3.9 6.5 -0.1] R<sub>E</sub>

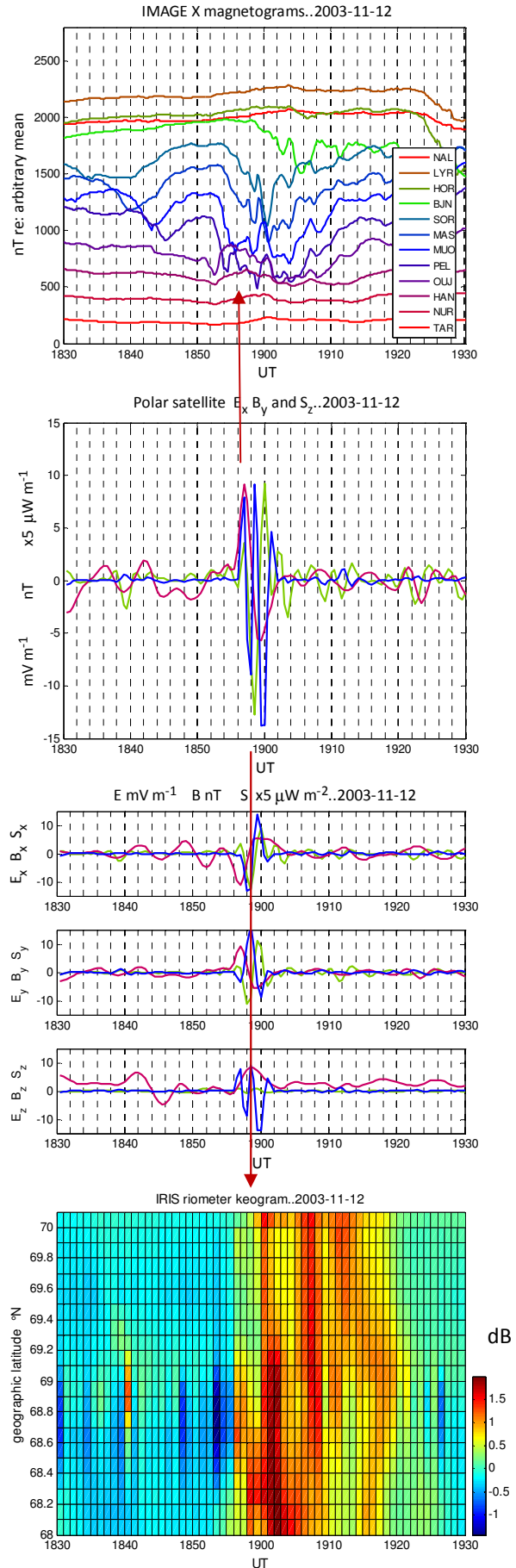
Polar trace at 1900UT 65°N 0°E

The Polar satellite was near the geomagnetic equator and the field line trace was over the Norwegian sea at the same geomagnetic latitude as the IRIS riometer.

Substorm activity was observed in ground magnetometers from OUJ to BJN but no signal was seen in Polar satellite data around the time of the substorm onset at 1852UT. At 1900UT an OGMD event with amplitude of 250nT and a duration of approximately 2 minutes was observed between MUO and PEL.

The Polar satellite Poynting flux data showed a pulse of oscillations between 1856UT and 1902UT with a peak  $-S_z$  deflection of  $-70 \mu\text{Wm}^{-2}$  at 1900UT. These oscillations may be related to the Polar satellite location near the geomagnetic equator.

The IRIS riometer keogram also showed enhanced absorption starting at 1856UT with a 1.8dB peak at 1902UT. This event is also discussed in Section 7.3.3.



**Group III Figure A7.11**

**1630 - 1730UT on 2003-11-22**

Polar GSE [-2.5 8.2 -0.1] R<sub>E</sub>

Polar GSM [-2.5 8.0 -1.8] R<sub>E</sub>

Polar trace at 1640UT 69°N 24°E

The Polar satellite was in the southern magnetosphere and the field line trace was near to IMAGE ground magnetometer MAS at 69.46°N 23.70°E

An OGMD event occurred at 1638UT at OUI-HAN with a negative magnetometer deflection about 2 minutes later at MAS further to the north suggesting that this precipitation began at lower latitudes.

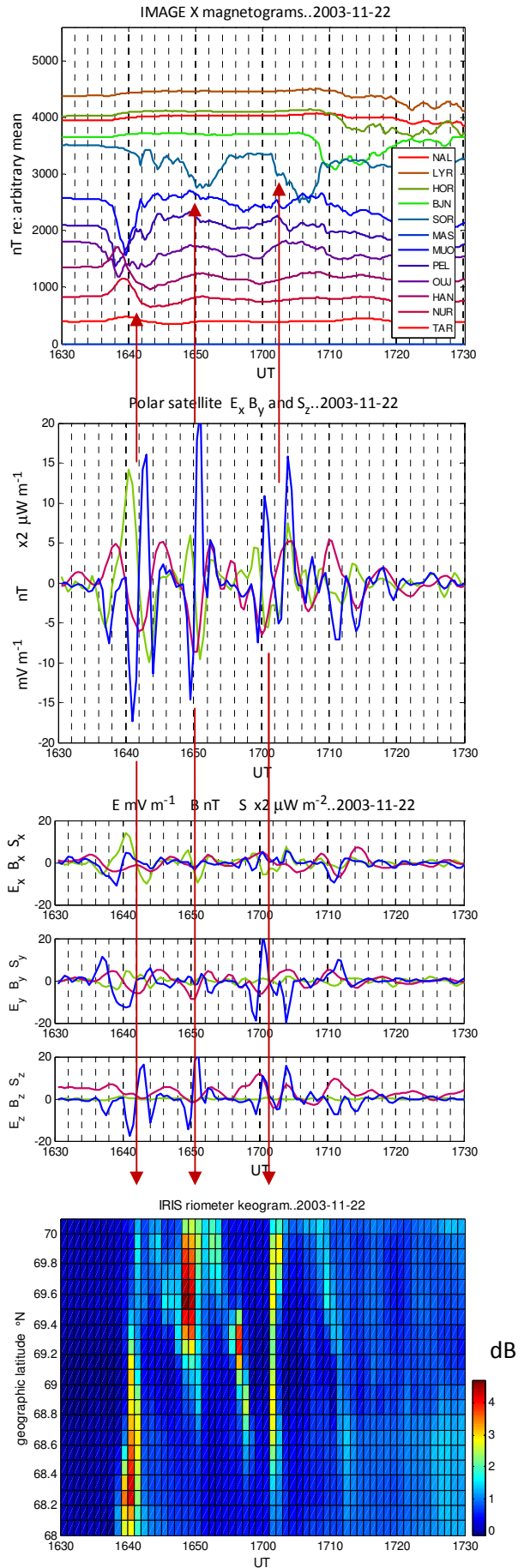
This event is described in Section 8.3.4.

The first, but weaker, Poynting flux impulse was also at 1638UT and was followed by other  $-S_z$  impulses at 1641UT, 1644UT, 1650UT, 1700UT and 1703UT giving a mean time between PFIs of about 4 minutes.

The strongest PFI at 1650UT coincided with a -500nT deflection at SOR.

The two strongest IRIS riometer 5dB absorption spikes at 1640UT and 1648UT were each one minute earlier than the two strongest  $-S_z$  Poynting flux impulses and the spike at 1701UT was one minute later than the next  $-S_z$  PFI.

Further discussion of this event is given in Sections 6.6.3 and 7.3.4.



**Group III Figure A7.12**

**1630 - 1730UT on 2003-12-15**

Polar GSE [0.8 8.2 0.2]  $R_E$

Polar GSM [0.8 8.2 -0.2]  $R_E$

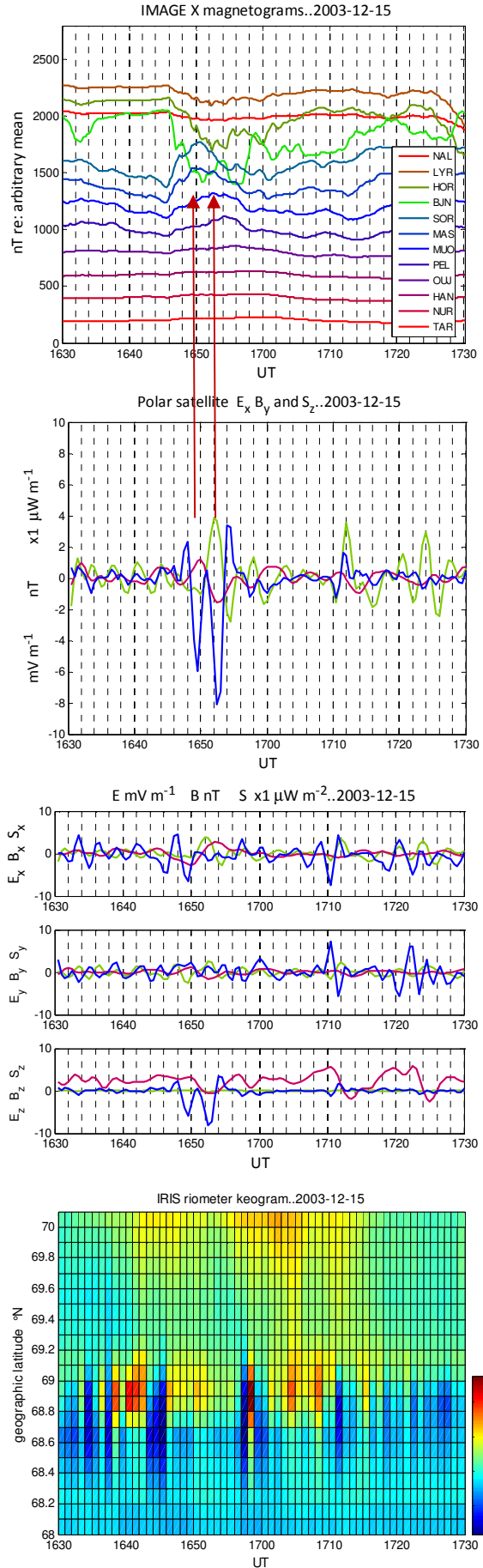
Polar trace at 1650UT 72°N 17°E

The Polar satellite high latitude field line trace was between IMAGE ground magnetometers at BJJ and SOR.

At 1646UT magnetometers at HOR and BJJ showed a sudden negative deflection whilst SOR MAS MUO PEL and OJJ showed a positive deflection. The peak positive deflection at SOR was at 1650UT. Two  $-S_z$  PFIs were observed at 1649UT and 1652UT during the -500nT high latitude substorm.

In this event the positive magnetometer activity at SOR mirrored the expansion phase of the substorm at BJJ so that the substorm resembled an OGMD event extended in time.

The IRIS riometer keogram showed evidence of activity to the north, as would have been expected, but to the south of this northerly precipitation it had the characteristic fluctuating enhanced absorption associated with magnetospheric Group I electric field oscillations. This provides an indication that such electric field phenomena may be found in the magnetosphere to the south of upward flowing conventional current sheets.



**Group IV      Figure A7.13**  
**2154 - 2254UT on 2002-10-17**

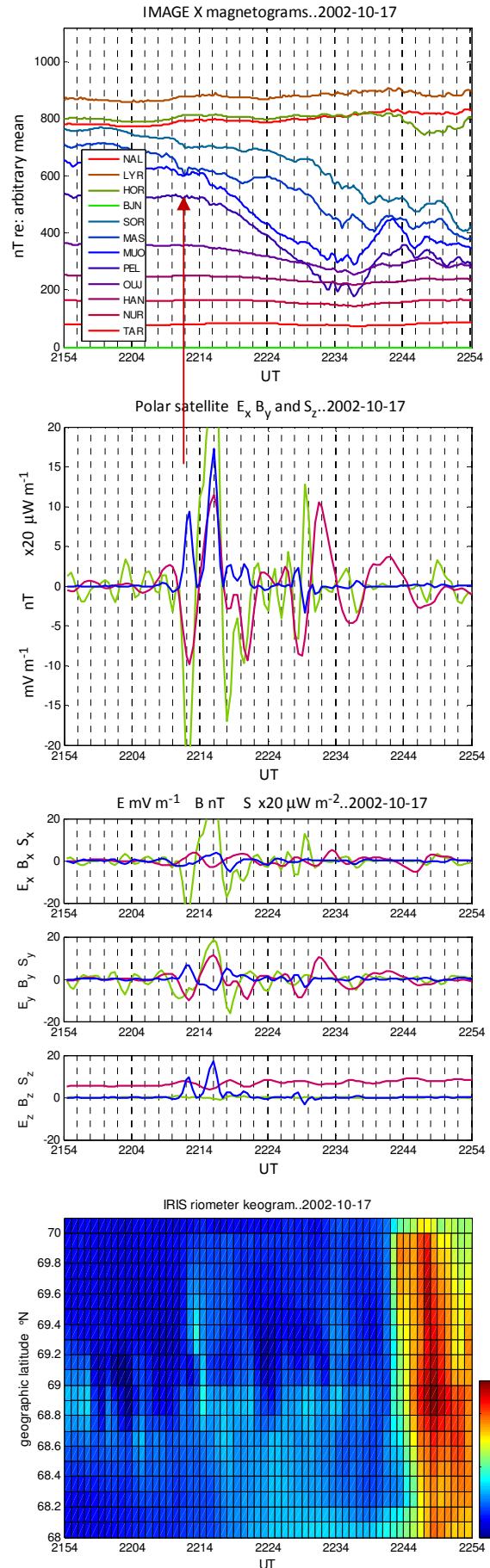
Polar GSE [-6.4 1.7 2.8] R<sub>E</sub>  
 Polar GSM [-6.4 2.2 2.4] R<sub>E</sub>  
 Polar trace at 2214UT 68°N -15°E

The Polar satellite was in the northern magnetosphere and the field line trace was between Greenland and Iceland at a geomagnetic latitude between IMAGE magnetometers BJN and HOR.

A very strong PFI with  $S_z$  180  $\mu\text{Wm}^{-2}$  was followed by another nearly twice as strong at +350  $\mu\text{Wm}^{-2}$  four minutes later. The magnetic field latitude was similar to that of the IMAGE ground magnetometer at BJN and the IMAGE magnetometers SOR MAS MUO and PEL all showed the onset of a gradual -700nT substorm expansion phase around this time.

The IRIS riometer was possibly too far to the south to record these powerful events and unrelated absorption was not seen until 2242UT.

The PFI vectors at 2212UT and 2216UT were in the GSM +x and -y directions.



**Group IV Figure A7.14**

**1730 - 1830UT on 2003-10-27**

Polar GSE [-7.3 4.8 1.5] R<sub>E</sub>

Polar GSM [-7.3 5.1 0.1] R<sub>E</sub>

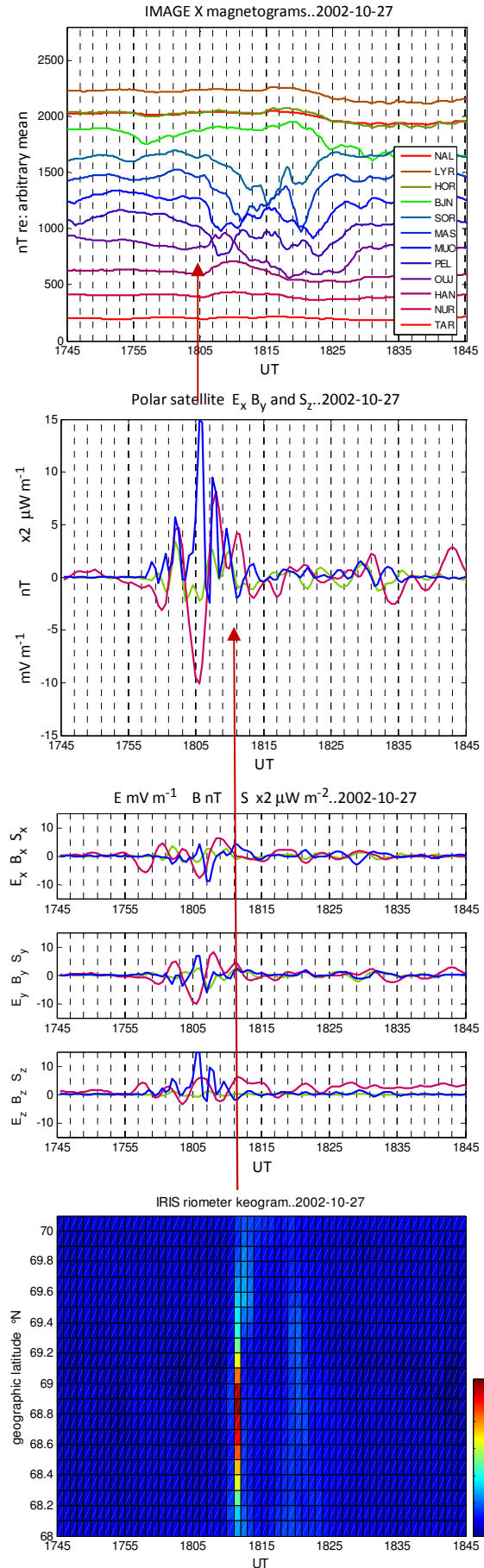
Polar trace at 1800UT 68°N 43°E

The Polar satellite was near the geomagnetic equator and the field line trace was over the Kola peninsula to the east of the IMAGE chain and at the geomagnetic latitude of OUJ.

Despite the longitudinal separation an OGMD event occurred at 1808UT, three minutes after a magnetospheric +30 μW m<sup>-2</sup> S<sub>z</sub> PFI.

The IRIS riometer keogram showed an absorption spike four minutes later at 1812UT so it could have been associated.

The PFI vector at 1806UT was in the GSM +x -y and +z directions suggesting that the source was tailward of the Polar satellite.



**Group IV Figure A7.15**

**2000 - 2100UT on 2003-10-16**

Polar GSE [-7.1 5.9 -1.2] R<sub>E</sub>

Polar GSM [-7.1 5.5 -2.5] R<sub>E</sub>

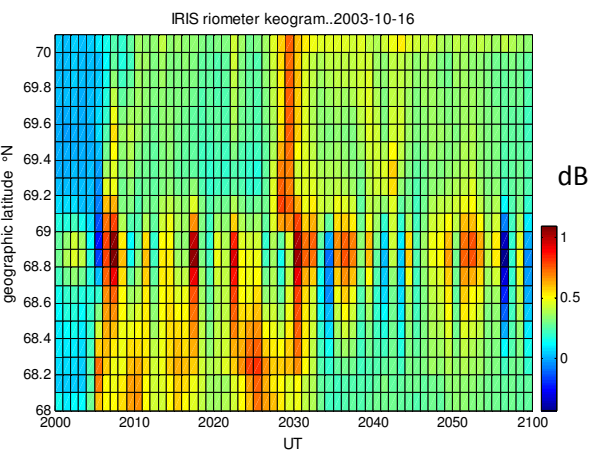
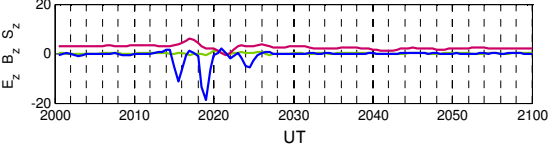
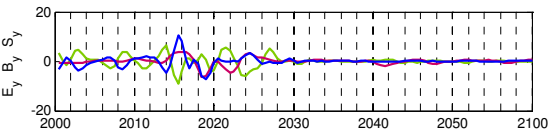
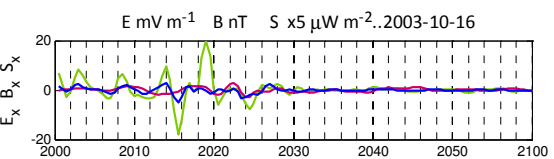
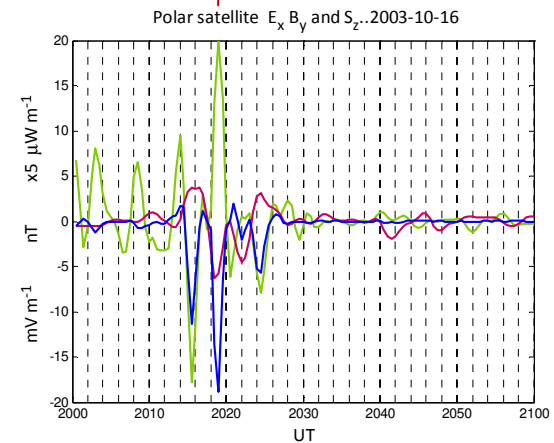
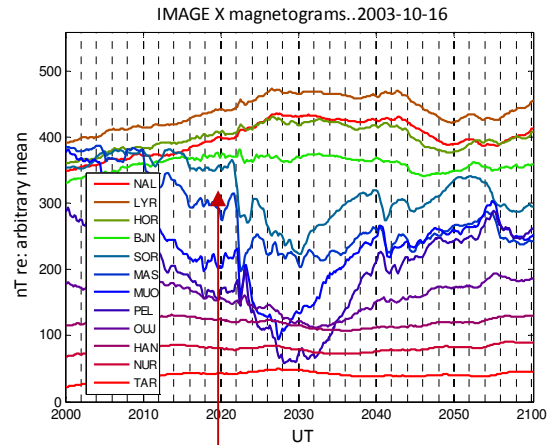
Polar trace at 2020UT 68°N -1°E

The Polar satellite was in the southern magnetosphere and the field line trace was over the Norwegian sea at a similar geomagnetic latitude to IMAGE ground magnetometer SOR and northwards of the IRIS riometer.

The start of the substorm precipitation at 2022UT very well defined at SOR and was preceded by two  $-S_z$  Poynting flux impulses of  $-50 \mu\text{Wm}^{-2}$  at 2016UT and  $-85 \mu\text{Wm}^{-2}$  at 2019UT.

Electric field oscillations with a frequency of 3.1mHz were present until 2030UT and the IRIS riometer keogram had the same character as the Group I electric field oscillations with 1dB bands of enhanced absorption at 2007UT, 2017UT, 2022UT, 2030UT, 2036UT and 2052UT. This observation is similar to the one described in Figure A7.12 above, where magnetospheric electric field oscillations were also observed to the south of high latitude precipitation.

The PFI vectors were in the GSM +x direction indicating a source tailward of  $-7.1R_E$ .



**Group IV Figure A7.16**

**1800 - 1900UT on 2003-11-09**

Polar GSE [-4.1 5.2 1.5]  $R_E$

Polar GSM [-4.1 5.4 0.4]  $R_E$

Polar trace at 1822UT 66°N 18°E

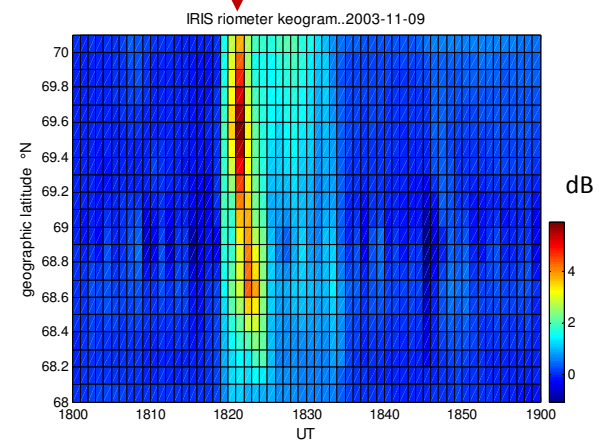
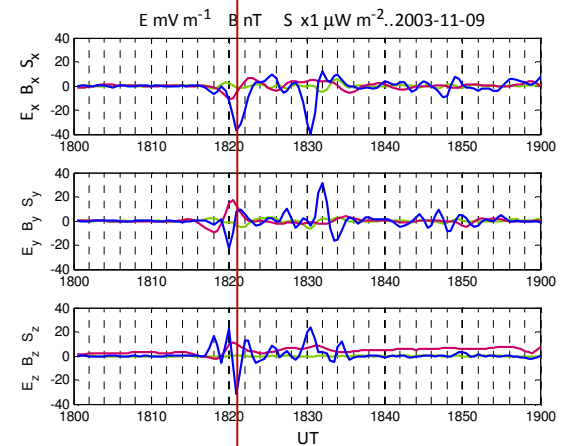
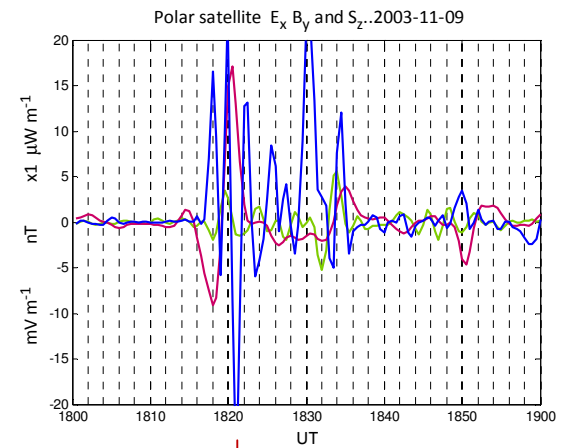
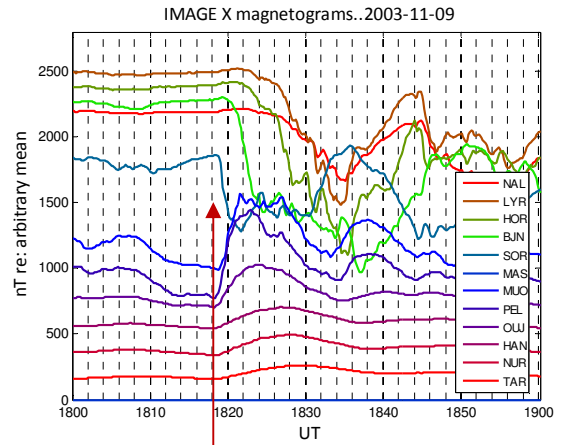
The Polar satellite was near the geomagnetic equator and the field line trace was between IMAGE ground magnetometers PEL and OUI.

Sudden negative magnetometer deflections corresponding to substorm onset were seen at SOR and MAS and one minute later at BJN.

An OGMD event at 1821UT coincided with a  $-S_z$  PFI at 1821UT suggesting that an ionospheric current sheet was incident between SOR and MUO which straddle the IRIS riometer location.

This current sheet is clearly seen in the IRIS riometer keogram as a spike with a latitudinal extent of approximately  $1.6^\circ$ .

This  $-S_z$  PFI was preceded by the first PFI of  $+18 \mu W m^{-2}$  at 1818UT. Further  $+S_z$  PFIs then occurred at 1820UT, 1822UT, 1826UT, 1830UT and 1834UT giving a mean interval between  $+S_z$  PFIs of 3.5 minutes. These multiple PFIs were observed throughout the expansion phase of the substorm at SOR and suggest that they were associated with the current feed along field lines. The PFI vector at 1818UT was in the GSM  $+x$  direction indicating a source tailward of GSM  $x = -4.1R_E$ . This event was also discussed in Section 6.5.4.



**Group IV      Figure A7.17**

**1600 - 1700UT on 2003-11-15**

Polar GSE [-2.7 8.9 -2.0] R<sub>E</sub>

Polar GSM [-2.7 8.1 -4.2] R<sub>E</sub>

Polar trace at 1630UT 72°N 20°E

The Polar satellite was in the southern magnetosphere and the field line trace was at a high latitude between IMAGE ground magnetometers BJN and SOR.

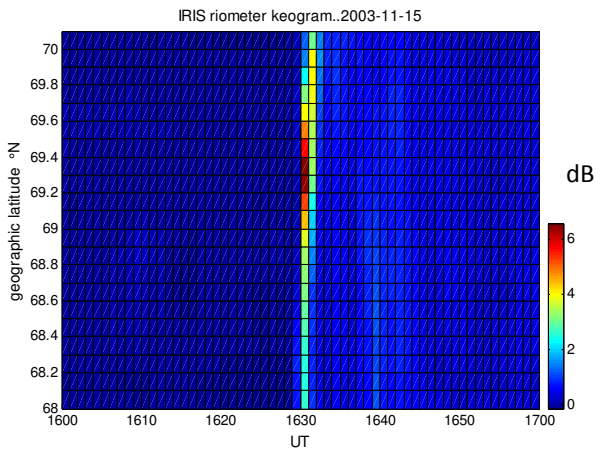
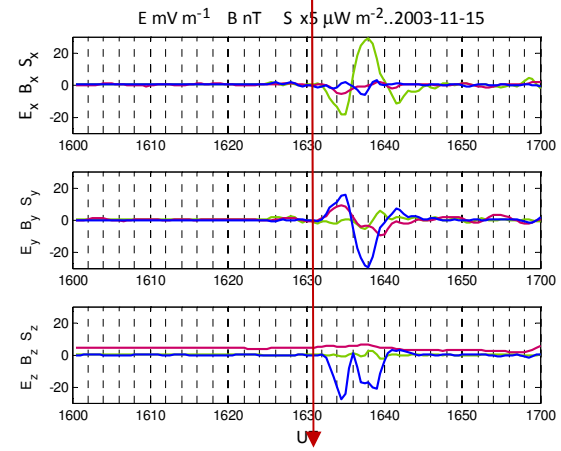
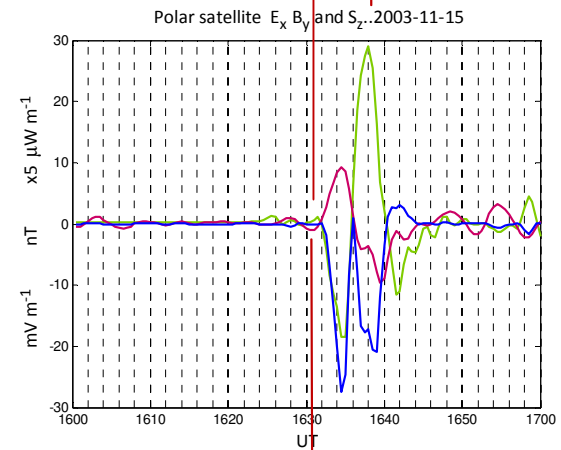
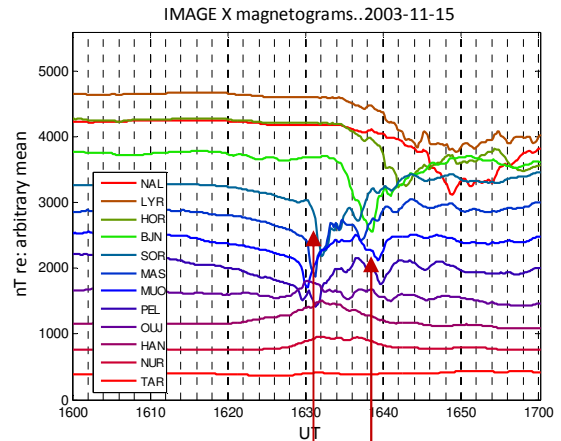
IMAGE magnetograms further to the south showed that a OGMD event occurred at 1630UT between PEL and OUI at the same time as the IRIS riometer keogram showed 6dB of enhanced absorption.

At 1634UT a  $-28\mu\text{Wm}^{-2}$   $-S_z$  PFI was observed coincident with substorm onset at BJN.

The pattern of events suggests that precipitation into the ionosphere initially began around latitude 65°N giving rise to eastward and westward ionospheric currents. The current system then moved northwards and took on the character of a high latitude substorm whose onset was marked by the first PFI on the high latitude Polar satellite field line.

The Ex:By ratio was  $\sim 3000\text{kms}^{-1}$  for this impulse doublet.

The PFI vector at 1634UT was in the GSM +x -y direction.



**Group V Figure A7.18**

**1730 - 1830UT on 2002-10-26**

Polar GSE [-6.0 6.3 -2.1] R<sub>E</sub>

Polar GSM [-6.0 5.5 -3.8] R<sub>E</sub>

Polar trace at 1745UT 73°N 35°E

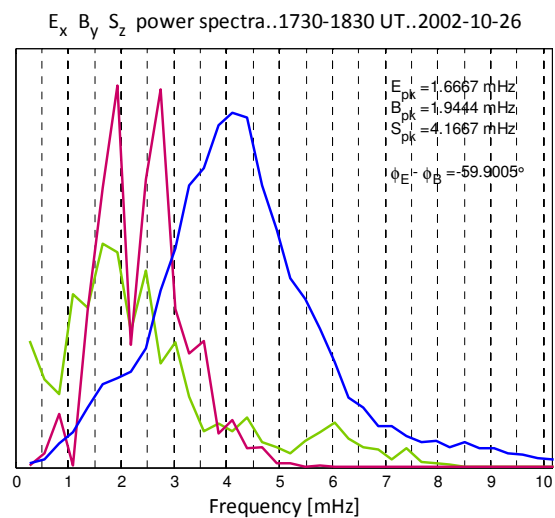
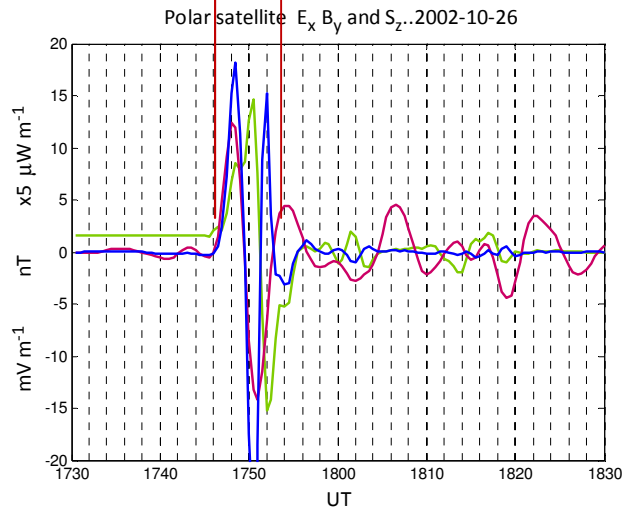
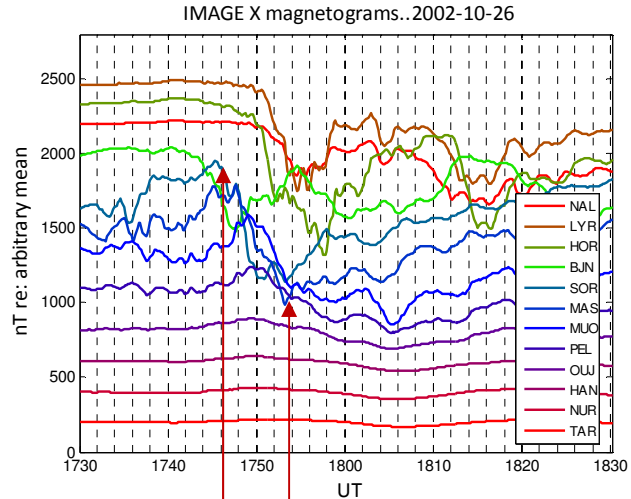
Polar trace at 1800UT 72°N 30°E

The Polar trace during this observation was to the Barents Sea at approximately the same geomagnetic latitude, but to the east of IMAGE magnetometer SOR. Electric field data was not available before 1746UT, the time when large amplitude magnetospheric magnetic oscillations began.

There were just two cycles of quadrature Poynting flux oscillation with an amplitude of +90/-150 μWm<sup>-2</sup>.

Also at 1746UT ground magnetometer SOR registered the negative deflection associated with the onset of a substorm.

The quadrature signal was seen in the Polar satellite data until 1753UT which corresponded to the end of the substorm expansion phase at SOR [Section 8.4].



**Group V Figure A7.19**

**1830 - 1930UT on 2002-11-09**

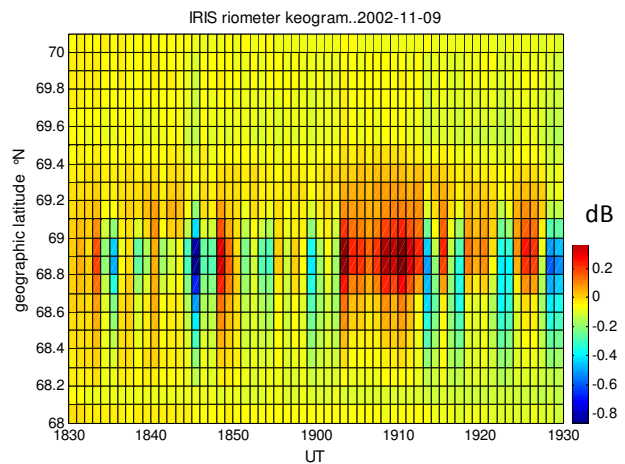
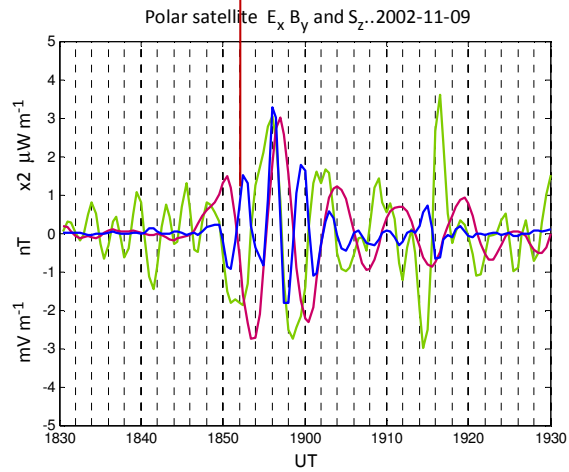
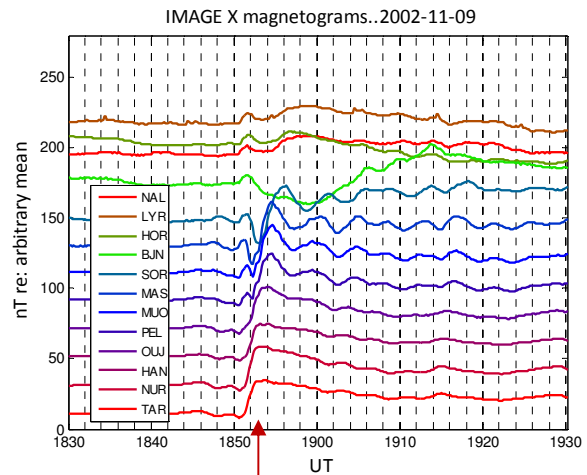
Polar GSE [-5.6 5.0 2.3] R<sub>E</sub>

Polar GSM [-5.6 5.4 1.4] R<sub>E</sub>

Polar trace at 1845UT 68°N 16°E

Polar trace at 1915UT 68°N 9°E

The Polar satellite field line trace during this observation was to the Lofoten Islands to the West of the IMAGE magnetometer chain at a geomagnetic latitude between SOR and MAS. Electric field oscillations were already present, and as with Group I events, this shows in the character of the IRIS riometer keogram. Magnetic oscillations then initiated the quadrature resonance at 1850UT. At 1852UT all the IMAGE ground magnetometers showed a positive deflection. SOR and MAS also showed a distinctive notch feature at 1853UT which was near the time of the peak  $-B_y$  deflection. The following  $+B_y$  maximum at 1857UT coincided with the time of the peak at SOR giving a frequency of about 2mHz in good agreement with the satellite spectral estimates. De-phasing of the quadrature signature occurred around 1916UT. A progressive phase advance together with an increasing resonant frequency was observed in the ground signal towards lower latitudes. The estimated notch frequency increased with latitude as expected from an impulsive source.



**Group V Figure A7.20**

**1800 - 1900UT on 2002-12-24**

Polar GSE [0.5 8.5 1.5] R<sub>E</sub>

Polar GSM [0.5 8.3 .4] R<sub>E</sub>

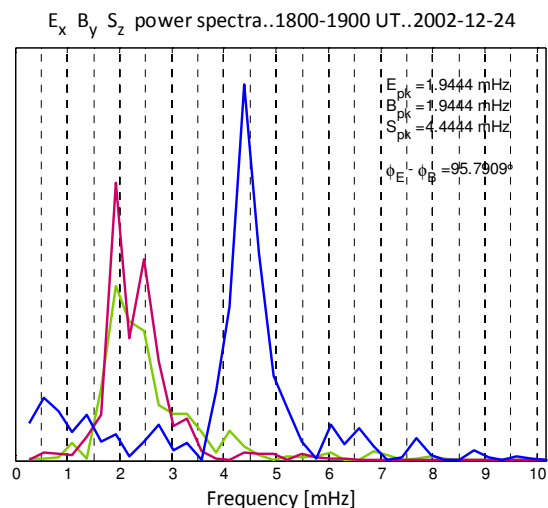
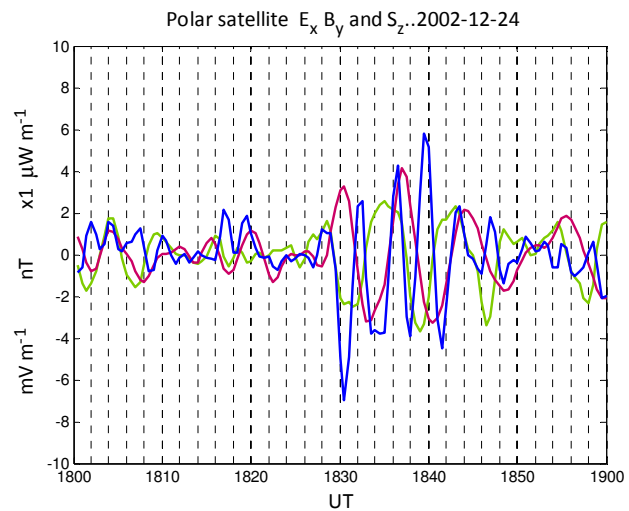
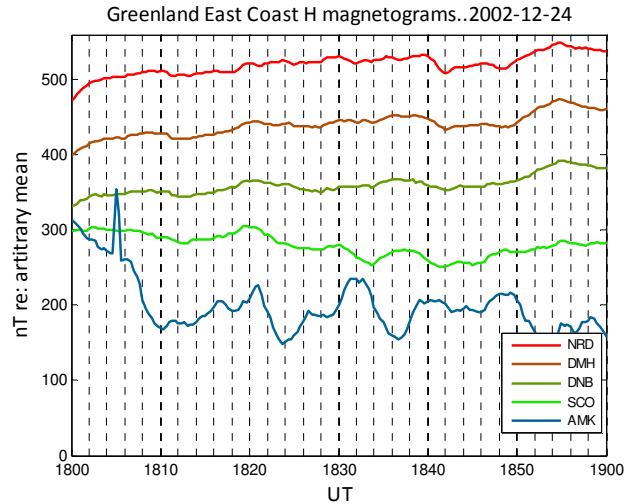
Polar trace at 1824UT 65°N -34°E

Polar trace at 1854UT 64°N -40°E

The Polar satellite field line trace was near Greenland magnetometer AMK [65.6°N -37.6°E] which recorded irregular oscillations with a component of 1.7mHz.

The quadrature oscillations observed by the Polar satellite instruments were present throughout this time interval but were strongest between 1830UT and 1850UT. The spectrum showed a sharp Poynting flux oscillation frequency of 4.4mHz.

Dividing the Poynting flux oscillation frequency by two gave 2.2mHz which was higher than the ground signal frequency at AMK. However there were peaks in the electric and magnetic field oscillations at 1.9mHz which was closer.



**Group V Figure A7.21**

**2100 - 2200UT on 2003-10-10**

Polar GSE [-5.7 2.0 1.9] R<sub>E</sub>

Polar GSM [-5.7 2.3 1.4] R<sub>E</sub>

Polar trace at 2130UT 67°N -3°E

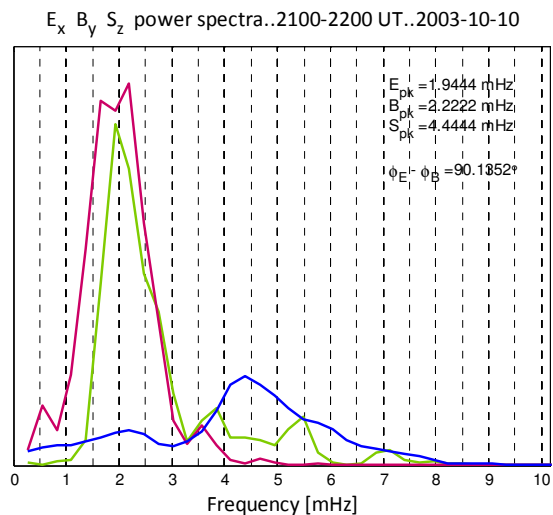
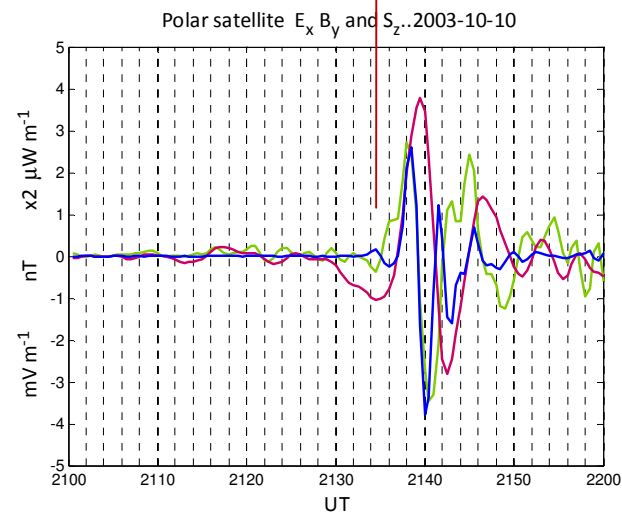
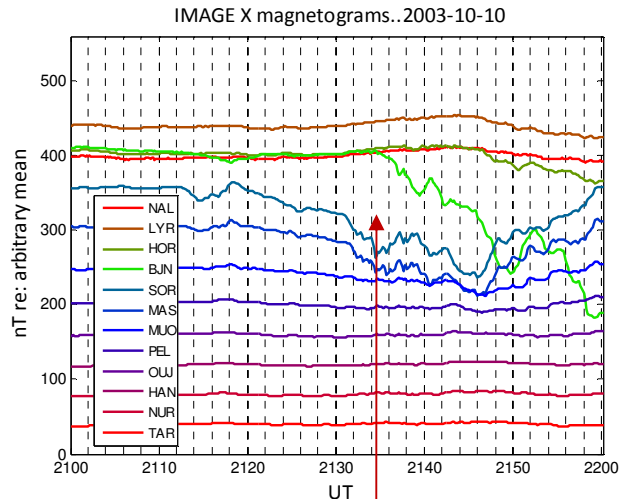
Polar trace at 2200UT 66°N -10°E

The Polar satellite field line trace was over the Norwegian Sea at the same geomagnetic latitude as ground magnetometer SOR.

IMAGE magnetograms showed that Pi2 oscillations commenced at 2132UT at SOR and MAS.

The quadrature oscillations were observed to commence at 2134UT at the location of the Polar satellite so there appeared to be a link between the quadrature resonance and the high latitude substorm at BJN [Section 8.4].

The amplitude of the Poynting flux oscillations decayed with a damping time of around 4 minutes and the pulse ended around 2150UT, which was the same time as the substorm expansion phase ended at BJN.



**Group V      Figure A7.22**

**2100 - 2200UT on 2003-10-19**

Polar GSE [-6.7 6.4 -1.5]  $R_E$

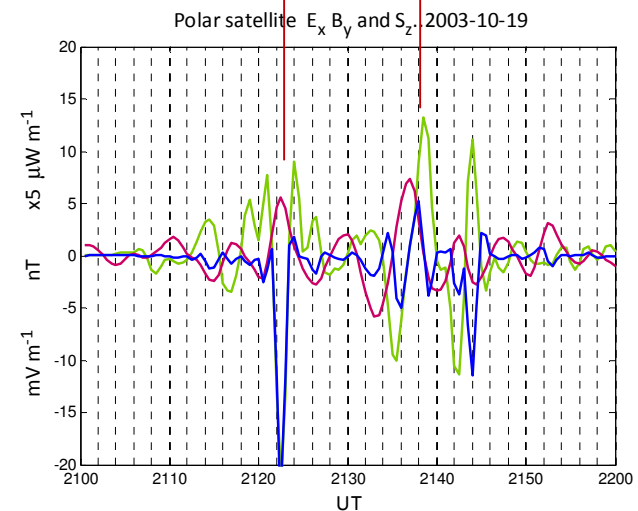
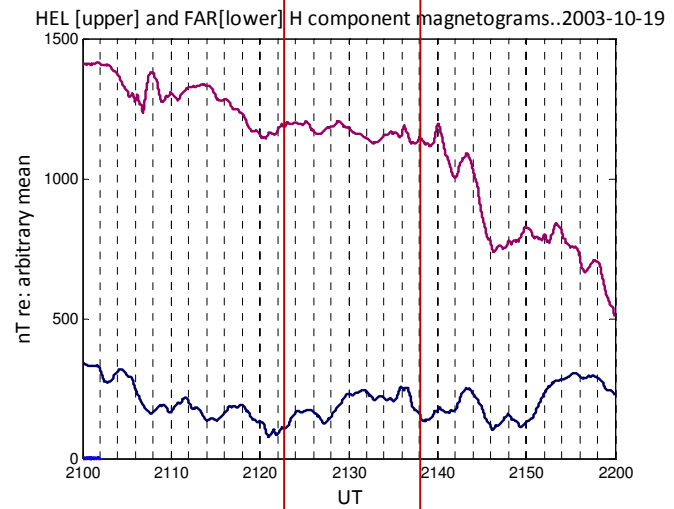
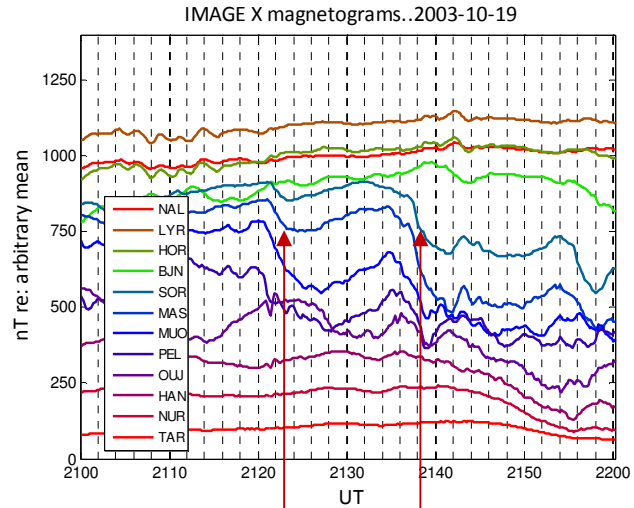
Polar GSM [-6.7 6.0 -2.7]  $R_E$

Polar trace at 2130UT 65°N -23°E

Polar trace at 2200UT 63°N -29°E

The Polar satellite field line trace was west of SAMNET ground magnetometer HEL in Iceland [63.8°N -20.6°E] and at a geomagnetic latitude between IMAGE magnetometers SOR and BJN. SOR registered a negative deflection coincident with a  $-100 \mu W m^{-2} -S_z$  impulse with a E:B ratio of  $3600 km s^{-1}$  at 2122UT [Figure 6.15]. Six minutes later, at 2128UT, a quadrature oscillation was set up, so it is possible that this impulse also initiated the resonance. The impulse was not seen in the HEL or FAR ground magnetometer data nor in the IRIS riometer keogram [Figure 6.16] geomagnetically to the south. The resonance frequency was 2.8mHz [6 minute] and a component with the same frequency appeared in the ground magnetometer oscillations at FAR. Final de-phasing occurred at 2150UT. IMAGE magnetograms showed a substorm onset at 2122UT.

This event is also referred to in Section 8.4.



**Group V Figure A7.23**

**1830 - 1930UT on 2003-10-26**

Polar GSE [-5.9 7.2 -1.4] R<sub>E</sub>

Polar GSM [-5.9 6.7 -3.0] R<sub>E</sub>

Polar trace at 1905UT 70°N 6°E

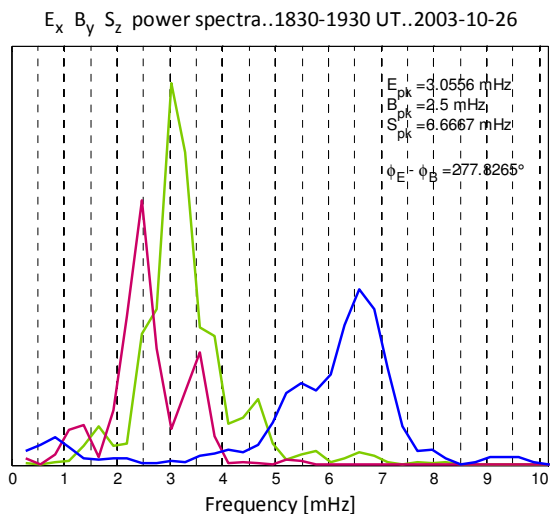
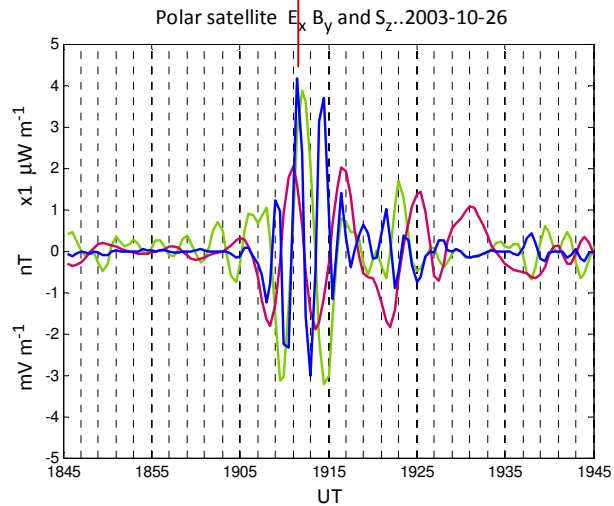
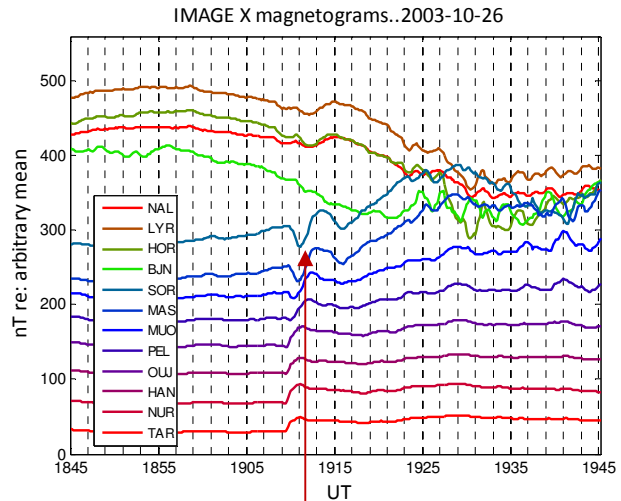
Polar trace at 1918UT 69°N 3°E

The Polar satellite was in the southern magnetosphere and the field line trace was over the Norwegian sea geomagnetically slightly south of the IMAGE ground magnetometer BJN.

A quadrature resonance commenced at 1905UT in Polar satellite data and 4 minutes later at 1909UT there was an increase in all the IMAGE X component magnetograms south of BJN. SOR and MAS then showed a distinctive notch feature at 1911UT which was the time of the peak resonance.

The time of the notch coincided with a +B<sub>y</sub> deflection and the subsequent ground magnetometer maxima coincided with the following -B<sub>y</sub> deflection at 1914UT, giving a frequency of 3.3mHz which was the same as the magnetospheric electric field oscillations and very near to half the Poynting flux frequency. The resonance ended around 1925UT.

The positive deflection [eastwards ionospheric Hall current] increased throughout the duration of the resonance, which may suggest that it was associated with a current channel to the ionosphere.



**Group V Figure A7.24**

**1600 - 1700UT on 2003-11-09**

Polar GSE [-4.4 7.1 0.2] R<sub>E</sub>

Polar GSM [-4.4 6.9 -1.8] R<sub>E</sub>

Polar trace at 1616UT 69°N 47°E

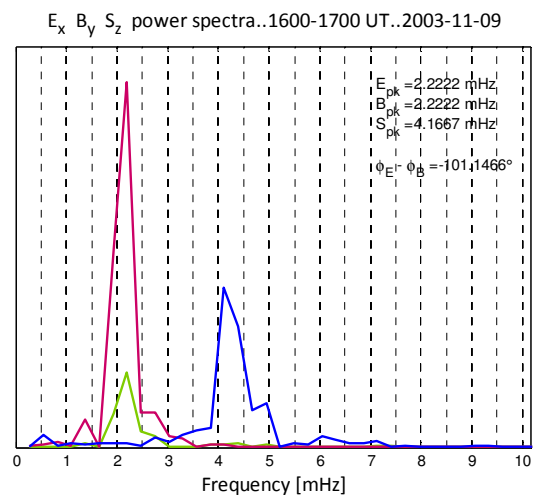
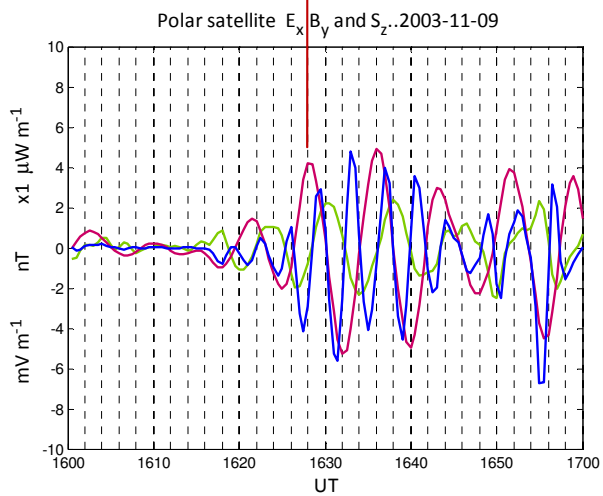
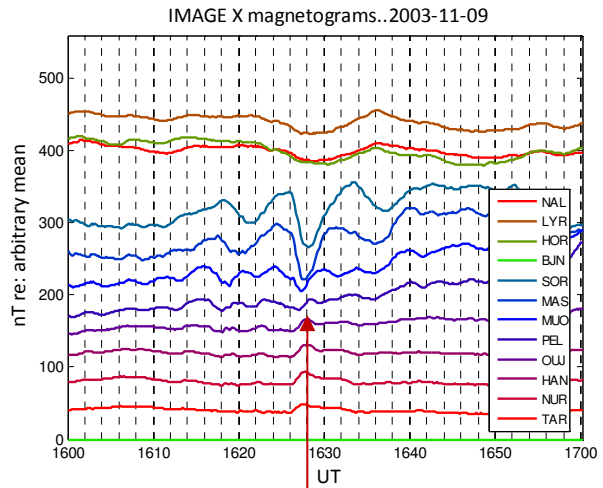
Polar trace at 1712UT 68°N 35°E

The Polar satellite field line trace was over the Barents sea at a similar geomagnetic latitude to IMAGE ground magnetometer SOR.

SOR and MAS recorded a notch at 1628UT and the average half-cycle time for these two signals was estimated at 4minutes, corresponding to a frequency of 2.1mHz. This was in agreement with the Polar satellite Poynting flux spectra which also had a half-frequency of 2.1mHz.

This half-cycle time decreased towards lower latitudes consistent with the impulsive resonance model.

Weak quadrature oscillations with a peak deflection of  $-7\mu\text{Wm}^{-2}$  commenced at approximately 1618UT, which was the time when oscillations began to appear in ground magnetometer data. The time of the notch minimum corresponded to the first strong +B<sub>y</sub> magnetic field oscillation in the Polar satellite data. Final de-phasing occurred at 1736UT [not shown]. No substorm or OGMD event was observed and there was no indication in the Polar satellite data of what initiated the resonance.



**Group V      Figure A7.25**

**1836 - 1936UT on 2003-11-18**

Polar GSE [-2.5 8.9 -1.4] R<sub>E</sub>

Polar GSM [-2.5 8.6 -2.6] R<sub>E</sub>

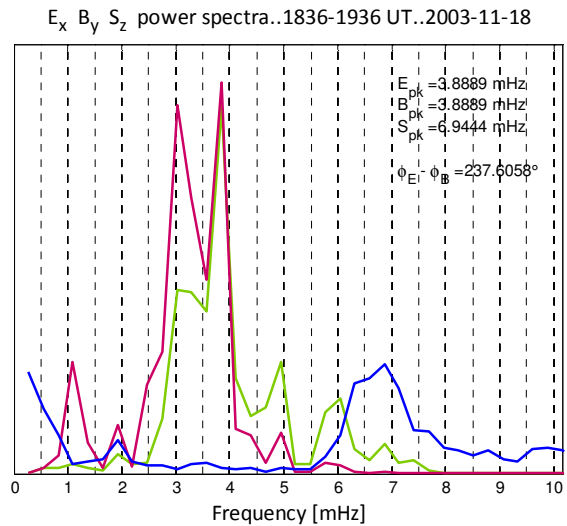
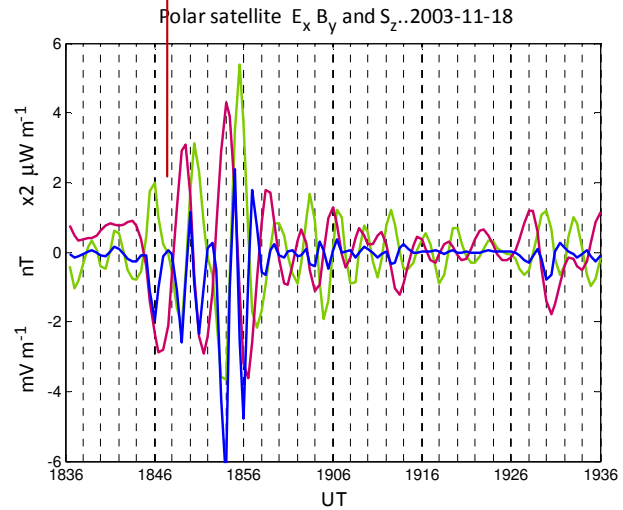
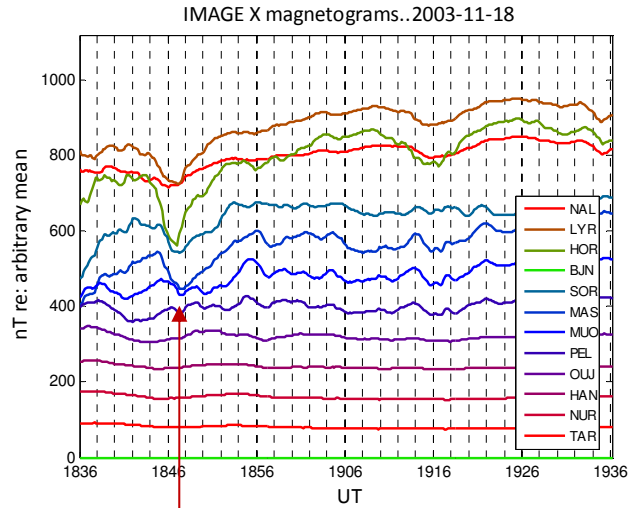
Polar trace at 1844UT 68°N -15°E

Polar trace at 1900UT 67°N -18°E

The Polar satellite field line trace was over the Greenland sea to the south and east of Greenland east coast ground magnetometer SCO [70.5°N -22.0°E] at a similar geomagnetic latitude to IMAGE ground magnetometer BJN.

Weak quadrature oscillations with a peak deflection of  $-16 \mu\text{Wm}^{-2}$  began at 1844UT and the main pulse ended at 1858UT. There was no indication in the Polar satellite data of what initiated the resonance. The HOR magnetogram showed a notch at 1847UT coincident with the first  $-B_y$  deflection.

Final de-phasing of the quadrature oscillations occurred around 1916UT.



**Group V      Figure A7.26**

**1700 - 1800UT on 2003-11-25**

Polar GSE [-1.8 8.7 -0.6] R<sub>E</sub>

Polar GSM [-1.8 8.6 -1.9] R<sub>E</sub>

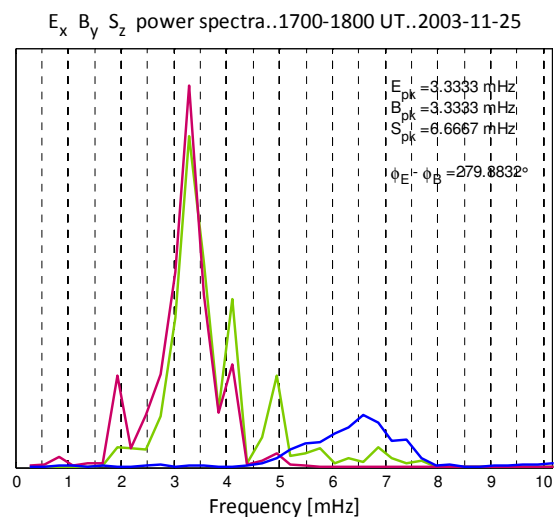
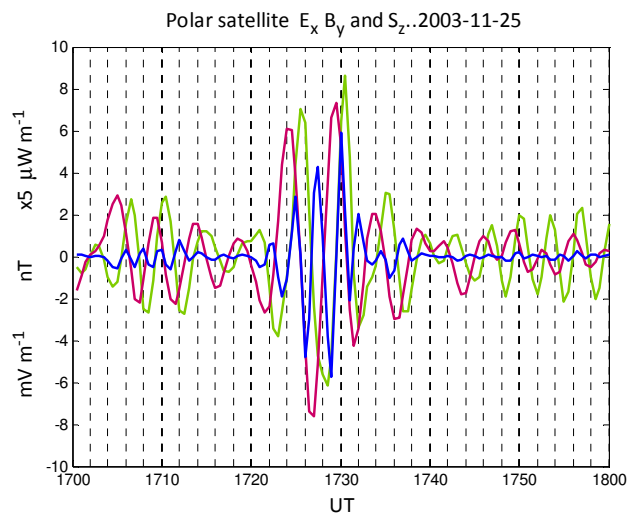
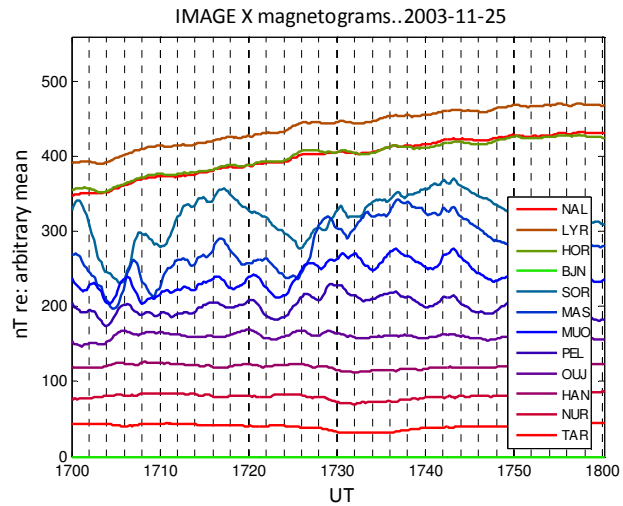
Polar trace at 1720UT 70°N 3°E

Polar trace at 1740UT 69°N -1°E

The Polar satellite field line trace was over the Norwegian sea at a similar geomagnetic latitude to IMAGE ground magnetometer BJT which was not operational.

A quadrature resonance with a frequency of 3.3mHz began at 1704UT but only exceeded 10 μWm<sup>-2</sup> between 1722UT and 1732UT.

There was no indication in the Polar satellite data of what initiated the resonance. Irregular oscillations were observed in the IMAGE data which included a frequency component of approximately 3mHz at MUO.



**Group V      Figure A7.27**

**1330 - 1430UT on 2003-12-15**

Polar GSE [2.1 9.0 -1.8] R<sub>E</sub>

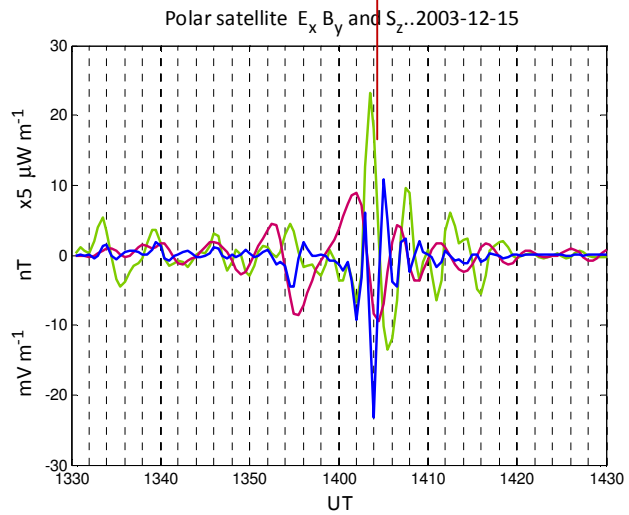
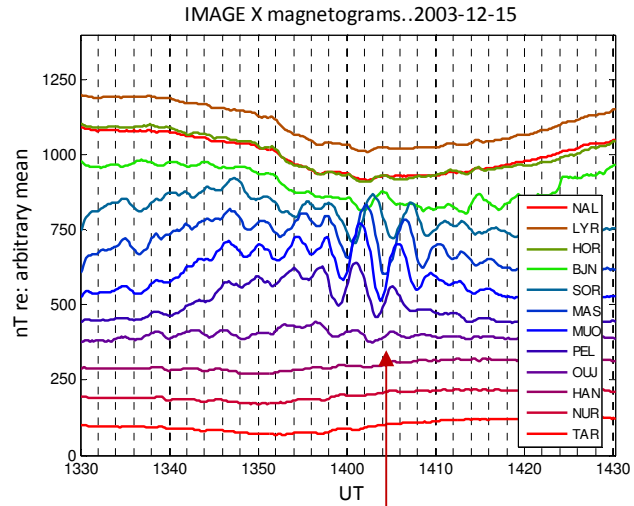
Polar GSM [2.1 8.6 -3.3] R<sub>E</sub>

Polar trace at 1400UT 72°N 17°E

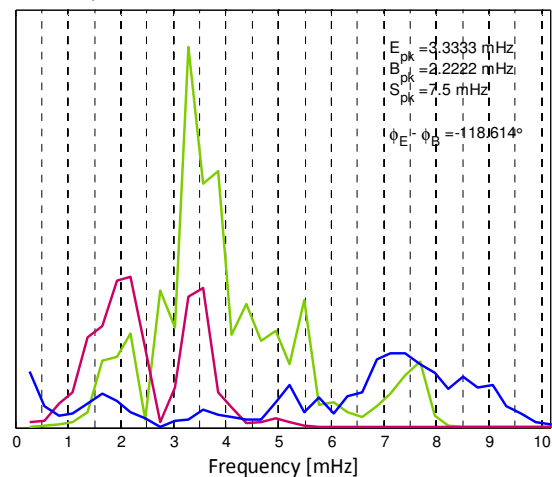
The Polar satellite field line trace was at a similar geomagnetic latitude to IMAGE ground magnetometer BJN. Oscillations with a frequency of 3.3mHz and a peak amplitude of 120nT were observed from SOR to PEL

The quadrature signal was indistinct but the electric field frequency was 3.3mHz in agreement with the ground oscillations. The maximum ground displacement coincided with a PFI caused by an +E<sub>x</sub> electric field impulse at 1404UT.

No corresponding event was observed in the IRIS riometer keogram at 1404UT.



E<sub>x</sub> B<sub>y</sub> S<sub>z</sub> power spectra..1330-1430 UT..2003-12-15



**Group V      Figure A7.28**  
**1436 - 1536UT on 2003-12-15**

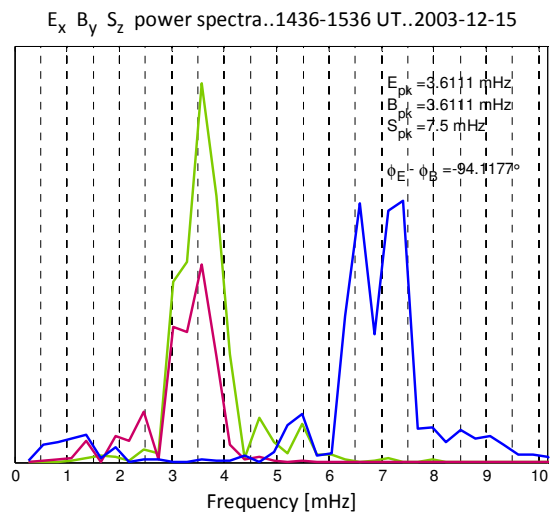
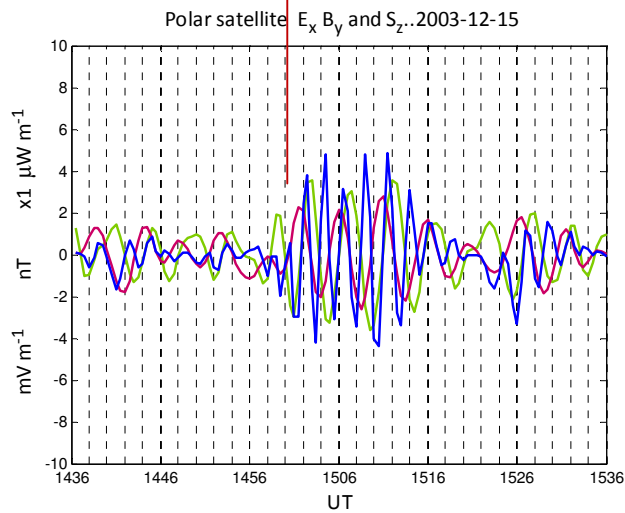
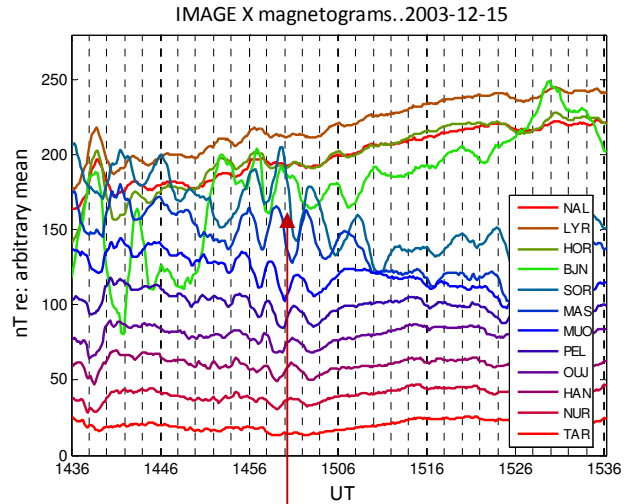
Polar GSE [1.6 8.9 -1.0]  $R_E$   
 Polar GSM [1.6 8.7 -2.1]  $R_E$   
 Polar trace at 1720UT 70°N 3°E  
 Polar trace at 1740UT 69°N -1°E

The Polar satellite field line trace was over the Barents Sea at a similar latitude to IMAGE ground magnetometer BJN.

Strong ground oscillations were initiated at 1854UT and were observed from BJN to MUO. The greatest amplitude of 20nT was recorded at SOR and had a frequency of 3.3mHz. These oscillations lasted until 1512UT.

The main quadrature resonance pulse in the Polar satellite data was between 1458UT and 1516UT and had a frequency of 3.5mHz in the  $E_x$  and  $B_y$  components. Thus the 18 minute duration of the resonance detected in the Polar satellite data was the same as the oscillations at SOR but delayed by 2 minutes. This suggests that the compression wave detected on the ground sustained the magnetospheric resonance.

No enhanced absorption signal was seen in the IRIS riometer keogram.



**Group VI Figure A7.29**

**2230 - 2330UT on 2002-09-11**

Polar GSE [-8.5 -2.0 1.7] R<sub>E</sub>

Polar GSM [-8.5 -1.6 2.1] R<sub>E</sub>

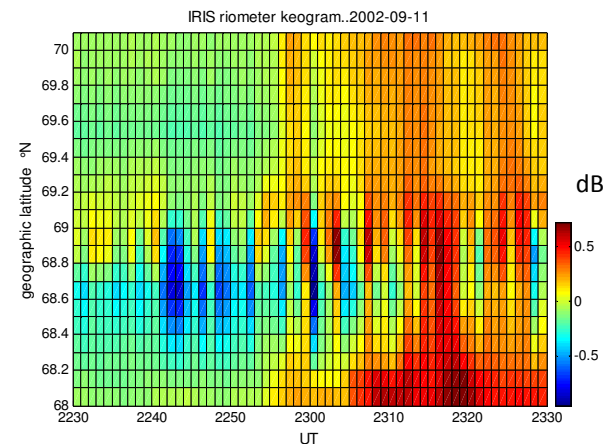
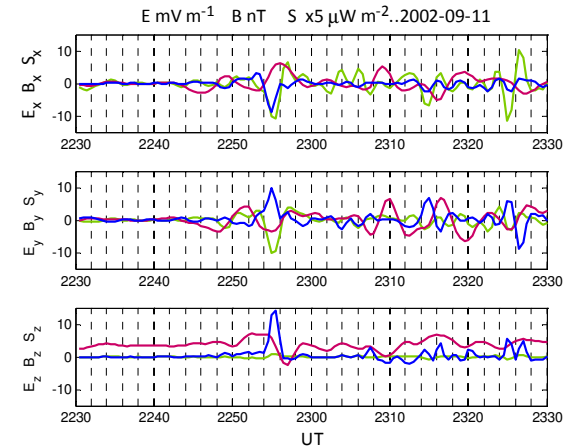
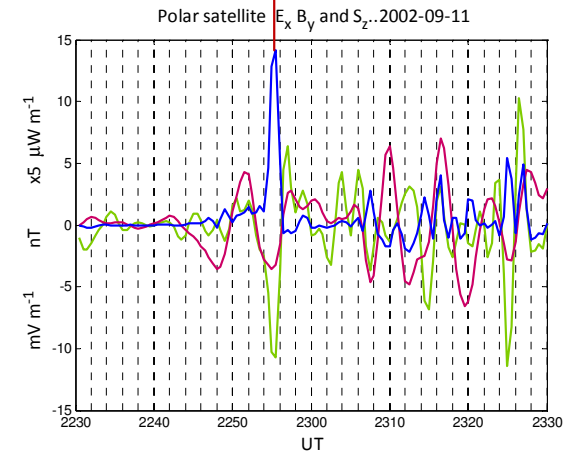
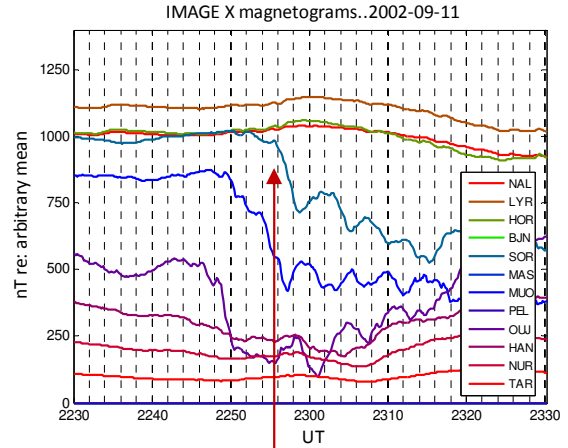
Polar trace at 2300UT 67°N 14°E

The Polar satellite was in the northern magnetosphere and the field line trace was near to the geomagnetic latitude of IMAGE ground magnetometer MAS although the Substorm onset occurred at 2249UT at MAS.

Ground magnetometers BJN, MUO and PEL were not operational but the +75μWm<sup>-2</sup> Poynting flux impulse at 2255UT was a minute before the substorm onset at 2256UT at SOR. If the field line tracing overestimated the latitude by 2° then the PFI would be exactly coincident with the substorm onset.

Electric field E<sub>x</sub> component oscillations [normal to the geomagnetic shell] were observed during the substorm and the IRIS keogram has the characteristic pattern of fluctuating enhanced absorption that is associated with magnetospheric Group I.

The PFI vector at 2255UT was in the GSM +x -y +z direction which suggests that the source was tailward of GSM x = -8.5R<sub>E</sub>.



**Group VI Figure A7.30**

**2200 - 2300UT on 2002-10-03**

PolarGSE [-9.1 2.9 -0.6] R<sub>E</sub>

Polar GSM [-9.1 2.7 -1.3] R<sub>E</sub>

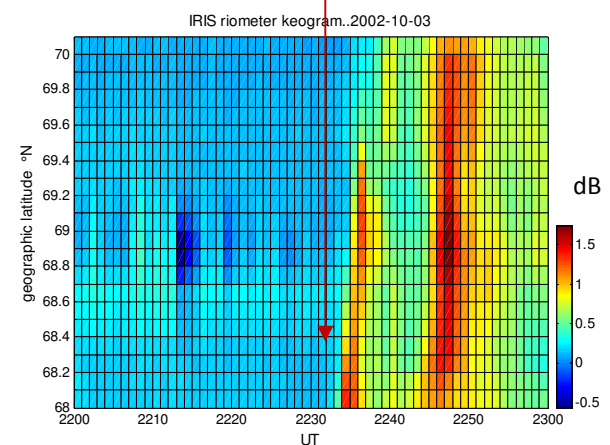
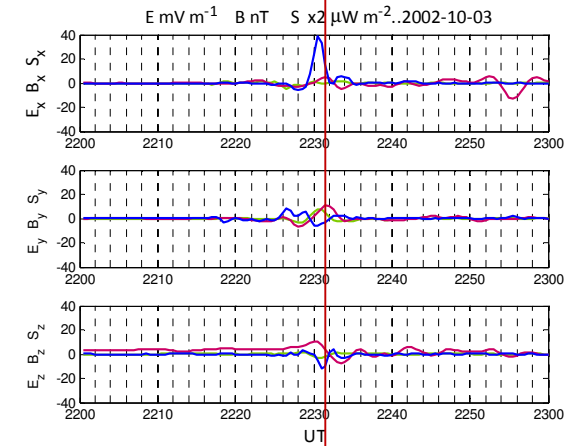
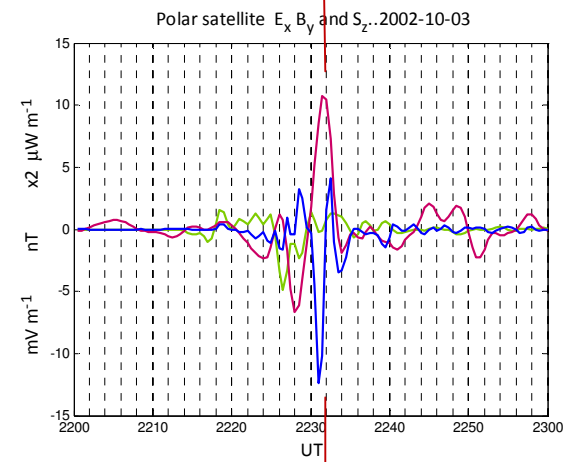
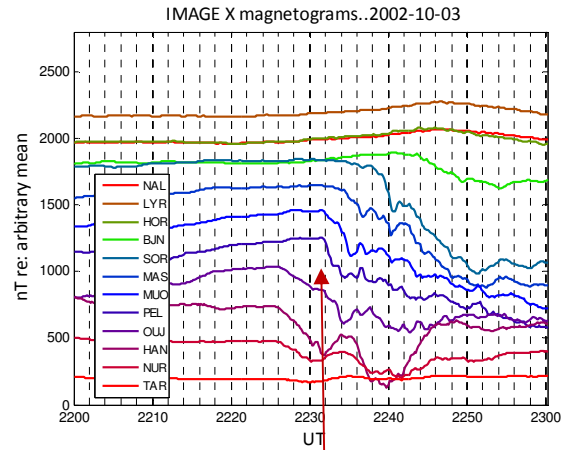
Polar trace at 2230UT 63°N -10°E

The Polar satellite was in the southern magnetosphere and the field line trace was over the Norwegian Sea at the same geomagnetic latitude as the IRIS riometer when a strong 80 μW m<sup>-2</sup> PFI was detected at 2231UT. This was during a sequence of substorm onsets which began at lower latitudes. The change in gradient associated with substorm onset also occurred at 2232UT at IMAGE ground magnetometers MAS and MUO which straddle the latitude of the IRIS riometer.

This result means that the PFI was coincident with the onset of the substorm precipitation if precipitation followed the geomagnetic shell.

The IRIS riometer keogram showed enhanced absorption to the south three minutes later at 2234UT.

The PFI vector was in the GSM -x -y -z direction suggesting that the source of the PFI was on the dusk side of the PSBL between the Earth and the Polar satellite at GSM x= -9.1R<sub>E</sub>.



**Group VI      Figure A7.31**  
**2100 - 2200UT on 2002-10-20**

Polar GSE [-7.6 3.5 1.9] R<sub>E</sub>  
 Polar GSM [-7.6 3.8 1.2] R<sub>E</sub>  
 Polar trace at 2144UT 67°N -12°E

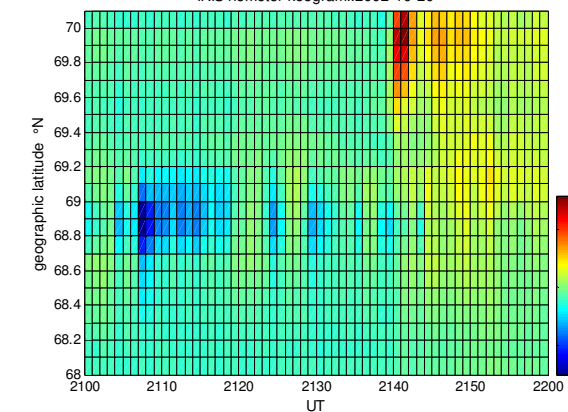
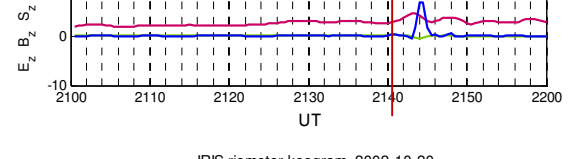
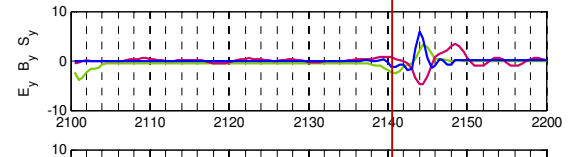
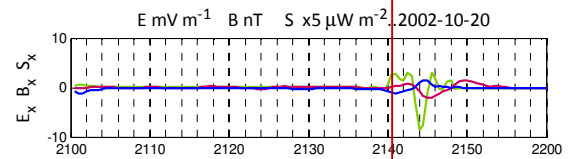
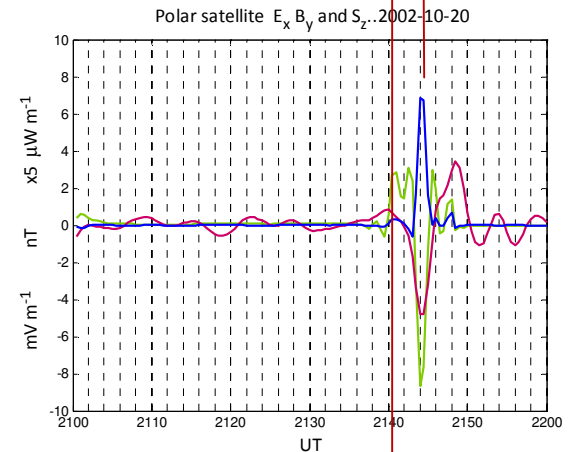
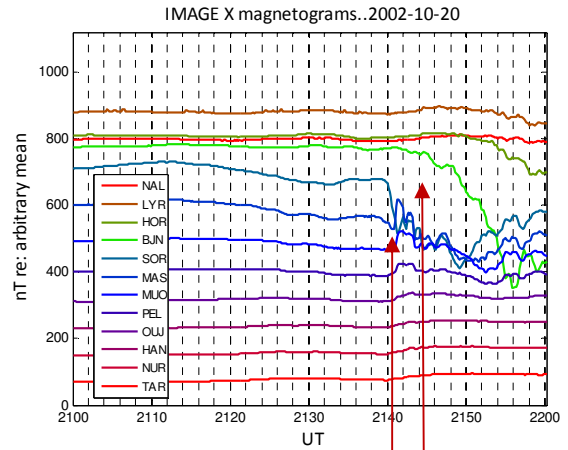
The Polar satellite field line trace was over the Norwegian Sea to the northeast of Iceland at the same geomagnetic latitude as IMAGE ground magnetometer BJN.

The sequence of events was that there was a well defined substorm onset at 2140UT at SOR prior to an IRIS riometer absorption spike at 2142UT at 69.9°N. A 35μWm<sup>-2</sup> S<sub>y</sub> S<sub>z</sub> PFI was detected at 2144UT coincident with the change of gradient associated with substorm onset at BJN.

This event therefore clearly suggests that the magnetospheric PFI is coincident with the onset of current precipitation at the same geomagnetic latitude as the Polar satellite field line trace.

The PFI was a good example of Group VI events where a dipolar magnetic field deflection was preceded by electric field activity 4 minutes prior to the main -Ex deflection that gave rise to the PFI.

Propagation of the PFI was in the GSM +x direction.



**Group VI Figure A7.32**

**1600 - 1700UT on 2002-12-14**

Polar GSE [0.5 9.4 -1.2] R<sub>E</sub>

Polar GSM [0.5 9.3 -2.0] R<sub>E</sub>

Polar trace at 1630UT 71°N 8°E

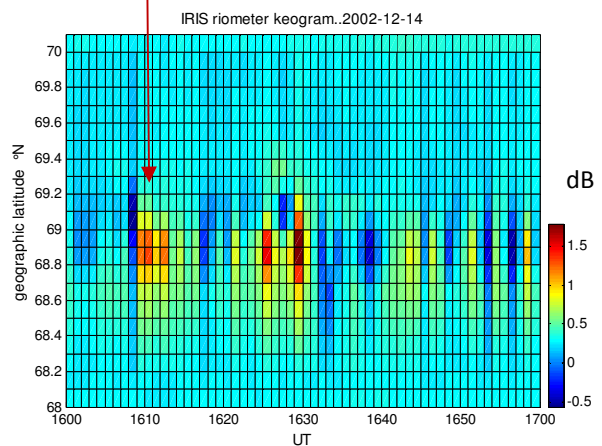
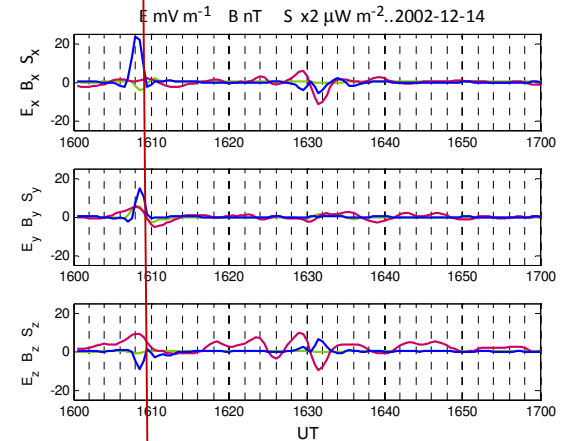
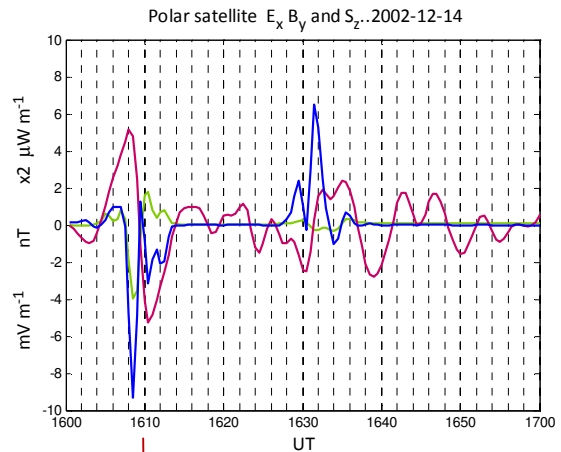
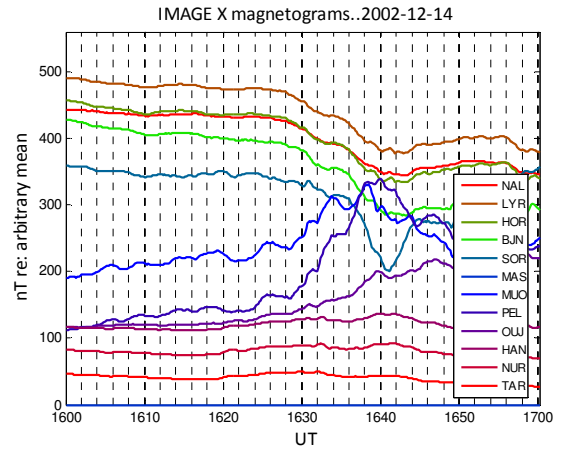
The Polar satellite had passed perigee and was in the southern magnetosphere at the time of the first  $-19 \mu\text{Wm}^{-2}$  S<sub>z</sub> PFI at 1608UT.

The second  $+13\mu\text{Wm}^{-2}$  PFI at 1631UT would not have been expected to give rise to a ground signal in the northern hemisphere.

The first event was coincident with an enhanced absorption spike in the IRIS riometer keogram at 1609UT although the Polar satellite field line trace was geomagnetically to the north of Kilpisjärvi.

The IRIS riometer keogram had the character of Group I oscillations.

The PFI vector at 1608UT was predominantly in the GSM -z direction and the PFI vector at 1632UT in the GSM -x direction.



**Group VI      Figure A7.33**

**1830 - 1930UT on 2003-09-30**

Polar GSE [-8.4 3.2 -0.5]  $R_E$

Polar GSM [-8.4 2.9 -1.4]  $R_E$

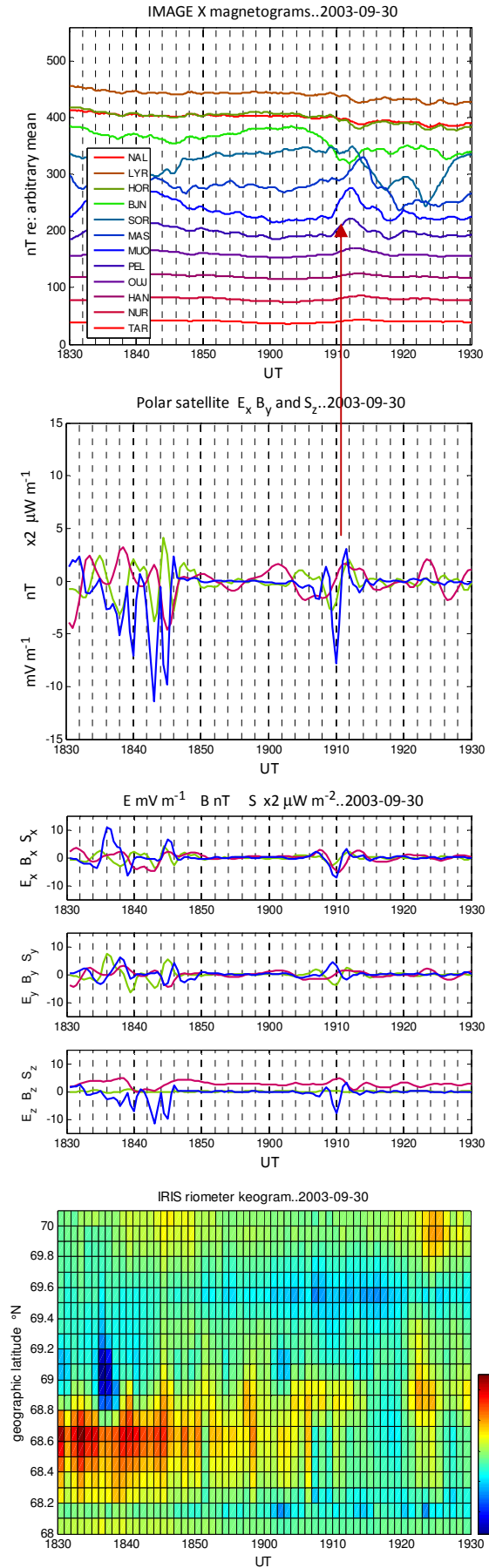
Polar trace at 1910 UT 72°N 38°E

The Polar satellite was in the southern magnetosphere and the field line trace was geomagnetically at the same latitude as the IRIS riometer, although further to the east.

IMAGE ground magnetometer SOR was to the north of the field line trace and substorm onset began two minutes after the PFI at 1910UT, a latitudinal feature that was seen in many other events. However there was no substorm at the latitude of the IRIS riometer and therefore no enhanced absorption at 1910UT.

Propagation of this event was in the GSE +x direction almost parallel to the x axis suggesting that the source was in the tail region beyond GSM = -8.4 $R_E$ .

The IRIS riometer keogram showed enhanced absorption at the time of the four -Sz PFIs around 1840UT. As these all had the same sign they are classified as magnetospheric Group IV.



**Group VI Figure A7.34**

**1800 -1900UT on 2003-10-03**

Polar GSE [-8.1 4.7 -2.2]  $R_E$

Polar GSM [-8.1 3.7 -3.6]  $R_E$

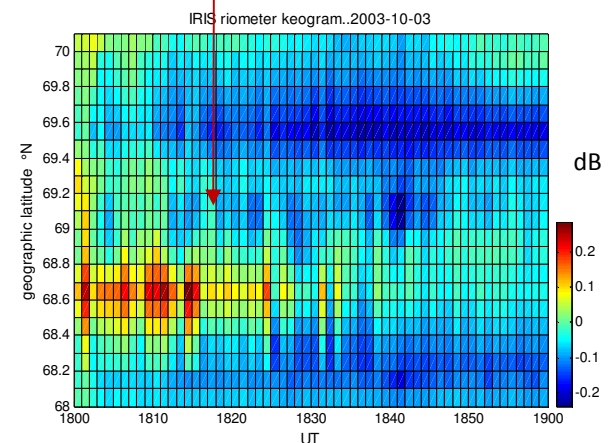
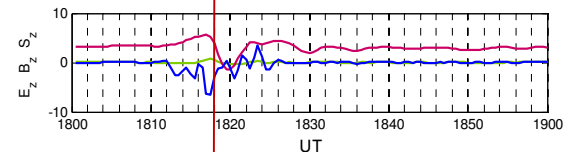
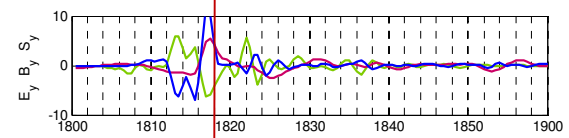
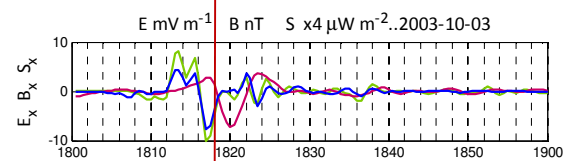
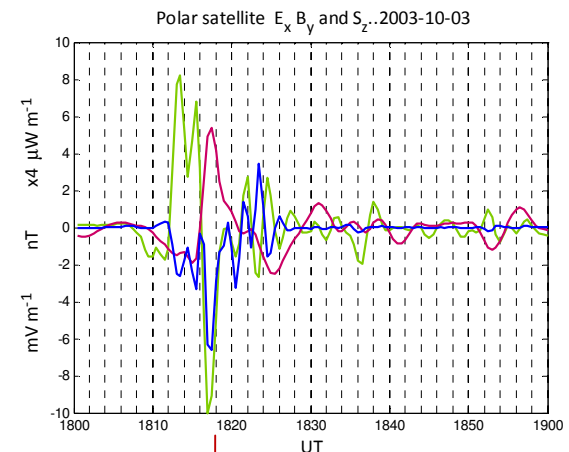
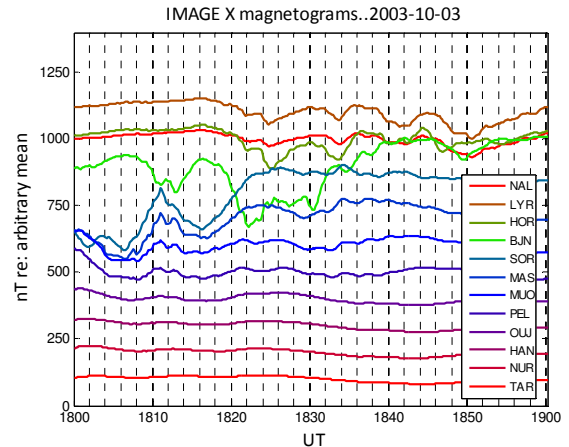
Polar trace at 1820UT 74°N 47°E

The Polar satellite was in the southern magnetosphere and the field line trace was over the Barents Sea to the north of Russia but near to the geomagnetic latitude of the IRIS riometer.

This is another example of a Group VI event where the PFI at 1817UT was preceded by four minutes of electric field activity and in fact the IRIS riometer keogram has the character associated with Group I electrical activity.

The high-latitude OGMD event at 1811UT between BJN and SOR was six minutes before the PFI, so is unlikely to be associated.

Propagation of the PFI was in the GSM +x -y direction suggesting a source tailward of GSM x = -8.1 $R_E$ .



**Group VI Figure A7.35**

**1900 - 2000UT on 2003-10-20**

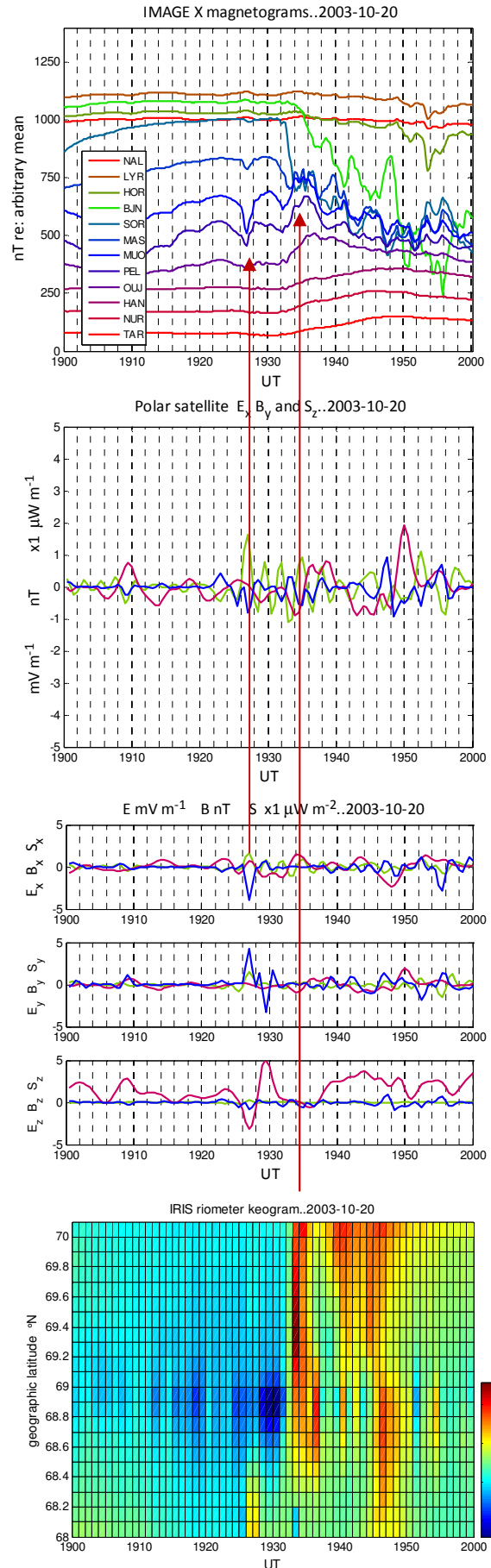
Polar GSE [-6.1 4.2 1.1]  $R_E$

Polar GSM [-6.1 4.4 0.0]  $R_E$

Polar trace at 1930UT 66°N 20°E

The Polar satellite field line trace was to the west of IMAGE ground magnetometer PEL which recorded a negative deflection at 1927UT. The Polar satellite was crossing the GSM x-y plane when an  $E_x$  deflection gave rise to a weak PFI also at 1927UT with  $S_x$  and  $S_y$  components. The absence of an  $S_z$  component is explained by Figure 6.7 and indicates that the source was near to this plane in the tail plasma sheet. However the propagation was in the GSM -y -z direction suggesting that the source may have been around GSM  $x \approx -6R_E$

This event was followed by a substorm onset six minutes later at 1933UT to the north at SOR and, consistent with this, the IRIS riometer keogram showed enhanced precipitation to the north from 1934UT onwards during the substorm expansion.



**Group VI Figure A7.36**

**2000 - 2100UT on 2003-10-26**

Polar GSE [-6.1 6.4 -0.3]  $R_E$

Polar GSM [-6.1 6.3 -1.5]  $R_E$

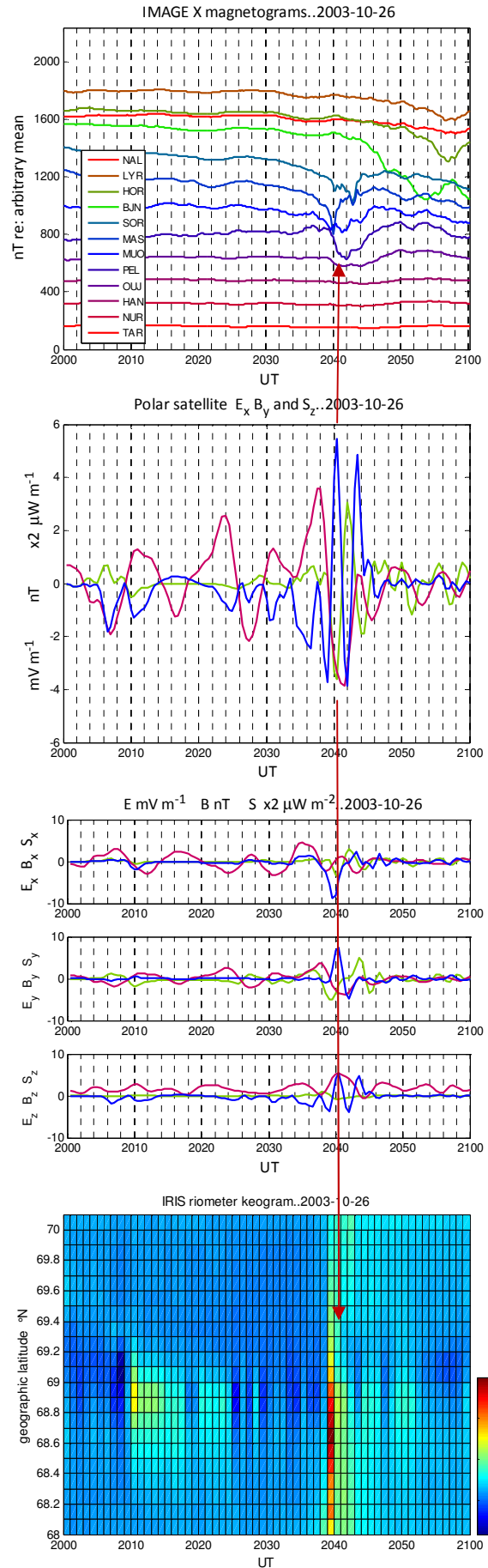
Polar trace at 2040UT 64°N -13°E

The Polar satellite was in the southern magnetosphere and the field line trace was to the southeast of Iceland at a similar geomagnetic latitude as IMAGE ground magnetometer SOR.

This event could have been classified as Group IV because of the multiple oscillations in the  $S_z$  field-aligned component, but these are not present in the  $S_x$  and  $S_y$  components. The Polar satellite was close to the tail equatorial region and the explanation of the sign of  $S_z$  in Figure 6.7 also suggests that other components might be present. Oscillating Poynting fluxes were often observed when the Polar satellite was in the PSBL equatorial region.

The spike in the IRIS riometer keogram at 2039UT coincided with the first - $S_z$  PFI and with the negative deflection at MAS, showing again that the PFIs are associated with precipitation.

The PFI vector, as observed by the Polar satellite at GSM  $x = -6.1R_E$  was predominantly sunward.



**Group VI Figure A7.37**

**1530 - 1630UT on 2003-11-25**

Polar GSE [-1.3 9.2 -1.7] R<sub>E</sub>

Polar GSM [-1.3 8.6 -3.6] R<sub>E</sub>

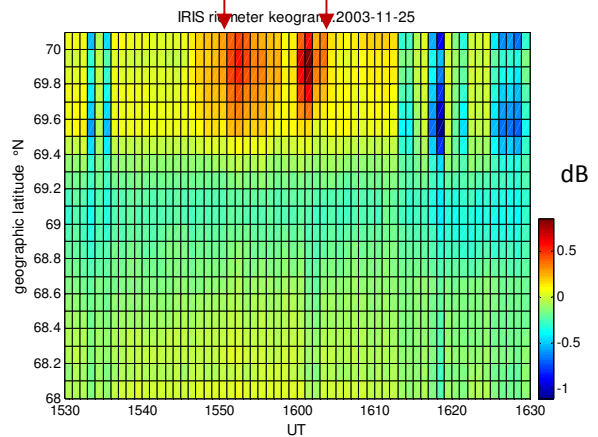
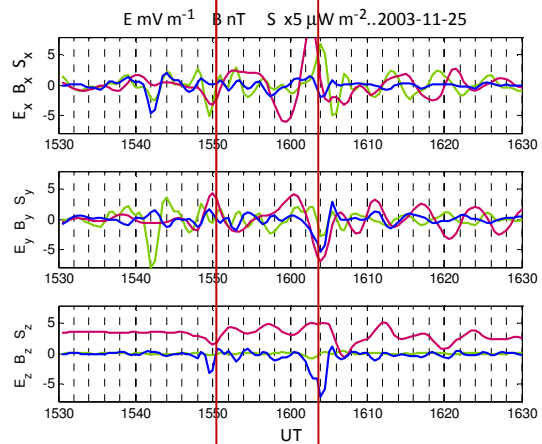
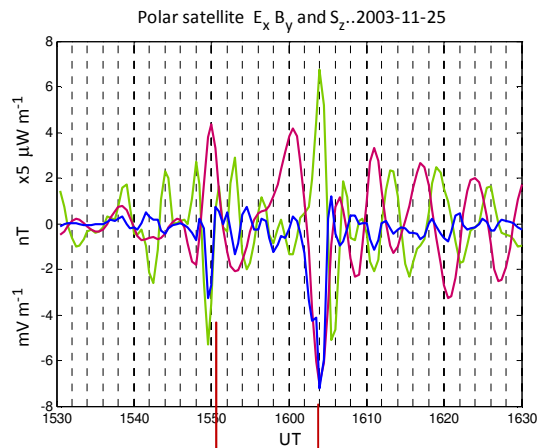
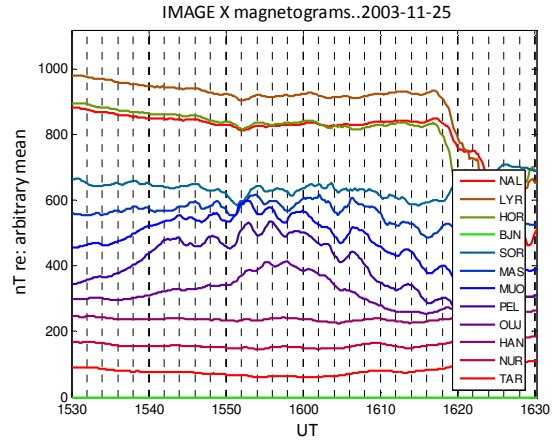
Polar trace at 73°N 22°E

The Polar satellite field line trace was over the Norwegian Sea between IMAGE ground magnetometers BJA and SOR.

Irregular oscillations preceding a high latitude substorm were observed in the SOR-PEL magnetograms from 1544UT onwards. Electric field oscillations with a frequency of 3.0 mHz were detected in Polar satellite data at the same time and magnetic field oscillations with the same frequency appeared after 1600UT. This resulted in the -35 μWm<sup>-2</sup> PFI at 1604UT which was followed by quadrature oscillations suggesting that quadrature resonances were set up on field lines after this event as in the event on 2003-10-19 [Figure A7.22].

The IRIS riometer keogram recorded enhanced absorption during the electric field oscillations not unlike that associated with Group I. The 0.7dB peak at 1601UT was three minutes before the higher latitude PFI consistent with the pattern of propagation towards higher latitudes.

The PFI vector at 1604UT was in the GSM +x and -y directions.



**Group VI      Figure A7.38**

**1700 - 1800UT on 2003-12-12**

Polar GSE [-0.6 6.1 1.7] R<sub>E</sub>

Polar GSM [-0.6 6.1 1.4] R<sub>E</sub>

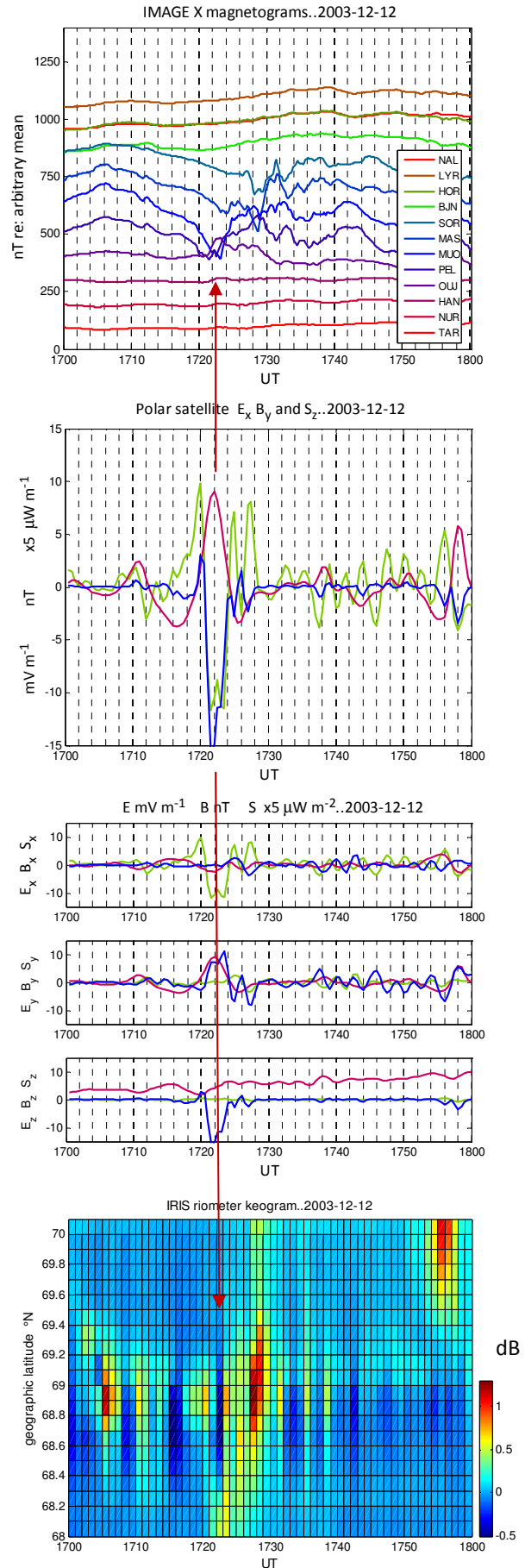
Polar trace at 1720UT 66°N -5°E

This is the only example where a -S<sub>z</sub> PFI was detected when the Polar satellite was in the northern magnetosphere. The field line trace was near to the geomagnetic latitude of IMAGE ground magnetometer SOR.

A -91 μWm<sup>-2</sup> S<sub>z</sub> component of Poynting flux impulse was detected at the Polar satellite location on the duskside at 1722UT at the same time as an OGMD event between PEL and OUI. This was followed by Pi2 oscillations with a duration of about 10 minutes. The 1.2dB absorption event in the IRIS riometer occurred five minutes later at 1727UT.

E<sub>x</sub> component signals were present in the magnetosphere and, as expected, the IRIS riometer keogram showed the character of Group I electric field oscillations.

The PFI vector at 1722UT was in the GSM +y and -z directions.



## Bibliography

- Aikio, A.T., H.J. Opgenoorth, M.A.L. Persson and K.U. Kaila 1993  
Ground-based measurements of an arc-associated electric field  
Journal of Atmospheric and Terrestrial Physics Vol. 55 No. 4/5 797-808
- Akasofu, S.-I. 1964  
The development of the auroral substorm  
Planet Space Sci. 12 273-282
- Alfvén, H. 1942  
Existence of Electromagnetic-Hydrodynamic Waves  
Nature No. 3805 October 3 405-6
- Alfvén, H. 1950  
Cosmical Electrodynamics  
Oxford Clarendon Press
- Alfvén, H. 1970  
Plasma physics, space research and the origin of the solar system  
Nobel Lecture December 11
- Allan, W. and E. M. Poulter 1992  
ULF waves - their relationship to the structure of the Earth's magnetosphere  
Rep. Prog. Phys. 55 533-598
- Aminaei, A., F. Honary, A.J. Kavanagh, E. Spanswick and A. Viljanen 2006  
Characteristics of night-time absorption spike events  
Ann. Geophys. 24 1887-1904
- Amm, O., P. Janhunen, H.J. Opgenoorth, T.I. Pulkkinen and A. Viljanen 2000  
Ionospheric shear flow situations observed by the MIRACLE network and the concept of Harang discontinuity  
Magnetospheric Current Systems Geophysical monograph 118 AGU
- Anderson, B.J. 1994  
An Overview of Spacecraft Observations of 10s to 600s Period Magnetic Pulsations in the Earth's Magnetosphere  
Solar Wind Sources of Magnetospheric Ultra-Low-Frequency Waves  
Geophysical Monograph 81 AGU
- Angelopoulos, V., James P. McFadden, David Larson, Charles W. Carlson, Stephen B. Mende, Harald Frey, Tai Phan, David G. Sibeck, Karl-Heinz Glassmeier, Uli Auster, Eric Donovan, Ian R. Mann, I. Johnathan Rae, Christopher T. Russell, Andrei Runov, Xu-Zhi Zhou, Larry Kepko 2008  
Tail reconnection triggering substorm onset  
Science Vol. 321 15 August
- Armstrong, James C., S.-I. Akasofu and Gordon Rostoker 1975  
A comparison of satellite observations of Birkeland currents with ground observations of visible aurora and ionospheric currents  
Journal of Geophysical Research 80 No. A4 February 1
- Baker, D.N., T.K. Pulkkinen, V. Angelopoulos, W. Baumjohann and R.L. McPherron 1996  
Neutral line model of substorms: past results and present view  
Journal of Geophysical Research 101 12,975

- Baker, Gregory J., Eric F Donovan and Brian J Jackel 2003  
A comprehensive survey of auroral latitude Pc5 pulsation characteristics  
Journal of Geophysical Research Vol. 108 No. A10 1384 doi:10.1029/2002JA009801
- Baker, Kile B., Mark J. Engebretson, Alan S. Rodger and Roger L. Arnoldy 1998  
The coherence scale length of band limited Pc3 pulsations in the ionosphere  
Geophysical Research Letters Vol. 25 No. 13 2357 – 2360 July 1
- Bamford, R, K.J. Gibson, A.J. Thornton, J. Bradford, R. Bingham, L. Gargate, L.O. Silva, R.A. Fonseca, M. Hapgood, C. Norberg, T. Todd, R. Stamper 2008  
The interaction of a flowing plasma with a dipole magnetic field: measurements and modelling of a diamagnetic cavity relevant to spacecraft protection  
Plasma Physics Controlled Fusion 50 124025 [11 pages]
- Baumjohann, Wolfgang, and Rudolf A Treumann 1997  
Basic Space Plasma Physics  
Imperial College Press ISBN 1 86094 079 X
- Birn, Joachim, and Michael Hesse 2000  
The current disruption myth  
Magnetospheric Current Systems Geophysical Monograph 118 AGU
- Birn, Joachim, and Eric Priest 2006  
Reconnection of magnetic fields  
Cambridge 978 0 52185420 7
- Block, L.P. and C.-G. Fälthammar 1990  
The Role of Magnetic-Field-Aligned Electric Fields in Auroral Acceleration  
Journal of Geophysical Research Vol. 95 No. A5 5877-5888 May 1
- Boas, Mary 1966  
Mathematical Methods in the Physical Sciences  
John Wiley Inc
- Braithwaite, Nicholas 2008  
Physics World - Letters December
- British Geological Survey  
Monthly Magnetic Bulletin for Hartland and Lerwick Observatories  
Murchison House West mains Road Edinburgh EH9 3LA Scotland
- Brittnacher, M., M. Filligam, G. Parks, G. Germany and J. Spann 1999  
Polar cap area and boundary motion during substorms  
Journal of Geophysical Research Vol. 104 12,251-12,262
- Brüning, K. and C.K. Goertz 1986  
Dynamics of a discrete auroral arc  
Journal of Geophysical Research Vol. 91 No. A6 7057-7064 June 1
- Chaplin, William J. 2006  
Music of the Sun  
Oneworld Publications ISBN-13:978-1-85168-451-9
- Chapman, S. 1951  
The Earth's Magnetism  
Methuen and Co. Ltd

- Chaston, C.C. 2006  
 ULF Waves and Auroral electrons  
 Magnetospheric ULF Waves: Synthesis and New Directions  
 Geophysical Monograph Series 169 AGU
- Chiu, Y.T and J.M. Cornwall 1980  
 Electrostatic model of a quiet auroral arc  
 Journal of Geophysical Research Vol. 85 543-556
- Choudhuri, Arnab Rai 1998  
 The Physics of Fluids and Plasmas [cgs units]  
 Cambridge University Press ISBN 0 521 55543 4
- Choy, Lawrence W., R.L Arnoldy, Wentworth Potter, Paul Kintner, and Laurence J. Cahill  
 Field-Aligned Particle Currents near an Auroral Arc 1971  
 Journal of Geophysical Research 8279-8298 December 1
- Clemmons, J.H., R. F. Pfaff, O. W. Lennartsson, F. S. Mozer, H. J. Singer, W. K. Peterson, J. D. Scudder,  
 C. A. Kletzing, P. J. Chi, D. D. Wallis and D. E. Larson 2000  
 Observations of travelling Pc5 waves and their relation to the magnetic cloud event  
 of January 1997  
 Journal of Geophysical Research Vol. 105 No. A3 5441-5452 March 1
- Coroniti, F.V. and C. F. Kennel 1970  
 Electron pulsation precipitations  
 Journal of Geophysical Research Space Physics Vol. 75 No. 7 March
- Cowley, S.W.H. and M. Lockwood 1992  
 Excitation and decay of solar wind driven flows in the magnetospheric-ionospheric system  
 Ann. Geophys. 10 103
- Cowley, S.W.H 1995  
 Where the solar wind blows  
 Physics World June
- Danielides, M.A., A. Ranta, N.Ivchenko, J.Jussila, G.Marklund and F.Primdahl 1999  
 Measurement of auroral characteristics by Auroral Turbulence III sounding rocket  
 Geophysica 35(1-2) 33-44
- Daum, P. 2007  
 VisAn MHD: a toolbox in Matlab for MHD computer model data visualisation and analysis  
 Ann. Geophys. 25 779-784
- Daum, P. 2009  
 Global MHD simulations of magnetospheric phenomena  
 PhD Thesis Lancaster University
- Dendy, Richard [ed.] 1993  
 Plasma Physics  
 Cambridge University Press ISBN 0 521 48452 9
- Dent, Z. 2003  
 ULF wave remote sensing of magnetospheric plasma density  
 PhD Thesis University of York

- Dombeck, J., C. Cattell and J.R. Wygant 2005  
Alfvén waves and Poynting flux observed simultaneously by Polar and FAST in the plasma sheet boundary layer  
Journal of Geophysical Research Vol. 110 A12S90
- Dungey, J.W. 1954  
Electrodynamics of the outer atmosphere  
Pennsylvania State University Ionosphere Research Laboratory Report
- Dungey, J.W. 1961  
Interplanetary magnetic field and the auroral zones  
Phys. Rev. Lett. 6 47
- Elkington, Scot R. 1994  
A Review of ULF Interactions With radiation Belt Electrons  
Solar Wind Sources of Magnetospheric Ultra-Low-Frequency Waves  
Geophysical Monograph 81 AGU
- Engebretson, Mark, Karl-Heinz Glassmeier and Martin Stellmacher 1998  
The dependence of high-latitude Pc5 wave power on solar wind velocity and on the phase of high-speed solar wind streams  
Journal of Geophysical Research Vol 103 No.A11 26271-26283 November 1
- Erlanson, R.E., L.J. Zanetti, M. J. Engebretson, R. Arnoldy, T. Bosinger and K. Mursula 1994  
Pc1 Waves Generated by a Magnetospheric Compression During the Recovery Phase of a Geomagnetic Storm  
Solar Wind Sources of Magnetospheric Ultra-Low-Frequency Waves  
Geophysical Monograph 81 AGU
- Fleisch, Daniel 2008  
A student's guide to Maxwell's equations  
ISBN 978-0-521-70147-1 CUP 2008
- Fukushima, Naoshi 1976  
General theorem for no ground magnetic effect of vertical currents connected with Pederson currents in the uniform-conductivity ionosphere  
Rep. Ionos Space Res. Jap. **30** 35-50
- Greenwald, R.A., K.B. Baker, J.R. Dudeney, M. Pinnock, T.B. Jones, E.C. Thomas, J.-P. Villain, J.-C. Cerisier, C. Senior, C. Hanuise, R.D. Hunsucker, G. Sofko, J. Koeler, E. Nielsen, R. Pellinen, A.D.M. Walker, N. Sato and H. Yamagishi 1995  
Darn/SuperDARN: a global view of the dynamics of high-latitude convection  
Space Sci. Rev. 71 761-796
- Greenwald, R.A., J.M. Ruohoniemi, W.A. Bristow, G.J. Sofko, J.-P. Villain, A. Huuskonen, S. Kokubun and L.A. Frank 1996  
Mesoscale dayside convection vortices and their relation to substorm  
Journal of Geophysical Research Vol. 101 21,697-21,713
- Gurnett, Donald A. and Amitava Bhattacharjee 2008  
Introduction to Plasma Physics  
CUP 2005 ISBN 0521364833
- Hapgood, M. A., 1992  
Space physics coordinate transformations: A user guide,  
*Planet. Space Sci.*, 40 (5), pp. 711-717

- Harrold, B.G., and J.C. Samson 1992  
 Standing ULF modes of the magnetosphere: A theory  
 Geophysical Research Letters 19 1811
- Harvey, P., F. S. Mozer, D. Pankow, J. Wygant, N. C. Maynard, H. Singer, W. Sullivan, P. B. Anderson, R. Pfaff, T. Aggson, A. Pedersen, C. G. Falthammar, and P. Tanskannen 1995  
 The electric field instrument on the Polar satellite  
*Space Science Reviews* 71: 583-596
- Hesse, Michael and Joachim Birn 2000  
 Near and mid-tail flow during substorms: small- and large-scale aspects of current disruption  
 Magnetospheric Current Systems Geophysical Monograph 118 AGU
- Howard, J.A. and F. W. Menk 2001  
 Propagation of 10-50 mHz ULF waves with high spatial coherence at high latitudes  
 Geophysical Research Letters Vol. 28 No. 2 231-234 January 1
- Hsu, Tung-Shin, and R.L. McPherron 2002  
 An evaluation of the statistical significance of the association between northward turnings of the interplanetary magnetic field and substorm expansion onsets  
 Journal of Geophysical Research Vol.107 No A11 1398
- Hughes, W.J. and D.J. Southwood 1976  
 The screening of micropulsation signals by the atmosphere and ionosphere  
 Journal of Geophysical Research 81 3234-3240
- Hughes, Jeffrey W. 1994  
 Magnetospheric ULF Waves: A Tutorial With a Historical Perspective  
 Solar Wind Sources of Magnetospheric Ultra-Low-Frequency Waves  
 Geophysical Monograph 81 AGU
- Itonaga, M. and K. Yumoto 1998  
 ULF waves and the ground magnetic field  
 Journal of Geophysical Research Vol.103 No. A5 9285-9291 May 1
- Jacobs, J.A. 1970  
 Geomagnetic Micropulsations [cgs units]  
 Springer-Verlag
- Jacquey, Christian 2000  
 Substorm associated tail current changes inferred from lobe magnetic field observations  
 Magnetospheric Current Systems Geophysical Monograph 118 AGU
- Jenkins and White 1957  
 Fundamentals of Optics  
 McGraw Hill
- Jones, D.S. 1965  
 Electrical and Mechanical Oscillations  
 Routledge and Kegan Paul
- Keiling, A., J.R. Yygant, C. Cattell, M. temerin, F.S. Mozer, C.A. Kletzing, J. Scudder, C.T. Russell, W. Lotko and A.V. Strelstov 2000  
 Large Alfvén wave power in the plasma sheet boundary layer during the expansion phases of substorms  
 Geophysical Research Letters 27 3169 – 3172

- Keiling, Andreas 2009  
Alfvén waves and their roles in the dynamics of the Earth's magnetotail: a review  
Space Science Review (2009) 142: 73-156
- Keiling, A., J.R. Wygant, C. Cattell, K.-H. Kim, C.T. Russell, D-K Milling, M.Temerin, F.S. Mozer and C.A Kletzing 2001  
Pi2 pulsations observed with the Polar satellite and ground stations: Coupling of trapped and fast mode waves to a midlatitude fast mode resonance  
Journal of Geophysical Research Vol. 106 No. A11 Pages 25891-25904 November 1
- Keiling, A., J.R. Wygant, C. Cattell, W. Peria, G. Parks, M. Temerin, F.S. Mozer, C.T. Russell and C.A. Kletzing 2002  
Correlation of Alfvén wave Poynting flux in the plasma sheet at 4 – 7 Re with ionospheric electron energy flux  
Journal of Geophysical Research Vol. 107 No. A7 1132 doi: 10.1029/2001JA900140
- Keller, F.J., W. Edward Gettys and Malcolm J. Skove 1993  
Physics Classical and Modern  
McGraw Hill ISBN 0-07-023460-4
- Kivelson, M.G., J. Etcheto and J.B. Trotignon 1984  
Global compressional oscillations in the terrestrial magnetosphere: The evidence and a model  
Journal of Geophysical Research 89 9851-9856
- Kivelson, M.G. and D.J Southwood 1985  
Resonant ULF waves: A new interpretation  
Geophysical Research Letters 12, 49-52
- Kivelson, Margaret Galland 2006  
ULF Waves From the Ionosphere to the Outer Planets  
Magnetospheric ULF Waves: Synthesis and New directions  
Geophysical Monograph Series 169 AGU 10.1029/169GM04
- Kivelson, Margaret G. and Christopher T Russell 1995  
Introduction to Space Physics  
Cambridge University Press ISBN 0 521 45714 9
- Knauer, W. 1966  
Diocotron instability in plasmas and gas discharges  
Journal of Applied Physics 37 (2) 602-611
- Korotova, G.J., and D. G. Sibeck 1994  
Generation of ULF Magnetic Pulsations in Response to Sudden Variations in Solar Wind Dynamic Pressure  
Solar Wind Sources of Magnetospheric Ultra-Low-Frequency Waves  
Geophysical Monograph 81 AGU
- Kosch, M.J., M.W.J. Scourfield and O. Amm 2001  
The importance of conductivity gradients in field-aligned current studies  
Adv. Space Res. Vol. 27 Nos 6-7 1277-1282
- Laurie, William 1997  
Fundamentals of Geophysics  
Cambridge University Press ISBN 0 521 46164 2

- Lester, Mark 2000  
HF coherent scatter radar observations of ionospheric convection during magnetospheric substorms  
Adv. Polar Upper Atmos. Res. 14 179-201
- Liou, K., P.T. Newell, C.-I. Meng, A.T.Y. Lui, M. Brittnacher and G. Parks 1997  
Dayside auroral activity as a possible precursor of substorm onsets: a survey using Polar ultraviolet imagery  
Journal of Geophysical Research Vol. 102 No. A9 19,835-19,843 September 1
- Liou, K., P.T. Newell and C.-I. Meng 1997  
Synoptic auroral distribution: a survey using Polar ultraviolet imagery  
Journal of Geophysical Research Vol. 102 No. A12 27,197-27,205 December 1
- Lu, Gang 2000  
A synthetic view of the magnetospheric-ionospheric current system associated with substorms  
Magnetospheric Current Systems Geophysical monograph 118 AGU
- Luhmann, J.G., S. M. Petrinec and C. T. Russell 1994  
Long Term Variations in the Solar Wind of Importance to ULF Phenomena  
Solar Wind Sources of Magnetospheric Ultra-Low-Frequency Waves  
Geophysical Monograph 81 AGU
- Lühr, Hermann and Wiebke Blawert 1994  
Ground Signatures of Travelling Convection Vortices  
Solar Wind Sources of Magnetospheric Ultra-Low-Frequency Waves  
Geophysical Monograph 81 AGU
- Lühr, H., A. Aylward, S.C. Buchert, A. Pajunpää, T. Holmboe and S.M. Zalewski 1998  
Westward moving dynamic substorm features observed with the iMAGE magnetometer network and other ground based instruments  
Ann. Geophys. 16 425-440
- Lui, A.T.Y. 1996  
Current disruption in the Earth's magnetosphere: observation and models  
Journal of Geophysical Research 101, 13,067
- Lui, C.-H. and C.E Seyler 1992  
Electron Acceleration by Alfvén Waves in the the Magnetosphere  
Journal of Geophysical Research Vol. 97, No. A4, 3955-3963 April 1
- Lundquist, S. 1947  
Experimental Investigations of Magneto-hydrodynamic waves  
Phys.Rev. 107, 1805-1809
- Lyatsky, W., R. D. Elphinstone, Q. Pao and L. I. Cogger 1999  
Field line resonance interference model for multiple auroral arc generation  
Journal of Geophysical Research Vol.104, No A1, Pages 263-268, January 1
- Lyons, L.R., T. Nagai, J.C. Samson, E. Zesta, T. Yamamoto, T. Mukai, A. Nishida and S. Kokubun 2000  
Structured currents associated with tail bursty flows during turbulent plasma sheet conditions  
Magnetospheric Current Systems Geophysical monograph 118 AGU
- Mann Ian R. and Andrew Wright 1999  
Diagnosing the Excitation Mechanisms of Pc5 Magnetospheric Flank Waveguide Modes and FLRs  
Geophysical Research Letters Vol. 26, No. 16, Pages 2609-2912, August 15

- Mann, I.R., T. P. O' Brien and D. K. Milling 2004  
Correlations between ULF wave power, solar wind speed and relativistic electron flux in the magnetosphere: solar cycle dependence  
Journal of Atmospheric and Solar-Terrestrial Physics 66 (2004) 187-198
- Mathie, R.A., I R Mann, F W Menk and D Orr 1999  
Pc5 ULF pulsations associated with waveguide modes observed with the IMAGE magnetometer array  
Journal of Geophysical Research Vol 104 No.A4 7025-7036 April 1
- Mathie, R.A. and I.R. Mann 2001  
On the solar wind control of Pc5 ULF pulsation power at mid-latitudes: Implications for MeV electron acceleration in the outer radiation belt.  
Journal of Geophysical Research 106 29783
- McLaughlin, J.A., I.De Moortel, A.W. Hood and C.S. Brady 2009  
Nonlinear fast magnetoacoustic wave propagation in the neighbourhood of a 2D magnetic X-point: oscillatory reconnection  
Astronomy and Astrophysics 493 227-240
- Menk, F.W., T K Yeoman, D M Wright, M Lester and F Honary 2003  
High-latitude observations of impulse-driven ULF pulsations in the ionosphere and on the ground  
Ann. Geophys. 21 559-576
- Mitchell, D.G., M.J. Engebretson, D.J. Williams, C.A. Cattell and R. Lundin 1990  
Pc5 pulsations in the outer dawn magnetosphere seen by ISEE 1 and 2  
Journal of Geophysics Research 95 967-975
- Morley, S.K. and M.P. Freeman 2007  
On the association between northward turnings of the interplanetary magnetic field and substorm onsets  
Geophysical Research Letters Vol. 34 L08104
- Mostl, C., C.J. Farrugia, C. Miklenic, M. Temmer, A.B. Galvin, J.G. Luhmann, E.K.J. Kilpua, M. Leitner, T. Nieves-Chinchilla, A. Veronig and H.K. Biernat 2009  
Multispacecraft recovery of a magnetic cloud and its origin from magnetic reconnection on the Sun  
Journal of Geophysical Research - Space Physics 114 A04102 DOI 10.1029/2008JA013657
- Newkirk, G. Jr., and L.A. Fisk 1985  
Variation of cosmic rays and solar wind properties with respect to the heliospheric current sheet 1. Five GeV protons and solar wind speed  
Journal of Geophysical Research 90 3391
- Nishida, A. 1964  
Ionospheric screening and sudden storm commencement  
Journal of Geophysical Research 69 1861
- Nosé, M., T Iyemori, M Takeda, F. Honary, S. Marple, J. Matzka, T .Ookawa, K .Takahashi, and C. Cifuentes-Nava 2006  
Automated detection of Pi2 pulsations to monitor substorm signatures: its application to real-time data and archived data  
Int. Conf. Substorms-8 XX: 1-6
- Ohanian, Hans C. 1988  
Classical Electrodynamics [cgs units]  
Allyn and Bacon Inc. ISBN 0 205 11303 6

- Ohanian, Hans C. 1994  
Principles of Physics  
W. W. Norton and Company ISBN 0-393-95773
- Opgenoorth, H., I. Haggstrom, P.J.S. Williams and G.O.L. Jones 1990  
Regions of strongly enhanced perpendicular electric fields adjacent to auroral arcs  
Journal of Atmospheric and Terrestrial Physics Vol. 52 No. 6-8 449-458
- Orr, D. 1984  
Magnetospheric hydromagnetic waves: their eigenperiods, amplitudes and phase variations; a tutorial introduction  
Journal of Geophysics 55: 76 - 84
- Pain, H.J. 1983  
The Physics of Vibrations and Waves  
John Wiley and Sons Ltd ISBN 0 471 901822
- Parks, George K.  
Physics of Space Plasmas  
Perseus Books 1991 ISBN 0-201-48987-2
- Paschmann, G., G. Haerendel, I. Papamastorakis, N. Sckopke, S.J. Bame, G.T. Gosling and C.T. Russell 1982  
Plasma and magnetic field characteristics of magnetic flux transfer events  
Journal of Geophysical Research Vol. 87 No. A4 2159-2168 April 1
- Peratt, Anthony L. 2003  
Characteristics for the Occurrence of a High-Current Z-Pinch Aurora as Recorded in Antiquity  
IEEE Transactions on Plasma Science Vol. 31 No. 6 December
- Petschek, H.E. 1964  
Magnetic field annihilation  
AAS-NASA Symposium on the Physics of Solar Flares  
NASA SP-50 p405
- Pitt, V. 1975  
The Penguin Dictionary of Physics  
Penguin Books
- Posch, J.L., M. J. Engebretson, A. T. Weatherwax, D. L. Detrick, W. J. Hughes and C. G. MacLennan 1994  
Characteristics of broadband ULF magnetic pulsations at conjugate cusp latitude stations  
Journal of Geophysical Research Vol. 104 No. A1 311-331 January 1
- Potapov, A.S. and V. A. Mazur 1994  
Pc3 Pulsations: From the Source in the Upstream Region to Alfvén resonances in the Magnetosphere.  
Theory and Observations  
Solar Wind Sources of Magnetospheric Ultra-Low-Frequency Waves  
Geophysical Monograph 81 AGU
- Poynting, J. H., 1884  
Phil. Trans. R. Soc. 175 343
- Prölss, Gerd W. 2004  
Physics of the Earth's Space Environment  
Springer ISBN 3-540-21426-7

- Rae, I.J., E. F. Donovan, I. R. Mann, F. R. Fenrich, C. E. J. Watt, D. K. Milling, M. Lester, B. Layraud, J. A. Wild, H. J. Singer, H. Rème and A. Balogh 2005  
Evolution and characteristics of global Pc5 ULF waves during a high solar wind speed interval  
Journal of Geophysical Research Vol. 110 A12211 doi:10.1029/2005JA011007
- Rae, I.J., I.R. Mann, Z.C. Dent, D.K. Milling, E.F. Donovan and E. Spanswick 2007a  
Multiple field line resonances: Optical, magnetic and absorption signatures  
Planetary and Space Science Volume 55 Issue 6, April 2007, Pages 701 – 713
- Rae, I.J., C.E.J. Watt, F.R. Fenrich, I.R. Mann, L.G. Ozeke and A. Kale 2007b  
Energy deposition in the ionosphere through a global field line resonance  
Ann. Geophys. 25 2529-2539
- Rasinkangus, R., K. Marsula, G. Kremser, H. J. Singer, B. J. Fraser, A. Korth and W. J. Hughes 1994  
Simultaneous occurrence of Pc5 and Pc1 Pulsations in the Dawnside Magnetosphere: CCRES Observations  
Solar Wind Sources of Magnetospheric Ultra-Low-Frequency Waves  
Geophysical Monograph 81 AGU
- Russell, C.T., and R.C. Elphic 1979  
ISEE observations of flux transfer events at the dayside magnetopause  
Geophysical Research Letters 6 33
- Saka, O., O Watanabe, K Okuda and D N Baker 1999  
A slow mode wave as a possible source of Pi2 and associated particle precipitation  
Ann. Geophys. 17 674-681
- Samson, J.C., J.A. Jacobs, and G. Rostoker  
Latitude-dependent characteristics of long-period geomagnetic pulsations  
Journal of Geophysical Research 76 3675 1971
- Samson, J.C., and G. Rostoker 1972  
Latitude-dependent characteristics of high latitude Pc4 and Pc5 micropulsations  
Journal of Geophysics Research 77 6133 – 6144
- Samson, J.C. 1972  
Three-dimensional polarisation characteristics of high-latitude Pc5 geomagnetic micropulsations  
Journal of Geophysics Research 77 6145
- Samson, J.C., R.A. Greenwald, J.M. Ruohoniemi, T.J. Hughes and D.D. Wallis 1991  
Magnetometer and radar observations of magnetohydrodynamic cavity modes in the Earth's magnetosphere  
Can. J. Phys. 69 929
- Samson, J.C., T.J. Hughes, F. Creutzberg, D.D. Wallis, R.A. Greenwald and J.M. Ruohoniemi 1991  
Observations of a detached discrete arc in association with field line resonances  
Paper number 91JA00796
- Samson, J.C., R.A. Greenwald, J.M. Ruohoniemi, T.J. Hughes and A.D.M. Walker 1992  
Field line resonances associated with MHD waveguides in the Earth's magnetosphere  
Geophysical Research Letters 19 441-444

- Samson, J.C. and R. Rankin 1994  
 The Coupling of Solar Wind Energy to MHD Cavity Modes, waveguide Modes and Field line Resonances in the Earth's Magnetosphere  
 Solar Wind Sources of Magnetospheric Ultra-Low-Frequency Waves  
 Geophysical Monograph 81 AGU
- Schwartz, Steve, Christopher J. Owen and David Burgess 2004  
 Astrophysical Plasmas [Astrophysics MSc Course Notes]  
 Astronomy Unit, Queen Mary and Westfield College
- Shue, J.-H., J. K. Chao, H. C. Fu, C. T. Russell, P. Song, K. K. Khurana and H. J. Singer 1997  
 A new functional form to study the solar wind control of the magnetopause size and shape  
 Journal of Geophysical Research Vol. 102 No.A5 9297-9511 May1
- Smith, M.S.  
 Modern Physics  
 Longmans 1960
- Song, P. 1994  
 Observations of Waves at the Dayside Magnetopause  
 Solar Wind Sources of Magnetospheric Ultra-Low-Frequency Waves  
 Geophysical Monograph 81 AGU
- Song, Yan, Robert L. Lysak and Naiguo Lin 1994  
 Control of the generation of field-aligned currents and transverse ULF waves by the magnetic helicity input  
 Solar Wind Sources of Magnetospheric Ultra-Low-Frequency Waves  
 Geophysical Monograph 81 AGU
- Southwood, D.J. 1974  
 Some features of field line resonances in the magnetosphere  
 Planet. Space Sci. 22 483 – 491
- Southwood, D.J., and M.G. Kivelson 1990  
 The magnetohydrodynamic response of magnetospheric cavity to changes in solar wind pressure  
 Journal of Geophysics Research 95 2301
- Spiegel, Murray R. 1972  
 Statistics  
 Mc Graw-Hill Book Company
- Stern, David. P. 1996  
 A brief history of magnetospheric physics during the space age  
 Reviews of Geophysics 34 1-31
- Stewart, B. 1861  
 On the great magnetic disturbance which extended from August 28th to September 7th, 1859, as recorded by photography at the Kew Observatory.  
 Phil. Trans. R. Soc. London 423
- Storey, L.R.O. 1953  
 An investigation of whistling atmospheric  
 Phil. Trans. R. Soc. London A 9 1953 Vol. 246 No. 908113-141

Sturrock, Peter A. 1994  
Plasma Physics [cgs units]  
Cambridge University Press ISBN 0 521 44810 7

Sung, Z.D. 1935  
The text of Yi-King (and its Appendixes)  
Chinese original with English translation  
The China Modern Education Company Shanghai

Takahashi, Kazue, Brian J. Anderson, Patrick T. Newell, Tatsundo Yamamoto and Natsuo Sato  
Propagation of Compressional Pc3 Pulsations From Space to the Ground: A Case Study Using  
Multipoint Measurements  
Solar Wind Sources of Magnetospheric Ultra-Low-Frequency Waves  
Geophysical Monograph 81 AGU

Takahashi, Kazue, Kan Liou, Kiyohumi Yumoto, Kentarou Kitamura, Masahito Nosé and Farideh  
Honary 2005  
Source of Pc4 pulsations observed on the nightside  
Journal of Geophysical Research Vol.110 A12207 doi: 10.1029/2005JA011093

Teboul, Michel 1987  
Ancient Chinese Auroral Records: Interpretation Problems and Methods  
History of Oriental Astronomy [Chapter 2.5]  
Cambridge University Press ISBN 0 521 34659 2

Toivanen, P.K., D.N. Baker, W.K Peterson, X. Li, E.F. Donovan, A.Viljanen, J.R. Wygant and C.A.  
Kletzing 2001  
Plasma sheet dynamics observed by the Polar spacecraft in association with substorm onsets  
Journal of Geophysical Research Vol. 106 No.A9 19,117-19,130 September 1

Toivanen, P.K., D.N. Baker, W.K Peterson, H.J. Singer, J.Watermann, J.R. Wygant, C.T. Russell and  
C.A. Kletzing 2003  
Polar observations of transverse magnetic pulsations initiated at Substorm onset in the high latitude  
plasma sheet  
Journal of Geophysical Research 108 (A7) 1267 doi: 10.1029/2001 JA009141

Thompson, S.M., and M.G. Kivelson 2001  
New evidence for the origin of giant pulsations  
Journal of Geophysical Research 106 21 237-21,255

Troitskaya, V.A. 1994  
Discovery of Sources of Pc2-4 Waves – A Review of Research in the Former USSR  
Solar Wind Sources of Magnetospheric Ultra-Low-Frequency Waves  
Geophysical Monograph 81 AGU

Tullet, P.F. 1998  
Magnetometer observations and wavelet analysis of geomagnetic disturbances  
QMW Astrophysics MSc Project

Tullet, P.F., and F. Honary 2010  
A null phase-difference technique for ULF wave direction-finding  
Radiation Effects and Defects in Solids: Incorporating Plasma Science and Plasma Technology  
Vol. 165 No.2 February 2010 187-191

- Verő, József, and Bertalan Zieger 1994  
Upstream Waves and Field Line Resonances – Pulsation research at the Nagycenk Observatory During Three Solar Cycles  
Solar Wind Sources of Magnetospheric Ultra-Low-Frequency Waves  
Geophysical Monograph 81 AGU
- Walker, A.D.M. 2005  
Magnetohydrodynamic Waves in Geospace  
IOP Publishing  
ISBN 0 7503 0910 5
- Wild, J.A., T.K. Yeoman, P. Eglitis and H. Opgenoorth 2000  
Multi-instrument observations of the electric and magnetic field structure of omega bands  
Ann. Geophys. 18 99-110
- Wild, J.A., T. K. Yeoman, and C. L. Waters 2005  
Revised time-of-flight calculations for high-latitude geomagnetic pulsations using a realistic magnetospheric magnetic field model  
Journal of Geophysical Research Vol. 110 A11206 doi: 10.1029/2004JA010964
- Williams, P.J.S., G.O.L. Jones, B. Jones, H. Opgenoorth and I. Häggström 1990  
High resolution measurements of magnetospheric electric field  
Journal of Atmospheric and Terrestrial Physics Vol. 52 No. 6-8 439-448
- Yagova, N.V., L. J. Lanzerotti, U. Villante, V. A. Pillipenko, S. Lepidi, P. Francia, V. O. Papitashvili and A. S. Rodger 2002  
ULF Pc5-6 magnetic activity in the polar cap as observed along a geomagnetic meridian in Antarctica  
Journal of Geophysical Research Vol. 107 No.A8 10.1029/2001JA900143
- Yeoman, T.K., D. K. Milling and D. Orr 1990  
Pi2 Pulsation Polarisation Patterns on the UK Sub-Auroral Magnetometer Network (SAMNET)  
Planet Space Sci. Vol. 38, No. 5, 589-602
- Yeoman, T.K. and M. Pinnock 1996  
The high latitude convection response to an interval of substorm activity  
Ann. Geophys. 14 518-530
- Yeoman, T.K., D. M. Wright, P. J. Chapman and A. B. Stockton-Chalk 2000  
High-latitude observations of ULF waves with large azimuthal wavenumbers  
Journal of Geophysical Research Vol. 105 No.A3 5453-5452 March 1
- Ziesolleck, C.W.S., and D. R. McDiarmid 1994  
Auroral latitude Pc5 field line resonances: Quantised frequencies, spatial characteristics and diurnal variation  
Journal of Geophysical Research Vol. 99 No. A4 5817-5830 April 1
- Ziesolleck, C.W.S., and D. R. McDiarmid 1995  
Statistical survey of auroral latitude Pc5 spectral and polarisation characteristics  
Journal of Geophysical Research Vol. 100 No. A10 19,299-19,312 October 1